Abstract

Title of Dissertation: Characterizing young debris disks through far-infrared and optical observations

Jessica K. Donaldson, Doctor of Philosophy, 2014

Dissertation directed by: Professor Douglas P. Hamilton
Department of Astronomy
University of Maryland

and

Dr. Aki Roberge
Exoplanets & Stellar Astrophysics Laboratory
NASA Goddard Space Flight Center

Circumstellar disks are the environments where extrasolar planets are born. Debris disks in particular are the last stage of circumstellar disk evolution, the youngest of which may harbor still-forming terrestrial planets. This dissertation focuses on examining the properties of dust grains in the youngest debris disks as a proxy to study the unseen parent planetesimal population that produces the dust in destructive collisions. The parent planetesimals are important to understanding the late stages of terrestrial planets because they can deliver volatile material, such as water, to young terrestrial planets.

We used the *Herschel Space Observatory* to study young debris disks (ages $\sim 10 - 30$ Myr) in the far-infrared where the thermal emission from the dust grains is brightest. We constructed spectral energy distributions (SEDs) of 24 debris disks and fit them with our debris disk models to constrain dust parameters such as temperature, dust location, and grain size. We also looked for correlations between

the stellar and disk parameters and we found a trend between the disk temperature and stellar temperature, which we fit as a power-law of $T_{disk} \propto T_*^{0.85}$.

One bright, well studied disk in our sample, HD32297, has a well populated SED, allowing us to fit it with a more detailed model to determine dust grain composition. The HD32297 disk has also been imaged in scattered light, so we used the image to constrain the dust location before fitting the SED. We found the dust grains are composed of a highly porous and icy material, similar to cometary grains. This suggests there are icy comets in this system that could deliver water to any terrestrial planets in the disk.

We followed up this system by observing it with the *Hubble Space Telescope* to get simultaneous spatial and spectral data of the disk. These data let us look for compositional changes with disk radius. We found the disk has a very red color at optical wavelengths in the innermost radius we probed ($\sim$ 110 AU). This could indicate the presence of organic material, or it could be a property of the scattering phase function of large grains. Further analysis of this data is ongoing.

Characterizing young debris disks through far-infrared and optical observations

by

Jessica K. Donaldson

Dissertation submitted to the Faculty of the Graduate School of the
University of Maryland at College Park in partial fulfillment
of the requirements for the degree of
Doctor of Philosophy
2014

Advisory Committee:

Professor Douglas P. Hamilton, chair
Dr. Aki Roberge
Professor L. Drake Deming
Professor Lee G. Mundy
Professor Douglas C. Hamilton

Preface

Portions of this dissertation have been published elsewhere. Chapter 3 was previously published in its entirety in *The Astrophysical Journal* (Donaldson et al. 2012). Results in Chapter 3 were also presented at the 217$^{\text{th}}$ meeting of the American Astronomical Society in January 2011. Chapter 4 will be submitted in its entirety to *The Astrophysical Journal* in the near future. Results form Chapter 4 have already been presented at The Universe Explored by Herschel conference at ESA/ESTEC in October 2013. Chapter 5 was previously published in its entirety in *The Astrophysical Journal* (Donaldson et al. 2013) and its results presented at the 4$^{\text{th}}$ National Capital Area Disk Meeting at The Space Telescope Science Institute in July 2012. Preliminary results from Chapter 6 were presented at the 221$^{\text{st}}$ meeting of the American Astronomical Society in January 2013.

Acknowledgements

A great many people have helped me over the years to get to this point in my career, and I would like to thank them all for their support. Most importantly, I would like to thank my advisor, Aki Roberge, who was happy to take me on as a first year student and give me a rich new dataset to work with. Aki has provided me with countless hours of support over the last few years. She has taught me a great deal and has been an invaluable resource in furthering my education in astronomy research. She has also been a great mentor and guide through the nuances of a career in academia. I am especially grateful for the help in networking and introducing me to so many astronomers from all over the world.

Many other colleagues and collaborators have also contributed to my success. I would like to thank the entire Herschel GASPS team for making me immediately feel welcome, and for all the help and encouragement I've received over the years. Specifically I would like to thank Bill Dent, Carlos Eiroa, Sasha Krivov, Francois Menard, Jean-Charles Augereau,

Geoff Mathews, Christine Chen, Gwendolyn Meeus, Goran Sandell, and Pablo Riviere-Marichalar for contributing to Chapters 3 and 4 with their comments. Sasha Krivov especially deserves many thanks for his prompt and in depth comments on my paper drafts and for the long and lively discussions we've had both in person and via email. I also want to thank Jeremy Lebreton and Jean-Charles Augereau for providing me with a copy of the GRaTer code to use in Chapter 5 and answer my many question on its use.

I would also like to thank Alycia Weinberger for giving me access to the data used in Chapter 6. Alycia has always been very approachable and happy to answer all of my questions. I would also like to thank Alycia for inviting me to shadow her during a remote observing run. Several former and current NASA postdocs have mentored me, being good listeners and providing sage wisdom, not just at Goddard, but also as familiar faces at conferences. These include Hannah Jang-Condell, John Debes, and Chris Stark. Grad student Erika Nesvold also deserves credit for listening and understanding. I would like to thank Prof. Doug P. Hamilton for always appearing delighted to answer many and varied questions both from me and from Aki as she learns to navigate the University's various regulations.

Many friends and family have also helped me succeed through many years of support. I would like to thank my parents for supporting and encouraging me, especially my father who infected me with an interest in science at a young age. Mia Bovill, who shared a small windowless office with me during my first two years of grad school, helped me through my early fears and I would have had a much harder time without her

reassurances. I owe a huge debt to my lifelong friends who have always been there for me. Rachel Reich, Sarah Stanley, Noramone Potter, Leah Clark, and Danielle Dunn have provide years of emotional support and I don't know what I would have done without them.

Contents

List of Tables

List of Figures

Chapter 1

Introduction

Exoplanets have been the subject of much interest in the last 20 years since the first detection of an exoplanet around a main sequence star (Mayor and Queloz 1995). With the launch of dedicated exoplanet spacecraft such as *Kepler*, we are finding planets are quite common (Petigura et al. 2013; Swift et al. 2013). These planets show a startling amount of diversity in their properties, and most planetary systems are very unlike the Solar System (e.g. Butler et al. 2006).

Hot Jupiters and other strange exoplanet configurations challenge the previously accepted models of planet formation that were created when the Solar System was the only example of a planetary system. If we want to understand the origin of exoplanets, we need to study the environments where they are born – the circumstellar disk. Habitability, for example, is something that is difficult to currently determine for today's known exoplanets. We cannot yet resolve the exoplanets well enough to search for signs of life or habitability. In a young circumstellar disk, however, the building blocks for like are spread out over the disk in the form of dust. Using the circumstellar disk as a tool, we can look for water and organic material that would likely be incorporated into planets forming in the disk.

This dissertation focuses on constraining the properties of young debris disks.

These disks are likely sites of the last stages of terrestrial planet formation. Understanding the geometry and composition of young debris disks is the first step in determining the potential habitability of terrestrial planets that form in these environments. This chapter provides background information on the study of planet formation and circumstellar disks. In Section 1.1, I present the basics of planet formation from the formation of the star to the fully formed planetary system. Section 1.2 reviews the observational characteristics of circumstellar disks, and Section 1.3 provides details on the debris disk.

1.1 Planet Formation

1.1.1 Star Formation

Our picture of planet formation starts with the collapse of a molecular cloud to form a protostar and its surrounding disk. Molecular cloud cores, where stars are born, are diffuse clouds of gas and dust ($n \sim 10^5$ cm^{-3}) and are often found in filaments that have a typical width of 0.1 pc (Arzoumanian et al. 2011). Small rotation of the molecular cloud carries a large amount of angular momentum, naturally leading to the formation of a disk as the cloud collapses. Stars form in clusters, and often form binaries or larger multiple systems (Duquennoy and Mayor 1991). Star formation is not an isolated process, but is influenced by its environment. However, for simplicity, we will assume a single isolated star from this point on.

The theory that the Solar System formed from the collapse of a gaseous cloud was proposed as far back as the 18th century. Kant (1755) and Laplace (1796) developed theories that a slow rotating gaseous cloud would collapse under its own self gravity. To conserve angular momentum, the infalling material rotated more rapidly and flattened along the spin axis, forming a disk.

The basic modern picture of star formation is summarized in Shu et al. (1987) as occurring in four main stages. It starts when the molecular cloud core reaches the critical Jeans mass and begins to collapse. Evidence suggests that molecular cloud structure is driven by turbulence, a consequence of which is the angular momentum will be non-zero (Larson 1981; McKee and Ostriker 2007). Even a slowly rotating cloud will have substantial angular momentum to drive the formation of a disk. Methods for shedding angular momentum to fuel accretion by the protostar are not fully understood and is a subject still studied extensively.

The molecular cloud core collapse from the inside out, forming a protostar surrounded by a massive envelope. Material accretes onto the protostar through the disk, driving a bipolar outflow that clears a cavity in the gaseous envelope. The surrounding material eventually settles onto the disk or is dispersed, ending the formation of the star.

The above steps of star formation roughly correspond to the observational classes of young stellar objects (YSOs) (Andre and Montmerle 1994; Andre et al. 1993; Lada and Wilking 1984). YSO classes are defined by the slope of their spectral energy distributions (SEDs) from the near- to mid-IR. Class 0 sources correspond to the initial collapse of the molecular cloud core. They show no near-IR emission and peak in the far-IR. Class 1 sources have more near-IR emission and are characterized by a slope that is flat or rising with increasing wavelength. This is due to the massive dusty envelope that surrounds the forming protostar. Class 2 sources are the classical T Tauri stars. Their emission is mostly stellar, with some near-IR emission from the disk and a decreasing emission out to the mid-IR. Class 3 sources show just the stellar photosphere in the near- to mid-IR. These sources are either naked stars, or debris disks with IR excesses that peak in the far-IR.

1.1.2 From Dust to Protoplanets

Planet formation begins with the growth of dust in the primordial disk. These disks are gas rich, with a gas-to-dust ratio presumably similar to the Interstellar Medium (ISM; 100:1). The dust grains begin primordial, then volatiles freeze-out onto the grains as the disk cools. These grains are small (sub-μm) so grain growth needs to occur to begin the formation of planetesimals. There are two main paths to planetesimal formation. Planetesimals form either through slow collisional aggregation or rapid agglomeration by gravitational instabilities in a thin dust layer at the mid-plane.

The full process of grain growth is not well understood. Most of what we know comes from laboratory experiments. Those show the collisions of dust grains lead to either sticking, bouncing, or fragmentation (Güttler et al. 2010). Growth of small dust grains by collisional aggregation is easier to understand in laboratory experiments and numerical simulations (Dominik et al. 2007). Growth from sub-μm to cm sizes is driven by Brownian motion and is well characterized by laboratory experiments.

When grains reach sizes of $\sim$ 1 cm, they decouple from the gas, which orbits at subkeplerian speeds due to the pressure gradient in the disk. The dust grains feel a gas drag from the difference in velocities and their vertical movement through the disk. This leads them to settle toward the midplane, growing through collisions along the way. Once in the midplane, the density of dust grains is much higher, so grain growth can proceed more rapidly (Dullemond and Dominik 2005).

Problems occur when grains reach $\sim$ 1 meter in size, often referred to as the meter-sized barrier. Meter-sized objects are subject to strong radial drift due to gas drag leading to large radial velocities. They must quickly build up their mass to

slow radial drift before they are lost to the star. Additionally, the large speeds due to radial drift mean that collisions of meter-sized objects are more likely to lead to fragmentation rather than growth.

One method of solving this problem is through planetesimal formation by gravitational instabilities at the midplane after settling (Goldreich and Ward 1973). There were several problems with the initial theory, including the role of turbulence, which would prevent dust grains from settling to the midplane (Cuzzi and Weidenschilling 2006). Recent progress in the field has solving some of these problems. First, the turbulent concentration model showed that turbulence can actually aid planetesimal formation by concentrating material in eddies (Cuzzi et al. 2008). In another model of streaming instabilities, the quick radial drift of meter-sized bodies helps to get them concentrated in towards pressure maxima (Johansen et al. 2006, 2007).

Planetesimals larger than $\sim$ 1 km are no longer affected by gas drag because they have a large mass-to-surface area ratio. They are more strongly affected by mutual gravitational interactions. Large bodies gravitationally focus the trajectories of passing bodies. This increases the probability of collisions and hence increases the growth or fragmentation rate.

The mass accretion rate depends on the gravitational focusing strength of the object, i.e. it is determined by the mass as $M^{4/3}$ (Weidenschilling et al. 1997). This begins the regime of runaway growth, where larger bodies grow faster than smaller bodies (Wetherill and Stewart 1993). Runaway growth ends when the largest bodies are massive enough to increase the random velocities of nearby planetesimals. This slows growth and begins the oligarchic growth regime where mass accretion grows as $M^{2/3}$ (Ida and Makino 1993).

In the oligarchic growth regime, regions of the disk are dominated by large

planetary embryos. The spacing between the embryos stays large ($\sim$ 10 Hill Radii), or they collide with one another (Kokubo and Ida 1998). Planetary embryos continue to accrete the surrounding planetesimals until they have swept up everything in their path (Wetherill and Stewart 1989). Their final mass after clearing the planetesimals is called the isolation mass and depends on the surface density of solids and the semi-major axis of the orbit.

1.1.3 Giant Planet Formation

There are two main competing theories for the formation of giant planets, core accretion and gravitational instabilities. Core accretion begins with the build up of solids as discussed in Section 1.1.2, and later accretion of a gaseous envelope (Bodenheimer and Pollack 1986; Mizuno 1980; Perri and Cameron 1974). In the core accretion model, a solid core of $\sim$ 10 $M_\oplus$ must form quickly before the dissipation of the gas disk. This is easier to achieve beyond the snow line where the isolation mass exceeds the critical core mass and giant planet formation is more likely.

Gas accretion onto the solid core begins when the gravitational potential energy of the core exceeds the thermal energy of the surrounding gas. This begins the stage of slow gas accretion called hydrostatic growth, where the gaseous envelope is in hydrostatic equilibrium, balancing the gas pressure due to heating by the continued accretion of planetesimals and the gravitational potential energy. This stage ends when a critical mass is reached, which triggers hydrodynamic instability that results in rapid gas accretion (Pollack et al. 1996). This runaway growth is no longer limited by the cooling properties of the gas envelope, but only by the availability of gas in the disk. Thus, this rapid growth only ends when the gas disk dissipates (Alibert et al. 2005; Hubickyj et al. 2005).

In the gravitational instability model, the disk has to be massive enough to be

unstable due to its own self gravity. This leads to direct fragmentation of the gas into massive planets (Boss 1997). The disk in this case has to be at the upper end of the range of observed disks, but not impossible at the early stages of the disk (e.g Eisner et al. 2005).

The basic theory of giant planet formation by gravitational instabilities says that the disk becomes unstable when the Toomre parameter $Q \lesssim 1$ (Toomre 1981), i.e. the disk is cold and massive. In order to have fragmentation into bound clumps, the cooling time of the gas needs to be short (Gammie 2001). Assuming these conditions are met, the disk fragments into planets in just a few orbits. This process is top down, initially rapid, then slowly sweeping up planetesimals, rather than bottom up and initially slow, like for core accretion (D'Angelo et al. 2010).

Core accretion and gravitational instabilities are two competing models, but perhaps not all giant planets are formed by the same mechanism. Gravitational instabilities are unlikely to occur inside of 40-100 AU because any disk that is massive enough to be unstable is too massive to cool efficiently at those distances (Rafikov 2005). Core accretion is not efficient beyond $\sim$ 40 AU because of the decreasing availability of solid material and the increasing dynamical timescales with distance (Dodson-Robinson et al. 2009). Core accretion may be a good explanation for the formation of the giant planets in the Solar System, but gravitational instabilities may better explain some of the directly imaged planets that are far from their stars (e.g. HR8799; Marois et al. 2008).

At some point, the gas disk is dispersed, and giant planet formation ceases. There are several mechanisms for disk dispersal, one being photoevaporation. Photoevaporation occurs when UV or x-ray radiation heats the disk surface via ionization of gas particles until the gas thermal speed is greater than the escape speed and the gas becomes unbound to the star (Hollenbach et al. 1994). Photoevaporation can

occur from UV or x-ray radiation due to either the central star, or nearby stars, such as nearby O and B stars, which are important in young clusters like Orion.

The escape of gas begins at the gravitational radius, R_g, where the sound speed is equal to the orbital velocity. Inside R_g, gas is bound to the system; outside, the gas is free to escape. Simulations show most of the mass loss occurs at R_g (Hollenbach et al. 1994). As the gas escapes, a pressure gradient drives the unbound gas away from the star as a wind (Clarke et al. 2001). Once a gap is formed, the isolated inner disk accretes onto the star. The inner edge of the outer disk is then directly irradiated (Alexander and Armitage 2007). Mass loss continues from R_g outwards until the entire gas disk is gone. What remains is the debris left over from planet formation - the planetesimals and the planets.

1.1.4 Terrestrial Planet Formation

After the dispersal of the gas disk, there are still $\sim$ 10 - 100 planetary embryos in the disk (Chambers 2011). Neighboring embryos pump up each other's eccentricities and inclinations until their orbits cross. These bodies continue to evolve through a series of giant impacts until they reach a configuration where the spacing leads to long-term stability (Goldreich et al. 2004). This same spacing is seen in exoplanet systems with multiple planets (Lovis et al. 2011).

Not all collisions lead to mergers. Oblique collisions can lead to breakup into multiple bodies (Agnor and Asphaug 2004). The Moon likely formed in an oblique collision where two embryos broke up and recoalesced after an exchange of material (Canup 2004). This is supported observationally by the fact that the Earth and the Moon have the same oxygen isotope ratios (Wiechert et al. 2001).

Accretion of volatiles probably occurred in the last stages of terrestrial planet formation. The location where the Earth formed was too hot for water ice to have

condensed. Additionally, any volatiles accreted would have escaped when the embryos were heated by impacts and radioactive decay (Pepin 2006). The Earth has a lot of water on its surface, however, so it must have accreted some of its mass late in its formation. Water could come from comets or water-rich asteroids formed beyond the snow-line (Morbidelli et al. 2000). Additional evidence for this theory comes from highly siderophile elements. They should have sunk to the core with the iron when the Earth differentiated, but they are found in the mantle (Drake and Righter 2002).

1.2 Observational Characteristics of Circumstellar Disk Classes

In this section, I will give a brief overview of the observational characteristics of the three main circumstellar disk classes, primordial, transitional, and debris disks. Starting with the primordial, or "protoplanetary" disks; these are gas-rich, optically thick disks around pre-main sequence stars. They usually have strong CO emission (Thi et al. 2001) and their fractional infrared luminosities are quite bright ($\sim$ 10-20% Roberge and Kamp 2010). Scattered light images of primordial disks show they have a flared vertical profile and sometimes have jets that have been attributed to stellar mass accretion (e.g. HH30, see Figure 1.1; Burrows et al. 1996).

The next class of disks, dubbed transitional disks, were first classified by a deficit of mid-IR flux. Figure 1.2 demonstrates the changes in the spectral energy distribution (SED) for the three classes of disks. Transitional disk SEDs are quite similar to primordial disks, except for a dip in the mid-IR. This dip corresponds to a lack of small dust grains in the inner portion of the disk. It was proposed that these disks are "in transition" from the primordial stage to the debris disk stage, possibly due

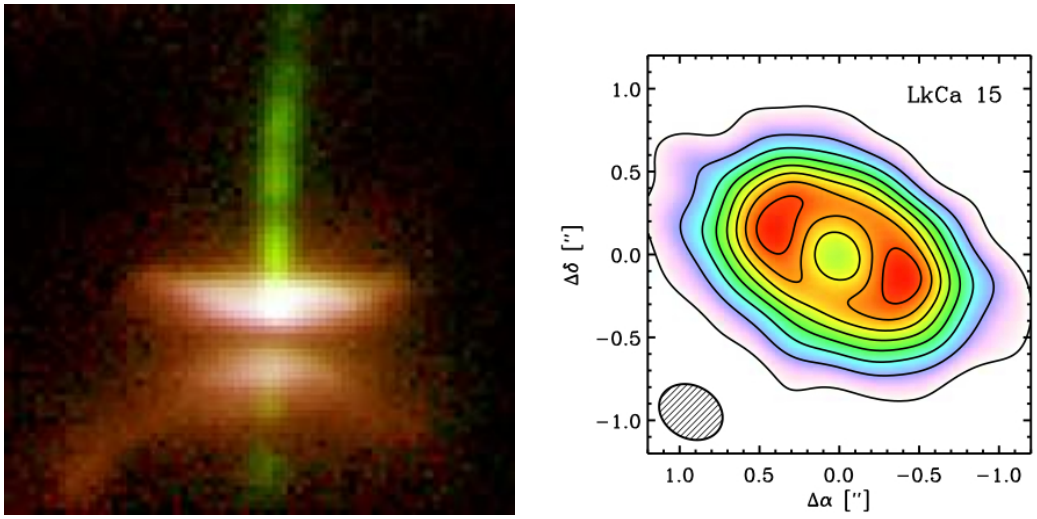

Figure 1.1: **Left:** HST image of the edge-on disk HH30 (Burrows et al. 1996). The image shows a flared disk profile with a dark center lane obscuring the star. The jet, driven by accretion onto the star, is also visible on both sides of the disk. **Right:** Sub-millimeter continuum image of the transitional disk, LkCa15 (Andrews et al. 2011). The disk shows a large cavity in the central regions of the disk, cleared of small dust grains.

to planet formation.

Transitional disks still show large quantities of sub-mm CO (e.g. Qi et al. 2004), so at least the outer disks still contain gas. Some transitional disks still show signs of weak accretion though, implying the inner regions also contain gas (Najita et al. 2007). But the inner disks are clear of small grains; sub-mm continuum images of several transitional disks show large cavities that indicate the absence of small dust grains in these regions (e.g. LkCa15, see Figure 1.1; Andrews et al. 2011; Brown et al. 2009; Mathews et al. 2012).

These cavities could be cleared out by giant planets; planet formation models have long shown that giant planets are capable of clearing the material from their orbits (Dodson-Robinson and Salyk 2011; Paardekooper and Mellema 2004). More recently, a few planet candidates have been directly imaged inside the cavities of transitional disks, seemingly validating this theory (e.g. LkCa15 b; Kraus et al.

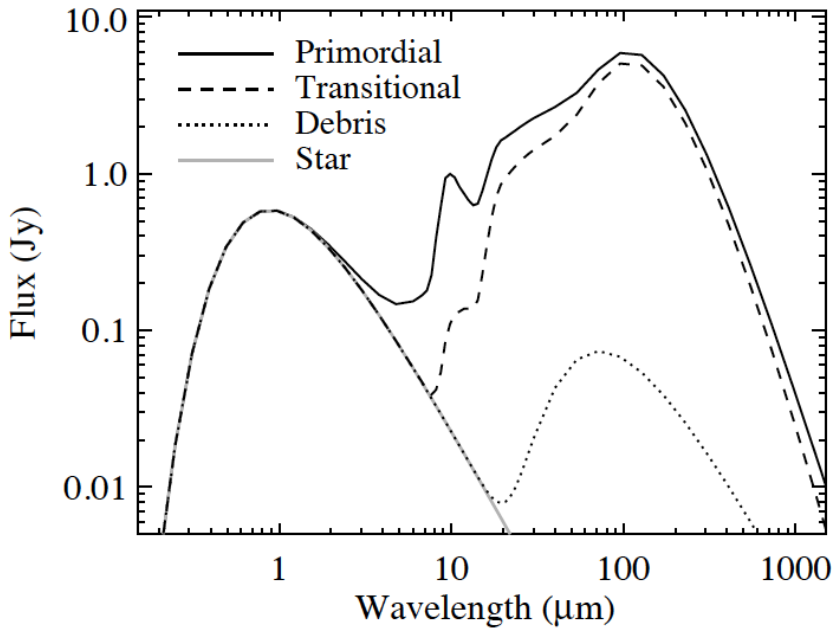

Figure 1.2: Demonstration of how an SED changes as a circumstellar disk evolves (Roberge and Kamp 2010). The central star is well approximated by a blackbody that peaks at short wavelengths. A primordial disk is surrounded by an optically thick disk and shows an excess infrared emission over that of the star. A transitional disk is defined by a drop of excess emission at near-IR wavelengths that is attributed to a clearing of the inner disk. A debris disk is the last stage, when the disk is optically thin and has a fractional dust luminosity well below that of primordial disk. The emission at mid-IR wavelengths is low or completely missing, and the peak of the emission is in the far-IR. Debris disk SEDs are often well characterized by a simple blackbody at a low temperature.

2012). However, several mechanisms other than giant planets have also been cited as explanations for these cavities, such as viscous evolution, grain growth, and photoevaporation (for a detailed review on transitional disks, see Espaillat et al. 2014).

The last disk class is the debris disk. Debris disks are the most long-lived, lasting from the dissipation of the gas disk at ~ 10 Myr (Mamajek 2009), through the lifetime of the star. Debris disks are gas-poor (or gas-free) and optically thin, with small fractional dust luminosities ($L_{IR}/L_* \lesssim 10^{-3}$). Their SEDs lack near- and mid-IR emission and peak in the far-IR. Images of edge-on debris disks show they are also geometrically thin, not flared like primordial disks (e.g. AU Mic; Krist et al.

2005). Other images show rings and cleared regions (Kalas et al. 2005; Schneider et al. 2005, 2006), which explains the lack of mid-IR emission.

1.3 Debris Disks

1.3.1 Origin of dust in debris disks

During the dissipation of the gas disk, the dust grains are expected to be swept along with the gas and removed from the disk as well. All that will be left are the planets and planetesimals that have already formed. But debris disks are full of detectable dust grains. These dust grains are not primordial, but secondary dust produced from collisions between the planetesimals. We know these dust grains must be continuously produced from planetesimal collisions because the dust is constantly removed on short timescales by processes such as Poynting-Robertson (P-R) drag, radiation pressure, and grain-grain collisions.

P-R drag is a process that causes micrometer-sized grains to spiral in towards the star due to interactions with stellar radiation. An effect of general relativity, the small particles essentially feel a headwind from the star's radiation as they orbit, leading to a loss of energy by the dust grains, causing them to spiral inwards. In a typical debris disk, this happens on a timescale of $10^{5.5}$ - $10^{7.5}$ yr (Hillenbrand et al. 2008).

Wyatt (2005), however, argues that for most currently detectable debris disks, the densities are too high for P-R drag to be significant. With high densities, the dust grains are more likely to be destroyed by grain-grain collisions, which has a much shorter typical timescale ($< 10^4 - 10^{5.5}$ yr; Hillenbrand et al. 2008). Grain-grain collisions are expected to be destructive rather than accreting because of the high velocities involved.

Radiation pressure is an extremely effective process that pushes small dust grains ($\lesssim 1\,\mu$m) out of a debris disk system. Radiation pressure will remove grains if the force of the incident radiation is stronger than the force of gravity. Small grains, which have a high surface area to mass ratio, will be removed more easily. Small grains affected by radiation pressure in a typical disk can be removed on timescales as short as $10 - 10^{2.5}$ yr (Hillenbrand et al. 2008). This timescale is very short, and therefore, radiation pressure is the dominant mechanism for the removal of small grains ($\lesssim 1\,\mu$m). Grains below the cutoff "blowout" size are not expected to be seen in a debris disk.

The dust originates from the breakup of planetesimals during collisions. Debris from the collision event continues to collide, grinding the dust into smaller and smaller grains. This collisional cascade effect leads to a steady state distribution of grain sizes (a) of $n(a)da \propto a^{-\kappa}da$, with $\kappa \sim 3.5$ as a typical value (Dohnanyi 1969).

1.3.2 Detection Methods

Circumstellar disks were first discovered 30 years ago through the detection of an infrared excess above the expected photospheric value with the *Infrared Astronomical Satellite* (IRAS; Aumann et al. 1984). At infrared wavelengths, circumstellar disks are much brighter than their host stars. This is because the dust grains orbiting the star absorb the stellar radiation at short wavelengths and thermally re-emit the radiation at long wavelengths.

By observing the system at multiple wavelengths, we can construct a spectral energy distribution (SED). The stellar signal can be fit with a stellar atmosphere model fit to the optical and near-IR data. The extension of that model into the far-IR shows the expected flux of a naked star. The thermal emission of the dust, being much colder than the star, peaks at longer wavelengths and dominates the flux

over the star in the far-IR. The shape of the SED provides a wealth of information about the dust in the disk. Dust temperature, location, grain size, and composition can all be constrained through modeling the SED.

The infrared excess emission of debris disks had been studied in detail since its discovery by IRAS, limited only by the need for space based mission to observe in the far-IR. Debris disk surveys with the *Infrared Space Observatory* (ISO) discovered the first evidence that the fractional infrared excesses compared to the stellar photosphere (L_{IR}/L_*) declines with age. Spangler et al. (2001) and Decin et al. (2003) found a power-law decrease in L_{IR}/L_* with age with a slope between -2 and -1. This is consistent with the expected slope of -1 for dust disks that are replenished by collisions (Dominik and Decin 2003).

The *Spitzer Space Telescope*'s MIPS instrument greatly improved the sensitivity in the mid-IR (Rieke et al. 2004). Several surveys were conducted to search for new debris disks with *Spitzer* (e.g. Meyer et al. 2006; Rieke et al. 2005). A few of the *Spitzer* surveys indicated that the IR excess of many debris disks were stronger at 70 μm than at 24 μm (Beichman et al. 2006; Su et al. 2006). This suggests the dust is cold, and therefore is located farther from the star. Yet some debris disks display different characteristics, with high 24 μm excesses, but little to no 70 μm excesses (Moór et al. 2009). Disks of both types appear around stars of nearly the same age, with little to no clear dependence on spectral type.

The infrared excess only gives an indirect measure of the disk geometry. Geometrical information is best derived through resolved images of the disk. In fact, circumstellar dust was not even confirmed to be in a disk until the resolved scattered light detection of the edge-on disk β Pictoris (Smith and Terrile 1984).

Although debris disks are much brighter than their host stars at far-IR wavelengths, far-IR detectors do not have the resolving power that is possible at optical

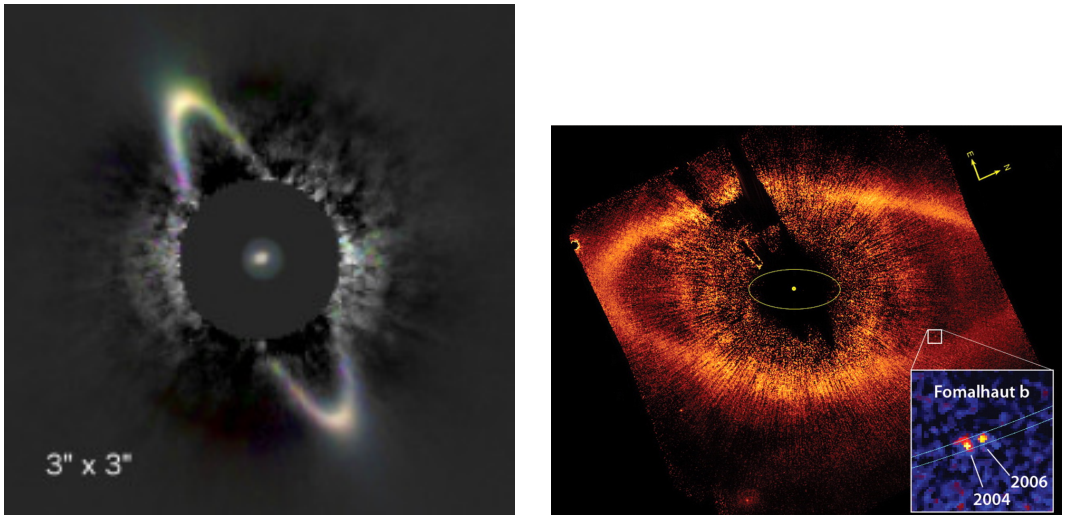

Figure 1.3: **Left:** Three color near-IR image of the HR4796A debris disk (Wahhaj et al. 2014). **Right:** HST image of the Fomalhaut disk with a planet candidate, Fomalhaut b, just inside the main ring (Kalas et al. 2008). These are just two examples of debris disks that have their dust confined to narrow rings.

and near-IR wavelengths. This is starting to change thanks to interferometers such as ALMA, but traditionally, optical and near-IR images of scattered light have been used to map out the geometry of debris disks. IR photometry probes the thermally reprocessed dust emission, but optical and near-IR images probe the stellar light that has scattered off small dust grains rather than absorbed. At these wavelengths, the star is incredibly bright and outshines the disk. A coronagraph is needed to block the stellar signal so the disk can be imaged. This also has the unfortunate side effect of blocking the inner portion of the disk.

The geometry of disks imaged in scattered light is affected by several mechanisms. The dust is produced at the location of the parent planetesimals, which are often confined to thin rings like the Asteroid and Kuiper belts. This had proved to be true in many imaged debris disks that show thin rings structures such as HR4796A (Schneider et al. 2005; Wahhaj et al. 2014), Fomalhaut (Kalas et al. 2008, 2005), and HD181327 (Schneider et al. 2006)(See Figure 1.3).

But dust also moves from its birthplace through processes such as radiation pres-

sure and P-R drag. Some disks have even been suspected of interacting with the surrounding ISM (Debes et al. 2009). Additionally, features such as asymmetries, clumps, and warps have all been cited as evidence of planets in the disk gravitationally interacting with the planetesimals as well as the dust. For example, one of the best studied debris disks, β Pictoris, has an inner disk inclined from the main outer disk, first detected as a warp (Heap et al. 2000). It was predicted this warp was driven by a planet on an inclined orbit (Augereau et al. 2001; Mouillet et al. 1997). The giant planet, β Pictoris b, was later detected by Lagrange et al. (2010) as predicted.

A similar, yet more controversial example, is that of the Fomalhaut debris disk. The disk was imaged by Kalas et al. (2005) with the *Hubble Space Telescope* ACS instrument, and it was found to be a thin eccentric ring that is offset from the star. The offset, eccentricity, and sharp inner edge of the ring led to the prediction of the presence of a planet orbiting just inside the ring (Quillen 2006).

Kalas et al. (2008) presented a direct detection confirmation of a planet, Fomalhaut b, just where it was predicted to be. However, the near-IR colors of the planet appear bluer than expected, causing some to debate whether it is a dust enshrouded planet, or just a large dust cloud (Currie et al. 2012; Janson et al. 2012). New STIS observations show the object is on a highly eccentric and inclined, ring-crossing orbit (Kalas et al. 2013). With such an orbit, Fomalhaut b is unlikely to be shaping the ring; the planet that is shaping the ring has yet to be found.

In addition of finding planets, scattered light images can also give us information about the grains themselves. The scattered light images can directly measure how the grain albedos change with wavelength. As shown in Figure 1.4 from Roberge and Kamp (2010), this can provide information about the composition of the grains. Small silicate grains ($\sim 0.1\,\mu$m) show a blue color due to Rayleigh scattering, while

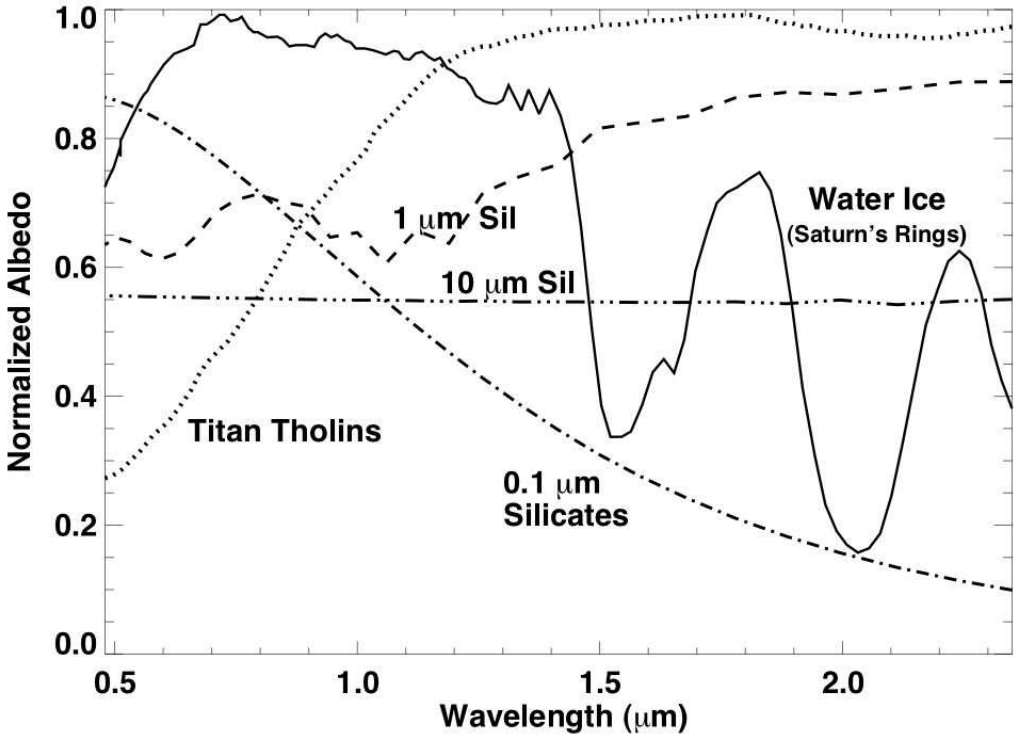

Figure 1.4: The albedo of grains as a function of wavelength in the optical and near-IR (Roberge and Kamp 2010). The color of scattered light spectra taken at these wavelengths can indicate the composition of the grains. Blue colors indicate small grains (i.e. Rayleigh scattering), while neutral colors indicate large silicate grains. Organic material, such as tholins, have very red colors and is seen on Titan and some other Solar System bodies.

larger silicate grains ($\gtrsim 2\,\mu$m) will scatter neutrally. Tholins, an organic material, will show a much redder color than silicates.

Debes et al. (2008) used spectrophotometry from seven HST images of the HR4796A disk in scattered light to show the disk has a red color consistent with the presence of tholins. However, Köhler et al. (2008) argues that this color could be due solely to silicate grains with a higher porosity. More detailed information on the spectral shape of the scattered light is needed to distinguish between these scenarios.

1.3.3 Modeling Debris Disk SEDs

Most debris disks have not been resolved, so modeling begins with the SED. A simple blackbody is a good first approximation of the flux from a thin ring. A better approximation is the modified blackbody. Small grains are inefficient absorbers at long wavelengths because the wavelengths are larger than their size. Similarly, they are also inefficient emitters at long wavelengths. A modified blackbody model takes this into account by reducing the optical depth at long wavelength ($\lambda > \lambda_0$) by a factor $(\lambda/\lambda_0)^{-\beta}$.

ISM dust has a typical value of $\beta = 2$ (Boulanger et al. 1996), but β in debris disks tend to be closer to 1 (e.g. Dent et al. 2000; Nilsson et al. 2010; Williams and Andrews 2006). The change in β from 2 to 1 in protoplanetary and debris disks has been attributed to grain growth (e.g. Draine 2006). As grains grow by agglomeration in primordial disks, the new larger grains are more efficient at emitting at long wavelengths and β decreases. Fitting an SED with a modified blackbody required detections at several wavelengths longer than λ_0 ($\lambda_0 \approx 100\,\mu$m). Without those data, a simple blackbody is sufficient.

Characteristic temperatures calculated from blackbody fitting can be converted into blackbody radii to estimate the size of the disk. But blackbody radii are not always good representations of true disk radii. Real grains are not as efficient at emitting as blackbodies, so real grains will be hotter farther from the star than blackbodies. Therefore, blackbody radii are only lower limits. The *Herschel* DEBRIS team were able to resolve several disks they observed with *Herschel* and were able to compare blackbody radii with true disk radii. They confirmed that true disk radii were often several times larger than blackbody radii (Booth et al. 2013).

Blackbodies are only an approximation. It is better to use real grain emissivities

as a function of grain size and composition to calculate the thermal emission of grains. The SED can be fit for a range of different radii and grain sizes using full radiative transfer to calculate the equilibrium temperature of the grains (see Chapter 2 for more details).

Unfortunately, SED fitting is degenerate. SEDs, on first order, give temperature. But grain temperature is affected by grain size, location, and composition. Dust grains get hotter as they get closer to the star. But the smaller a grain is, the more inefficient it is at radiating, so it will end up hotter farther from the star than a blackbody. So both grain size and location are linked, and the SED fitting can be degenerate. To break the degeneracy, we need both images of the disk, as well as good SED coverage. The images constrain the location of the dust, so the SED fitting can focus on the grain properties, such as grain size and composition.

A good demonstration of this technique is the detailed modeling of the debris disk HD181327 by Lebreton et al. (2012) as part of the GASPS survey. HD181327 is a nearly face-on disk imaged in scattered light with HST by Schneider et al. (2006). Lebreton et al. (2012) fixed the radial profile in their model to the one found by Schneider et al. (2006). They then focused their SED modeling on the dust composition. They used a cometary grain model (e.g. Greenberg 1998): a silicate core with a porous mantel of carbon and water ice. Lebreton et al. (2012) found the HD181327 disk contained grains with a high water ice fraction.

The *Herschel* DUNES team has also combined resolved images and SEDs to constrain detailed models of debris disks. Their *Herschel* PACS observations of the HD207129 debris disk were well resolved, the first time a resolved ring-like structure was seen in the far-IR (Marshall et al. 2011). They used the resolved images and the SED to study the detailed collisional evolution of the disk (Löhne et al. 2012).

1.4 GASPS – A Herschel Key Programme

The *Herschel Space Observatory* provided a unique opportunity for sensitive debris disk surveys. *Herschel* covered a wide wavelength range in the far-IR to sub-mm of $55-671\,\mu$m (Pilbratt et al. 2010) and has nearly four times the spatial resolution of *Spitzer* at similar wavelengths – $7''$ ($\lambda/100\,\mu$m) for *Herschel* and $25''$ ($\lambda/100\,\mu$m) for *Spitzer*. The better spatial resolution greatly improves the sensitivity by avoiding confusion with interstellar cirrus and background galaxies.

Herschel has two photometric instruments, the Photodetector Array Camera and Spectrometer (PACS) covering a wavelength range of $55-210\,\mu$m (Poglitsch et al. 2010) and the Spectral and Photometric Imaging REceiver (SPIRE) covering the wavelength range of $194-671\,\mu$m (Griffin et al. 2010). Debris disk infrared excess typically peaks within the PACS wavelength range, so PACS was more sensitive to faint debris disks than previous instruments. This allowed for detection of fainter systems that have a lower dust density, and therefore are closer analogs to the more sparse Solar System Kuiper belt. The addition of longer wavelength data from PACS at 100 and $160\,\mu$m and from SPIRE at 250, 350, and $500\,\mu$m is helpful in characterizing the cold dust grains in these systems.

Herschel had several large Open Time Key Programmes (OTKP) to survey debris disks. DUst around NEarby Stars (DUNES; Eiroa et al. 2013) surveyed all F, G, and K type stars within 20 pc and found $20.2\pm2\%$ harbored detectable debris disks. Disc Emission via a Bias-free Reconnaissance in the IR and Sub-mm (DEBRIS) conducted a flux-limited survey of nearby stars (A through M type). Both surveys were able to resolve several disks, allowing for a more detailed modeling of those systems (e.g. Booth et al. 2013; Löhne et al. 2012; Marshall et al. 2011).

The *Herschel* OTKP GAS in Protoplanetary Systems (GASPS; Dent et al.

2013) was the only one to specifically target young debris disks. The GASPS survey targeted young nearby star clusters with well determined ages ranging from 1-30 Myr. The survey aimed to study the evolution of gas and dust over the transition from a gas-rich protoplanetary disk to a gas-poor debris disk.

The survey consisted of PACS photometry at 70 and 160 μm (plus some 100 μm data) with later follow-up of the 160 μm detected debris disks with the SPIRE instrument at 250, 350, and 500 μm. A few of the brighter targets were chosen to search for gas. The PACS Integral Field Spectrometer (IFS) was used to measure the far-IR fine structure cooling lines of [C II] (157.7 μm) and [O I] (63.2 μm).

The 24 debris disks in the sample come from four associations with ages $\sim$ 10 - 30 Myr, the TW Hydrae Association (TWA), the β Pictoris Moving Group (BPMG), Upper Scorpius (UpSco), and the Tucana-Horologium Association (Tuc-Hor). From these four associations, 67 stars were chosen for having either a known debris disk, or no known IR emission. These targets are listed in Table 1.1. Any primordial disks in these associations were removed from the sample. Additionally, four field stars with debris disks were also observed by GASPS because they are bright, well known targets in the GASPS age range. These include HD32297 (Donaldson et al. 2013), 49 Ceti (Roberge et al. 2013), HR1998 and HD158352 (Meeus et al. 2012). These targets were analyzed separately because their age estimate are less precise than those in stellar associations.

This dissertation focuses on characterizing the properties of dust in young ($\sim$ 10-30 Myr) debris disks. These young disks are likely sites of ongoing terrestrial planet formation as planetesimals are accreted by large bodies. By studying the dust, we learn about the population of unseen planetesimals that produce the dust in mutual collisions. In Chapter 2, I discuss our observations and modeling of debris disks in the 30 Myr association, Tucana-Horologium. Chapter 3 presents an expanded ob-

servational sample of 10-30 Myr disks, and I analyze trends in the data. In Chapter 4, I present more detailed modeling of one well observed 30 Myr-old debris disk, HD32297. The wealth of information on this disk allows us to constrain the dust composition from the SED. In Chapter 5, I use a new coronagraphic spectroscopy technique to observe the HD32297 disk with HST to look for compositional changes with distance from the star.

Table 1.1: GASPS Debris Disk Sample

Target	Association	Stellar Distance (pc)	Spectral Type	IR Excess
AT Mic	BPMG	10.2	M4.5e	N
CD-64 1208	BPMG	36	M0 or K7	N
GJ 3305	BPMG	30	M0.5	N
HD 139084A/B	BPMG	40	K0V	N
HD 146624	BPMG	43	A0V	N
HD 164249	BPMG	47	F5V	Y
HD 172555	BPMG	29	A5IV/V+K7	Y
HD 174429	BPMG	50	K0Vp	N
HD 181296	BPMG	48	A0Vn+M7	Y
HD 181327	BPMG	51	F5/F6V	Y
HD 199143	BPMG	48	F8V	N
HD 203	BPMG	39	F2IV	Y
HD 29391	BPMG	30	F0V+M0.5	N
HD 35850	BPMG	27	F7V	Y
HD 45081	BPMG	39	K6/7	N
HIP 10679/80	BPMG	34	G2V	Y
HIP 11437	BPMG	42	K8	Y
HIP 12545	BPMG	41	M0	N
GSC 8056-482	Tuc-Hor	25	M3Ve	N
HD 105	Tuc-Hor	40	G0V	Y
HD 12039	Tuc-Hor	42	G4V	Y
HD 1466	Tuc-Hor	41	F9V	Y
HD 16978	Tuc-Hor	47	B9V	N
HD 202917	Tuc-Hor	46	G5V	Y

Continued on next page

Table 1.1 continued

Target	Association	Stellar Distance (pc)	Spectral Type	IR Excess
HD 224392	Tuc-Hor	49	A1V	N
HD 2884	Tuc-Hor	43	B9V	N
HD 2885	Tuc-Hor	53	A2V	N
HD 3003	Tuc-Hor	46	A0V	Y
HD 30051	Tuc-Hor	58	F2/F3IV/V	Y
HD 3221	Tuc-Hor	46	K5V	N
HD 44627	Tuc-Hor	46	K2V	N
HD 53842	Tuc-Hor	57	F5V	N
HD 55279	Tuc-Hor	64	K3V	N
HIP 107345	Tuc-Hor	42	M1	N
HIP 3556	Tuc-Hor	39	M1.5	N
TWA02AB	TWA	52	M0.5	N
TWA05Aab	TWA	50	M1.5	N
TWA07	TWA	38	M1	Y
TWA10	TWA	57	M2.5	N
TWA11	TWA	67	A0	Y
TWA12	TWA	32	M2	N
TWA13AB	TWA	38	M2e	N
TWA16	TWA	66	M1.5	N
TWA21	TWA	69	K3	N
TWA23	TWA	37	M1	N
TWA25	TWA	44	M0	N
1RXSJ160044.7-234330	UpSco	145	M2	N
HIP76310	UpSco	145	A0V	Y
HIP77815	UpSco	145	A5V	N
HIP77911	UpSco	145	B9V	Y
HIP78099	UpSco	145	A0V	N
HIP78996	UpSco	145	A9V	Y
HIP79156	UpSco	145	A0V	Y
HIP79410	UpSco	145	B9V	Y
HIP79439	UpSco	145	B9V	Y
HIP79878	UpSco	145	A0V	Y

Continued on next page

Table 1.1 continued

Target	Association	Stellar Distance (pc)	Spectral Type	IR Excess
HIP80088	UpSco	145	A9V	Y
HIP80130	UpSco	145	A9V	N
USco J160210.9-200749	UpSco	145	M5	N
USco J160245.4-193037	UpSco	145	M5	N
USco J160801.4-202741	UpSco	145	K8	N
Usco J153557.8-232405	UpSco	145	K3	N
Usco J154413.4-252258	UpSco	145	M1	N
Usco J160108.0-211318	UpSco	145	M0	N
Usco J160654.4-241610	UpSco	145	M3	N
Usco J160856.7-203346	UpSco	145	K5	N
Usco J161402.1-230101	UpSco	145	G4	N

Chapter 2

Absorption and Scattering of Radiation by Dust Grains in Debris Disks

2.1 Optical Constants

The response of a material to an applied electric field is characterized by the material's dielectric function, ϵ, also called the permittivity. In an insulating material, like a silicate grain, charges are not free like in a conductor, but can only shift slightly when subjected to an electric field, i.e. the material is polarized. The dielectric function measures how the electric field interacts with a medium and how the electric field is affected in turn.

The dielectric function is complex ($\epsilon = \epsilon' + i\epsilon''$), where the imaginary part, ϵ'', describes how a wave is attenuated as it propagates through a medium, and the real part, ϵ', describes the phase velocity. The dielectric function is related to the complex index of refraction, m, as $m = \sqrt{\epsilon/\epsilon_0}$, where ϵ_0 is the permittivity of free

space. The complex functions m and ϵ are referred to as optical constants, though they are not constant, but vary with wavelength.

To describe the absorption and scattering of dust grains, we start by defining an efficiency factor, Q, where Q_{abs} is the absorption efficiency of a dust grain, Q_{sca} is the scattering efficiency, and $Q_{ext} = Q_{sca} + Q_{abs}$ is the total extinction efficiency. Q is a dimensionless factor that quantifies the efficiency of the grain's absorption or scattered compared to perfect absorption or scattering (Q = 1). For convenience, we will also define the factor, $x = 2\pi a/\lambda$, the grain size relative to the wavelength of the photons in question.

There are two important limits for Q, one where the grain size is small compared to the wavelength ($x << 1$) and one where the grains are much larger than the wavelength ($x >> 1$). In the first limit, where grains are small compared to the wavelength, the efficiencies can be calculated with Rayleigh-Gans theory, and approximately come out to

$$Q_{sca} = \frac{8}{3}x^4 \left|\frac{m^2-1}{m^2+2}\right|^2, \qquad Q_{abs} = 4x\,\mathrm{Im}\left\{\frac{m^2-1}{m^2+2}\right\}. \tag{2.1}$$

If $(m^2-1)/(m^2+2)$ is a weak function of wavelength, then Q_{sca} and Q_{abs} vary with wavelength as

$$Q_{sca} \propto \frac{1}{\lambda^4} \qquad Q_{abs} \propto \frac{1}{\lambda}. \tag{2.2}$$

Short wavelengths are more efficiently scattered and absorbed, which is why ISM extinction from interstellar dust grains reddens obscured sources.

In the limit of large x (i.e. large grains, small wavelengths), grains are essentially opaque and act more like blackbodies ($Q_{sca,abs} \to 1$). In the limit of small x (i.e. small grains, long wavelengths), Q_{abs} can often be approximated as a power-law with wavelength

$$Q_{abs} = Q_0 \left(\frac{\lambda}{\lambda_0}\right)^{-\beta}. \tag{2.3}$$

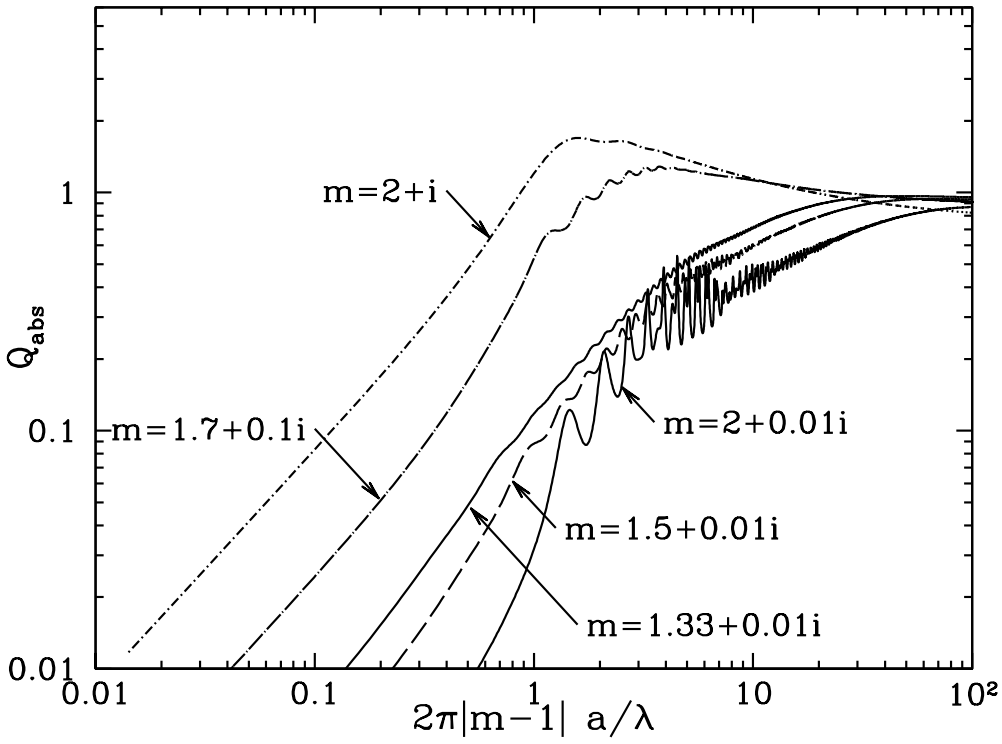

Figure 2.1: Absorption efficiency factor, Q_{abs}, for various complex values of m as a function of $|m-1|x$. As $|m-1|x \to \infty$, $Q_{abs} \to 1$. For small values of x, Q_{abs} is well described by a power-law. Figure 22.1 from Draine (2011).

This is the motivation for the modified blackbody function introduced in Section 1.3.3. For grains with sizes comparable to the wavelength, the absorption and scattering efficiencies can be calculated more accurately with Mie theory (Mie 1908). Mie theory gives accurate solutions to Maxwell's equations for the assumptions of spherical and homogeneous grains. Figure 2.1 shows Q_{abs} calculated with Mie theory for several different complex values of m.

Optical constants are determined experimentally by measuring transmission, reflectance and refraction angles at a range of wavelengths. Advancements in this field were led by Draine and Lee (1984) for silicates and graphite and improved upon by Laor and Draine (1993), and Weingartner and Draine (2001). Optical constants for other common grain compositions such as water ice and organic compounds have

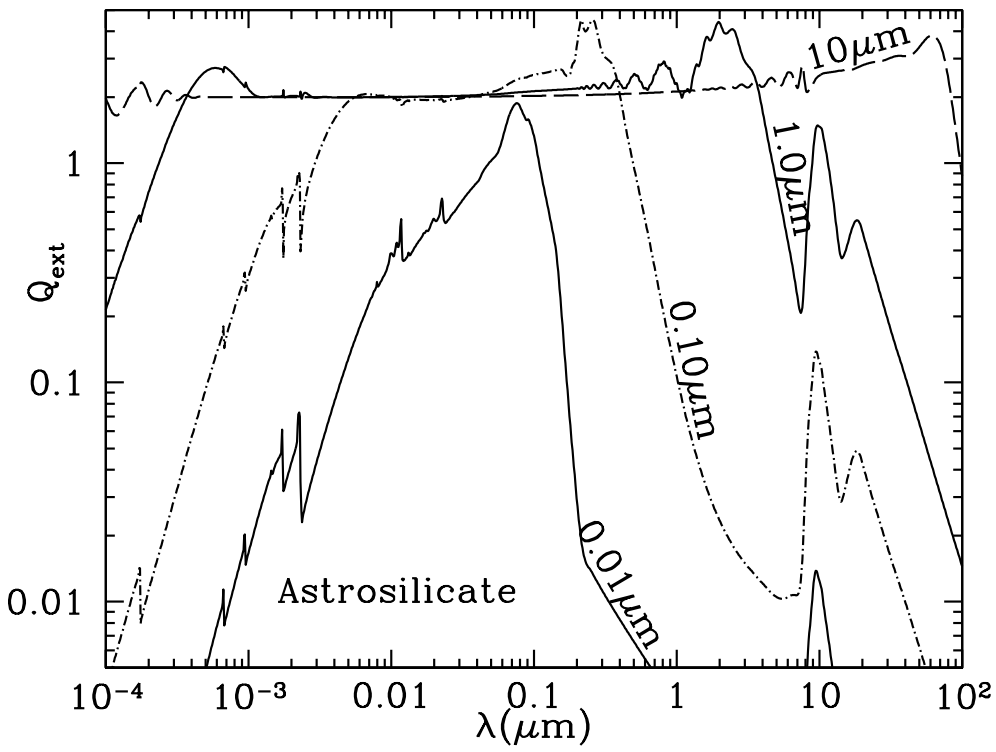

Figure 2.2: Extinction efficiency factor, Q_{ext}, for spherical astrosilicate grains of various sizes ranging from $0.01\,\mu$m (small x) to $10\,\mu$m (large x) as a function of wavelength. Small silicate grains ($\lesssim 1\,\mu$m) show strong features at 9.7 and $18\,\mu$m. Once grains reach larger sizes ($\gtrsim 1\,\mu$m), the grains become opaque at these wavelengths and the silicate features disappear. Figure 22.6 from Draine (2011).

also been measured.

There are a few spectral features common to astrophysical dust grains, such as those in the ISM. Small silicate grains show strong absorption features at 9.7 and $18\,\mu$m. For a large grain ($\gtrsim 1\,\mu$m), these features are absent because the grain itself is optically thick at these wavelengths. Figure 2.2 shows the extinction efficiency, Q_{ext}, for astronomical silicate grains of different sizes vs. wavelength. Small grains ($< 1\,\mu$m) show strong absorption features while the largest grains ($\sim 10\,\mu$m) are optically thick ($Q_{sca} = Q_{abs} = 1$) up to wavelengths of tens of microns.

Polycyclic Aromatic Hydrocarbons (PAHs) also show a number of features at

3.3, 6.2, 7.7., 8.6, 11.3, and 12.7 μm. ISM extinction curves show a strong feature at 2175Å possibly due to graphite. Some of these features, most notably the silicate features, are commonly seen in primordial disks. Although a few debris disks do have silicates features (e.g. β Pic; Telesco and Knacke 1991), most do not. This is likely because grains have grown too large in typical debris disks.

2.2 Thermal Equilibrium

Debris disks are optically thin, so we can ignore effects such as extinction and scattering off multiple grains. To characterize the thermal emission of a dust grain in a debris disk, we only have to calculate the absorption and re-emission by individual grains depending on their size, distance from the star, and their optical constants. We will assume spherical, homogeneous grains so we can use Mie theory to calculate the absorption and scattering efficiencies of the grains from their optical constants.

Dust grains are heated by UV and visible radiation from the central star and cool through thermal emission in the infrared. Over time, a grain of size, a, and distance, r, from the star will reach an equilibrium temperature where the absorbed energy is balanced by the emitted.

A spherical grain with radius, a, absorbs starlight over a projected cross-section, πa^2. The stellar flux, $F_*(\nu)$, incident on the grain depends not only on the spectral type of the star, but also on the distance between the grain and the star, r, as $F_* \propto 1/r^2$. The rate of energy absorbed by the dust grain is then

$$\left(\frac{dE}{dt}\right)_{abs} = \int \pi a^2 \, Q_{abs}(\nu, a) \, F_*(\nu) \, d\nu. \tag{2.4}$$

The absorbed energy will heat the dust grain and it will emit thermally in all directions over its surface area, $4\pi a^2$. The flux of the thermal emission of the grain can be described by the flux of a blackbody with dust temperature, T_d, modified by

the efficiency of the grain compared to a blackbody, Q. This gives a total rate of emitted energy as

$$\left(\frac{dE}{dt}\right)_{emit} = \int 4\pi a^2 \, Q_{abs}(\nu, a) \, \pi B_\nu(T_d) \, d\nu. \tag{2.5}$$

Equating these two expressions gives us the equation for the thermal equilibrium of the dust grain

$$\int Q_{abs}(\nu, a) \, F_*(\nu) \, d\nu = \int 4\pi \, Q_{abs}(\nu, a) \, B_\nu(T_d) \, d\nu. \tag{2.6}$$

For a given grain size, a, and distance, r, Equation 2.6 can be solved to get the equilibrium grain temperature. If Q_{abs} does not depend on ν (e.g. blackbody, $Q_{abs} = 1$), then Equation 2.6 is trivial to solve. If Q_{abs} does not have a simple analytical form, then T_d can be solved iteratively.

2.3 Radiation Pressure

Radiation pressure can have a large effect on a debris disk's shape and the dust grain population. If a dust grain is small enough (i.e. it has a large surface area-to-mass ratio), the force of a star's incident radiation can push the grain out of the system. Slightly larger grains will remain bound to the system, but their orbits will be perturbed outwards. Figure 2.3 from Krivov (2010) illustrates how the structure of a disk is affected by radiation pressure. Grains produced in a planetesimal belt will spread outwards over time and grains below a certain size will be lost to the system.

The repulsive force of a star's radiation is given by

$$\vec{F}_{rad} = \frac{L_* \, A}{4\pi \, c \, r^2} \, Q_{pr} \, \hat{r}, \tag{2.7}$$

where A is the cross-sectional area of the grain, L_* is the star's luminosity, c is the speed of light, and r is the distance between the grain and the star. Q_{pr} is the

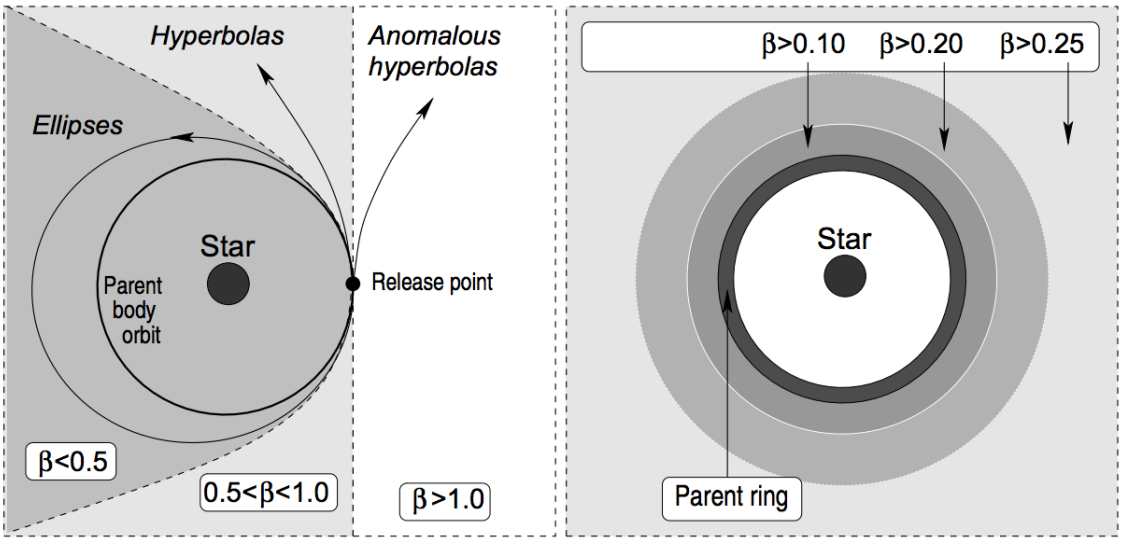

Figure 2.3: Effect of radiation pressure on a dust grain for different values of β, the ratio between radiation pressure and gravity. **Left:** Orbits of grains as a function of β assuming an initially circular orbit. Grains with $\beta < 0.5$ will remain bound to the star on elliptical orbits, and grains with $\beta > 0.5$ will be ejected from the system. **Right:** A diagram of how grains with different β values will be distributed in the disk. Figure 1 from Krivov (2010).

radiation pressure efficiency, which includes the effects from both absorption and scattering, and ranges from 0 (no absorption or scattering) to 2 (backscattering). Q_{pr} effectively measures the transfer of momentum from the radiation to the grain.

The force of radiation pressure is proportional to the cross-sectional area of the grain the starlight is hitting, which for a spherical grain of radius, a, is πa^2. The gravitational force on a spherical grain, on the other hand, is proportional to the grain's mass, $m = 4\pi\rho\, a^3/3$. Therefore, the ratio of the force of radiation pressure to the gravitational force is inversely proportional to the grain size – smaller grains are blown out more easily.

To calculate the smallest grain size that will be bound to the system, we define the parameter, β, as the ratio of the radiation pressure, F_{rad}, to the force of gravity, F_{grav}:

$$\beta = \frac{F_{rad}}{F_{grav}} = \frac{3L_* Q_{pr}}{16\pi a c G M_* \rho}. \tag{2.8}$$

In the case of a perfect absorber ($Q_{pr} = 1$), Equation 2.8 can be written as

$$\beta = 0.574 \left(\frac{L_*}{L_\odot}\right) \left(\frac{M_\odot}{M_*}\right) \left(\frac{1\,\mathrm{g\,cm^{-3}}}{\rho}\right) \left(\frac{1\,\mu\mathrm{m}}{a}\right) \tag{2.9}$$

(Burns et al. 1979).

We can also use β to define the effective gravitational force

$$\vec{F}_{eff} = -\frac{GM_*m}{r^2}(1-\beta)\,\hat{r}. \tag{2.10}$$

For a grain to escape the system, the magnitude of the grain's kinetic energy must exceed its effective potential energy

$$\frac{1}{2}mv^2 > \frac{GM_*m}{r}(1-\beta), \tag{2.11}$$

where a grain on an initially circular orbit has a velocity $v^2 = GM_*/r$. This gives $\beta > 0.5$ as the condition for a spherical grain on a circular orbit to escape the system (see also Figure 2.3). Equation 2.9 can then be used to calculate the grain size this corresponds to, the so-called "blowout size". This blowout size increases with the luminosity of the central star.

Grains smaller than the blowout size are not expected to be present in a debris disk. However, the calculation of the blowout size presented above is only an approximation. We made several assumptions in the derivation, including spherical grains, circular orbits, and blackbody grains. Actual small dust grains are likely non-spherical and inefficient absorbers compared to a blackbody. This can lead to a large difference between the calculated blowout size and the grain size derived from the SED.

2.4 SED modeling code for optically thin disks

Our SED modeling code works by calculating the flux emitted by dust grains of size, a, in a thin ring of width, dr, at distance, r, from the star and then integrating over grain size and distance to calculate the flux from the entire disk. For a grain of size, a, at location, r, the equilibrium temperature, T_d, is calculated from Equation 2.6. As Q_{abs} is not a simple function of λ, the equilibrium temperature is calculated iteratively. A grain of size, a, and temperature, T_d, has a luminosity of

$$L_{grain}(\nu) = 4\pi a^2 \, Q_{abs}(\nu, a) \, \pi B_\nu(T_d). \tag{2.12}$$

The density of dust grains with size, a, in a thin ring at distance, r, is a function of the disk surface density, $\Sigma(r)$, and the grain size distribution, dn(a). This gives a total luminosity of the ring of

$$L_{ring}(\nu) \propto 2\pi r \, \Sigma(r) \, dr \, \cdot \, 4\pi a^2 \, Q_{abs}(\nu, a) \, \pi B_\nu(T_d) \, dn(a). \tag{2.13}$$

The total flux from the entire disk is calculated by integrating Equation 2.13 over grain size and disk radius

$$L_{total}(\nu) \propto \int_{r_{min}}^{r_{max}} 2\pi r \, \Sigma(r) \, dr \int_{a_{min}}^{a_{max}} 4\pi a^2 \, Q_{abs}(\nu, a) \, \pi B_\nu(T_d) \, dn(a). \tag{2.14}$$

The disks fit with our SED modeling code in Chapters 3 and 5 are characterized by three geometrical parameters and three dust grain parameters. The geometry is characterized by an inner disk radius, an outer disk radius, and a power-law surface density decreasing with increasing disk radius. The grains have a minimum grain size, a maximum grain size and a power-law grain size distribution that decreases with increasing grain size. Disks are thought to have minimum grain sizes close to the blowout size, but no actual maximum grain size. For computational efficiency, we fix the maximum grain size to a value beyond the point where grains have a

significant contribution to the far-IR SED, here 1 mm. The mass of the disk in grains smaller than a_{max} is given by

$$M_{disk} = \int_{r_{min}}^{r_{max}} \Sigma(r)\, 2\pi r\, dr \int_{a_{min}}^{a_{max}} \rho \frac{4\pi}{3} a^3\, dn(a)\,, \tag{2.15}$$

where ρ is the density of the dust grains, assumed to be constant with grain size.

2.5 Scattered light

2.5.1 Phase function

Unlike the thermal emission, scattering off dust grains can be highly anisotropic. Small dust grains can be highly forward (or back) scattering. Therefore, to calculate the scattered light of a debris disk, we need to know how the scattered light is angularly distributed.

The phase function, $\Phi(\phi)$, characterizes the angular distribution of scattered light as a function of ϕ, the angle between the star and the observer, as

$$\Phi = \frac{1}{Q_{sca}} \frac{dQ_{sca}}{d\Omega}. \tag{2.16}$$

The integration of the phase function over a sphere is equal to unity ($\int \Phi\, d\Omega = 1$), and the phase function for isotropic scattering has no dependence on angle ($\Phi = 1/4\pi$). The first moment of the phase function is a measure of the asymmetry between forward and backscattering and is given by

$$\langle \cos\phi \rangle = \int \cos\phi\, \Phi(\phi, \lambda)\, d\Omega. \tag{2.17}$$

Henyey and Greenstein (1941) came up with an analytic function to model anisotropic scattering of dust grains. Their phase function is often used characterize the angular distribution of scattered light for dust grains in various astrophysical

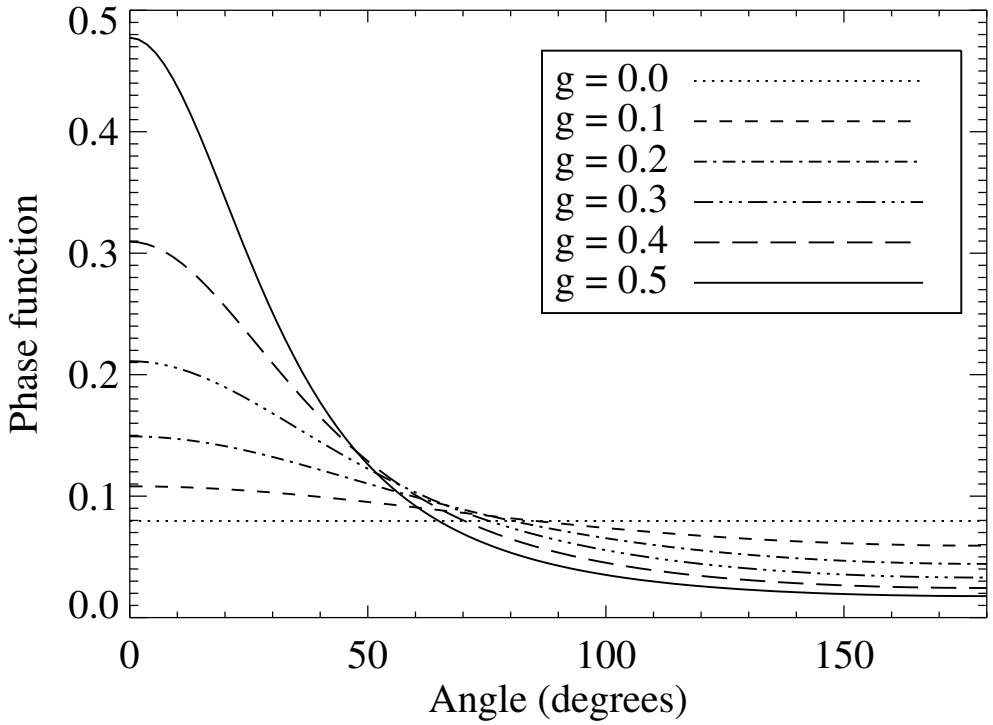

Figure 2.4: The Henyey-Greenstein phase function as a function of angle for several values of the anisotropy factor, g, from 0 from 0.5. As g grows, the phase function becomes more forward scattering. Negative values of g are backscattering.

situations. Their function takes the form

$$\Phi(\phi) = \frac{1}{4\pi} \frac{1 - g^2}{(1 + g^2 - 2g\cos\phi)^{3/2}}, \tag{2.18}$$

where $g = \langle \cos\phi \rangle$. The parameter g ranges from -1 (pure backscattering) to 1 (pure forward scattering) with $g = 0$ for isotropic scattering. Figure 2.4 shows the Henyey-Greenstein phase function for a few different values of g.

2.5.2 Projection of a 3D inclined disk

To produce a model of an inclined scattered light disk, we need to calculate the projected image of a three-dimensional disk onto the two-dimensional plane of the sky. We start by defining two coordinate systems, the observer's and the disk's. The observer's coordinate system is defined by the plane of the sky, x and y, and the line-of-sight direction, l. The disk's coordinate system, shown in Figure 2.5, is defined by x_{disk}, y_{disk}, and z_{disk} in cartesian coordinates or r_{disk}, θ_{disk}, and z_{disk} in cylindrical coordinates. The origin of both coordinate systems is the central star. The two coordinate systems are inclined by an angle, i, which is a rotation around the x_{disk} axis given by

$$y = y_{disk} \cos i - z_{disk} \sin i \tag{2.19}$$

$$l = y_{disk} \sin i + z_{disk} \cos i. \tag{2.20}$$

For simplicity, we assume that the x-axis is aligned with the x_{disk} axis.

For any point in the disk, the amount of light scattered towards the observer is determined by the phase function and the angle, ϕ, between the line-of-sight direction and the central star (see Figure 2.5). The angle ϕ is given by $\phi = \cos^{-1}(l/d_{star})$ where d_{star} is the distance from the grain to the star ($d^2_{star} = x^2_{disk} + y^2_{disk} + z^2_{disk}$). The distance, l, given by Equation 2.20, can also be written in cylindrical coordinates with the relation $y_{star} = r_{disk} \sin \theta_{disk}$ giving a final value for ϕ of

$$\phi = \cos^{-1}\left(\frac{r_{disk} \sin\theta_{disk} \sin i + z_{disk} \cos i}{d_{star}}\right). \tag{2.21}$$

For each point in the disk in (x, y, l) space, the intensity is given by

$$I_{3D}(x, y, l) \propto \frac{\rho(x, y, l)\Phi(\phi(x, y, l))}{d^2_{star}}, \tag{2.22}$$

where ρ is the dust density at (x, y, l) and Φ is the phase function. To get the

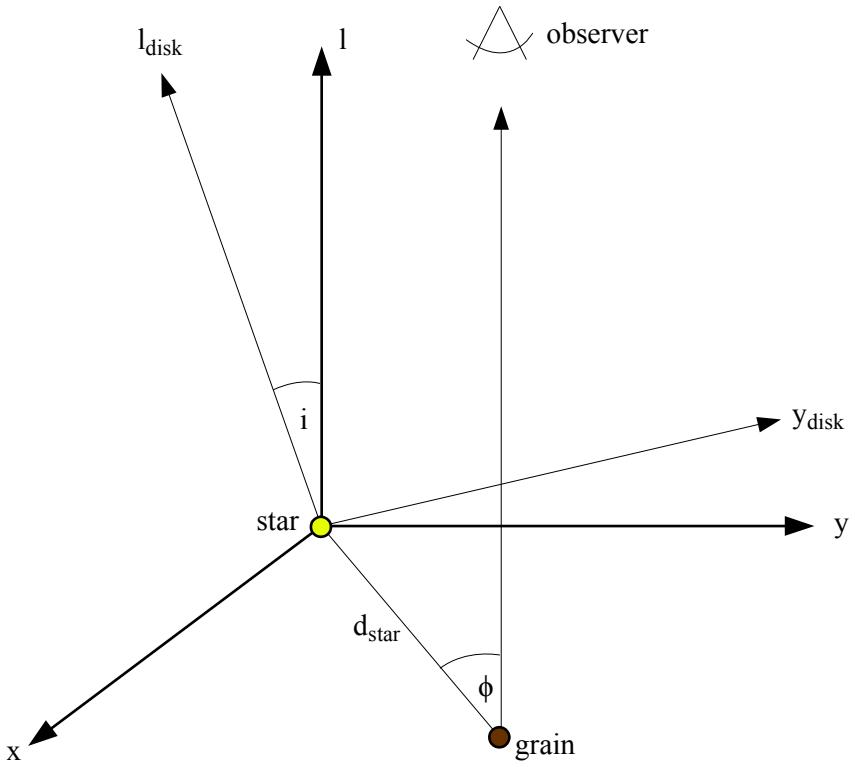

Figure 2.5: Coordinate system used from scattered light models for the observer (x, y, l) and the disk (x_{disk}, y_{disk}, z_{disk}). The two coordinate systems are inclined by an angle, i, rotated around the x=x_{disk} axis. The position angle of the disk is already assumed to be aligned along the observer's x-axis. The angle between the observer and the star, ϕ, is given by $\phi = \cos^{-1}(l/d_{star})$.

projected image on the plane of the sky, Equation 2.22 is integrated along the line of sight.

Chapter 3

Herschel PACS Observations and Modeling of Debris Disks in the Tucana-Horologium Association

3.1 Introduction

Debris disks are the last stage of circumstellar disk evolution, in which the gas from the protoplanetary and transitional disk phases has been dissipated and the dust seen comes from collisions between planetesimals. In the youngest debris disks, $\lesssim 100$ Myr-old, terrestrial planets may still be forming (Kenyon and Bromley 2006). Giant planets must form before the gas dissipates; their gravitational interactions with planetesimals and dust can leave signatures in debris disks. Cold debris disks may be Kuiper-belt analogs, signaling the location and properties of planetesimals remaining in the disk.

To be suitable for life, terrestrial planets in habitable zones must have volatiles such as water brought to their surfaces from beyond the ice line. Planetesimals in

Kuiper Belt-like debris disks may provide this reservoir of volatiles (Lebreton et al. 2012). We do not yet have the capability to detect the planetesimals in these disks, but we can detect the smaller dust grains. These dust grains are believed to be produced through the collisions of the larger planetesimals, and therefore are likely to have similar compositions to the larger undetected bodies. The properties and locations of the dust grains in Kuiper Belt analogs can provide clues to the properties of the hidden planetesimals. Additionally, dust structures in the disk may point to unseen exoplanets (e.g. β Pic b; Lagrange et al. 2010).

To measure the cold dust in the outer regions of debris disks, we need great sensitivity at far-infrared wavelengths where the thermal emission from the cold dust grains peaks ($\geq 70\,\mu$m). The *Herschel Space Observatory* (Pilbratt et al. 2010) provides a unique opportunity for sensitive debris disk surveys. *Herschel*'s PACS instrument (Poglitsch et al. 2010) is sensitive to the cold dust with a wavelength range of $55 - 210\,\mu$m. Additionally, *Herschel*'s spatial resolution is almost 4 times better than *Spitzer* at similar wavelengths, and therefore reducing confusion with background galaxies and interstellar cirrus and making it easier for *Herschel* to detect faint, cold debris disks.

In this chapter, we present results of a sensitive *Herschel* debris disk survey in the 30-Myr-old Tucana-Horologium Association. This work is part of the *Herschel* Open Time Key Programme "Gas in Protoplanetary Systems" (GASPS; Dent et al. in prep, Mathews et al. 2010). The GASPS survey targets young, nearby star clusters with well determined ages, spread from 1-30 Myr. This spread of ages covers the stages of planet formation from giant planet formation (~ 1 Myr; Alibert et al. 2005) to the late stages of terrestrial planet formation (10-100 Myr; Kenyon and Bromley 2006). The targets in each group were chosen to span a range of spectral types from B to M.

The 30 Myr-old Tucana-Horologium Association is the oldest in the GASPS survey. The Tucana-Horologium Association, discovered independently by Zuckerman and Webb (2000) and Torres et al. (2000), is a group of $\sim$ 60 stars with common proper motion and an average distance of 46 pc (Zuckerman and Song 2004). About $\sim 1/3$ of the targets have debris disk systems known from previous *Spitzer* surveys (Hillenbrand et al. 2008; Smith et al. 2006).

We obtained *Herschel* PACS photometry of the seventeen GASPS targets in the Tucana-Horologium Association. We also obtained PACS spectra for two of the targets. Previously unpublished *Spitzer* IRS spectra for three targets are presented. In Section 3.2, we present our methods and results of data reduction and aperture photometry. In Section 3.3, we fit blackbody and modified blackbody models to the detections and upper limits to determine dust temperatures and fractional luminosities. We further analyze some of the disks with our optically thin dust disk model in Section 3.4. Additionally, we discuss the detection of a marginally resolved disk in our sample in Section 3.5 and present conclusions in Section 3.6.

3.2 Observations and Data Reduction

The stellar properties of the seventeen Tucana-Horologium stars observed are listed in Table 3.1. These stars have spectral types ranging from B9-M3 and distances of 25-64 pc. PACS scan map observations were obtained for all seventeen Tucana-Horologium targets at 70 and 160 μm. Additional observations at 100 μm were taken for five targets. The stars were observed at two scan angles, 70 deg and 110 deg. The two scans were combined to reduce the excess noise caused by streaking in the scan direction, as suggested by the Herschel PACS Instrument Calibration Centre (ICC)[1]. Each scan map was executed with the medium scan speed ($20''\mathrm{s}^{-1}$) and consisted

of 10 legs with scan lengths of 3′ and scan leg separation of 4″. The number of repetitions varied from 1 to 4 based on the expected flux density of the star. The on-source time for each observation is given in Table 3.2. Two targets, HD105 and HD3003, were also observed in the PACS LineScan mode at 63 μm and 190 μm, targeting the OI fine structure line and DCO+ respectively.

Table 3.1: Stellar Properties in the 30 Myr-old Tucana-Horologium Association

Star	R.A. (J2000)	Dec. (J2000)	Spectral[a] Type	T_*[b] (K)	Distance[c] (pc)
HD2884[d]	00:31:32.67	-62:57:29.58	B9V	11250	43 ± 1
HD16978	02:39:35.36	-68:16:01.00	B9V	10500	47 ± 1
HD3003[d]	00:32:43.91	-63:01:53.39	A0V	9800	46 ± 1
HD224392	23:57:35.08	-64:17:53:64	A1V	9400	49 ± 1
HD2885[d]	00:31:33.47	-62:57:56.02	A2V	8600	53 ± 10
HD30051	04:43:17.20	-23:37:42.06	F2/3IV/V	6600	58 ± 4
HD53842	06:46:13.54	-83:59:29.51	F5V	6600	57 ± 2
HD1466	00:18:26.12	-63:28:38.98	F9V	6200	41 ± 1
HD105	00:05:52.54	-41:45:11.04	G0V	6000	40 ± 1
HD12039	01:57:48.98	-21:54:05.35	G3/5V	5600	42 ± 2
HD202917	21:20:49.96	-53:02:03.14	G5V	5400	46 ± 2
HD44627[d]	06:19:12.91	-58:03:15.52	K2V	5200	46 ± 2
HD55279	07:00:30.49	-79:41:45.98	K3V	4800	64 ± 4
HD3221	00:34:51.20	-61:54:58.14	K5V	4400	46 ± 2
HIP107345	21:44:30.12	-60:58:38.88	M1	3700	42 ± 5
HIP3556	00:45:28.15	-51:37:33.93	M1.5	3500	39 ± 4
GSC8056-482	02:36:51.71	-52:03:03.70	M3Ve	3400	25

[a] Spectral types listed are from the SIMBAD Astronomical Database
[b] Calculated from stellar modeling. See Section 3.3
[c] Distances from the *Hipparcos* Catalog (Perryman and ESA 1997)
[d] Binary or multiple star system

[1]PICC-ME-TN-036: `http://herschel.esac.esa.int/twiki/pub/Public/PacsCalibrationWeb/PhotMiniScan_ReleaseNote_20101112.pdf`

Table 3.2: Herschel PACS Photometry Results

Star	Wavelength (μm)	Obs. Flux (mJy)	Stellar Flux (mJy)	On-source Time (s)
		Debris Disks		
HD105	70	128.3 ± 7.0	3.1	72
	100	151.2 ± 5.7	1.7	144
	160	81.2 ± 12.3	0.6	144
HD3003	70	59.7 ± 3.8	7.6	72
	100	19.0 ± 2.4	4.1	144
	160	< 18.2	1.5	144
HD1466	70	13.0 ± 0.9	2.8	720
	160	< 10.6	0.6	720
HD30051	70	23.4 ± 1.1	3.2	720
	160	16.8 ± 2.4	0.6	720
HD202917	70	33.9 ± 1.6	1.6	360
	100	29.9 ± 2.5	0.8	144
	160	17.7 ± 3.8	0.3	360
HD12039	70	10.5 ± 0.8	2.3	720
	160	< 15.5	0.5	720
		Non-Excess Stars		
HD2884	70	7.7 ± 1.4	12.1	360
	160	< 18.6	2.3	360
HD16978	70	15.4 ± 1.7	15.8	144
	160	< 14.4	3.1	144
HD224392	70	8.6 ± 1.1	8.7	540
	160	< 10.0	1.7	540
HD2885	70	16.0 ± 1.4	16.5	360
	160	< 8.5	3.3	360
HD53842	70	9.9 ± 3.3	2.3	72
	100	< 9.2	1.3	144
	160	< 15.4	0.5	144
HD44627	70	< 3.5	1.4	360
	160	< 10.3	0.3	360
HD55279	70	< 3.1	0.9	360
	160	< 8.5	0.1	360

Continued on next page

Table 3.2 continued

Star	Wavelength (μm)	Obs. Flux (mJy)	Stellar Flux (mJy)	On-source Time (s)
HD3221	70	< 3.7	2.4	360
	160	< 10.4	0.4	360
HIP107345	70	< 3.3	0.9	360
	160	< 10.8	0.2	360
HIP3556	70	< 16.5	1.3	72
	100	< 16.9	0.7	144
	160	< 17.4	0.2	144
GSC8056-482	70	< 3.6	1.6	360
	160	< 20.4	0.3	360

3.2.1 Photometry

The data were reduced with HIPE 7.2 (Ott 2010) using the standard reduction pipeline. The final maps have pixel scales of 3.2/3.2/6.4″pixel^{-1} in the 70/100/160 μm images respectively, corresponding to the native pixel scales of the PACS detectors. The two scans were reduced separately, then averaged together. The flux values were measured using an IDL aperture photometry code with apertures of 5.5/5.6/10.5″ for the 70/100/160 μm images respectively, as recommended for faint sources. Aperture corrections were applied based on the encircled energy fraction from PACS observations of Vesta provided by the Herschel PACS ICC[2]. The sky annulus for error estimation was placed 20-30″ away from star center for the 70 and 100 μm images and 30-40″ away for the 160 μm images. For three of the targets, HD2884, HD2885 and HD53842, the fields were contaminated by nearby stars and background galaxies, so the sky annulus was offset to a nearby clean field.

The RMS pixel uncertainty, σ_{pix}, was estimated by calculating the standard devi-

[2]PICC-ME-TN-037: `http://herschel.esac.esa.int/twiki/pub/Public/PacsCalibrationWeb/pacs_bolo_fluxcal_report_v1.pdf`

ation of the pixels in the sky annulus. The total statistical error in the measurement is given by

$$\sigma_{tot} = \frac{\sigma_{pix}}{\alpha_{corr} x_{corr}} \sqrt{n_{ap}\left(1 + \frac{n_{ap}}{n_{sky}}\right)}, \tag{3.1}$$

where α_{corr} is the aperture correction factor to correct for the flux lost from using a small aperture, x_{corr} is the correlated noise correction factor[2] (0.95 at 70 and 100 μm, 0.88 at 160 μm) that accounts for the noise between pixels for our given choice of pixel size created while processing the projected sky map, and n_{ap} and n_{sky} are the number of pixels in the aperture and annulus respectively. An absolute calibration error was also added in quadrature with the statistical error to give the total uncertainty reported in Table 3.2. The absolute calibration errors given by the Herschel PACS ICC are 2.64/2.75/4.15% for the 70/100/160 μm images respectively[2]. Upper limits for all non-detections were determined using the 3σ errors from the same aperture photometry method as above.

The PACS photometry fluxes and upper limits are listed in Table 3.2. Six of the seventeen targets were determined to have infrared excesses above the photosphere. A significant excess is defined here as a 70 μm photosphere-subtracted flux greater than 3σ. One of our targets, HD2884, was previously suspected to have an infrared excess (Smith et al. 2006). In the PACS data, this target seems to have less flux than the expected photospheric value at 70 μm. The *Spitzer* IRS spectrum also shows no hint of an IR excess. Smith et al. (2006) notes the possibility of contamination of HD2884 with a background galaxy, but could not separate the two sources with *Spitzer*'s spatial resolution. Figure 3.1 shows the confused field of HD2884 observed with *Herschel* and *Spitzer* at 70 μm. *Herschel*'s improved spatial resolution allows us to properly resolve the sources and avoid contamination. We determine that HD2884 has no detectable debris disk.

HD53842 has a photosphere subtracted flux that is only 2.3σ above the noise at

70 μm. The *Spitzer* IRS spectrum from Moór et al. (2009) also shows a marginal excess at 14-35 μm but may suffer from contamination. The *Spitzer* 24 μm image shows two nearby stars within 15″ whose Point Spread Functions (PSFs) appear to overlap with that of HD53842. These sources are also seen in the PACS images (see Fig. 3.2) and make an accurate determination of the flux difficult. We are unable to confirm if HD53842 has a debris disk.

3.2.2 Spectroscopy

Two targets, HD105 and HD3003, were observed in the LineScan mode of the PACS instrument. The lines targeted were [OI] at 63.185 μm and DCO+ at 189.570 μm. The continuum detection limit was 202 mJy at 63 μm. The photometry detection at 70 μm was below this limit for both HD105 and HD3003, and the noise levels in the spectra are comparable to or larger than the flux at 70 μm. Therefore, we conclude that the continuum is not detected in these observations. There are also no emission lines detected above the noise.

Upper limits to the line fluxes were calculated by integrating over a Gaussian with a width equal to the instrumental Full-Width Half-Maximum (FWHM) and a height given by the standard deviation of the noise, placed at the wavelength where the line is expected. The upper limits are given in Table 3.3.

The three targets with previously unpublished *Spitzer* spectra (HD1466, HD2884 and HD3003) were observed with the IRS spectrograph (Houck et al. 2004), using the Short-Low (5.2-14 μm) and Long-Low modules (14-38 μm; $\lambda/\Delta\lambda \sim 60$). These three systems were observed as part of the *Spitzer* GTO program 40651 (PI: J. Houck). We carried out the bulk of the reduction and analysis of our spectra with the IRS team's SMART program (Higdon et al. 2004).

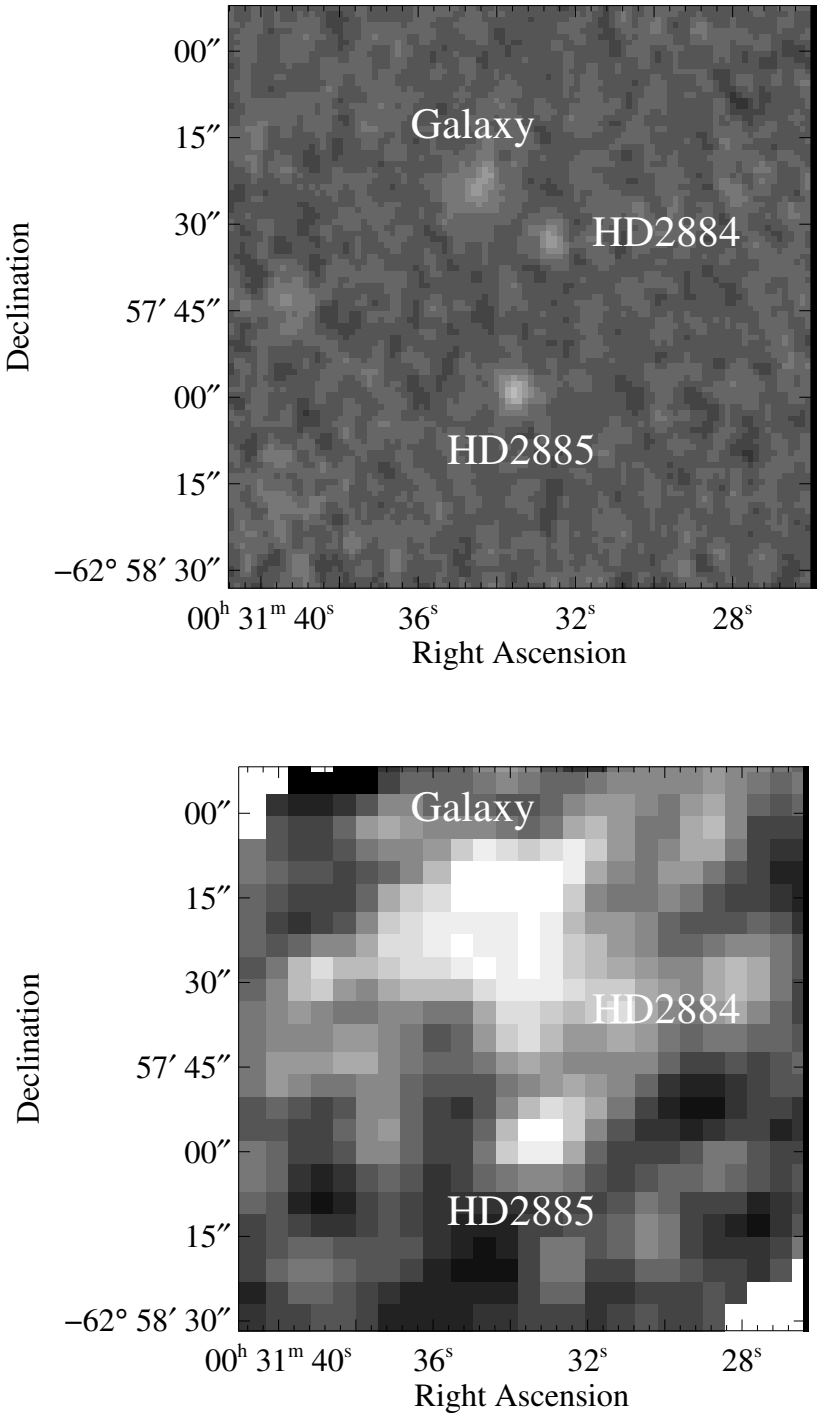

Figure 3.1: The field of HD2884 and HD2885 at 70 μm with *Herschel* (top) and *Spitzer* (bottom). The better spatial resolution of *Herschel* allows the sources to be cleanly separated and avoids contamination of photometry.

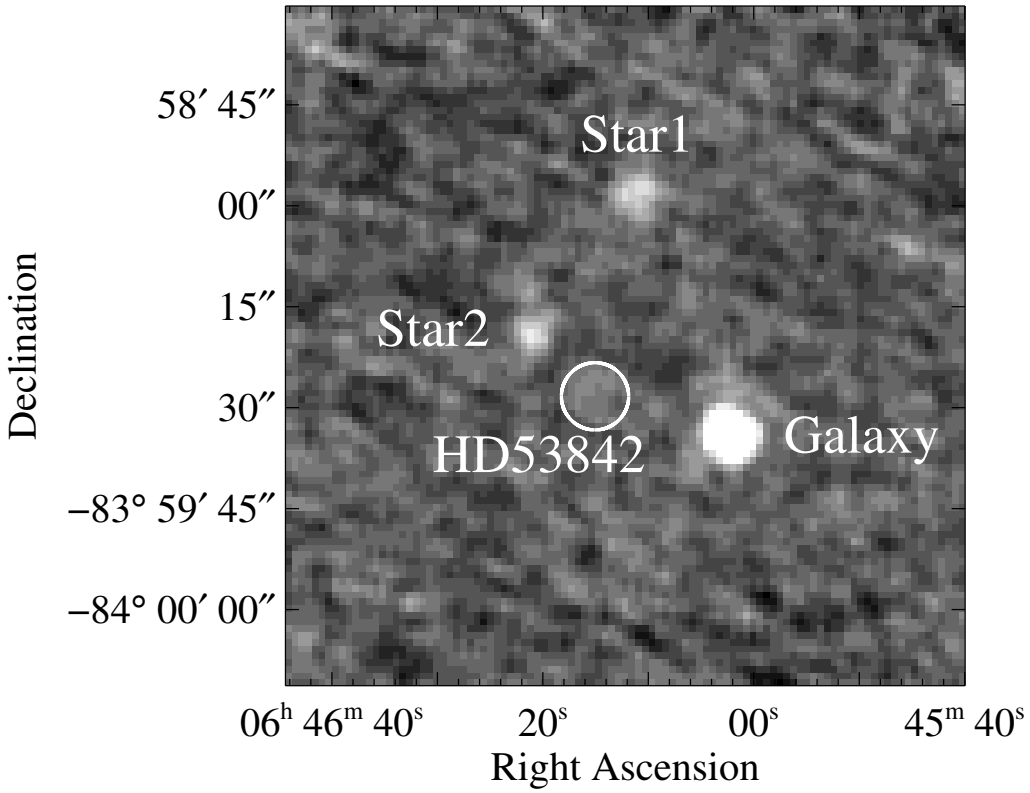

Figure 3.2: The field of HD53842 at 70 μm with *Herschel*. The star is barely detected at 70 μm (3σ detection). The nearby sources may have contaminated the *Spitzer* IRS spectrum of HD53842.

Table 3.3: Herschel Spectroscopy: 3σ Line Upper Limits

Star	Line	Wavelength (μm)	3σ Upper Limit (W/m^2)
HD105	[OI]	63.185	$< 9.63 \times 10^{-18}$
	DCO+	189.570	$< 1.18 \times 10^{-17}$
HD3003	[OI]	63.185	$< 1.43 \times 10^{-17}$
	DCO+	189.570	$< 8.55 \times 10^{-18}$

3.3 Blackbody and Modified Blackbody Fits

We constructed spectral energy distributions for all sources using data from *Hipparcos, 2MASS, Spitzer* (IRAC, IRS, and MIPS), *AKARI, IRAS*, the *WISE* preliminary release, and our new *Herschel* data. The SEDs of debris disk stars are shown in Figure 3.3 and those of non-excess stars in Figure 3.4. The data used for these figures are listed in Table 3.6. For each target, we fitted the stellar photosphere with NextGen models of stellar atmospheres (Hauschildt et al. 1999). The best fitting stellar model was determined through χ^2 minimization with effective temperature and the normalization factor as free parameters. The *Spitzer* IRS spectra were binned to a resolution of $\Delta\lambda/\lambda \sim 0.1$ and only the data with $\lambda > 8\,\mu$m were used to determine the fit of the excess.

For our six disk detections, we fitted the excess emission with a standard single temperature blackbody model with two parameters, the temperature and the fractional disk luminosity. This model is a simplified disk representation that assumes all the dust is at the same temperature, and behaves like a perfect blackbody. While this model is simple, it gives a good first estimate of the dust temperature and abundance, and unlike more physical models, one can get a fit even with very few data points. The best fit was determined through χ^2 minimization. We also calculated the goodness-of-fit for each best fitting model for comparison with more detailed models described in Section 3.4. The goodness-of-fit, Q, is the probability that a χ^2 value this poor will occur by chance given the error in the data. Q is given by the normalized incomplete gamma function

$$Q(a,x) = \frac{\Gamma(a,x)}{\Gamma(a)}\,; \quad a = \frac{N}{2} \quad x = \frac{\chi^2}{2}, \tag{3.2}$$

where $\Gamma(a,x)$ and $\Gamma(a)$ are incomplete and complete gamma functions respectively, and N is the number of degrees of freedom. Q varies from 0 to 1, with larger values

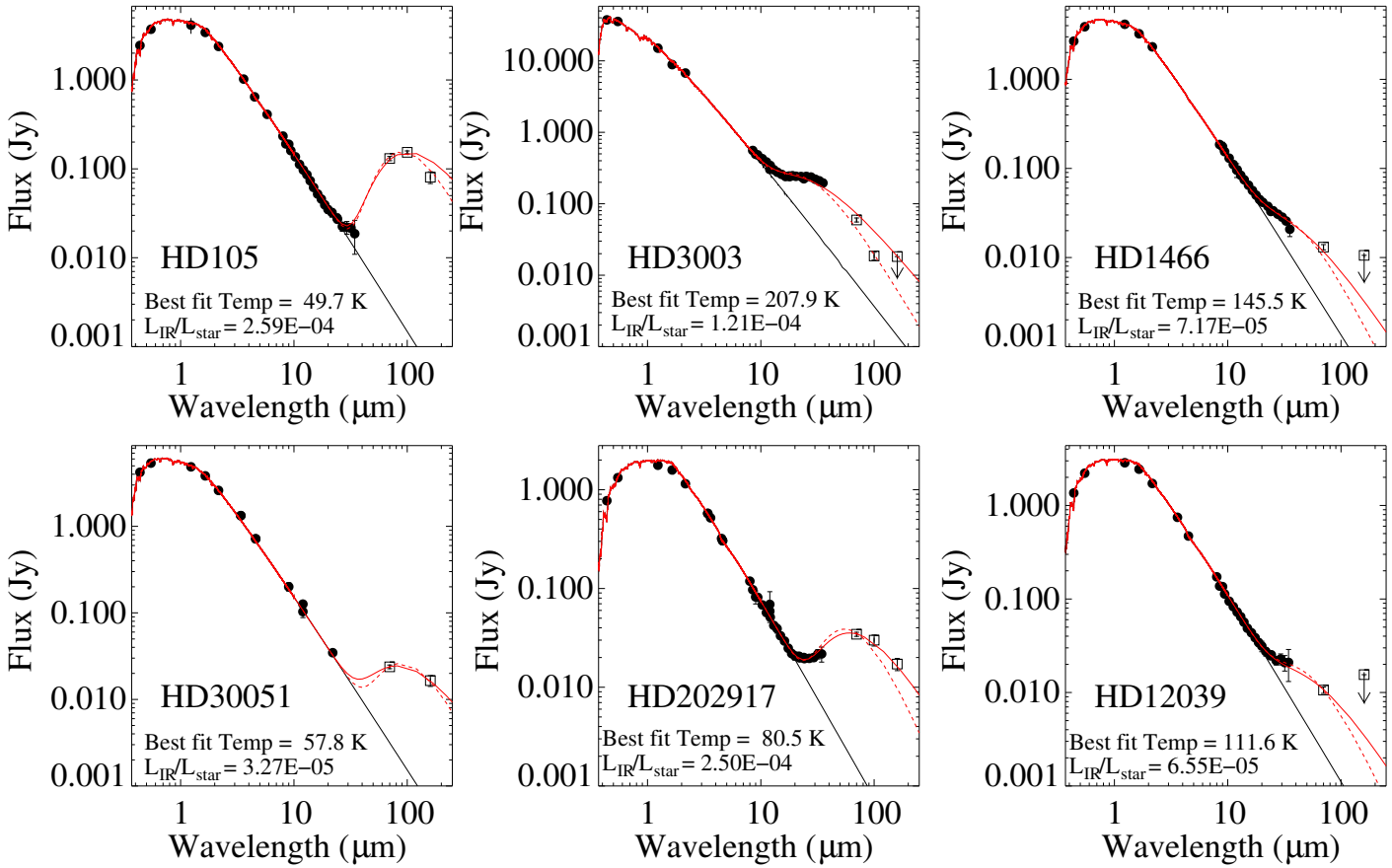

Figure 3.3: Single temperature blackbody fits to the SEDs of the 6 debris disks in the sample. Filled circles are data from the literature, open squares are the *Herschel* PACS data. The solid black curve is the fit to the stellar photosphere using the NextGen models (Hauschildt et al. 1999). The red curve shows the best fitting single temperature blackbody model. The figure label for each disk displays the best fitting temperature and the fractional IR luminosity $L_{\rm IR}/L_*$. The dashed red lines show the best-fitting modified blackbody models. Available MIPS 70 μm data are not plotted here, as they are consistent with the PACS data, which have smaller uncertainties.

indicating better fits. An acceptable model is one that has a value of $Q \gtrsim 10^{-3}$ (Press et al. 1992).

The Q values, however, are largely influenced by the IRS spectrum. The IRS spectra have more data points compared to the few PACS photometry points. Therefore, fits that may appear to be just as good, can have very different Q values if the uncertainties in the IRS spectra are different. The point of the Q value is not to compare the goodness-of-fit between disks, but to compare between models of a given disk.

From the fits, we determined the disk temperatures and the fractional infrared luminosities ($L_{\rm IR}/L_*$). For the remaining sources, we determined upper limits on $L_{\rm IR}/L_*$ by fitting blackbody models to the flux upper limits. Upper limits on $L_{\rm IR}/{\rm L}_*$ depend on temperature, so the largest $L_{\rm IR}/L_*$ value found assuming dust temperatures from 10-300 K was adopted. The results of the fits to the disks are given in Table 3.4. The disks display a large range of temperatures and $L_{\rm IR}/L_*$ values, showing no correlation with spectral type.

We also fit the disks with a modified blackbody model. This model assumes that at longer wavelengths, the grains no longer emit as blackbodies, but instead the dust emissivity is decreased by a factor $(\lambda/\lambda_0)^{-\beta}$ for $\lambda > \lambda_0$, due to a lower dust opacity at longer wavelengths compared to a blackbody. Here $\lambda_0 = 2\pi a_{blow}$, where a_{blow} is the blowout size due to radiation pressure. We do not have sub-mm or mm data to constrain the parameter β, therefore we assume $\beta = 1.0$ for these models based on previous measurements for debris disks (Dent et al. 2000; Nilsson et al. 2010; Williams and Andrews 2006). ISM dust has $\beta \approx 2.0$ (Boulanger et al. 1996), but debris disks are expected to have lower values of β due to the presence of larger grains (Draine 2006). The results of the modified blackbody fits are also shown in Table 3.4. The use of modified blackbody models shifts the characteristic temperatures

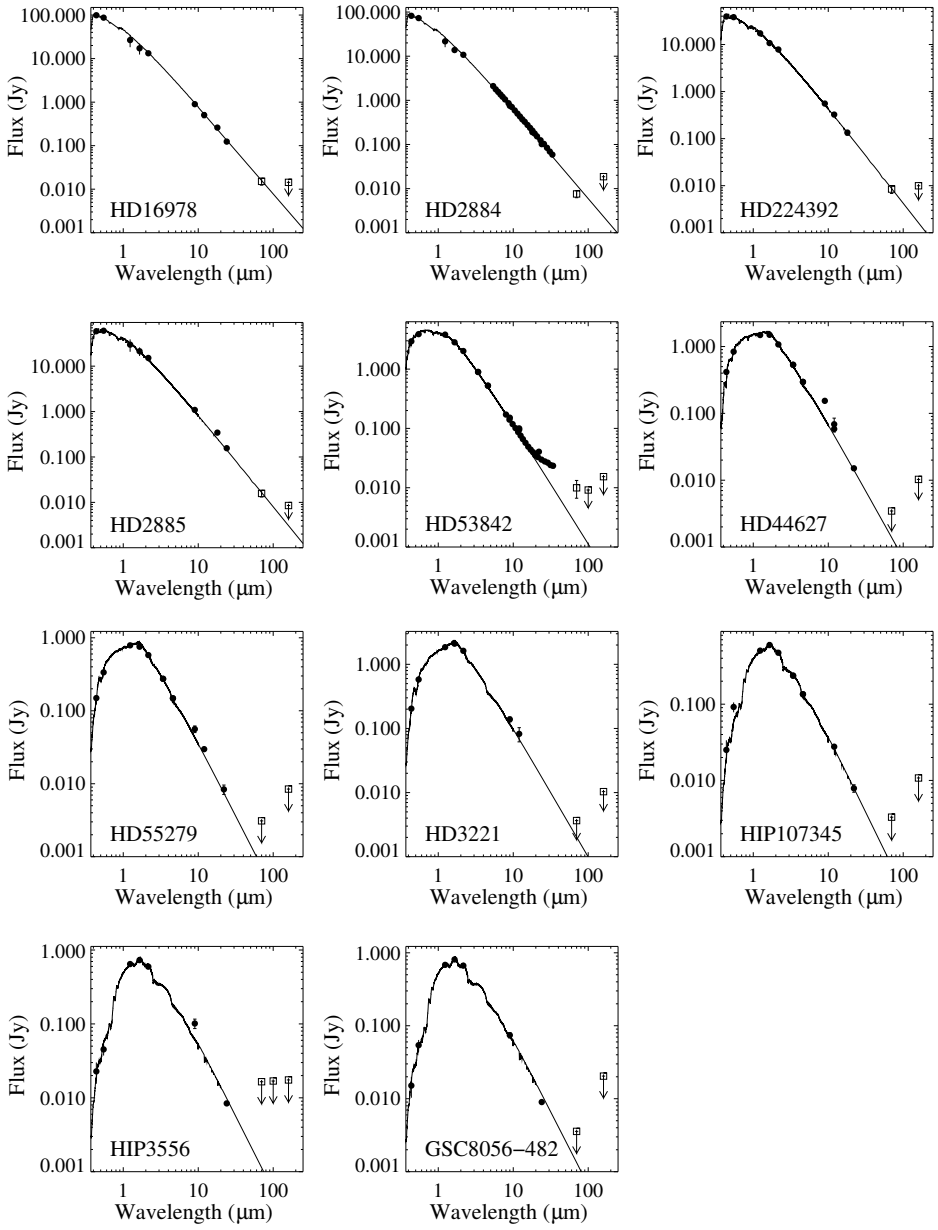

Figure 3.4: Spectral energy distributions for the 11 stars that were not found to have debris disks. The solid curve is the fit to the stellar photosphere using the NextGen models (Hauschildt et al. 1999). Upper limits for $L_{\rm IR}/L_*$ are shown in Table 3.4. Available MIPS 70 μm data are not plotted here, as they are consistent with PACS data for every source except HD2884, which lies in a confused field (see Fig. 3.1). HD53842 has only a marginal detection of an excess at 70 μm and also lies in a confused field (see Fig. 3.2). Consequently, we are unable to determine if HD53842 has a debris disk.

Table 3.4: Model Fit Results

Debris Disks			
Blackbody Fits			
Star	Temp (K)	L_{IR}/L_*	Q
HD105	49.7 ± 1.4	$(2.59 \pm 0.05) \times 10^{-4}$	0.004
HD3003	207.9 ± 2.5	$(1.21 \pm 0.01) \times 10^{-4}$	0.00
HD1466	145.5 ± 6.7	$(7.21 \pm 0.11) \times 10^{-5}$	0.61
HD30051	57.8 ± 6.4	$(3.27 \pm 0.20) \times 10^{-5}$	0.82
HD202917	80.5 ± 1.5	$(2.50 \pm 0.01) \times 10^{-4}$	0.93
HD12039	111.6 ± 6.2	$(6.55 \pm 0.39) \times 10^{-5}$	0.38
Modified Blackbody Fits			
HD105	40.3 ± 1.2	$(2.41 \pm 0.90) \times 10^{-4}$	0.11
HD3003	160.6 ± 1.6	$(1.08 \pm 0.01) \times 10^{-4}$	0.00
HD1466	106.8 ± 4.3	$(6.33 \pm 0.03) \times 10^{-5}$	0.002
HD30051	39.8 ± 2.8	$(2.81 \pm 0.05) \times 10^{-5}$	0.82
HD202917	64.6 ± 1.1	$(2.50 \pm 0.01) \times 10^{-4}$	0.13
HD12039	85.1 ± 3.7	$(6.33 \pm 0.33) \times 10^{-5}$	0.43
Non-Excess Stars			
	Blackbody L_{IR}/L_*	Modified Blackbody L_{IR}/L_*	
HD2884	$< 2.9 \times 10^{-6}$	$< 6.7 \times 10^{-6}$	
HD16978	$< 1.9 \times 10^{-6}$	$< 8.6 \times 10^{-7}$	
HD224392	$< 5.0 \times 10^{-6}$	$< 1.6 \times 10^{-5}$	
HD2885	$< 2.7 \times 10^{-6}$	$< 1.8 \times 10^{-5}$	
HD53842	$< 6.4 \times 10^{-5}$	$< 2.9 \times 10^{-4}$	
HD44627	$< 1.9 \times 10^{-4}$	$< 1.7 \times 10^{-4}$	
HD55279	$< 8.6 \times 10^{-4}$	$< 2.5 \times 10^{-3}$	
HD3221	$< 2.4 \times 10^{-4}$	$< 1.3 \times 10^{-3}$	
HIP107345	$< 8.4 \times 10^{-4}$	$< 4.2 \times 10^{-4}$	
HIP3556	$< 1.2 \times 10^{-3}$	$< 5.4 \times 10^{-4}$	
GSC8056-482	$< 1.2 \times 10^{-3}$	$< 5.3 \times 10^{-4}$	

to lower values, a trend which was also noticed by Carpenter et al. (2009). The goodness-of-fit was improved for HD105, HD3003, and HD12039 with the use of the modified blackbody model, but made worse for HD1466 and HD202917.

The blackbody and modified blackbody models provide a first look at the disk properties. For example, disks with low characteristic temperature such as HD105,

HD30051, and HD202917, are likely to have large inner gaps and copious amounts of cold dust far from the star. To test this idea, we need a more physical model of the disk.

3.4 Dust Disk Model

To further investigate the disk properties, we fit the disks with an optically thin dust disk model. Rather than assuming the grains to be perfect blackbodies, the dust model assumes the grains have a particular emissivity that is dependent on the size of the dust grains and the wavelength of radiation being absorbed or emitted. For the Tucana-Horologium disks, we make the assumption that the grains are purely silicate in composition, specifically, astronomical silicates (Draine and Lee 1984; Laor and Draine 1993; Weingartner and Draine 2001). The poorly populated SEDs and lack of resolved imaging prevents us from fitting more complex grain compositions.

The geometry of the disks is described by three parameters: the inner and outer radius (r_{min} and r_{max}) and the radial surface density profile. The azimuthally symmetric radial surface density profile is characterized by a power-law with index q, such that the surface density Σ varies with radius as $\Sigma(r)dr \propto r^q dr$. A power-law index of $q = 0$ is expected for a transport dominated disk, and an index of $q = -1.5$ is expected for a collisionally dominated disk (Krivov et al. 2006; Strubbe and Chiang 2006).

The population of dust grains is also characterized by three parameters: the minimum and maximum dust grain sizes in the disk (a_{min} and a_{max}), and the distribution of grains with sizes between a_{min} and a_{max}. The grain size distribution is typically assumed to be a power-law with index κ such that the number density varies with grain size a as $n(a)da \propto a^\kappa da$, where a value of $\kappa \sim -3.5$ is expected for

a steady-state collisional cascade (Dohnanyi 1969).

As discussed in Section 2.4, the model iteratively determines the equilibrium dust temperature at each radius for each grain size by balancing radiation absorbed from the star with radiation re-emitted through the formula

$$\int_0^\infty Q_{abs}(\nu,a)\left(\frac{R_*}{r}\right)^2 B_\nu(T_{eff})d\nu = \int_0^\infty 4Q_{abs}(\nu,a)B_\nu(T_d(r,a))d\nu, \tag{3.3}$$

where $B_\nu(T_{eff})$ is the blackbody flux coming from the surface of the star with temperature T_{eff} and radius R_*, $B_\nu(T_d(r,a))$ is the blackbody flux radiating from the dust grain of size a at a distance r away from the star, and $Q_{abs}(\nu,a)$ is the dust absorption coefficient calculated by Draine and Lee (1984) for an astronomical silicate grain of size a. The total flux is then determined by summing up over all radii and grain sizes according to the formula

$$\begin{aligned} F_\nu = A &\int_{a_{min}}^{a_{max}} \left(\frac{a}{a_{max}}\right)^\kappa da \\ &\cdot \int_{r_{min}}^{r_{max}} 4\pi a^2 Q_{abs}(\nu,a)\pi B_\nu(T_d(r,a))2\pi r \left(\frac{r}{r_{min}}\right)^q dr, \end{aligned} \tag{3.4}$$

where A is a normalization constant that includes the distance to the system and the total amount of material in the disk.

3.4.1 Model Parameters

The Tucana-Horologium debris disks are faint (all are under 150 mJy at 70 μm), so the SEDs of these targets are not well sampled due to lack of detections at the longer wavelengths. For this reason, we must fix some of the model parameters. In particular, because of the lack of sub-mm and longer wavelength data, we are unable to constrain parameters that affect this region of the SED, specifically cold grains that are larger than 1 mm or farther out than $\sim$ 120AU. Therefore, we fix the maximum grain size and the outer radius to these values. For HD202917, we fixed

the outer radius to 80 AU to be consistent with HST imaging (Krist 2007; Mustill and Wyatt 2009). The radial surface density profile also cannot be constrained with the current data. Hence we fix the power-law index of the radial density profile to $q = -1.5$, the value expected for collisionally dominated disks.

The SEDs of HD105, HD3003, and HD202917 are populated enough to get well constrained fits with only these three parameters fixed. However, HD1466 and HD12039 were only detected at 70 μm with PACS. The models for these disks were further constrained by fixing the minimum grain size and the grain size distribution. The grain size distribution was fixed to a power-law index of $\kappa = -3.5$, the value expected for a steady-state collisional cascade, and the minimum grain size was fixed to the expected blowout size for astronomical silicates. This is the size at which the radiation pressure is half of the gravity; grains this size and smaller are ejected from the system. The blowout size is calculated from the formula given in Backman and Paresce (1993) as

$$\left(\frac{a_{blow}}{1\,\mu m}\right) = 1.15 \left(\frac{L_*}{L_\odot}\right) \left(\frac{M_\odot}{M_*}\right) \left(\frac{1\text{g cm}^{-3}}{\rho}\right) \tag{3.5}$$

assuming constant density, spherical grains produced from planetesimals on circular orbits. This equation assumes that the grains are spherical, have a certain composition, all have the same density, and that the density is uniform throughout the grain. For astronomical silicates, we assume a grain density of 2.5 g cm^{-3}. This simple equation provides a good estimate of the expected minimum grain size, but it relies heavily upon many assumptions and must be treated solely as an estimate, accurate perhaps to only an order of magnitude.

3.4.2 Results

To determine the best model for each system, we compared a grid of models to the SED and found the set of parameters that produced the χ^2 minimum value. The error of each fit parameter was determined from the 1σ confidence interval in the χ^2 distribution after fixing the other parameters to their best fit values. The best fitting parameters and the errors are displayed in Table 3.5, and the best fitting SED models are shown in Figure 3.5. The HD30051 disk could not be fit at all with this model because its SED has too few data points, having not been known to have a debris disk before *Herschel*.

Lower limits on the disk masses are also given in Table 3.5. These masses are calculated by summing up the mass of silicate grains with an assumed uniform density of 2.5 g cm^{-3}, with sizes between $a_{\rm min}$ and $a_{\rm max}$ and disk radii between $r_{\rm min}$ and $r_{\rm max}$. The mass also depends on the normalization constant and the radial density profile of the disk. It is a lower limit on the mass because it only takes into account the dust smaller than 1 mm, and not larger pebbles and planetesimals hidden in the disk.

HD105

HD105, a G0V star 40 pc away, has the largest IR excess in the PACS wavebands of all the Tucana-Horologium disks in this sample, yet shows very little mid-IR excess in the *Spitzer* IRS spectrum. This disk was observed with *Spitzer* as part of the Formation and Evolution of Planetary Systems (FEPS) Legacy Survey (Meyer et al. 2006). Meyer et al. (2004) first fit the disk with models from Wolf and Hillenbrand (2003) that used Draine and Lee (1984) grain emissivities for astronomical silicates and graphite in ISM ratios and found an inner radius of 45 AU for a fixed

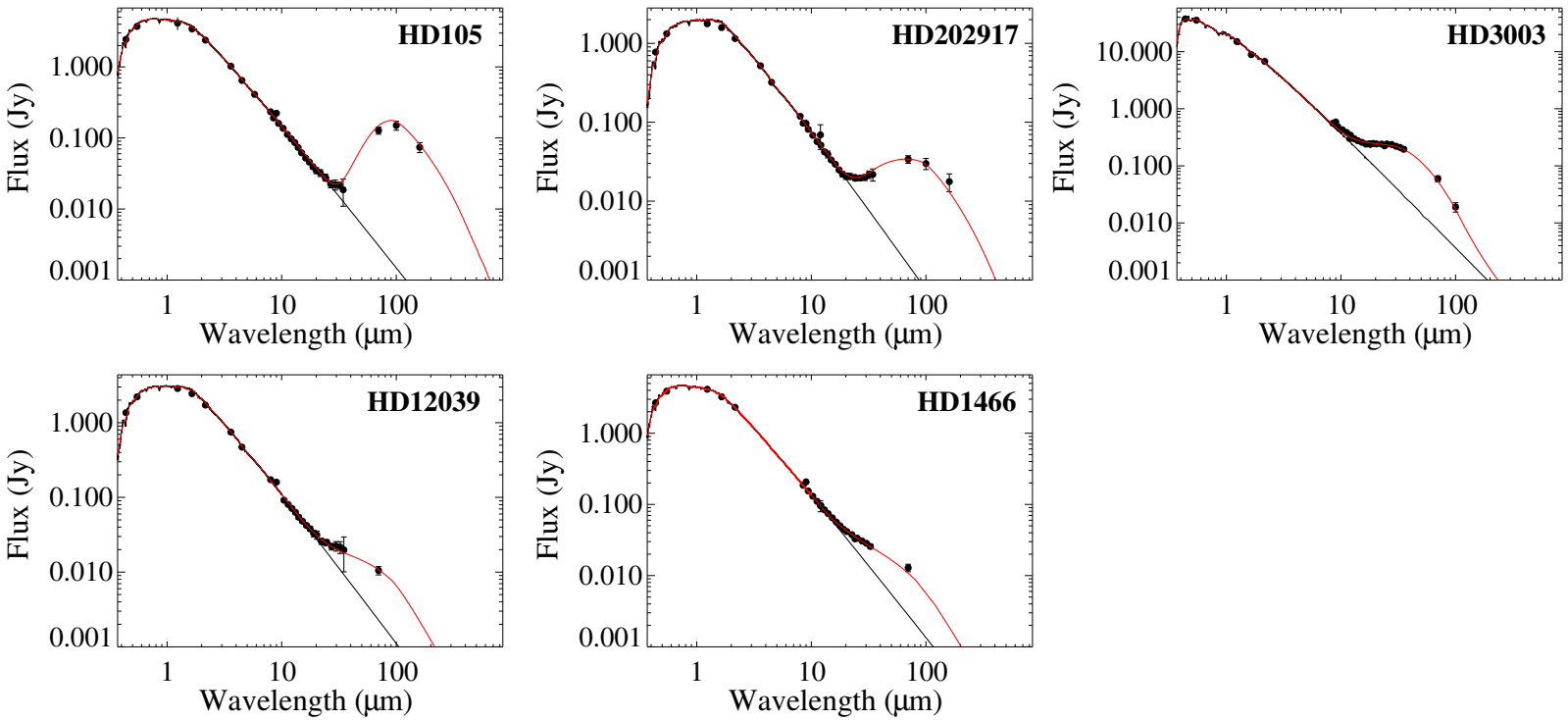

Figure 3.5: Best fitting models for the five of the debris disks with well populated SEDs. The solid black lines shows the stellar photospheres that are fit with the NextGen models (Hauschildt et al. 1999). The best fitting models of the disks are shown in red. The best fitting model parameters are given in Table 3.5.

minimum grain size of 5 μm. They assumed a flat radial density profile (q=0), a grain size distribution power-law index of $\kappa = -3.5$, an outer radius of 300 AU, and a maximum grain size of 100 μm.

Hollenbach et al. (2005) found an even lower χ^2 value using the Wolf and Hillenbrand (2003) models with a minimum grain size of 21 μm and a lower inner radius of 19 AU, but confirmed that the inner cavity must be $\geq$ 13 AU because of the lack of IR excess at $\lambda \lesssim 35\,\mu$m. The *Spitzer* IRS spectrum also shows no evidence of gas lines, and Hollenbach et al. (2005) determined the gas mass to be $< 0.1\,M_J$ between 10–40 AU for a constant surface density.

Later FEPS modeling by Hillenbrand et al. (2008) used multi-temperature blackbodies to fit the HD105 disk, and found an inner radius of 36.8 AU. This is a lower limit to the inner radius since the grains were assumed to be large blackbody grains. Smaller grains could reach the same temperatures farther from the star.

The smaller error bars of the *Herschel* PACS measurements, and the addition of the 100 μm data point, better map the characteristic turnover point in the SED and lessens the severity of the model degeneracy. Our results are consistent with those of Meyer et al. (2004), Hollenbach et al. (2005), and Hillenbrand et al. (2008).

The lack of mid-IR excess in this disk indicates an absence of both small grains and grains within a large inner cavity. The dust begins at about the distance of the Solar System's Kuiper belt (52 AU using our best fitting model) and extends to some distance beyond (see Section 3.6 for an estimate of the outer radius of HD105). The lack of detectable dust interior to this region may be due to one or more planets orbiting inside this dust ring (Moro-Martín and Malhotra 2005). Apai et al. (2008) searched for massive planets in the HD105 disk using VLT/NACO angular differential imaging and found none. However, the survey was only sensitive to planets with masses $> 6\ M_J$ at distances > 15 AU.

The minimum grain size for this disk (8.9 μm) is much larger than the expected blowout size of 0.5 μm. This suggests either the calculation of the blowout size is inaccurate, or the small grains are efficiently removed by some other mechanism. The calculation of the blowout size is just an estimate with several assumptions built in, such as grain density and composition, and a change in the assumptions could lead to a drastically different blowout size. For instance, if the grains were porous, they would be less massive at a certain size, and the larger grains could be more easily blown out of the system.

HD202917

HD202917 is a G5V star 46 pc away. The disk was observed with *Spitzer* by Bryden et al. (2006) and analyzed as part of the FEPS survey by Hillenbrand et al. (2008) and Carpenter et al. (2008). Smith et al. (2006) fit the disk with a blackbody grain model to get a lower limit on the disk inner radius. They found the inner radius to be > 7.4 AU. Hillenbrand et al. (2008) fit a multi-temperature blackbody model to the disk that gave an inner radius of 2.5 AU, also a lower limit. HD 202917 was also resolved in scattered light by HST/ACS, giving a disk outer radius of R $\approx$ 80 AU (Krist 2007; Mustill and Wyatt 2009). For this reason, we fixed $r_{max} = 80$ AU rather than the usual value of 120 AU.

The fit is not well constrained in a_{min}, but the fit with the lowest χ^2 value has $a_{min} = 0.3\,\mu$m, equal to the blowout size. We found the best fitting inner radius to be 46 AU. This result is larger than the previous lower limits due to the presence of small grains in the model. We find this disk to be consistent with a belt of material between 45 and 80 AU.

Table 3.5: Best Fitting Model Parameters

Target	a_{min} [a]	a_{blow}	a_{max} [a]	κ [a]	r_{min} [a]	r_{max} [a]	q [a]	Q [b]	Mass ($M_\oplus$) [c]
HD105	$8.9^{+11.1}_{-4.4}\,\mu$m	$0.5\,\mu$m	*1000 μm*	$-3.3^{+0.3}_{-0.4}$	52^{+36}_{-7}AU	*120 AU*	*-1.5*	0.15	4.3×10^{-4}
HD202917	$< 2.8\,\mu$m[d]	$0.3\,\mu$m	*1000 μm*	-3.4 ± 0.1	46^{+9}_{-3} AU	*80 AU*	*-1.5*	0.70	3.4×10^{-4}
HD3003	$3.5^{+0.5}_{-0.3}\,\mu$m	$3.4\,\mu$m	*1000 μm*	$-4.4^{+0.1}_{-0.2}$	$7.8^{+0.3}_{-0.2}$ AU	*120 AU*	*-1.5*	8.0×10^{-11}	7.0×10^{-6}
HD12039	*0.4 μm*	$0.4\,\mu$m	*1000 μm*	*-3.5*	14 ± 3 AU	*120 AU*	*-1.5*	0.88	1.7×10^{-4}
HD1466	*0.5 μm*	$0.5\,\mu$m	*1000 μm*	*-3.5*	$7.8^{+2.1}_{-1.8}$ AU	*120 AU*	*-1.5*	0.30	6.2×10^{-5}

[a] Model parameters

[b] Model goodness-of-fit

[c] Lower limit on dust mass is calculated from the model parameters

[d] Unconstrained parameter, limits given are 3σ confidence

Model parameters in italics are fixed

HD3003

HD3003 is an A0V star with a warm disk first detected by IRAS (Oudmaijer et al. 1992). Smith et al. (2006) also observed the HD3003 disk with *Spitzer* MIPS at 24 and 70 μm. Smith et al. (2006) modeled the disk with blackbody grains at a single radius and found a dust temperature of 230 K at a radius of 6.7 AU. Smith and Wyatt (2010) added unresolved ground based mid-IR photometry from TIMMI2, VISIR, Michelle and TReCS and found a blackbody temperature of 265 K with a radius of 4 AU. Smith and Wyatt (2010) also make the point that HD3003 is a binary, and a disk of this temperature must be circumstellar not circumbinary in order to be stable.

With the new PACS data, we found a lower blackbody temperature of 208 K. This is still highest temperature of all the disks in the sample, implying the grains are either very close to the star, or smaller than 1 μm in size. But HD3003 is an A0 star, and has a blowout size of 3.4 μm. Therefore, the temperature is likely due to the distance from the star. Our model of the HD3003 disk gives an inner radius of 7.8 AU and a minimum grain size consistent with the estimated blowout size. The goodness-of-fit is very small for HD3003, with $Q = 8 \times 10^{-11}$, despite reproducing the PACS data quite well. This small value is driven mostly by the small error bars on the *Spitzer* IRS spectrum. However, this goodness-of-fit is indeed larger than the value found for the blackbody models.

The grain size distribution, however, departs from the expected shape. The best fit grain size distribution power-law index value of $\kappa = -4.4$ is much steeper than the $\kappa = -3.5$ value expected for a steady state collisional cascade. HD3003 is the only binary system with a confirmed disk in the sample. The apparent binary separation is $\sim 0.1''$ (Mason et al. 2001). If this projected separation were a true binary separation, the companion would be about 4.6 AU from HD3003. Smith and

Wyatt (2010) suggest the binary must have a semi-major axis > 14.4 AU for the disk to be stable. If the system is unstable rather than in steady state equilibrium, then it could have a κ value very different from the steady state value. Other possibilities are explored in Section 3.6.3.

HD12039

HD12039 is a G3/5V star 42 pc away with a debris disk first detected using data from the FEPS Legacy Program (Hines et al. 2006). The FEPS team analyzed *Spitzer* observations with IRAC, IRS, and MIPS (24, 70, and 160 μm). The disk was not detected with *Spitzer* at 70 and 160 μm. A blackbody fit gave a characteristic disk temperature of 110 K and a lower limit on the radius of 6 AU. Hines et al. (2006) also fit the disk with the models of Wolf and Hillenbrand (2003) that uses astronomical silicates, with flat surface density profile ($q = 0$) and a Dohnanyi (1969) distribution of grains from 0.4-1000 μm. The best fitting model yielded an inner radius of 28 AU.

The best-fitting model in Hines et al. (2006) was very dependent on the MIPS 70 μm upper limit. With the PACS 70 μm detection, the disk radius is better constrained. We fit the disk with a surface density profile of $q = -1.5$, a minimum grain size at the blowout limit, and a Dohnanyi (1969) grain size distribution, similar to the modeling done by Hines et al. (2006). But, in contrast to Hines et al. (2006), we found a smaller inner radius of 14 ± 3 AU. This difference is due mainly to our measured disk flux at 70 μm that Hines et al. (2006) did not have.

HD1466

HD1466 is an F9V star 41 pc away with an excess detected by Smith et al. (2006) at both 24 and 70 μm with *Spitzer* MIPS. Smith et al. (2006) found a minimum radius of 7.2 AU. Our physical disk model fit gave an inner radius of 7.8 AU, consistent with previous results.

HD30051

The HD30051 disk, unfortunately, has very little mid-IR data available to constrain the disk parameters. With only two data points showing IR excess, we were unable to model the disk in any more detail than a blackbody model. But the best-fitting blackbody temperature of 58 K indicates the main component of the disk is far from the star. Keeping the assumption of large pure blackbody grains, the disk would be centered around $\sim$ 45 AU. This is a lower limit on the disk radius because smaller silicate grains would have a temperature of 58 K tens of AU farther out.

3.5 Resolving the HD105 Debris Disk

3.5.1 Radial Profile

One disk in our sample, HD105, is marginally resolved at 70 μm in the *Herschel* PACS images. HD105 is the brightest disk in our sample. It may not be the most extended, but for the other disks an extended structure would fall below the background noise. We determined that the HD105 disk was resolved in two ways. The first was to compare the azimuthally averaged radial profile of the disk to a reference star, Arcturus. Figure 3.6 (a) shows the azimuthally averaged radial profiles of the two images. These profiles were calculated by measuring the mean

flux within annuli of one arcsecond width around the star. Scan maps with a smaller pixel scale of $1''$ pixel^{-1} were created for this purpose. The uncertainties in the measurements were determined by calculating the standard deviation in the flux within each annulus. This method leads to an overestimation of the errors because the PACS PSF changes radially across each annulus due to its tri-lobed shape. The azimuthally averaged radial profile of HD105 shown in Figure 3.6 (a) is extended beyond the PSF with a FWHM of $6.1 \pm 0.8''$ compared to the PSF FWHM of $5.3 \pm 0.5''$. The error in the FWHM is determined from the uncertainties in the brightness by calculating the distance away from the FWHM where the brightness profile plus and minus the errors would be equal to half the maximum brightness. This is not a strong detection of extended structure given the large (and overestimated) errors. Therefore, we also used a second method to determine if the disk is resolved.

The second method tries to avoid problems with the PACS PSF tri-lobe shape by averaging over brightness contours rather than annuli. Figure 3.7 shows the PACS 70 μm images of HD105 and the reference star Arcturus scaled to the same peak brightness with brightness contours overlaid. The fluxes in the regions between the contours were averaged and the uncertainty measured from the standard deviation. The contours used for Figure 3.6 (b) are 15, 30, 50, 70, 85, and 100% of the peak brightness for HD105 and Arcturus. For Arcturus, which is brighter than HD105, the 1, 2, 5, and 10% contours are also used. The radius adopted for each mean flux value was the mean distance of the region between the contours. This method is unable to map the brightness profile of HD105 far from the star because it quickly falls below the background. But it is clear from Figure 3.6 (b) that the disk is extended with a FWHM of $7.2 \pm 0.5''$ beyond the PSF that has a FWHM of $6.1 \pm 0.4''$.

The PACS PSF size is given by the *Herschel* PACS ICC as a two-dimensional Gaussian with FWHM of $5.5 \times 5.8''$. The FWHM reported here for HD105 was not

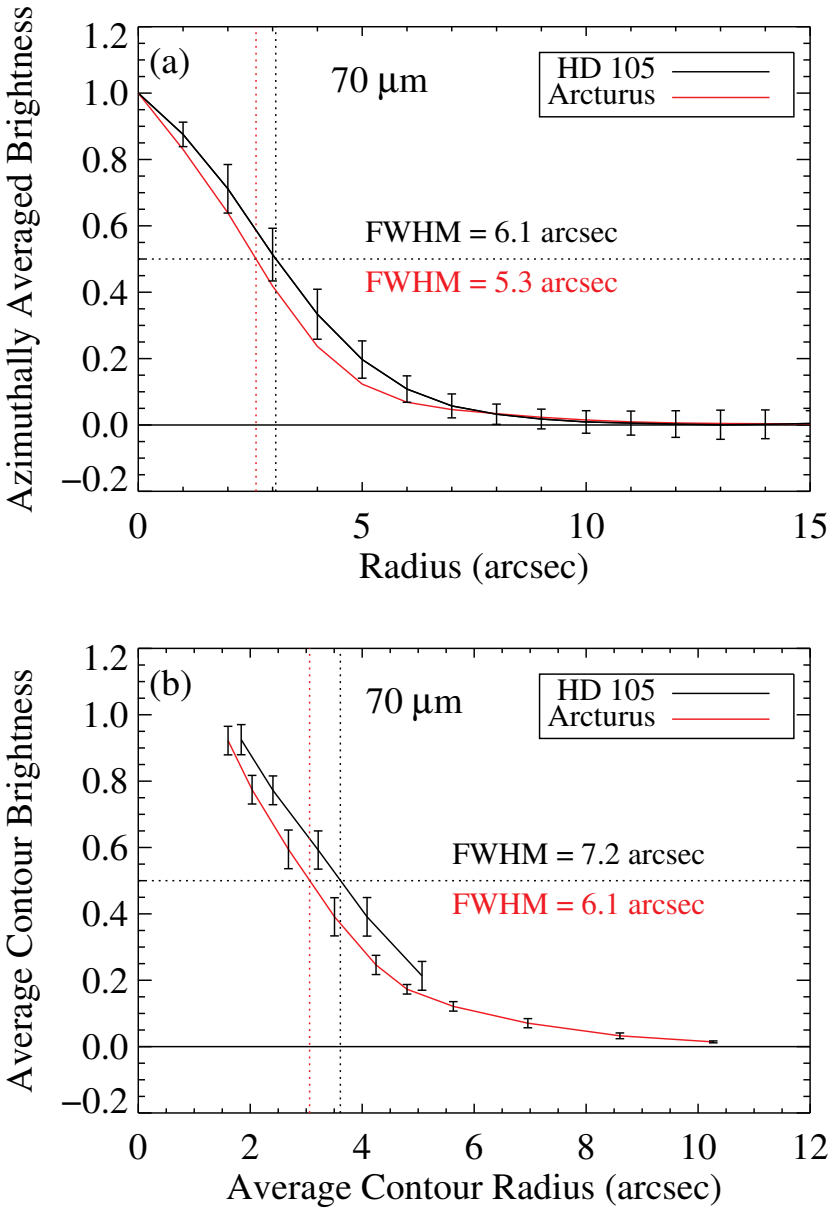

Figure 3.6: (a): Azimuthally averaged radial brightness profiles for HD105 and the reference star Arcturus at 70 μm. The radial profiles are azimuthally averaged over annuli with one arcsecond widths. (b): Averaged brightness profiles from contours for HD105 and Arcturus at 70 μm. HD105 is extended beyond the PSF in both profiles.

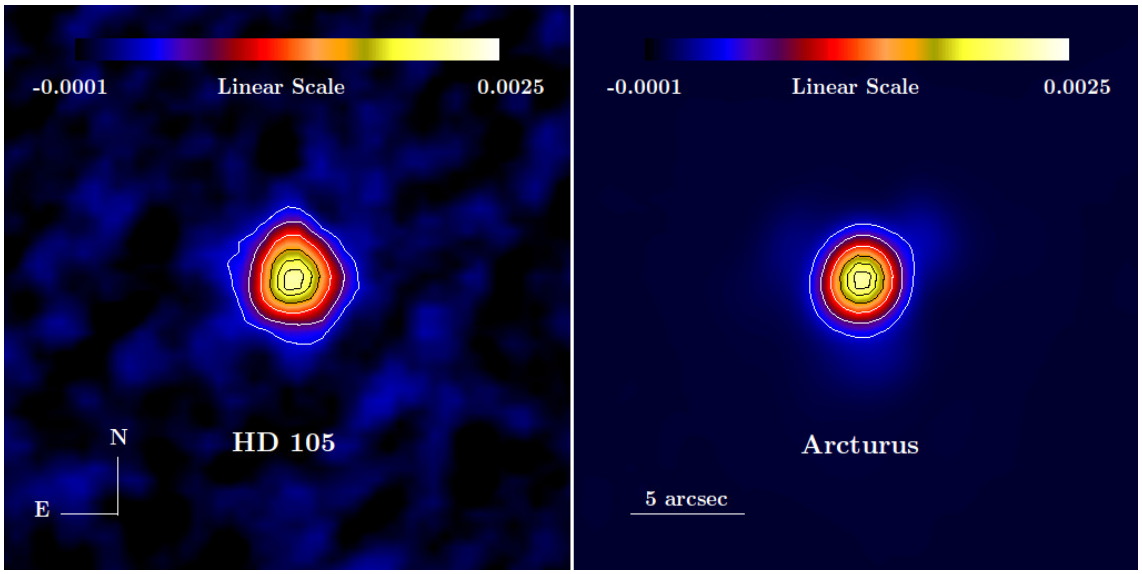

Figure 3.7: Images of HD105 (left) and a PSF reference star Arcturus (right) at 70 μm. Brightness contours are overlaid at 15, 30, 50, 70, 85 and 95% of the peak brightness.

calculated in the same way. Therefore, the FWHM values should not be directly compared to the PACS PSF FWHM when determining the physical size of the disk. The FWHM values are given only to show that the disk is indeed significantly extended beyond the PSF. In Section 3.5.2, we determine the physical size of the disk without using the FWHM.

3.5.2 Determining the Outer Radius

Without data at wavelengths longer than 160 μm, the outer radius cannot be determined from SED fitting alone. However, resolved imaging provides geometrical information. The marginally resolved image of HD105 constrains the outer radius of the disk.

To determine the outer radius of the disk, we produced a synthetic image of the disk using the parameters from the best fitting SED model. We then convolved our model with the PACS PSF[3] and rotated it to the position angle of the observation

for direct comparison. We varied the outer radius and determined the χ^2 value between the model and the images of HD105. Once the outer radius of the model is greater than a certain value, the surface brightness at that radius is so low that it falls below the noise level. Therefore, we can only place a lower limit on the outer radius of the disk. We found a disk outer radius of > 280 AU.

There are, of course, several assumptions that go into this model. The first is that the ring is circular and face-on. The second is that the dust surface density distribution follows an $r^{-1.5}$ profile. This is expected to be the case for collisionally dominated disks. Several resolved images of disks have shown more complicated structure such as rings with sharper density profiles, clumps, warps, and other asymmetries. These structures would have less of an effect on the SED, which is fairly insensitive to the density profile, but would strongly affect the analysis of the *Herschel* images. The outer radius derived here is the first such constraint put on the disk, but an image with higher spatial resolution is needed to better determine the spatial extent.

3.6 Discussion

We detected IR-excesses in $\sim 1/3$ of the stars in our sample. The Tucana-Horologium disks we detect all have some similarities. They are optically thin debris disks with relatively low fractional luminosities compared with younger protoplanetary disks, which have typical fractional luminosities of $L_{\rm IR}/L_* \sim 0.1$ (Cieza et al. 2012). As of yet, none of the Tucana-Horologium systems have shown any significant amount of gas. However, these disks do show a remarkable amount of variety for systems of the same age (~ 30 Myr). The single temperature blackbody fits give a range in

[3] `http://pacs.ster.kuleuven.ac.be/pubtool/PSF/`

temperature of 50-208 K. Although the hottest disk is around an A0 star (HD3003), the other six disks still display a temperature range of 50-146 K with no apparent dependence on spectral type. Any trends that may exist would be hard to see in a such a small sample. Our further modeling also shows a variety in other disk properties. Three of these properties, minimum grain size, the grain size distribution power-law, and inner holes, will be discussed in the following sections.

3.6.1 Minimum Grain Size

The minimum grain size in debris disks is expected to be approximately equal to the blowout size due to radiation pressure. Any grains smaller than this limit would be ejected from the system on a timescale of a few thousand years. But there are a few problems with using the blowout size as a limit. First, there are many assumptions that go into the blowout size calculation. The grains are assumed to be spherical, have a constant density, and start out on circular orbits. Additionally, the grain composition must be assumed. As circumstellar grain composition is hard to determine due to the lack of mid-IR solid state features from most debris disks, (e.g. Jura et al. 2004), ISM grain composition is commonly used. But densities can differ greatly between silicates, graphite and ices, all of which are expected to be present in debris disks. Porosity may also play a role in changing this grain size limit (Lebreton et al. 2012). For these reasons, it is difficult to interpret the minimum grain size results based on the blowout size.

Only two disks in our sample had well constrained minimum grain sizes. For HD105, the minimum grain size found was more than an order or magnitude greater than the blowout size. Here, either the calculated blowout size is inaccurate, pointing to a different grain composition or porosity, or larger grains are efficiently removed by some other mechanism. Thébault and Wu (2008) show that dynamically cold

disks have fewer small grains. The smaller velocity of the collisions decreases the production rate of the small grains while the destruction rate increases. This produces a disk dominated by larger grains with orbits mostly confined to the planetesimal ring, very similar to what is observed around HD105. For HD3003, the minimum grain size is similar to the blowout size.

3.6.2 Inner Holes

The range of temperatures seen in the blackbody fits imply inner gaps with radii from 4.5 to 52 AU. The largest inner hole is in the HD105 disk. Giant planets could be responsible for these holes. However, there are also viable mechanisms to explain the holes without planets (Kennedy and Wyatt 2010). For instance, dust parent bodies may preferentially form at outer locations. This can be expected as a result of photoevaporative clearing of the inner gas disk and pile-up of dust at its inner edge (e.g. Alexander and Armitage 2007) or as a consequence of rapid planetesimal formation in spiral arms of a self-gravitating disk (e.g. Rice et al. 2006). Resolved imaging showing the sharpness of the hole's edge could put more constraints on the processes that created the inner hole, as was done in the case of the Fomalhaut debris ring (Chiang et al. 2009).

3.6.3 An Unusual Debris Disk?

The disk of HD3003 was found to have a grain size distribution much steeper than the typical Dohnanyi (1969) steady state collisional cascade. A steeper distribution implies two possibilities: the disk has an overabundance of small grains, or a paucity of large grains. The minimum grain size we find for HD3003 ($a_{min} = 3.5\,\mu$m) is large enough that we suspect the explanation to be the paucity of large grains. We believe the minimum grain size to be correct, as it is consistent with both the blowout size

and the lack of a 10 μm silicate feature in the IRS spectrum which is only seen in disks with small (sub-μm) grains (Kessler-Silacci et al. 2006).

We investigated other explanations of the SED slope. The lack of flux at longer wavelengths could mean a smaller outer radius than was assumed. The disk could be tidally truncated by its binary companion if the other star were close enough to the disk. We tried fixing the grain size distribution power-law index to $\kappa = -3.5$ and varying r_{max} from 15-120 AU. These models were not able to reproduce the observed data.

The unusual behavior of the HD3003 SED has been seen in older debris disks in the DUNES sample (Eiroa et al. 2010). Ertel et al. (2012) detected three debris disks with *Herschel* whose slopes are also inconsistent with a Dohnanyi (1969) distribution. They give three possible explanations for the underabundance of large grains. First, there is a departure from the steady state collisional cascade conditions. HD3003 is a denser disk, so it should be collision dominated not transport dominated. However, the distribution can still deviate from Dohnanyi (1969) by processes such as radiation pressure that causes a wavy distribution that is steeper at some points (Campo Bagatin et al. 1994; Thébault et al. 2003). The second possibility is that grains of a different composition would have a different absorption coefficient, Q_{abs}, which may affect the SED slope. And lastly, a sheparding planet could result in a spatial separation of the small and large grains, leaving the large grains farther from the star and, therefore, cooler and harder to detect.

An idea not proposed in Ertel et al. (2012), but possibly relevant here, is enhanced stirring of the planetesimal disk by the companion star. The true separation of HD3003's companion star is unknown. If it is close enough, it could violently stir the disk. If the orbit of the binary is eccentric, then a close passage of the companion would excite the disk, raising the mean eccentricity of the disk particles,

and thereby increasing their relative velocities (Mustill and Wyatt 2009). Numerical simulations show that the waviness of the grain size distribution depends on the collision velocities. The amplitude and the peak-to-peak wavelength of ripples in the grain size distribution increase with higher velocities (Krivov et al. 2006; Thébault et al. 2003; Wyatt et al. 2011). Larger ripples mean the size distribution will be steeper for grain sizes above the blowout limit, as is seen in HD3003. However, the strange behavior of the SED is not yet understood, and will require more data and further modeling to determine its cause.

3.7 Summary/Conclusion

We observed seventeen stars in the Tucana-Horologium Association with the PACS instrument on the *Herschel Space Observatory*. We detected six debris disks, including one previously unknown disk and put sensitive upper limits on those not detected. We modeled the disks with a thermal dust disk model and were able to place tighter constraints on several disk parameters, such as the inner disk radius, minimum grain size, and grain size distribution. Additionally, we marginally resolved one disk and were able to put a lower limit on the outer radius. Future work will include *Herschel* SPIRE observations to better populate the sub-mm portion of the SEDs, and resolved imaging with ALMA to break degeneracies by determining the disk geometry. These data will also be combined with other targets of different ages to examine the statistical properties of the entire GASPS sample.

Table 3.6: Archive Data Used In SED Fitting.

HD105		
System	Wavelength (μm)	Flux (mJy) Reference

Continued on next page

Table 3.6 – continued from previous page

Instrument	Wavelength (μm)	Flux (mJy)	Reference
Hipparcos	0.44	2020 ± 27.91	Høg et al. (2000)
Hipparcos	0.55	3504 ± 32.27	Høg et al. (2000)
2MASS	1.25	4139 ± 76.25	Cutri et al. (2003)
2MASS	1.65	3425 ± 69.41	Cutri et al. (2003)
2MASS	2.17	2383 ± 43.90	Cutri et al. (2003)
Spitzer/IRAC	3.6	1023 ± 7.36	Carpenter et al. (2008)
Spitzer/IRAC	4.5	645.4 ± 7.87	Carpenter et al. (2008)
Spitzer/IRAC	5.8	410.5 ± 4.27	Carpenter et al. (2008)
Spitzer/IRAC	8.0	230.7 ± 1.52	Carpenter et al. (2008)
AKARI	9	223.1 ± 9.59	Yamamura et al. (2010)
Spitzer/IRS	5-37		Carpenter et al. (2008)
Spitzer/MIPS	24	28.29 ± 0.25	Carpenter et al. (2008)
HD202917			
System	Wavelength (μm)	Flux (mJy)	Reference
Hipparcos	0.44	619.2 ± 10.84	Høg et al. (2000)
Hipparcos	0.55	1233 ± 14.76	Høg et al. (2000)
2MASS	1.25	1770 ± 34.25	Cutri et al. (2003)
2MASS	1.65	1585 ± 55.47	Cutri et al. (2003)
2MASS	2.17	1150 ± 23.31	Cutri et al. (2003)
WISE	3.4	575.86 ± 17.23	Wright et al. (2010)
Spitzer/IRAC	3.6	519.2 ± 3.74	Carpenter et al. (2008)
Spitzer/IRAC	4.5	320.8 ± 3.91	Carpenter et al. (2008)
WISE	4.6	304.36 ± 5.94	Wright et al. (2010)
Spitzer/IRAC	8.0	117.3 ± 1.44	Carpenter et al. (2008)
AKARI	9	96.55 ± 12.4	Yamamura et al. (2010)
IRAS	12	101.5 ± 23.8	Moshir et al. (1992)
WISE	12	58.93 ± 1.04	Wright et al. (2010)
WISE	22	19.82 ± 1.01	Wright et al. (2010)
Spitzer/IRS	5-37		Carpenter et al. (2008)
Spitzer/MIPS	24	20 ± 0.8	Smith et al. (2006)
HD3003			
Instrument	Wavelength	Flux	Reference

Continued on next page

Table 3.6 – continued from previous page

Instrument	Wavelength (μm)	Flux (mJy)	Reference
	(μm)	(mJy)	
Hipparcos	0.44	35400 ± 456.5	Høg et al. (2000)
Hipparcos	0.55	35290 ± 292.6	Høg et al. (2000)
2MASS	1.25	15070 ± 513.6	Cutri et al. (2003)
2MASS	1.65	8870 ± 621.4	Cutri et al. (2003)
2MASS	2.17	6760 ± 124.5	Cutri et al. (2003)
AKARI	9	586.1 ± 9.77	Yamamura et al. (2010)
IRAS	12	446.0 ± 31.22	Moshir et al. (1992)
AKARI	18	237.7 ± 15.7	Yamamura et al. (2010)
Spitzer/IRS	5-37		This Work
Spitzer/MIPS	24	223.9 ± 9.0	Smith et al. (2006)
HD12039			
Instrument	Wavelength (μm)	Flux (mJy)	Reference
Hipparcos	0.44	1103 ± 17.27	Høg et al. (2000)
Hipparcos	0.55	2073 ± 22.91	Høg et al. (2000)
2MASS	1.25	2885 ± 61.11	Cutri et al. (2003)
2MASS	1.65	2445 ± 85.59	Cutri et al. (2003)
2MASS	2.17	1718 ± 41.15	Cutri et al. (2003)
Spitzer/IRAC	3.6	747.3 ± 5.38	Carpenter et al. (2008)
Spitzer/IRAC	4.5	470.9 ± 5.75	Carpenter et al. (2008)
Spitzer/IRAC	8.0	170.4 ± 1.13	Carpenter et al. (2008)
AKARI	9	159.9 ± 6.9	Yamamura et al. (2010)
Spitzer/IRS	7-37		Carpenter et al. (2008)
Spitzer/MIPS	24	25.65 ± 0.23	Carpenter et al. (2008)
HD1466			
Instrument	Wavelength (μm)	Flux (mJy)	Reference
Hipparcos	0.44	2248 ± 31.06	Høg et al. (2000)
Hipparcos	0.55	3686 ± 37.34	Høg et al. (2000)
2MASS	1.25	4147 ± 68.75	Cutri et al. (2003)
2MASS	1.65	3244 ± 107.6	Cutri et al. (2003)

Continued on next page

Table 3.6 – continued from previous page

Instrument	Wavelength (μm)	Flux (mJy)	Reference
2MASS	2.17	2314 ± 36.23	Cutri et al. (2003)
AKARI	9	207.1 ± 20.8	Yamamura et al. (2010)
IRAS	12	141 ± 16.92	Moshir et al. (1992)
Spitzer/IRS	5-37		This Work
Spitzer/MIPS	24	32.90 ± 1.3	Smith et al. (2006)
HD30051			
Instrument	Wavelength (μm)	Flux (mJy)	Reference
Hipparcos	0.44	3660 ± 50.56	Høg et al. (2000)
Hipparcos	0.55	5163 ± 47.55	Høg et al. (2000)
2MASS	1.25	4867 ± 89.66	Cutri et al. (2003)
2MASS	1.65	3829 ± 119.9	Cutri et al. (2003)
2MASS	2.17	2599 ± 52.66	Cutri et al. (2003)
WISE	3.4	1329 ± 61.35	Wright et al. (2010)
WISE	4.6	717.4 ± 14.69	Wright et al. (2010)
AKARI	9	237.4 ± 21.9	Yamamura et al. (2010)
IRAS	12	152 ± 15.2	Moshir et al. (1992)
WISE	12	126.2 ± 2.11	Wright et al. (2010)
WISE	22	34.67 ± 1.37	Wright et al. (2010)
HD16978			
Instrument	Wavelength (μm)	Flux (mJy)	Reference
Hipparcos	0.44	95730 ± 1234	Høg et al. (2000)
Hipparcos	0.55	87120 ± 722.1	Høg et al. (2000)
2MASS	1.25	26620 ± 7349	Cutri et al. (2003)
2MASS	1.65	17260 ± 4337	Cutri et al. (2003)
2MASS	2.17	13250 ± 439.5	Cutri et al. (2003)
AKARI	9	1068 ± 6.11	Yamamura et al. (2010)
IRAS	12	743.0 ± 66.87	Moshir et al. (1992)
AKARI	18	257.7 ± 12.1	Yamamura et al. (2010)
Spitzer/MIPS	24	124.0 ± 4.96	Rebull et al. (2008)
HD2884			

Continued on next page

Table 3.6 – continued from previous page

Instrument	Wavelength (μm)	Flux (mJy)	Reference
Instrument	Wavelength (μm)	Flux (mJy)	Reference
Hipparcos	0.44	79260 ± 1022	Høg et al. (2000)
Hipparcos	0.55	72860 ± 604	Høg et al. (2000)
2MASS	1.25	21720 ± 5128	Cutri et al. (2003)
2MASS	1.65	13790 ± 965.9	Cutri et al. (2003)
2MASS	2.17	10750 ± 356.6	Cutri et al. (2003)
AKARI	9	895.2 ± 31.0	Yamamura et al. (2010)
IRAS	12	1300 ± 78	Moshir et al. (1992)
AKARI	18	188.4 ± 14.8	Yamamura et al. (2010)
Spitzer/IRS	5-37		This work
Spitzer/MIPS	24	101.7 ± 8.6	Smith et al. (2006)
HD224392			
Instrument	Wavelength (μm)	Flux (mJy)	Reference
Hipparcos	0.44	37070 ± 478	Høg et al. (2000)
Hipparcos	0.55	37710 ± 312.6	Høg et al. (2000)
2MASS	1.25	17320 ± 590.3	Cutri et al. (2003)
2MASS	1.65	10730 ± 306.5	Cutri et al. (2003)
2MASS	2.17	7840 ± 151.7	Cutri et al. (2003)
AKARI	9	660.5 ± 18.2	Yamamura et al. (2010)
IRAS	12	477 ± 28.62	Moshir et al. (1992)
AKARI	18	113 ± 15.59	Yamamura et al. (2010)
HD2885			
Instrument	Wavelength (μm)	Flux (mJy)	Reference
Hipparcos	0.44	54530 ± 703.1	Høg et al. (2000)
Hipparcos	0.55	59330 ± 491.8	Høg et al. (2000)
2MASS	1.25	29820 ± 8003	Cutri et al. (2003)
2MASS	1.65	21340 ± 4192	Cutri et al. (2003)
2MASS	2.17	15160 ± 502.8	Cutri et al. (2003)
AKARI	9	1291 ± 18.6	Yamamura et al. (2010)

Continued on next page

Table 3.6 – continued from previous page

Instrument	Wavelength (μm)	Flux (mJy)	Reference
AKARI	18	340.6 ± 25.6	Yamamura et al. (2010)
Spitzer/MIPS	24	156.1 ± 4.5	Smith et al. (2006)
	HD53842		
Instrument	Wavelength (μm)	Flux (mJy)	Reference
Hipparcos	0.44	2529 ± 37.28	Høg et al. (2000)
Hipparcos	0.55	3716 ± 37.65	Høg et al. (2000)
2MASS	1.25	3813 ± 101.9	Cutri et al. (2003)
2MASS	1.65	2831 ± 80.83	Cutri et al. (2003)
2MASS	2.17	2015 ± 38.98	Cutri et al. (2003)
WISE	3.4	894.4 ± 31.9	Wright et al. (2010)
WISE	4.6	525.0 ± 10.7	Wright et al. (2010)
AKARI	9	179.4 ± 8.49	Yamamura et al. (2010)
IRAS	12	140.0 ± 10.0	Moshir et al. (1992)
WISE	12	100.1 ± 16.7	Wright et al. (2010)
WISE	22	40.4 ± 1.29	Wright et al. (2010)
Spitzer/IRS	7-37		Moór et al. (2009)
Spitzer/MIPS	24	31.0 ± 1.3	Moór et al. (2009)
	HD44627		
Instrument	Wavelength (μm)	Flux (mJy)	Reference
Hipparcos	0.44	318.1 ± 8.21	Høg et al. (2000)
Hipparcos	0.55	767.2 ± 12.72	Høg et al. (2000)
2MASS	1.25	1486 ± 32.86	Cutri et al. (2003)
2MASS	1.65	1497 ± 28.95	Cutri et al. (2003)
2MASS	2.17	1075 ± 23.77	Cutri et al. (2003)
WISE	3.4	533.0 ± 14.93	Wright et al. (2010)
WISE	4.6	295.5 ± 5.77	Wright et al. (2010)
AKARI	9	181 ± 5.09	Yamamura et al. (2010)
IRAS	12	101 ± 16.16	Moshir et al. (1992)
WISE	12	58.39 ± 1.03	Wright et al. (2010)
WISE	22	15.06 ± 0.81	Wright et al. (2010)

Continued on next page

Table 3.6 – continued from previous page

Instrument	Wavelength (μm)	Flux (mJy)	Reference
HD55279			
Instrument	Wavelength (μm)	Flux (mJy)	Reference
Hipparcos	0.44	110.5 ± 6.01	Høg et al. (2000)
Hipparcos	0.55	304.0 ± 8.96	Høg et al. (2000)
2MASS	1.25	787.9 ± 16.69	Cutri et al. (2003)
2MASS	1.65	754.9 ± 39.65	Cutri et al. (2003)
2MASS	2.17	579.6 ± 13.88	Cutri et al. (2003)
WISE	3.4	273.9 ± 6.38	Wright et al. (2010)
WISE	4.6	148.1 ± 2.89	Wright et al. (2010)
AKARI	9	65.96 ± 5.85	Yamamura et al. (2010)
WISE	12	29.78 ± 0.61	Wright et al. (2010)
WISE	22	8.36 ± 1.23	Wright et al. (2010)
HD3221			
Instrument	Wavelength (μm)	Flux (mJy)	Reference
Hipparcos	0.44	141.1 ± 6.239	Høg et al. (2000)
Hipparcos	0.55	512.0 ± 9.904	Høg et al. (2000)
2MASS	1.25	1852 ± 30.71	Cutri et al. (2003)
2MASS	1.65	2098 ± 65.72	Cutri et al. (2003)
2MASS	2.17	1625 ± 26.93	Cutri et al. (2003)
AKARI	9	162.7 ± 11.6	Yamamura et al. (2010)
IRAS	12	121.0 ± 20.57	Moshir et al. (1992)
HIP107345			
Instrument	Wavelength (μm)	Flux (mJy)	Reference
Hipparcos	0.44	16.24 ± 4.654	Høg et al. (2000)
Hipparcos	0.55	78.94 ± 8.231	Høg et al. (2000)
2MASS	1.25	503.6 ± 11.60	Cutri et al. (2003)
2MASS	1.65	596.3 ± 12.08	Cutri et al. (2003)
2MASS	2.17	472.4 ± 11.31	Cutri et al. (2003)
WISE	3.4	236.5 ± 5.51	Wright et al. (2010)

Continued on next page

Table 3.6 – continued from previous page

Instrument	Wavelength (μm)	Flux (mJy)	Reference
WISE	4.6	135.1 ± 2.64	Wright et al. (2010)
WISE	12	27.71 ± 0.54	Wright et al. (2010)
WISE	22	7.88 ± 0.89	Wright et al. (2010)
		HIP3556	
Instrument	Wavelength (μm)	Flux (mJy)	Reference
Hipparcos	0.44	17.48 ± 4.012	Høg et al. (2000)
Hipparcos	0.55	41.43 ± 5.780	Høg et al. (2000)
2MASS	1.25	645.8 ± 11.90	Cutri et al. (2003)
2MASS	1.65	730.3 ± 16.14	Cutri et al. (2003)
2MASS	2.17	595.3 ± 14.81	Cutri et al. (2003)
AKARI	9	118.0 ± 14.8	Yamamura et al. (2010)
Spitzer/MIPS	24	8.4 ± 0.34	Rebull et al. (2008)
		GSC8056-482	
Instrument	Wavelength (μm)	Flux (mJy)	Reference
Zeiss/FOTRAP	0.44	15.13 ± 4.82	Torres et al. (2006)
Zeiss/FOTRAP	0.55	54.15 ± 9.77	Torres et al. (2006)
2MASS	1.25	683 ± 14.62	Cutri et al. (2003)
2MASS	1.65	809.66 ± 17.33	Cutri et al. (2003)
2MASS	2.17	666.19 ± 16.77	Cutri et al. (2003)
AKARI	9	86.52 ± 14.8	Yamamura et al. (2010)
Spitzer/MIPS	24	9.0 ± 0.36	Rebull et al. (2008)

Chapter 4

Young Debris Disks in the Herschel GASPS Survey: Relations Between Dust and Stellar Properties

4.1 Introduction

Debris disks are the dusty remnants of the formation of a planetary system. Planet formation begins in the gas-rich protoplanetary disk, which dissipates after about 10 Myr; mutual collisions of the remaining solid material form the debris disk. About 20% of nearby main-sequence F, G, and K stars are known to harbor a debris disk (Eiroa et al. 2013).

In the youngest debris disks (< 100 Myr), planet formation has not completely finished. Giant planets must have already formed by the debris disk stage since their formation requires large amounts of gas to be present in their surroundings.

Terrestrial planets, however, may still be accreting material from planetesimal impacts. These young debris disks may be the link between the gas-rich primordial disks and fully formed planetary systems.

Debris disks are often detected through their thermal infrared dust emission. Their dust is quickly destroyed on timescales of thousands of years, and therefore, the dust must be continually replenished by collisional cascade from the longer-lived larger km-sized planetesimals. Assuming that the bulk of the surface brightness we observe at any given time is emitted by dust still located close to its formation site, the dust provides a lens for studying the unseen planetesimals.

Many surveys of the thermal emission from debris disks have sought to characterize their properties. These include surveys in the infrared (IR) from space observatories such as IRAS (Aumann et al. 1984; Moór et al. 2006), ISO (Decin et al. 2003; Spangler et al. 2001), and *Spitzer* (Meyer et al. 2006; Rieke et al. 2004), and from ground-based sub-millimeter (sub-mm) surveys (Najita and Williams 2005; Nilsson et al. 2010, 2009). These surveys generally have a gap in spectral coverage with few or no observations between the mid-IR and sub-mm. The *Herschel Space Observatory* (Pilbratt et al. 2010) has provided excellent sensitivity and spatial resolution at far-IR wavelengths. Combining data from *Herschel*'s two photometric instruments, PACS (Poglitsch et al. 2010) and SPIRE (Griffin et al. 2010) at wavelength 70-500 μm with data from previous IR and sub-mm surveys, we can obtain full spectral coverage of even the faint debris disks.

This is one of the goals of the *Herschel* Open Time Key Programme entitled "Gas in Protoplanetary Systems" (GASPS; Dent et al. 2013). GASPS aimed to study the gas and dust in protoplanetary disks and young debris disks to track the evolution from one to the other. Disks were chosen from nearby stellar associations with ages 1-30 Myr with a range of spectral types, disk masses, and other stellar

properties.

This chapter focuses exclusively on the debris disks in the GASPS sample. In Section 4.2, we discuss the *Herschel* observations and basic data reductions and Section 4.3 describes the flux extraction. In Section 4.4, we describe how we fit the data with modified blackbodies, which are used to compare disk properties in Section 4.6. Sections 4.7 and 4.8 further discuss the results of the correlations, which are interpreted in the discussion in Section 4.9.

4.2 Sample, Observations, and Data Reduction

In this chapter, we used a subset of the GASPS sample (see Tables 4.1 and 4.2). We focus only on the debris disks, the targets in the older associations ($\sim$ 10 Myr or older). These associations include TW Hydrae Association (TWA, 10 Myr-old; Barrado Y Navascués 2006), Upper Scorpius (UpSco, 11 Myr-old; Pecaut et al. 2012), Beta Pictoris Moving Group (BPMG, 12 Myr-old; Barrado y Navascués et al. 1999), and Tucana-Horologium Association (Tuc-Hor, 30 Myr-old; Zuckerman and Song 2004). These associations are also discussed further in previous GASPS papers (Donaldson et al. 2012; Mathews et al. 2013; Riviere-Marichalar et al. 2014, 2013).

Table 4.1: Summary of Stellar Associations

Association	Age (Myr)	# disks/ # targets	Ave. distance (pc)
TWA	10	2/11	50
UpSco	11	8/21	145
BPMG	12	8/18	37
Tuc-Hor	30	7/17	46

Table 4.2: List of Herschel Observations

Object Name	Wavelength (μm)	ObsID	Duration (s)	Scan Angle
AT Mic	70/160	1342209488	276	70
	70/160	1342209489	276	110
CD-64 1208	70/160	1342209059	276	70
	70/160	1342209060	276	110
	100/160	1342209061	276	70
	100/160	1342209062	276	110
GJ 3305	70/160	1342224850	276	70
	70/160	1342224851	276	110
	100/160	1342224852	276	70
	100/160	1342224853	276	110
HD 139084A/B	70/160	1342216483	276	70
	70/160	1342216484	276	110
	100/160	1342216485	276	70
	100/160	1342216486	276	110
HD 146624	70/160	1342215617	276	70
	70/160	1342215618	276	110
	100/160	1342215619	276	70
	100/160	1342215620	276	110
HD 164249	100/160	1342215574	276	70
	100/160	1342215575	276	110
	250/350/500	1342239902	307	–
HD 174429	70/160	1342215576	276	70
	70/160	1342215577	276	110
	100/160	1342215578	276	70
	100/160	1342215579	276	110
HD 181296	100/160	1342209055	276	70
	100/160	1342209056	276	110
	250/350/500	1342239922	307	–
HD 181327	100/160	1342209057	276	70
	100/160	1342209058	276	110
	250/350/500	1342241086	307	–
HD 199143	70/160	1342208861	1122	70

Continued on next page

Table 4.2 continued

Object Name	Wavelength (μm)	ObsID	Duration (s)	Scan Angle
	70/160	1342208862	1122	110
HD 203	70/160	1342188366	220	63
	100/160	1342221118	276	70
	100/160	1342221119	276	110
HD 29391	70/160	1342190967	220	63
	100/160	1342216153	276	70
	100/160	1342216154	276	110
HD 35850	100/160	1342217746	276	70
	100/160	1342217747	276	110
HD 45081	70/160	1342212832	1122	70
	70/160	1342212833	1122	110
HIP 10679/80	70/160	1342189193	220	63
	100/160	1342223862	276	70
	100/160	1342223863	276	110
HIP 11437	70/160	1342189210	220	63
	100/160	1342223864	276	70
	100/160	1342223865	276	110
HIP 12545	70/160	1342223574	276	70
	70/160	1342223575	276	110
GSC 8056-482	70/160	1342214199	558	70
	70/160	1342214200	558	110
HD 105	70/160	1342188367	220	63
	100/160	1342220762	220	70
	100/160	1342220763	220	110
	250/350/500	1342245915	307	–
HD 12039	70/160	1342213258	1122	70
	70/160	1342213259	1122	110
	250/350/500	1342261622	307	–
HD 1466	70/160	1342216458	1122	70
	70/160	1342216459	1122	110
	250/350/500	1342259401	307	–
HD 16978	70/160	1342212834	276	70

Continued on next page

Table 4.2 continued

Object Name	Wavelength (μm)	ObsID	Duration (s)	Scan Angle
	70/160	1342212835	276	110
HD 202917	70/160	1342208847	558	70
	70/160	1342208848	558	110
	100/160	1342218958	220	70
	100/160	1342218959	220	110
	250/350/500	1342245531	307	–
HD 224392	70/160	1342211627	840	70
	70/160	1342211628	840	110
HD 2884/5	70/160	1342212627	558	70
	70/160	1342212628	558	110
HD 3003	70/160	1342189394	220	63
	100/160	1342218802	220	70
	100/160	1342218803	220	110
	250/350/500	1342259399	307	–
HD 30051	70/160	1342217442	1122	70
	70/160	1342217443	1122	110
	100/160	1342224210	672	70
	100/160	1342224211	672	110
	250/350/500	1342239925	307	–
HD 3221	70/160	1342212625	558	70
	70/160	1342212626	558	110
HD 44627	70/160	1342220772	558	70
	70/160	1342220773	558	110
HD 53842	70/160	1342188886	220	63
	100/160	1342211957	276	70
	100/160	1342211958	276	110
HD 55279	70/160	1342211959	558	70
	70/160	1342211960	558	110
HIP 107345	70/160	1342218960	558	70
	70/160	1342218961	558	110
HIP 3556	70/160	1342188368	220	63
	100/160	1342210632	276	70

Continued on next page

Table 4.2 continued

Object Name	Wavelength (μm)	ObsID	Duration (s)	Scan Angle
	100/160	1342210633	276	110
TWA02	70/160	1342189163	220	63
	100/160	1342211995	276	70
	100/160	1342211996	276	110
TWA05	70/160	1342213111	1122	70
	70/160	1342213112	1122	110
TWA07	70/160	1342188515	220	63
	100/160	1342211993	276	70
	100/160	1342211994	276	110
TWA10	70/160	1342213854	1122	70
	70/160	1342213855	1122	110
TWA11	70/160	1342188519	220	63
	100/160	1342213852	276	70
	100/160	1342213853	276	110
	250/350/500	1342261492	307	–
TWA12	70/160	1342222458	1122	70
	70/160	1342222459	1122	110
TWA13	100/160	1342213113	276	70
	100/160	1342213114	276	110
TWA16	70/160	1342213856	558	70
	70/160	1342213857	558	110
	100/160	1342213858	558	70
	100/160	1342213859	558	110
TWA21	70/160	1342211983	1122	70
	70/160	1342211984	1122	110
TWA23	70/160	1342222618	276	70
	70/160	1342222619	276	110
	100/160	1342222620	276	70
	100/160	1342222621	276	110
TWA25	70/160	1342213624	276	70
	70/160	1342213625	276	110
	100/160	1342213626	276	70

Continued on next page

Table 4.2 continued

Object Name	Wavelength (μm)	ObsID	Duration (s)	Scan Angle
	100/160	1342213627	276	110
1RXSJ160044.7-234330	70/160	1342215496	840	70
	70/160	1342215497	840	110
HIP 76310	100/160	1342215621	276	70
	100/160	1342215622	276	110
	250/350/500	1342240001	307	–
HIP 77815	70/160	1342215474	276	70
	70/160	1342215475	276	110
HIP 77911	70/160	1342189656	220	63
	100/160	1342215480	276	70
	100/160	1342215481	276	110
	250/350/500	1342240000	307	–
HIP 78099	70/160	1342215486	276	70
	70/160	1342215487	276	110
	250/350/500	1342239999	307	–
HIP 78996	70/160	1342215502	558	70
	70/160	1342215503	558	110
	250/350/500	1342239998	307	–
HIP 79156	70/160	1342215414	558	70
	70/160	1342215415	558	110
	250/350/500	1342239994	307	–
HIP 79410	70/160	1342215404	276	70
	70/160	1342215405	276	110
	250/350/500	1342239993	307	–
HIP 79439	70/160	1342215402	558	70
	70/160	1342215403	558	110
	250/350/500	1342239992	307	–
HIP 79878	100/160	1342215615	276	70
	100/160	1342215616	276	110
	250/350/500	1342239997	307	–
HIP 80088	100/160	1342215514	276	70
	100/160	1342215515	276	110

Continued on next page

Table 4.2 continued

Object Name	Wavelength (μm)	ObsID	Duration (s)	Scan Angle
	250/350/500	1342239995	307	–
HIP 80130	70/160	1342215510	276	70
	70/160	1342215511	276	110
	100/160	1342215512	276	70
	100/160	1342215513	276	110
USco J160210.9-200749	70/160	1342215434	276	70
	70/160	1342215435	276	110
USco J160245.4-193037	70/160	1342214580	276	70
	70/160	1342214581	276	110
USco J160801.4-202741	70/160	1342215450	276	70
	70/160	1342215451	276	110
	100/160	1342215452	276	70
	100/160	1342215453	276	110
Usco J153557.8-232405	70/160	1342215623	276	70
	70/160	1342215624	276	110
	100/160	1342215625	276	70
	100/160	1342215626	276	110
Usco J154413.4-25225	70/160	1342215482	276	70
	70/160	1342215483	276	110
	100/160	1342215484	276	70
	100/160	1342215485	276	110
Usco J160108.0-211318	70/160	1342215464	276	70
	70/160	1342215465	276	110
Usco J160654.4-241610	70/160	1342215498	276	70
	70/160	1342215499	276	110
	100/160	1342215500	276	70
	100/160	1342215501	276	110
Usco J160856.7-203346	70/160	1342215454	276	70
	70/160	1342215455	276	110
	100/160	1342215456	276	70
	100/160	1342215457	276	110
Usco J161402.1-230101	70/160	1342215506	276	70

Continued on next page

Table 4.2 continued

Object Name	Wavelength (μm)	ObsID	Duration (s)	Scan Angle
	70/160	1342215507	276	110
	100/160	1342215508	276	70
	100/160	1342215509	276	110

The two youngest associations, UpSco and TWA, include a few primordial disks in the GASPS sample. We removed from the sample the disks that had previously been identified as primordial, either because they contain large amounts of gas or they have too much IR excess to be debris disks. We focused only on stars with known debris disks or IR excess non-detections. This leaves 67 sources amongst the 4 associations. The stellar properties of these 67 stars are listed in Table 4.3.

A handful of debris disks in the GASPS sample are not members of these four associations. These include HD32297 (Donaldson et al. 2013), 49 Ceti (Roberge et al. 2013), HR1998 and HD158352 (Meeus et al. 2012). We chose not to include these disks since they have poorly determined ages. These four disks are discussed in more detail in previous papers.

The targets were observed using the PACS instrument onboard the Herschel Space Observatory with the scan map mode. Simultaneous 70 and 160 μm observations were performed for most targets, with follow-up simultaneous 100 and 160 μm observations for many.

The scan map technique scans over the target at a speed of $20''$ s^{-1} with legs of $3'.5$ in length and $4''$ steps between the legs. For most targets, 2 maps are produced at scan angles of 70 and 110° and later combined to reduce noise due to streaking in the scan direction.

The targets with excesses detected by PACS were followed up with the SPIRE instrument at longer wavelengths as part of an OT2 proposal (OT2_aroberge_3: PI:

Table 4.3: Stellar Properties

Target	Association	Stellar Distance (pc)	Spectral Type	Stellar Temperature (K)	A_V
AT Mic	BPMG	10.2	M4.5e	2800	–
CD-64 1208	BPMG	36	M0 or K7	3600	–
GJ 3305	BPMG	30	M0.5	3700	–
HD 139084A/B	BPMG	40	K0V	5000	–
HD 146624	BPMG	43	A0V	9250	–
HD 164249	BPMG	47	F5V	6600	–
HD 172555	BPMG	29	A5IV/V+K7	7750	–
HD 174429	BPMG	50	K0Vp	5200	–
HD 181296	BPMG	48	A0Vn+M7	9250	–
HD 181327	BPMG	51	F5/F6V	6600	–
HD 199143	BPMG	48	F8V	6000	–
HD 203	BPMG	39	F2IV	6750	–
HD 29391	BPMG	30	F0V+M0.5	7250	–
HD 35850	BPMG	27	F7V	6200	–
HD 45081	BPMG	39	K6/7	4200	–
HIP 10679/80	BPMG	34	G2V	5800	–
HIP 11437	BPMG	42	K8	4400	–
HIP 12545	BPMG	41	M0	3700	–
GSC 8056-482	Tuc-Hor	25	M3Ve	3600	–

Continued on next page

Table 4.3 continued

Target	Association	Stellar Distance (pc)	Spectral Type	Stellar Temperature (K)	A_V
HD 105	Tuc-Hor	40	G0V	6000	–
HD 12039	Tuc-Hor	42	G4V	5800	–
HD 1466	Tuc-Hor	41	F9V	6200	–
HD 16978	Tuc-Hor	47	B9V	10250	–
HD 202917	Tuc-Hor	46	G5V	5600	–
HD 224392	Tuc-Hor	49	A1V	8750	–
HD 2884	Tuc-Hor	43	B9V	10750	–
HD 2885	Tuc-Hor	53	A2V	8000	–
HD 3003	Tuc-Hor	46	A0V	9000	–
HD 30051	Tuc-Hor	58	F2/F3IV/V	6600	–
HD 3221	Tuc-Hor	46	K5V	4400	–
HD 44627	Tuc-Hor	46	K2V	5000	–
HD 53842	Tuc-Hor	57	F5V	6600	–
HD 55279	Tuc-Hor	64	K3V	4800	–
HIP 107345	Tuc-Hor	42	M1	3800	–
HIP 3556	Tuc-Hor	39	M1.5	3500	–
TWA02AB	TWA	52	M0.5	3500	–
TWA05Aab	TWA	50	M1.5	3400	–
TWA07	TWA	38	M1	3800	–
TWA10	TWA	57	M2.5	3600	–

Continued on next page

Table 4.3 continued

Target	Association	Stellar Distance (pc)	Spectral Type	Stellar Temperature (K)	A_V
TWA11	TWA	67	A0	9250	–
TWA12	TWA	32	M2	3700	–
TWA13AB	TWA	38	M2e	4000	–
TWA16	TWA	66	M1.5	3500	–
TWA21	TWA	69	K3	4600	–
TWA23	TWA	37	M1	3600	–
TWA25	TWA	44	M0	3700	–
1RXSJ160044.7-234330	UpSco	145	M2	3300	0.5
HIP76310	UpSco	145	A0V	9000	0.1
HIP77815	UpSco	145	A5V	7750	0.79
HIP77911	UpSco	145	B9V	10250	0.34
HIP78099	UpSco	145	A0V	9000	0.52
HIP78996	UpSco	145	A9V	7250	0.4
HIP79156	UpSco	145	A0V	10250	0.74
HIP79410	UpSco	145	B9V	9750	0.64
HIP79439	UpSco	145	B9V	9250	0.63
HIP79878	UpSco	145	A0V	9500	–
HIP80088	UpSco	145	A9V	7500	0.63
HIP80130	UpSco	145	A9V	8000	0.93
USco J160210.9-200749	UpSco	145	M5	3500	0.8

Continued on next page

Table 4.3 continued

Target	Association	Stellar Distance (pc)	Spectral Type	Stellar Temperature (K)	A_V
USco J160245.4-193037	UpSco	145	M5	3500	1.1
USco J160801.4-202741	UpSco	145	K8	4200	1.5
Usco J153557.8-232405	UpSco	145	K3	4800	0.7
Usco J154413.4-252258	UpSco	145	M1	3700	0.6
Usco J160108.0-211318	UpSco	145	M0	3500	–
Usco J160654.4-241610	UpSco	145	M3	3200	–
Usco J160856.7-203346	UpSco	145	K5	4600	1.4
Usco J161402.1-230101	UpSco	145	G4	5200	2.0

A. Roberge). These observations consisted of simultaneous 250, 350, and 500 μm observations taken with the small scan map mode with a scan speed of 30$''$ s^{-1}. All targets were integrated to the confusion limit, 2 repetitions, for a total time of 307 s.

The PACS data reduction was done in HIPE 10 (Ott 2010) using the standard pipelines. Sources brighter than 100 mJy were reduced with the Bright Point Source script, and fainter sources were reduced with the Deep Survey Point Source script. The final pixel scale of the reduced images was chosen to be the same as the detector's natural pixel scale to avoid as much correlated pixel noise as possible (3.2$''$ pixel^{-1} for 70 and 100 μm images and 6.4$''$ pixel^{-1} for the 160 μm images). The SPIRE observations were also reduced in HIPE 10 with the Small Scan Map script, producing images with pixel scale of 6, 10, and 14$''$ pixel^{-1} for the 250, 350, and 500 μm images respectively.

4.3 Analysis

We performed aperture photometry on all the PACS data. The aperture was centered on the target by fitting a 2D Gaussian to the image. For all sources brighter than 100 mJy, we used aperture radii of 12, 12, 22$''$ for the 70, 100, and 160 μm images respectively. For sources fainter than 100 mJy, we used the aperture radii of 5.5, 5.6, and 10$''$.5. We determined the source flux by integrating the pixels inside the circular aperture. We applied aperture corrections by dividing the flux by the following aperture correction factors ($\alpha_{\rm cor}$): 0.794, 0.766, and 0.81 for bright sources with the larger apertures in the 70, 100, and 160 μm images respectively, and 0.597, 0.550, and 0.628 for the faint sources with the smaller apertures[1].

[1]PICC-ME-TN-037: `http://herschel.esac.esa.int/twiki/pub/Public/PacsCalibrationWeb/pacs_bolo_fluxcal_report_v1.pdf`

To estimate the background rms uncertainty, we placed an annulus at 20-30″ for the 70 and 100 μm images and 30-40″ for the 160 μm images. The background rms ($\sigma_{\rm rms}$) is estimated as the standard deviation of the pixels inside of the annulus. The rms uncertainty is corrected for correlated pixel noise by dividing by the correction factors ($\chi_{\rm cor}$) 0.95 for the 70 and 100 μm images and 0.88 for the 160 μm images. The rms uncertainty is also divided by the aperture correction factors given above ($\alpha_{\rm cor}$). The total uncertainty is then given by Equation 4.1.

$$\sigma = \frac{\sigma_{\rm rms}}{\alpha_{\rm cor}\chi_{\rm cor}}\sqrt{n_{\rm beam}\left(1+\frac{n_{\rm beam}}{n_{\rm sky}}\right)}, \tag{4.1}$$

where $n_{\rm beam}$ is the number of pixels inside the aperture and $n_{\rm sky}$ is the number of pixels in the sky annulus. An absolute calibration error of 3% for 70 and 100 μm images and 5% for the 160 μm images is then added in quadrature with the total uncertainty. The results are listed in Table 4.4. For non-detections, 3σ upper limits are listed instead.

We also performed aperture photometry on the SPIRE data. HIPE produces maps with units of Jy beam^{-1}. We converted the image to Jy pixel^{-1} by dividing by the beam area (423, 751 and 587 arcsec^2 beam^{-1} for the 250, 350, and 500 μm images respectively) and multiplying by the pixel area (36, 100, 196 arcsec^2 pixel^{-1} for the 250, 350, and 500 μm images respectively). Because the images have a lot of contamination from background galaxies, we did not center the apertures by fitting a 2D Gaussian as was done for the PACS images. Instead, we centered the apertures at the expected stellar position. We measured the source flux using circular apertures with radii of 22, 30, and 42″ for the 250, 350, and 500 μm images respectively. We estimated the background by placing an annulus 60-90″ from the center of the aperture. We then subtracted the mean of the background flux multiplied by the number of pixels inside the aperture ($n_{\rm beam}$).

We applied an aperture correction by multiplying the flux by the factors 1.219,

Table 4.4: Aperture Photometry Results

Target	F70 (mJy)	F100 (mJy)	F160 (mJy)	F250 (mJy)	F350 (mJy)	F500 (mJy)
AT Mic	14.8 ± 2.1	–	< 15.5	–	–	–
CD-64 1208	< 5.4	< 6.3	< 11.8	–	–	–
GJ3305	< 5.6	< 6.1	< 11.0	–	–	–
HD139084	< 5.8	< 9.5	< 28.2	–	–	–
HD146624	10.5 ± 2.4	< 7.1	< 17.7	–	–	–
HD164249	–	539.9 ± 17.1	242.1 ± 51.2	74.3 ± 7.1	18.5 ± 5.6	< 22.5
HD172555	164.8 ± 8.5	106.7 ± 4.7	27.0 ± 7.0			
HD174429	< 6.0	< 6.7	< 11.7			
HD181296	–	262.4 ± 8.7	122.7 ± 10.4	29.9 ± 5.1	< 17.6	< 21.2
HD199143	< 4.4	–	< 10.7	–	–	–
HD203	72.1 ± 4.7	32.9 ± 2.7	< 15.4	–	–	–
HD29391	20.7 ± 3.9	19.5 ± 4.2	21.3	–	–	–
HD35850	–	33.6 ± 5.7	< 15.1	–	–	–
HD45081	< 2.8	–	< 8.0	–	–	–
HIP10679	52.0 ± 4.2	31.0 ± 2.7	< 27.3	–	–	–
HIP11437	75.7 ± 4.7	54.2 ± 3.0	41.0 ± 6.1	–	–	–
HIP12545	< 7.0	–	< 18.9	–	–	–
HIP76310	–	366.2 ± 11.8	183.6 ± 17.7	75.3 ± 7.8	35.5 ± 7.4	25.4 ± 8.2
HIP77911	322.2 ± 12.3	214.0 ± 7.9	123.4 ± 12.0	38.3 ± 5.8	< 18.2	< 20.9

Continued on next page

Table 4.4 continued

Target	F70 (mJy)	F100 (mJy)	F160 (mJy)	F250 (mJy)	F350 (mJy)	F500 (mJy)
HIP78996	9.3 ± 1.4	–	< 16.7	< 16.0	< 19.6	< 20.7
HIP79156	< 5.8	–	< 13.7	< 15.6	< 19.8	< 19.6
HIP79410	18.7 ± 2.2	–	< 19.8	< 16.5	< 21.6	< 21.6
HIP79439	5.5 ± 1.4	–	< 14.9	< 16.5	< 20.7	< 21.2
HIP79878	–	< 8.8	< 23.1	< 17.8	< 20.7	< 23.1
HIP80088	–	61.1 ± 2.9	45.7 ± 6.1	< 15.9	< 19.7	< 20.4
TWA07	93.9 ± 5.2	60.2 ± 4.4	44.7 ± 8.3	25.4 ± 4.2	19.4 ± 5.0	< 20.2
TWA11	6130.6 ± 184.2	3789.7 ± 114.0	1688.0 ± 86.2	562.2 ± 40.0	250.8 ± 18.7	94.2 ± 9.5
HD105	152.9 ± 9.0	175.3 ± 7.0	147.8 ± 16.2	62.1 ± 6.4	45.8 ± 6.5	27.6 ± 6.5
HD12039	11.5 ± 1.0	–	< 11.1	< 16.0	< 18.5	< 23.7
HD1466	11.1 ± 1.1	–	< 11.5	< 15.5	< 18.3	< 21.3
HD16978	13.6 ± 2.2	–	< 19.0			
HD181327	–	1422.8 ± 42.9	825.0 ± 43.0	373.8 ± 26.8	194.6 ± 14.9	89.2 ± 9.4
HD202917	33.5 ± 1.8	24.8 ± 2.5	15.5 ± 2.9	< 16.4	< 18.4	< 21.5
HD224392	6.4 ± 1.1	–	< 13.1	–	–	–
HD2884	7.0 ± 2.0	–	< 18.2	–	–	–
HD2885	15.9 ± 1.7	–	< 18.2	–	–	–
HD3003	54.0 ± 4.4	19.5 ± 2.6	< 23.3	< 14.9	< 18.2	19.7
HD30051	22.5 ± 1.2	12.7 ± 1.3	< 15.4	< 15.3	< 17.6	< 21.6
HD3221	< 3.8	–	< 12.0	–	–	–

Continued on next page

Table 4.4 continued

Target	F70 (mJy)	F100 (mJy)	F160 (mJy)	F250 (mJy)	F350 (mJy)	F500 (mJy)
HD44627	< 4.1	–	< 11.1	–	–	–
HD53842	< 22.4	< 16.2	< 23.1	–	–	–
HD55279	< 4.3	–	< 13.2	–	–	–
HIP107345	< 4.2	–	< 13.8	–	–	–
HIP3556	< 11.9	< 7.9	< 21.3	–	–	–
GSC8056-482	< 5.5	–	< 12.7	–	–	–
TWA02	< 17.6	< 8.7	< 29.7	–	–	–
TWA05	< 3.6	–	< 14.2	–	–	–
TWA10	< 3.5	–	< 16.8	–	–	–
TWA12	< 3.3	–	< 15.5	–	–	–
TWA13A	–	< 7.6	< 18.1	–	–	–
TWA16	< 4.1	< 4.4	< 7.7	–	–	–
TWA21	< 3.8	–	< 14.3	–	–	–
TWA23	< 5.9	< 7.3	< 17.7	–	–	–
TWA25	< 6.3	< 6.7	< 14.3	–	–	–
HIP77815	< 6.0	–	< 22.1	–	–	–
HIP78099	< 5.4	–	< 14.1	< 16.1	< 19.2	< 21.5
HIP80130	< 5.7	< 7.5	< 14.7	–	–	–
1RXSJ160044.7-234330	< 4.0	–	< 15.8	–	–	–
J160210.9-200749	< 6.5	–	< 14.9	–	–	–

Continued on next page

Table 4.4 continued

Target	F70 (mJy)	F100 (mJy)	F160 (mJy)	F250 (mJy)	F350 (mJy)	F500 (mJy)
J160245.4-193037	< 6.6	–	< 15.5	–	–	–
J160801.4-202741	< 6.7	–	< 15.4	–	–	–
J153557.8-232405	< 5.9	< 7.0	< 13.6	–	–	–
J154413.4-252258	< 6.4	< 5.9	< 18.4	–	–	–
J160108.0-211318	< 5.5	–	< 16.3	–	–	–
J160654.4-241610	< 6.0	< 6.4	< 12.7	–	–	–
J160856.7-203346	< 7.8	< 7.4	< 19.4	–	–	–
J161402.1-230101	< 5.3	< 7.8	< 10.8	–	–	–

1.193, and 1.194 for the 250, 350, and 500 μm images respectively[2]. We color corrected the SPIRE fluxes by assuming they would lie in the Rayleigh-Jeans regime of a simple blackbody function. The color correction factors we multiplied to the data assuming Rayleigh-Jeans are 0.9417, 0.9498, and 0.9395[2] for the 250, 350, and 500 μm images respectively. The total error is calculated in the same way as for the PACS data. The final fluxes, uncertainties, and upper limits for the SPIRE data are listed in Table 4.4.

4.4 Spectral energy distributions

For each of our 67 targets, we collected archive data from several catalogs, including the Hipparcos Tycho 2 catalog (Perryman and ESA 1997), the WISE All sky survey (Wright et al. 2010), the 2MASS point source catalog (Cutri et al. 2003), the Akari all sky survey (Yamamura et al. 2010) and IRAS (Moór et al. 2006). We also included *Spitzer* Enhanced data products,[3] if available; these include 8 μm IRAC measurements, 16 and 22 μm IRS measurements, and 24 μm MIPS measurements and IRS spectra. For those targets without enhanced data products, we retrieved *Spitzer* photometry data from various sources in the literature (Carpenter et al. 2009, 2006; Low et al. 2005; Rebull et al. 2008; Zuckerman et al. 2011).

We used the archive data with wavelengths less than 5 μm to fit the photosphere of the star. We used ATLAS9 stellar photosphere models (Castelli and Kurucz 2004) to fit stars with temperatures greater than 7000 K. For stars with temperature less than 7000 K, we used the PHOENIX stellar atmosphere models (Hauschildt et al. 1999). Extincted stars were dereddened with a Fitzpatrick (1999) extinction law

[2]SDRG 5.7: `http://herschel.esac.esa.int/hcss-doc-9.0/`

[3]`irsa.ipac.caltech.edu/applications/Spitzer/SHA/`

before fitting the stellar models. The A_V values of the extincted stars are taken from Preibisch and Zinnecker (1999), Preibisch et al. (2002) and Hernández et al. (2005) and are listed in Table 4.3.

We color corrected the Akari data using the best fit stellar temperature and the color correction factors given in the Akari IRC Data User Manual[4]. The WISE bands 1-3 data were also color corrected with the assumption that they are in the Rayleigh-Jeans tail of a stellar blackbody (color correction factors of 1.0084, 1.0066, and 1.0088 for bands 1-3).

4.4.1 Modified blackbody fits

We fit the IR excess data with blackbody models to determine the disk characteristic temperature and fractional infrared luminosity. The blackbody temperature is a direct link to the inner edge of a debris disk, where the dust is hottest and brightest. This temperature can be translated into a dust radius, assuming perfect blackbody grains. As real grains are less efficient, they are likely hotter farther from the star. Therefore, the blackbody radius derived in this way indicates a lower limit on the dust radius.

Sources with 70 μm flux more than 3σ above the expected photosphere value are determined to have an IR excess. We fit the data of targets identified as having IR excesses with modified blackbodies of the form

$$F_\nu(T) \propto B_\nu(T)\left(1 - e^{-\tau_\nu}\right) \propto B_\nu(T)\tau_\nu \tag{4.2}$$

for small optical depth (τ_ν). For a simple blackbody, τ_ν is a constant at all wavelengths. For the modified blackbody, the optical depth is not constant at longer

[4] http://www.sciops.esa.int/SA/ASTROF/docs/IRC_IDUM_1.3.pdf

wavelengths, but instead takes the form

$$\begin{aligned} \tau_\nu &= \tau_0 && \text{for } \lambda < \lambda_0 \\ &= \tau_0 \left(\frac{\lambda}{\lambda_0}\right)^{-\beta} && \text{for } \lambda > \lambda_0. \end{aligned} \tag{4.3}$$

We fit the models to the data with the Levenberg-Marquardt χ^2 minimization routine `MPFIT` (Markwardt 2009). We fixed $\lambda_0 = 100\,\mu$m and constrained β to vary only between 0 and 2. Many of the disks lacked enough long wavelength data for the fits to be sensitive to changes in β. In those cases, we fixed $\beta = 0$.

The best fitting modified blackbody models are plotted in Figure 4.1 and the parameters of the best fitting models are listed in Table 4.5 with their statistical error bars. In Table 4.5, we also listed the fractional infrared luminosities ($L_{\rm IR}/L_*$) calculated by integrating the blackbody models and the stellar models over all wavelengths.

For non-excess sources, we used the blackbody models to estimate upper limits on $L_{\rm IR}/L_*$ by fitting a suite of blackbody models to the upper limits with temperatures of 10-300 K with a step size of 1 K while requiring the models to lie below the upper limits. We calculated $L_{\rm IR}/L_*$ values for each temperature and the highest $L_{\rm IR}/L_*$ value is the upper limit. Upper limits on $L_{\rm IR}/L_*$ are listed in Table 4.6.

4.5 Multiplicity in systems hosting debris disks

The presence of a stellar companion can have profound consequences on the formation and evolution of circumstellar disks. For instance, it has been established that binaries tighter than about 100 AU are much less likely to host protoplanetary disks or debris disks than observed in control samples of single stars or wide binary systems (e. g. Cieza et al. 2009; Duchêne 2010; Kraus et al. 2012; Rodriguez and

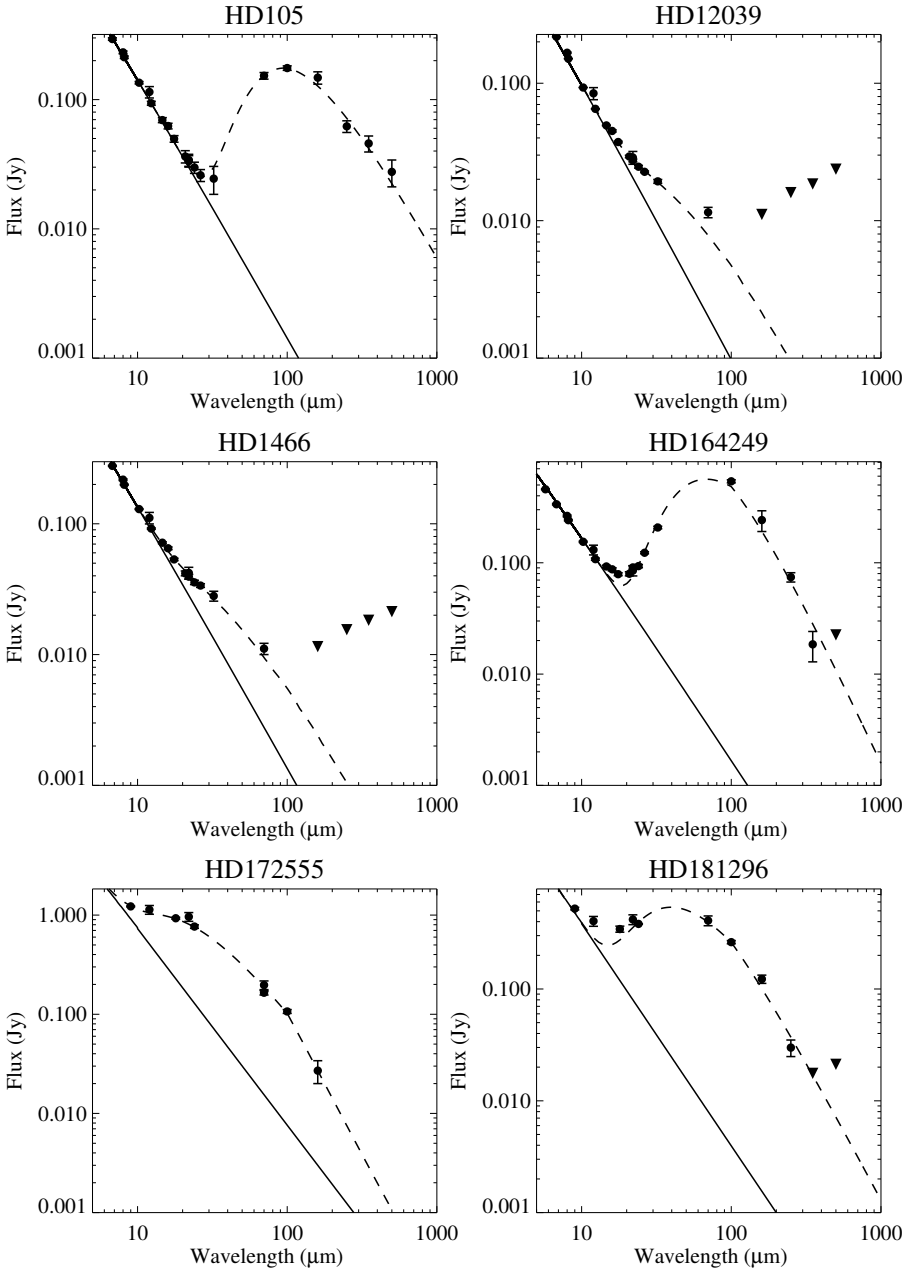

Figure 4.1: Spectral energy distribution (SEDs) of the 24 debris disks detected. The data used in the SED modeling includes the *Herschel* PACS (60, 100, & 160 μm) and SPIRE (250, 350, & 500 μm) analyzed in this chapter as well as data from the literature, including Hipparcos, 2MASS, WISE, Akari, IRAS, and *Spitzer*. Upper limits from PACS and SPIRE are shown as inverted triangles. The data with wavelengths $< 5\,\mu$m was fit with stellar photosphere models (solid line). The IR excesses are fit with modified blackbody models (dashed line).

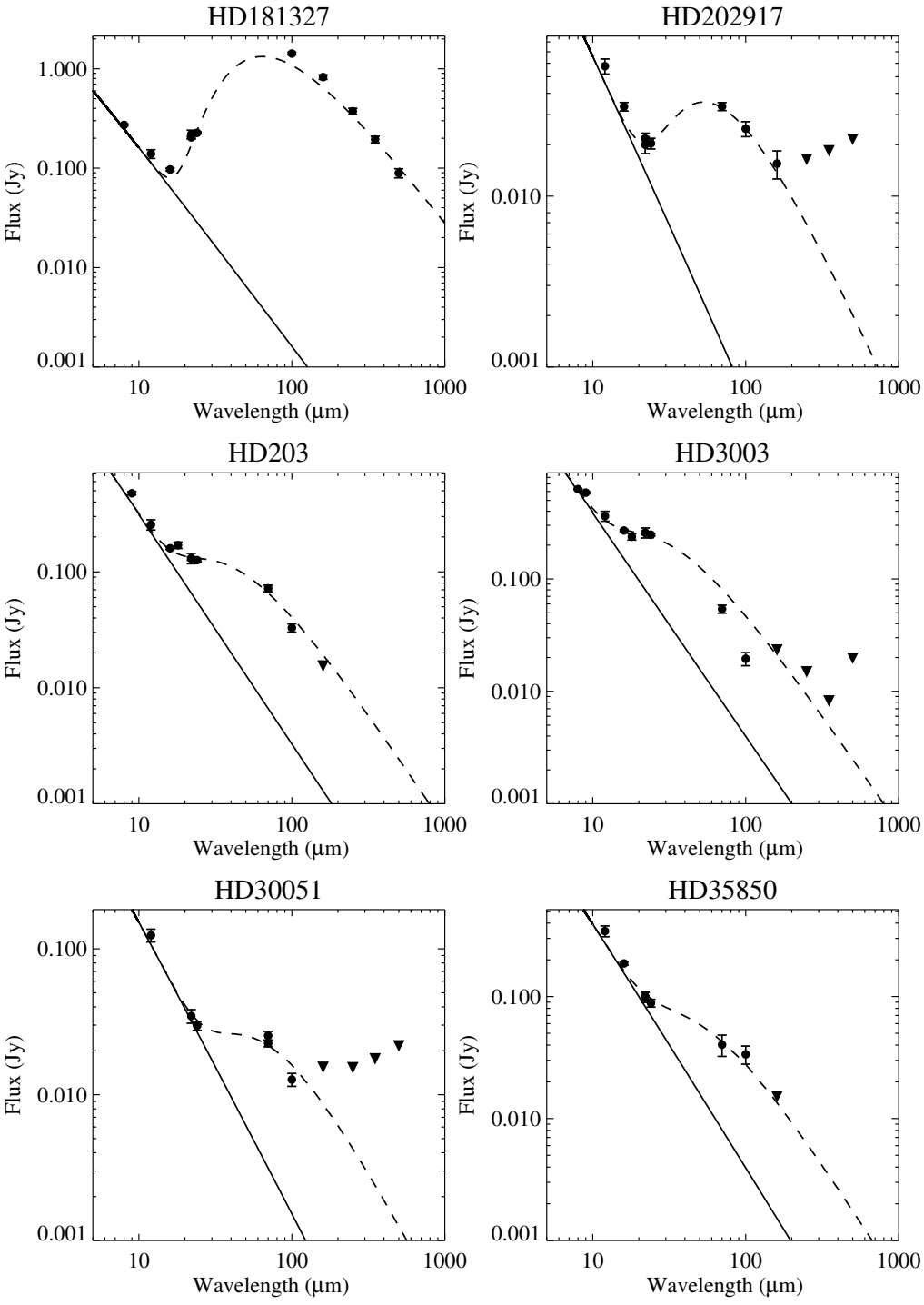

Figure 4.1 (continued)

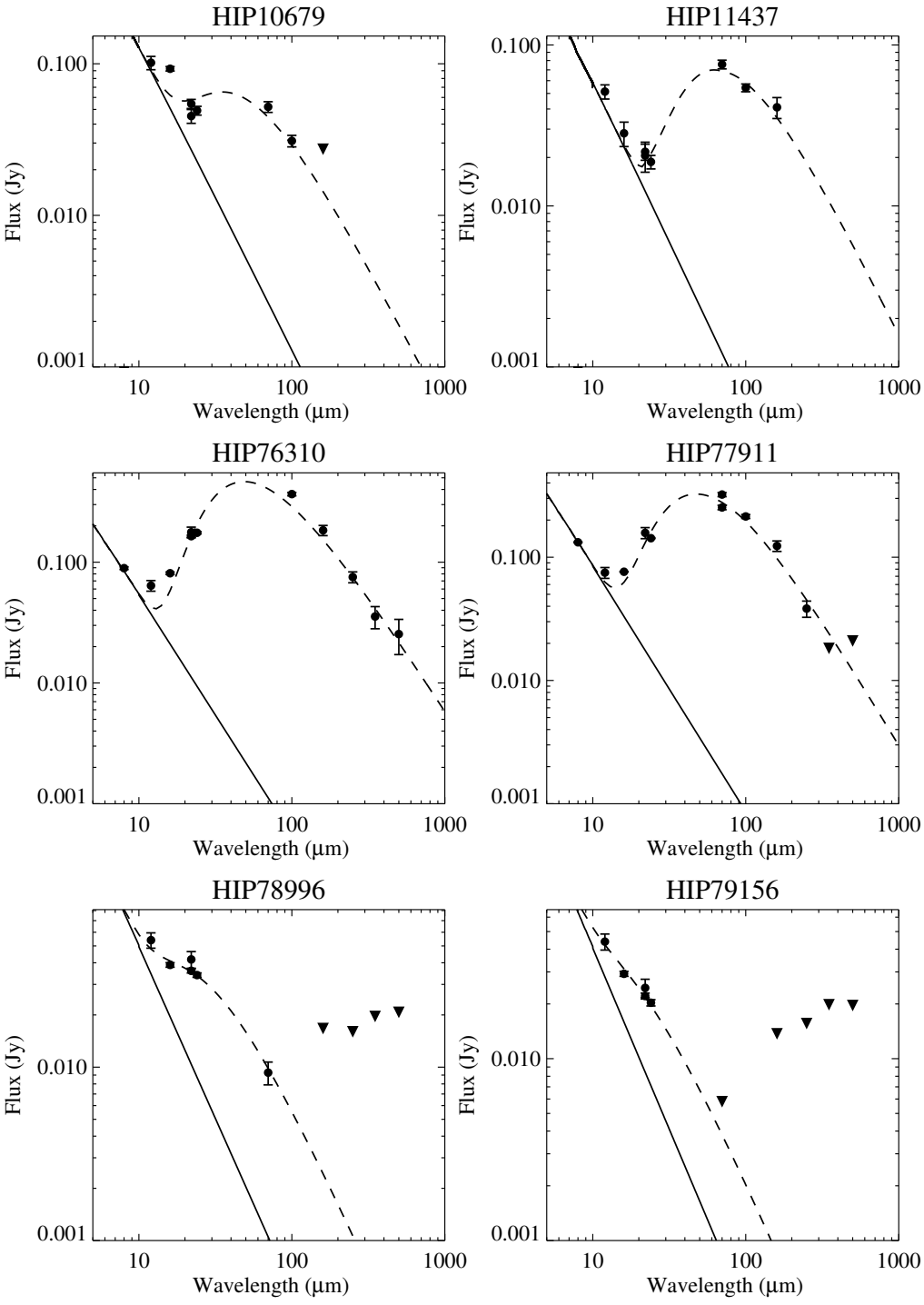

Figure 4.1 (continued)

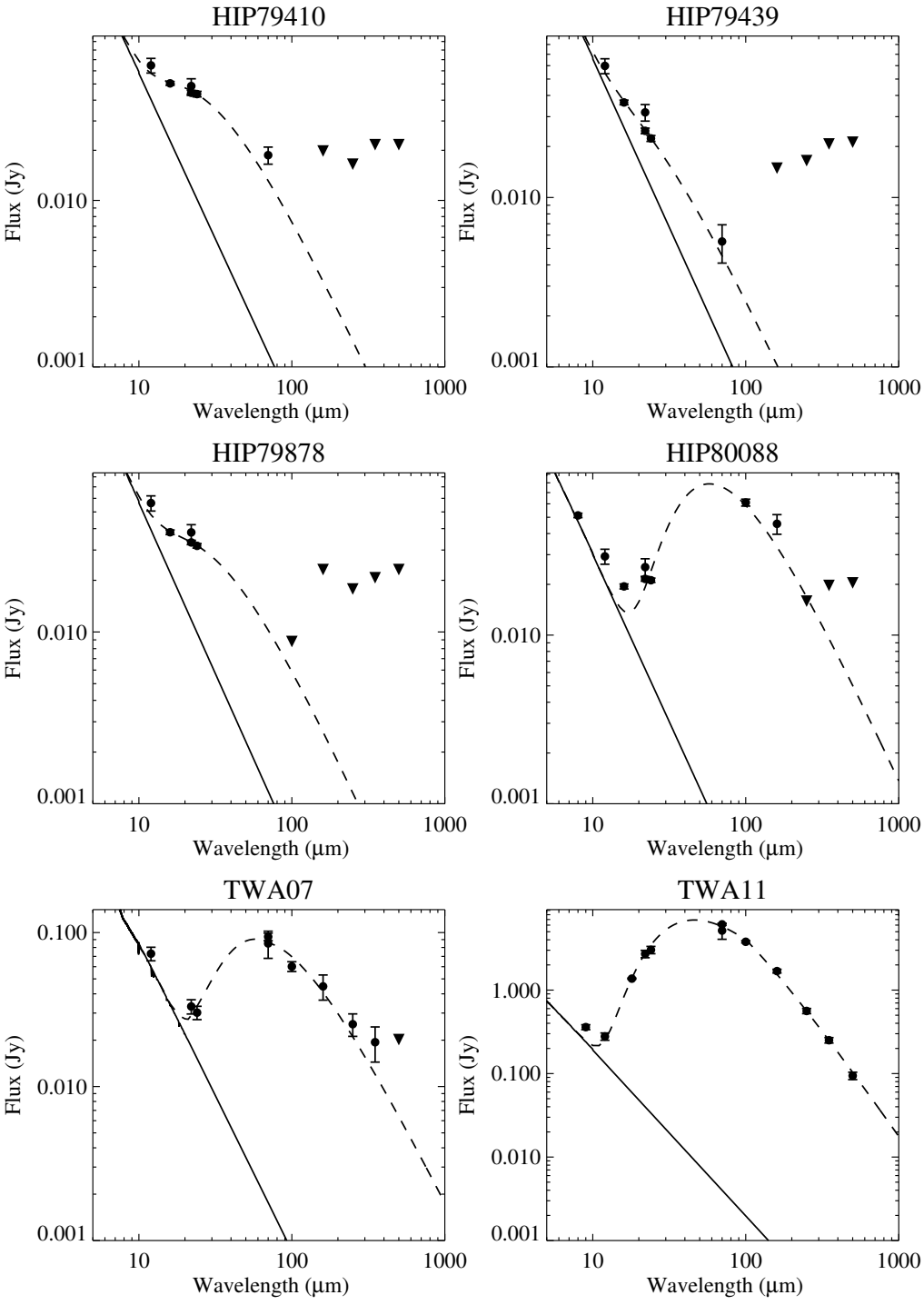

Figure 4.1 (continued)

Table 4.5: Modified Blackbody Results

Target	temperature (K)	β	LIR/L_*
HD164249	74.5 ± 0.6	0.9 ± 0.1	9.4×10^{-4}
HD172555	286.1 ± 3.7	1.1 ± 0.6	6.1×10^{-4}
HD181296	124.4 ± 1.6	0.6 ± 0.1	2.1×10^{-4}
HD203	146.6 ± 2.4	0	1.5×10^{-4}
HD35850	119.5 ± 8.4	0	6.3×10^{-5}
HIP10679	125.8 ± 3.5	0	3.2×10^{-4}
HIP11437	75.3 ± 2.5	0	5.2×10^{-4}
HD105	53.0 ± 2.1	0.1 ± 0.1	3.2×10^{-4}
HD12039	151.0 ± 5.6	0	8.5×10^{-5}
HD1466	181.1 ± 7.5	0	8.9×10^{-5}
HD181327	76.9 ± 0.4	0.2 ± 0.1	3.1×10^{-3}
HD202917	91.0 ± 2.0	0	2.8×10^{-4}
HD3003	200.3 ± 2.4	0	1.3×10^{-4}
HD30051	90.1 ± 7.1	0	4.5×10^{-5}
TWA07	80.6 ± 2.7	0	7.9×10^{-4}
TWA11	110.6 ± 0.5	0.6 ± 0.1	5.1×10^{-3}
HIP76310	104.3 ± 0.8	0	1.3×10^{-3}
HIP77911	106.8 ± 0.8	0.1 ± 0.1	3.8×10^{-4}
HIP78996	229.2 ± 10.2	0	3.2×10^{-4}
HIP79156	333.1 ± 21.9	0	1.2×10^{-4}
HIP79410	226.6 ± 9.6	0	1.4×10^{-4}
HIP79439	270.9 ± 27.4	0	6.3×10^{-5}
HIP79878	204.5 ± 12.0	0	9.5×10^{-5}
HIP80088	87.6 ± 0.9	0	5.7×10^{-4}

Zuckerman 2012). The nearby young associations provide a unique view on the earliest epochs of the debris disks phenomenon and, thus, offer important clues about the evolution of debris disks and their connection to multiple stellar systems. We have thus constructed a sample of 50 objects observed within GASPS from Tuc-Hor, BPMG, TWA, and UpSco and compiled their multiplicity properties, which have been probed in many past studies (Bergfors et al. 2010; Biller et al. 2007; Brandeker et al. 2003; Chauvin et al. 2010, 2005; Ehrenreich et al. 2010; Evans et al. 2012; Kasper et al. 2007; Lowrance et al. 2005; Malo et al. 2013; Masciadri et al. 2005;

Table 4.6: L_{IR}/L_* Upper limits

Target	LIR/L_* limit	Target	LIR/L_* limit
AT MIC	$< 2.7 \times 10^{-4}$	TWA02	$< 9.1 \times 10^{-4}$
CD-64 1208	$< 2.2 \times 10^{-5}$	TWA05	$< 8.7 \times 10^{-5}$
GJ3305	$< 4.6 \times 10^{-4}$	TWA10	$< 1.1 \times 10^{-3}$
HD139084	$< 1.5 \times 10^{-4}$	TWA12	$< 9.1 \times 10^{-4}$
HD146624	$< 1.4 \times 10^{-5}$	TWA13A	$< 1.6 \times 10^{-3}$
HD174429	$< 3.4 \times 10^{-4}$	TWA16	$< 1.7 \times 10^{-3}$
HD199143	$< 3.0 \times 10^{-5}$	TWA21	$< 4.3 \times 10^{-4}$
HD29391	$< 2.9 \times 10^{-5}$	TWA23	$< 1.5 \times 10^{-3}$
HD45081	$< 1.8 \times 10^{-4}$	TWA25	$< 8.6 \times 10^{-4}$
HIP77815	$< 3.0 \times 10^{-4}$	HIP78099	$< 1.7 \times 10^{-4}$
HIP12545	$< 5.1 \times 10^{-4}$	HIP80130	$< 3.3 \times 10^{-4}$
HD16978	$< 1.7 \times 10^{-5}$	1RXSJ160044.7-234330	$< 8.3 \times 10^{-3}$
HD224392	$< 1.7 \times 10^{-6}$	J160210.9-200749	$< 2.0 \times 10^{-2}$
HD2884	$< 5.7 \times 10^{-7}$	J160245.4-193037	$< 2.0 \times 10^{-2}$
HD2885	$< 1.6 \times 10^{-5}$	J160801.4-202741	$< 7.4 \times 10^{-3}$
HD3221	$< 2.6 \times 10^{-4}$	J153557.8-232405	$< 4.9 \times 10^{-3}$
HD44627	$< 3.0 \times 10^{-4}$	J154413.4-252258	$< 5.8 \times 10^{-3}$
HD53842	$< 4.6 \times 10^{-4}$	J160108.0-211318	$< 4.3 \times 10^{-3}$
HD55279	$< 8.1 \times 10^{-4}$	J160654.4-241610	$< 5.7 \times 10^{-3}$
HIP107345	$< 8.7 \times 10^{-4}$	J160856.7-203346	$< 2.2 \times 10^{-3}$
HIP3556	$< 8.8 \times 10^{-4}$	J161402.1-230101	$< 2.7 \times 10^{-3}$
GSC8056-482	$< 8.3 \times 10^{-4}$		

McCarthy et al. 2004; Metchev and Hillenbrand 2009). To ensure completeness and avoid spurious association at the largest separations, our analysis focused on companions located in the approximate 5–1000 AU range of projected separation.

With this composite sample, we find that the frequency of the debris disk phenomenon is virtually the same in multiple systems as it is for single stars (7/25 vs. 17/43, respectively). Thus, multiplicity alone does not result in adverse conditions to form planetesimals. However, not all stellar companions have the same influence. As shown in Fig. 4.2, the binary population hosting at least one debris disk is dominated by wide systems, with only one system with a separation smaller than

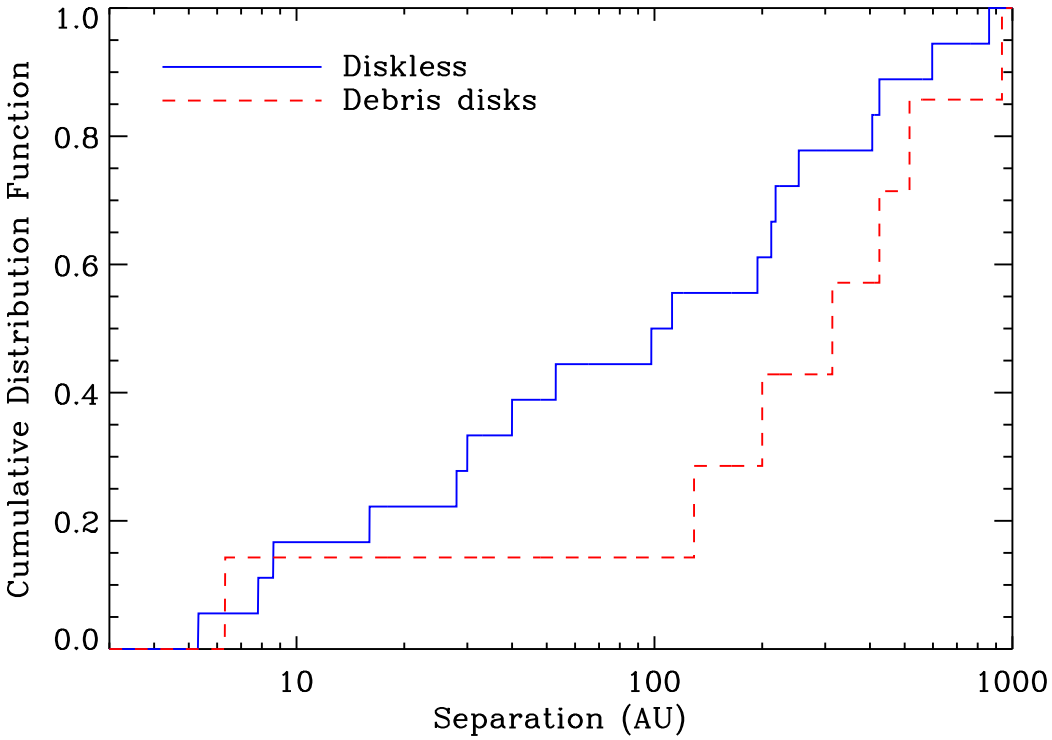

Figure 4.2: Cumulative histogram showing the distribution of binary separations among debris disks.

200 AU. Furthermore, this system HD12039 in the Tuc-Hor association, was first discovered to be a binary by Biller et al. (2007) but unconfirmed by Evans et al. (2012), so that its status is uncertain pending further high-resolution observations. Regardless, the distribution of separation for binaries with debris disks is in marked contrast to the separation distribution for diskless systems: the difference between the two distributions is significant at the 98.4% level. This confirms that close binaries are much less likely to host debris disks, as observed in the general population of debris disk systems, indicating that this aversion is present at all stages of the debris disks phenomenon.

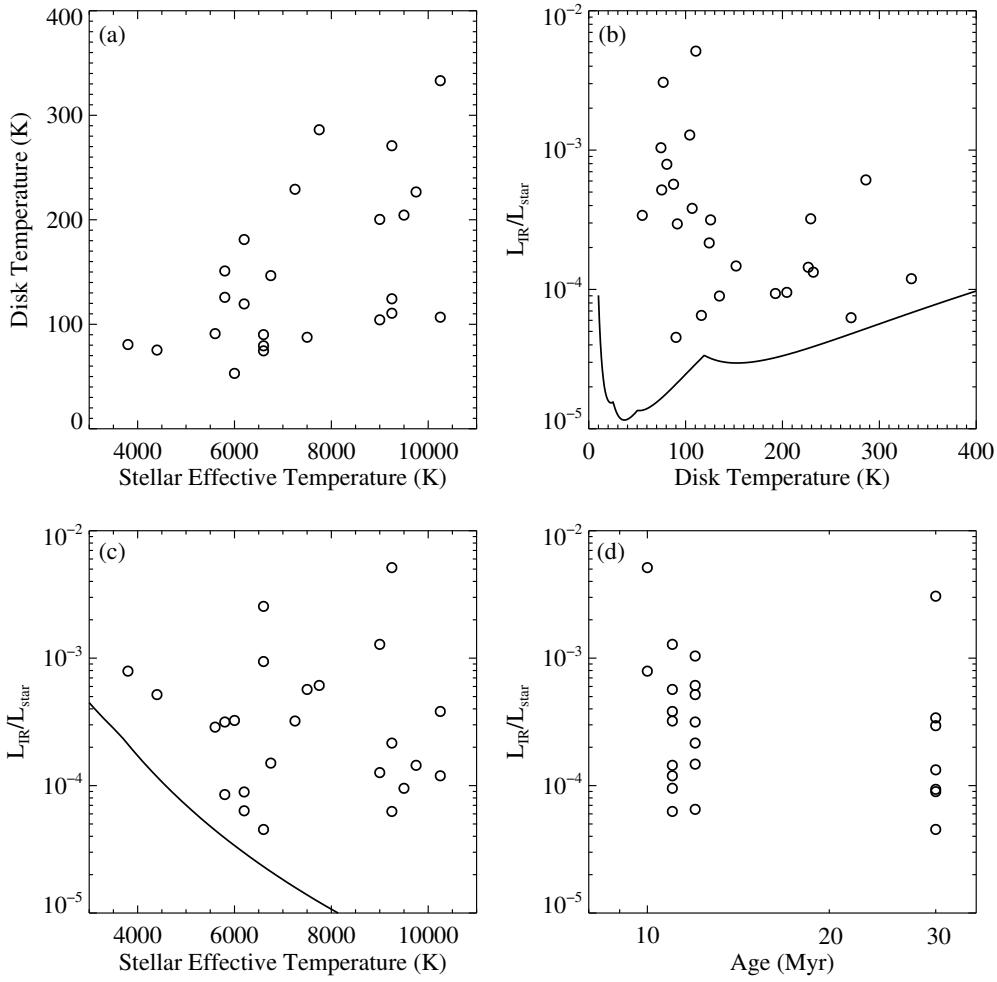

Figure 4.3: Relations between disk and star parameters from the modified blackbody fits. (a) Disk temperature vs. stellar temperature. (b) Fractional dust luminosity ($L_{\rm IR}/L_*$) vs. disk temperature. The solid line represents a cut of the average $L_{\rm IR}/L_*$ detection limits of the sample (calculated in Section 4.7) cut at $T_{\rm eff} = 6500$ K. (c) $L_{\rm IR}/L_*$ vs. stellar temperature. The solid line represents the detection limits cut at $T_d = 100$ K. (d) $L_{\rm IR}/L_*$ vs. age.

4.6 Correlations

We used the best fit parameters of the modified blackbody models to look for correlations between the stellar and disk parameters of the sample. Figure 4.3 shows the relations between the different parameters: the disk temperature, the stellar effective temperature, the fractional disk luminosity ($L_{\rm IR}/L_*$) and the age.

To quantify the correlations, we calculated the linear correlation coefficient, r, from Press et al. (1992)

$$r = \frac{\Sigma_i (x_i - \bar{x})(y_i - \bar{y})}{\sqrt{\Sigma_i (x_i - \bar{x})^2} \sqrt{\Sigma_i (y_i - \bar{y})^2}}, \tag{4.4}$$

where $\bar{x}$ and $\bar{y}$ are the mean values of the x and y data. A value of r above 0.3 shows a reasonable correlation and a value above 0.5 indicates a strong correlation. Additionally, we calculated the probability, P, that $|r|$ should have a larger value even if no correlation exists

$$P = \mathrm{erfc}\left(\frac{|r|\sqrt{N}}{\sqrt{2}} \right), \tag{4.5}$$

where erfc is the complementary error function and N is the number of data points.

The disk parameters show a large scatter and the plots show that most parameters are not correlated with one another. We calculated the r and P values for the all combinations of the disk parameters, $L_{\rm IR}/L_*$, age, $T_{\rm eff}$ and $T_{\rm d}$. All but one of the combinations had correlation coefficients below 0.3. This confirms that most are not correlated.

The only plot that shows a hint of a correlation is the plot of disk temperature vs. stellar temperature (Figure 4.3 (a)). There is a distinct lack of data in the upper lefthand corner of the plot, representing a lack of warm disks around late-type stars. The warm disks (those $\gtrsim$ 125 K) display a trend of increasing disk temperature with increasing stellar temperature. The cold disks (those $\lesssim$ 125 K) also show an increasing trend, but not as steep as the warm disks.

For the entire sample, the correlation coefficient is $r = 0.54$ and the probability of zero correlation is $P = 0.008$. When we split the disks into two populations, warm and cold disks, we get $r = 0.73$ and $P = 0.015$ for the warm disks and $r = 0.62$ and $P = 0.025$ for the cold disks. This suggests the disk temperature and stellar temperature are indeed correlated. We analyze this trend in Section 4.8, but first,

in Section 4.7 we show that the lack of warm disks around late-type stars in not due to the sensitivity of the dataset.

4.7 Detection Limits

To investigate the correlations seen in Section 4.6, we found we first need to be sure the trends we see are not due to the detection limits. In this section, we estimate the average detection limit for the sample as it depends on factors such as spectral type and dust temperature. The GASPS dataset is not a uniform sample. The integration time of each target was determined from a variety of factors, such as spectral type, distance, and the *Spitzer* 70 μm detections and upper limits, if any. Therefore, the detection limits vary widely amongst the sample. However, we can still estimate the average detection limits using the mean values of these parameters.

Assuming the stellar spectrum is well described by the Rayleigh Jeans law in the mid- and far-IR and that the dust can be described by a blackbody, the fractional dust luminosity ($L_{\rm IR}/L_*$) detection limit at a particular wavelength is given by

$$\frac{L_\nu}{L_*} = \left(\frac{\sigma_{F_d}}{F_*}\right) \frac{kT_d^4 \left(e^{h\nu/kT_d} - 1\right)}{h\nu T_*^3} \tag{4.6}$$

(Bryden et al. 2006; Roberge et al. 2012), where σ_{F_d} is the flux detection limit of the observations, F_* is the flux of the star at the given wavelength, T_d is the dust temperature, and T_* is the stellar temperature.

To determine the average detection limit for the sample, we set σ_{F_d} to the average of the 3σ upper limits for all the non-detections. We calculated F_* as the Rayleigh-Jeans approximated flux of a star of a given spectral type at the wavelength in question and at a distance equal to the average stellar distance of the sample (44 pc).

Using Equation 4.6, we calculated grids of $L_{\rm IR}/L_*$ detection limits vs. stel-

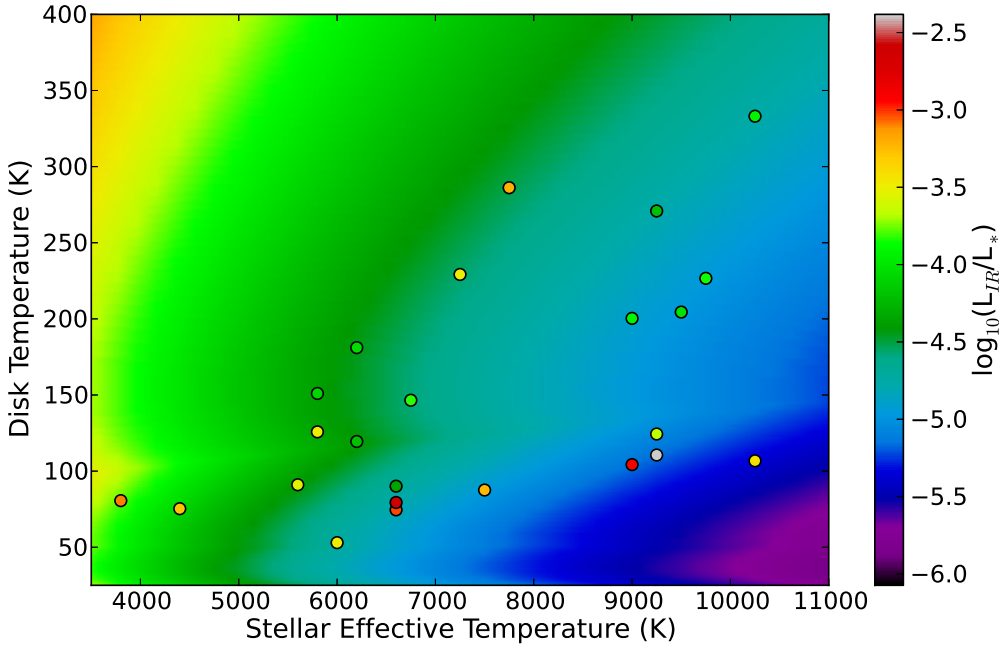

Figure 4.4: The color map shows the projected contours of the average fractional dust luminosity ($L_{\rm IR}/L_*$) detection limits in the disk temperature vs stellar temperature plane. For detected disks, parameters of the best modified blackbody models are also plotted, and their colors correspond to their $L_{\rm IR}/L_*$ value.

lar effective temperature and dust temperature for all three of the *Herschel* PACS bandpasses. We also included the detection limits from the *Spitzer* MIPS 24 μm band by assuming a 1σ accuracy of 6% of the stellar flux. The 24 μm MIPS data is more sensitive than *Herschel* data to debris disks warmer than $\sim$ 100 K.

The final $L_{\rm IR}/L_*$ detection limit curve is derived by combining the three PACS detection limits and the MIPS detection limits. In regions where they overlap, the most sensitive value is used for the final detection limit curve.

In Figure 4.4, we plot the contour map of the three-dimensional surface of the detection limits projected in the plane defined by the stellar temperature and the disk temperature. The colors of the contours correspond to the $L_{\rm IR}/L_*$ detection limits (logarithmic scaling, see colorbar). The data from the modified blackbody fits are also displayed with symbol colors corresponding to the $L_{\rm IR}/L_*$ value of the

best fitting blackbody model. For a disk to be detected, it must have an $L_{\rm IR}/L_*$ value larger than the detection limit contour in that region of the plot.

The data are more sensitive to disks around early type stars; the stars' high luminosity makes their disks brighter. The sensitivity decreases for warm disks since they radiate more efficiently at wavelengths shorter than the PACS bandpasses. There are no disks filling out the upper lefthand corner of this plot; this corresponds to a lack of high temperature disks around late-type stars. This is the portion of the plot where the GASPS sample is the least sensitive. However, this paucity of data is not solely a sensitivity effect. Disks bright enough to be detected in this region are found around warmer stars.

4.8 Interpretation of the temperature trend

Many disks show evidence of two distinct dust populations. Morales et al. (2011, 2009) and Chen et al. (2014) all fit SEDs of *Spitzer* detected disks with blackbody models and found that many of them required a second blackbody component to generate a good fit. Evidence for two distinct dust components has also been seen in imaging of nearby debris disks. Su et al. (2013) found evidence of unresolved inner dust belts in the *Spitzer* images of Vega and Fomalhaut inside the resolved outer belts. Resolved far-IR images of Fomalhaut with *Herschel* (Acke et al. 2012) and sub-mm images of AU Mic with ALMA (MacGregor et al. 2013) both show unresolved thermal emission near the central star. This thermal emission is far too bright to be coming from the star, and likely originates from a second unresolved dust belt in the system.

Only a handful of the disks in our sample show indications in their SEDs of having two dust populations. This may be just due to the sensitivity, especially

for the faint disks. However, the full dataset shown in Figure 4.4 suggests there are two distinct categories the disks fall into. The first category is the cold disks. These disks have characteristic temperatures that are $\lesssim$ 125 K, and the average temperature does not vary much with the spectral type of the star. The second group is the warm disks with characteristic temperatures $\gtrsim$ 125 K. These disks have a large spread in temperatures (and larger uncertainties on average) but seem to have a general upwards trend in disk temperature with stellar temperature.

We separated the disks into two populations at a temperature of $\sim$ 125 K. This is the temperature where disks appear to split into two different trends. Figure 4.5 shows a histogram of the temperatures of the disks. As Chen et al. (2014) also saw in a sample of $\sim$ 500 disks with *Spitzer*, we see a sharp peak in the cold disks ($\sim$ 100 K) and a more uniform distribution out to warmer temperatures.

We fit both populations with a power-law function where the disk temperature, T_d, changes with stellar temperature, T_*, as $T_d \propto T_*^{\alpha}$. The best fits give $\alpha = 0.85 \pm 0.1$ for the cold disks with a reduced chi-squared value of $\chi^2_R = 69$, and $\alpha = 0.95 \pm 0.3$ for the warm disks with $\chi^2_R = 89$ (see Figure 4.6). These values are consistent with each other, implying the cold and warm populations could have the same trend, but it is difficult to be certain with the large uncertainty on the fit to the warm disks.

The fit to cold disks does not depend on the temperature chosen to separate the cold and warm disks. The cold disks have lower uncertainties on the dust temperatures, so the fit to the trend does not significantly change even if we use the entire sample, not just the cold disks. The warm disks, however, are sensitive to the choice of dividing temperature. We fit the trend of the cold and warm disks with different choices for the temperature separating the two groups from 100 K to 150 K in increments of 5 K. We chose 125 K as the temperature at which the fit to the warm disks has the lowest χ^2_R value. Above 150 K, there are not enough good data

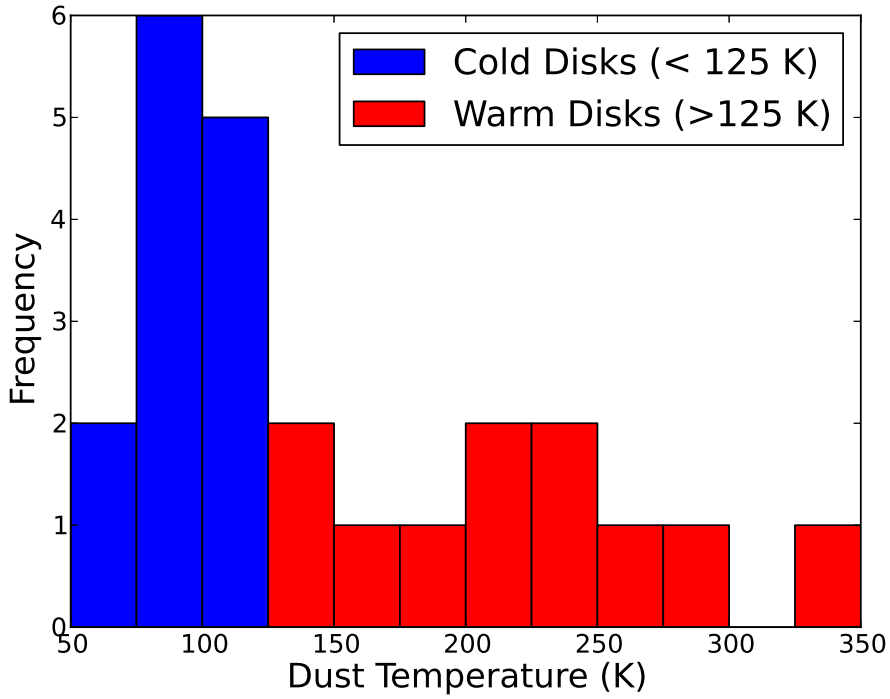

Figure 4.5: Histogram of the best fit blackbody disk temperatures for the 24 debris disks. The disks fall into two categories, the cold disks (< 125 K) that cluster around 100 K, and the warm disks (> 125 K) that have a uniform distribution of temperatures from 125 to 350 K.

to constrain the trend, and the fit diverges.

Next we explore what value of α we would expect to get for a few simple models. We start with a constant temperature model. Morales et al. (2011) claimed their *Spitzer* data showed warm disks all show the same temperature, regardless of spectral type. A constant dust temperature model ($T_d = \text{const}$) would give $\alpha = 0$. The cold disks are definitely not consistent with this, and even with the large uncertainties in the warm disk trend, the fit is also not consistent with $\alpha = 0$.

Next we try a constant radius model, where the location of the dust is independent of the central star. If we assume the true dust radius, R_x, is equal to the blackbody radius R_{BB}, and is a constant, then

$$T_d \propto R_{BB}^{-1/2} L_*^{1/4} \propto L_*^{1/4}. \tag{4.7}$$

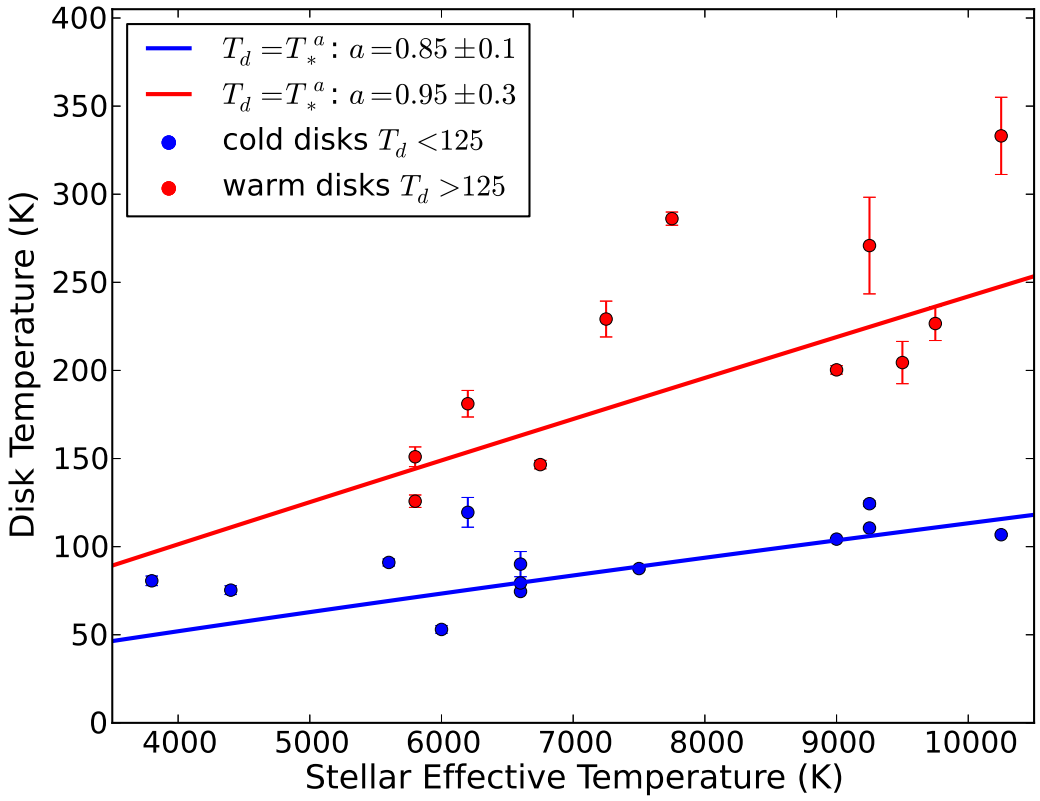

Figure 4.6: Characteristic disk temperature vs. stellar effective temperature for the GASPS disks, separated into cold disks (blue) and warm disks (red). The two populations are fit with a power-law in temperature.

Assuming $L_* \propto M_*^{3.5}$ and $R_* \propto M_*^{2/3}$, this gives $\alpha \sim 7/4$.

But how good is the assumption that the true disk radius is equal to the blackbody radius? In studies where the disk radius is spatially resolved, the true disk radius is often larger than the blackbody radius calculated from the SED (e.g. Booth et al. 2013; Rodriguez and Zuckerman 2012). This is because real dust grains are not as efficient as blackbodies at radiating their heat at long wavelengths. Consequently, the grains will be hotter farther from the star than a true blackbody would be.

If, in the calculation above, we do not assume $R_x = R_{BB}$, but instead we multiply

R_{BB} by a factor Γ, to get the true radius, i.e. $R_x = \Gamma R_{BB}$. Γ can also be a function of spectral type and ranges from $\sim$ 1 to 10 (Booth et al. 2013; Lestrade et al. 2012; Marshall et al. 2011; Rodriguez and Zuckerman 2012; Wyatt et al. 2012). Pawellek et al. (2014) attempted to constrain how Γ changes with spectral type, and they found $\Gamma \propto T_*^{-1.2\pm0.2}$ (A. V. Krivov, personal communication). Adding this to our derivation of α, we get

$$T_d \propto \Gamma^{1/2} L_*^{1/4} \propto T_*^{1.15}. \tag{4.8}$$

Our warm disks are consistent with this trend. The cold disks could be consistent as well if we take into consideration the uncertainty in the calculations, not just of Γ, but also our simplification of L_*, M_*, and R_* relations.

Another model we tried is one where the disk radius is a function of the spectral type, i.e. $R_x \propto M_*^{\beta}$. From Equation 4.7, we get

$$T_d \propto M_*^{-\beta/2} L_*^{1/4} \propto T_*^{-\beta+7/4} \tag{4.9}$$

if $R_x = R_{BB}$. With our calculated values of α, this would give values of $\beta = 0.9$ for the cold disks and $\beta = 0.8$ for the warm disks.

Both the cold and the warm disks show a large scatter around the best fit model, resulting in large χ^2_R values. This is likely due to real variations in the disks away from an idealized system. Planets, binary companions, stellar flybys and other factors can all affect the end result of a planetary system, which is why we see such a large variation in disks and exoplanets systems. With more data, we can get better statistics, but the large scatter will likely remain.

Several other teams have collected *Herschel* data on debris disks, such as DUNES (Eiroa et al. 2013), DEBRIS (Matthews et al. 2010), and a few other smaller programs. With ALMA nearing completion, faint debris disks will be visible in the sub-mm/mm regime. The collection of all these datasets together will provide a

robust test of the trends seen in the GASPS data, as well as determine whether the trend changes with stellar age.

4.9 Discussion

Planetesimal belts are often shaped by the gravitationally dominant planets around them. The temperature trend seen in our young debris disk sample could point to an underlying trend in the planets themselves or the trend in the cold disks could be due to planet formation efficiency.

Core accretion efficiency drops with distance from the star because of the combined effects of increases in dynamical timescales and the decrease in surface density of solid material (Dodson-Robinson et al. 2009). Planetesimals, however, are easier to form because they need less solid material. They can likely form at some distance beyond where planets can form (Kennedy and Wyatt 2010).

Planets can clear out the inner edge of the belt through gravitational interaction. The inner edge of the disk can therefore represent the outer limit of where planets can form. The blackbody temperature probes the inner edge of a debris disk and therefore the limit of planet formation efficiency. This does not take into account the effects of planet migration, which could be significant in some systems.

If the temperature trend is driven by planet formation, we can derive the approximate form it should take. The timescale to form a giant planet depends on the stellar mass. To first order, Kenyon and Bromley (2008) give the timescale as

$$t \propto P/\Sigma, \tag{4.10}$$

where P is the orbital period and Σ is the surface density of solids. Using Newton's form of Kepler's third law and the surface density scaling like the Minimum Mass Solar Nebula (MMSN; Hayashi 1981; Weidenschilling 1977) gives and $\Sigma \propto \Sigma_0 a^{-3/2}$,

where Σ_0 is the initial surface density of solids. Σ_0 scales with disk mass, which has been shown to scale with stellar mass ($\Sigma_0 \propto M_d \propto M_*$) (Andrews et al. 2013). Together, the timescale to form a planet is

$$t \propto R_x^3 M_*^{-3/2}. \tag{4.11}$$

Given a constant maximum time for planet formation, the location of the outermost planet, and therefore the inner edge of the debris disk, should scale with stellar mass as

$$R_x \propto M_*^{-1/2}. \tag{4.12}$$

The form we derive for our cold disk population, however, is closer to $\mathrm{R}_x \propto \mathrm{M}_*$. The difference could come from a number of assumptions, most notably, the form of the MMSN. Other forms have been predicted in the literature (e.g. Desch 2007). The large scatter in our data could indicate that the density distribution may vary a lot in different disks, as suggested by observational studies of protoplanetary disks (e.g. Andrews and Williams 2007).

Ballering et al. (2013) recently reported the existence of a similar temperature trend amongst the cold debris disks observed with *Spitzer*. Using similar calculations as above, they derive various predictions for an $R_d \propto M_*^{\gamma}$ power-law. However, they only fit the temperature trend with a linear relation and try no other power-law forms. They do not report a trend in the warm disks.

Chen et al. (2014) also reanalyzed a sample of 499 debris disks with *Spitzer* data. They fit their dust temperatures with a power-law as a function of stellar luminosity and found $T_d \propto L_*^{0.13}$ for their cold disks. This approximately gives $\alpha \sim 0.9$, which is very similar to our results.

Morales et al. (2011) reported a constant temperature for the warm disks detected with *Spitzer*, regardless of spectral type. Though the scatter in the warm

disks is quite large in both our *Herschel* data and the *Spitzer* data in Morales et al. (2011), the constant temperature model does not appear to fit the trend we see. Morales et al. (2011) do not report a trend in their cold disk sample.

4.10 Summary

The results of this study of young debris disks suggest a divergence into two types: cool "classical" debris disks with $T_{\rm d} < 125$ K, and warm disks, with $T_{\rm d} = 125-300$K. The cold debris disks in our sample show a trend of increasing disk temperature with stellar temperature. This trend is well fit by a model where the disk location scales linearly with stellar mass ($R_d \propto M_*$). Since the inner edge of the disk can be shaped by the outermost planet in the system, we believe this trend probes the radial limit of planet formation in young circumstellar disks. The warm disks are, on average, 50 times lower mass than the cool debris disks. They show a similar trend of increasing disk temperature with stellar temperature, although the large scatter makes the analysis more difficult. These warm disks could show an analogous trend probing the limit of terrestrial planet formation inside the ice line.

More data of young debris disks with an instrument as sensitive as *Herschel* are crucial to confirming the form of this trend. Many such data have been taken in various programs with *Herschel*, and their data will soon be published. The combination of their data with the GASPS data presented here should confirm or deny our current findings. ALMA also provides the needed sensitivity at longer wavelengths, allowing us to probe cold and faint disks.

Chapter 5

Modeling the HD32297 Debris Disk with far-IR Herschel Data

5.1 Introduction

Debris disks are circumstellar disks composed of dust produced during collisions of planetesimals. In the youngest disks (10-100 Myr), the planetesimals may deliver volatiles such as water to still-forming terrestrial planets. Although the planetesimals themselves are undetectable, the dust they produce radiates thermally in the infrared (IR) and sub-millimeter (mm) and scatters starlight at optical and near-IR wavelengths. These grains provide clues to the composition of their parent bodies.

The outer regions of several debris disks have been imaged in scattered light. Resolved images can constrain the morphology of the disk's outer regions, but the composition of their grains cannot be uniquely determined from these images alone. Mid-IR spectra - useful for determining grain composition in younger protoplanetary disks - also fail to provide constraints on the dust composition in most debris disks; by this point, the remaining grains are too large to emit solid state features in the

mid-IR (Chen et al. 2006). While there are a few notable exceptions, most debris disks require modeling of the full spectrum, from optical to mm wavelengths, to probe the grain composition.

The *Herschel Space Observatory* (Pilbratt et al. 2010) was launched in May 2009, presenting a new opportunity for sensitive far-IR and sub-mm observations. The PACS (Poglitsch et al. 2010) and SPIRE (Griffin et al. 2010) instruments have photometric and spectroscopic capabilities spanning a wavelength range of $\sim 60-500\,\mu$m. These data are crucial for detailed modeling of a disk's spectral energy distribution (SED) because they span the wavelength range where the thermal emission from debris disks typically peaks.

Unfortunately, SED modeling of debris disks is hampered by degeneracies in the models between disk geometry and grain properties. Thankfully, resolved imagery can be used to break some of the degeneracies by providing geometrical constraints. We have used the *Herschel Space Observatory*'s PACS and SPIRE instruments to obtain far-IR and sub-mm photometry and spectroscopy of the disk surrounding the $\sim$ 30 Myr-old (Kalas 2005) A-star, HD32297. This edge-on disk has been imaged several times in scattered light, thereby constraining the disk geometry. The *Herschel* observations fill in a large gap in the SED, which allows us to model the grain composition in more detail.

The HD32297 disk (112 pc away; van Leeuwen 2007) was first resolved in the near-IR out to a distance of $3.3''$ (400 AU) from the star with HST NICMOS (Schneider et al. 2005) and later resolved at several other near-IR wavelengths (Debes et al. 2009; Mawet et al. 2009). Recently, Angular Differential Imaging (ADI) has been used to resolve the disk in the near-IR with ground-based facilities (Boccaletti et al. 2012; Currie et al. 2012). Additionally, the disk has been marginally resolved at mid-IR (Fitzgerald et al. 2007b; Moerchen et al. 2007) and millimeter wavelengths

(Maness et al. 2008).

The HD32297 debris disk has a few unique features; one of the more luminous debris disks ($L_{\rm IR}/L_* \sim 10^{-3}$), HD32297 is also one of only a handful of debris disks where circumstellar gas has been detected. Redfield (2007) detected Na I in absorption towards HD32297 that was not found towards any neighboring stars. The additional peculiarity of brightness asymmetries and warping seen in scattered light images were analyzed by Debes et al. (2009), who concluded that these features could be caused by the disk's motion through the interstellar medium (ISM).

The *Herschel* data presented here were acquired as part of the *Herschel* Open Time Key Programme entitled "Gas in Protoplanetary Systems" (GASPS; Dent et al. 2012). The PACS data were taken as part of the main program, and the SPIRE data were taken as part of an Open Time proposal to follow up GASPS debris disks at longer wavelengths (OT2_aroberge_3; PI: A. Roberge). Here we present the PACS and SPIRE observations of HD32297 as well as the results of the modeling of the entire SED. In Sections 5.2 and 5.3, we present the data and describe the data reduction. In Section 5.4, we describe the SED modeling and we discuss the results in Section 5.5.

5.2 Observations and Data Reduction

Observations of HD32297 at 70, 100, and 160 μm were taken with the *Herschel* PACS instrument in ScanMap mode with the medium scan speed of $20''{\rm s}^{-1}$. The 70 μm observations consisted of 8 scan legs at a scan angle of 63° with scan lengths of $3'$, and $2''$ separation between the legs, for a total observing time of 220 seconds. The 100 and 160 μm observations were taken simultaneously with slightly larger maps of 10 legs with the same leg length and separation as the 70 μm observation. We

took 100 and 160 μm data at two different scan angles, 70 and 110°, with a total duration of 276 seconds per scan angle. We then combined the observations at the two scan angles to reduce noise due to streaking in the scan direction. We reduced the data with HIPE 8.2 (Ott 2010) using the standard reduction pipeline. We chose the final maps to have a pixel scale corresponding to the native pixel scale of the PACS detectors, 3.2″ for the 70 and 100 μm images and 6.4″ for the 160 μm images.

We also took simultaneous images of HD32297 at 250, 350, and 500 μm with the SPIRE instrument. The observations were made in the Small Scan Map mode with a scan speed of 30″s^{-1}, with two repetitions and a total observation time of 307 seconds. We reduced the data with HIPE 8.2, producing final maps with pixels scales of 6, 10, and 14″ for the 250, 350, and 500 μm images respectively. HIPE produces SPIRE images with units of Jy beam^{-1}, which we converted into Jy pixel^{-1} for analysis using beam areas of 423, 751, and 1587 arcsec^2 for the 250, 350, and 500 μm images respectively.

The *Herschel* PACS spectroscopy of HD32297 was taken in two modes, the lineSpec and rangeSpec modes. The lineSpec observations targeted the [O I] 63.2 μm line with a duration of 3316 seconds. The rangeSpec observations targeted six lines, [O I] at 145.5 μm, [C II] at 157.7 μm, two o-H_2O lines at 78.7 and 179.5 μm, and 2 CO lines at 72.8 and 90.2 μm. The total rangeSpec observation time was 5141 seconds, divided into three observing segments, covering the six lines two at a time. A deep follow-up rangeSpec observation was performed targeting just the [C II] 157.7 μm line with a duration of 4380 seconds. We reduced the spectroscopic data using HIPE 8.2 and applied an aperture correction in HIPE to account for point source flux loss. We produced spectra with a pixel scale corresponding to the native resolution of the instrument.

5.3 Analysis

5.3.1 Herschel PACS photometry

The HD32297 disk is a spatially unresolved point source to *Herschel*. The full-width at half-maximum of the *Herschel* PACS beam at 70 μm is 5.6″, so the bulk of the thermal emission must be within $\sim$ 300 AU. This is consistent with resolved images which suggest the disk peaks at $\sim$ 110 AU (Boccaletti et al. 2012; Currie et al. 2012; Debes et al. 2009). Aperture photometry was performed with apertures of 12″ for the 70 and 100 μm images and 22″ for the 160 μm image.

We applied aperture corrections provided by the *Herschel* PACS ICC[1], but color corrections were not applied. We calculated the uncertainty in the flux from the standard deviation of the sky background in an annulus around the aperture. We placed the annulus between 20-30″ from the central star for the 70 and 100 μm images and between 30-40″ for the 160 μm image. An absolute calibration error of 2.64, 2.75, and 4.15%[1] for the 70, 100, and 160 μm images respectively was added in quadrature to the uncertainty measured from the sky background. Results from the *Herschel* PACS photometry observations are given in Table 5.1.

5.3.2 Herschel SPIRE photometry

Aperture photometry was performed with aperture radii of 22, 30, and 42″ for the 250, 350, and 500 μm images respectively. The sky background was estimated from an annulus with radius of 60-90″ from the central star and subtracted from the measured flux. Aperture corrections were applied according to the SPIRE data

[1]PICC-ME-TN-037: `http://herschel.esac.esa.int/twiki/pub/Public/PacsCalibrationWeb/pacs_bolo_fluxcal_report_v1.pdf`

Table 5.1: *Herschel* PACS and SPIRE photometry results

Obs. Id	Wavelength (μm)	Flux $\pm$ Error (Jy)
1342193125	70	1.038 ± 0.029
1342217452-3	100	0.770 ± 0.022
1342217452-3	160	0.403 ± 0.020
1342240033	250	0.153 ± 0.012
1342240033	350	0.071 ± 0.008
1342240033	500	0.045 ± 0.007

reduction guide[2]. A color correction[2] of $\sim 5\%$ was applied assuming a Rayleigh-Jeans law slope of $F_\nu \propto \nu^2$. This correction could be off by 5% if the slope of the SED in the sub-mm is steeper than Rayleigh-Jeans. The uncertainties in the flux measurements come from the standard deviation of the sky background added in quadrature with a 7% absolute calibration error. Results from the *Herschel* SPIRE photometry are listed in Table 5.1.

5.3.3 Herschel PACS spectroscopy

The PACS spectrometer is an Integral Field Unit (IFU) spectrometer that has a 5×5 array of spaxels (spatial pixel) with each spaxel covering a $9.4'' \times 9.4''$ region. We verified that the star was well-centered on the central spaxel during the observations by comparing the observations to a model of the transmission of a theoretical PSF through the PACS IFU. We shifted the model PSF and calculated the fractional flux in the different spaxels as a function of offset. Comparison to observations of HD32297 indicate the star is not significantly offset. This method is the same as the one used by Howard et al. (in preparation) for PACS observations of Taurus that had pointing errors.

We use data from the central spaxel only for analysis. No lines were detected

[2]SDRG 5.7: `http://herschel.esac.esa.int/hcss-doc-9.0/`

in the lineSpec or the first rangeSpec observation. We calculated continuum flux values by fitting straight lines to the data, and the results are listed in Table 5.2. We excluded five pixels on each edge from the continuum fit because PACS spectra have enhanced noise at the edges. Emission in the [C II] 157.7 μm line was seen in the second deep rangeSpec observation. The continuum flux was found by fitting a line to the spectrum while masking out 0.5 μm around the line center. The rms noise was also calculated in the region surrounding the line. The number of pixels used to calculate the noise was chosen such that the signal-to-noise in the emission line was maximized, i.e. the rms noise was minimized.

The line flux was integrated over the three pixels surrounding the line (marked by the gray bar in Figure 5.1). The uncertainty in the line flux was found by propagating the rms noise. Upper limits on the other lines were found using the same method of error propagation at the expected line center. These values are reported in Table 5.2. The integrated line flux of the [C II] line is detected at the 3.7σ level above the continuum in the central spaxel from the deep rangeSpec observation. All 25 spaxels were searched for a significant [C II] line signal, and no other emission was found with more than a 2σ significance. Since the line is present only in the central spaxel, we believe the gas is associated with the star rather than from the surrounding ISM.

5.3.4 Column density of C II in HD32297

With the flux of the [C II] line, we can determine the column density of C II for comparison to the Na I column density found by Redfield (2007). The [C II] 158 μm line arises from the transition between the two fine structure lines of the electronic ground state. Since the next electronic energy level is three orders of magnitude higher, we can assume a two level population with a high accuracy. Following

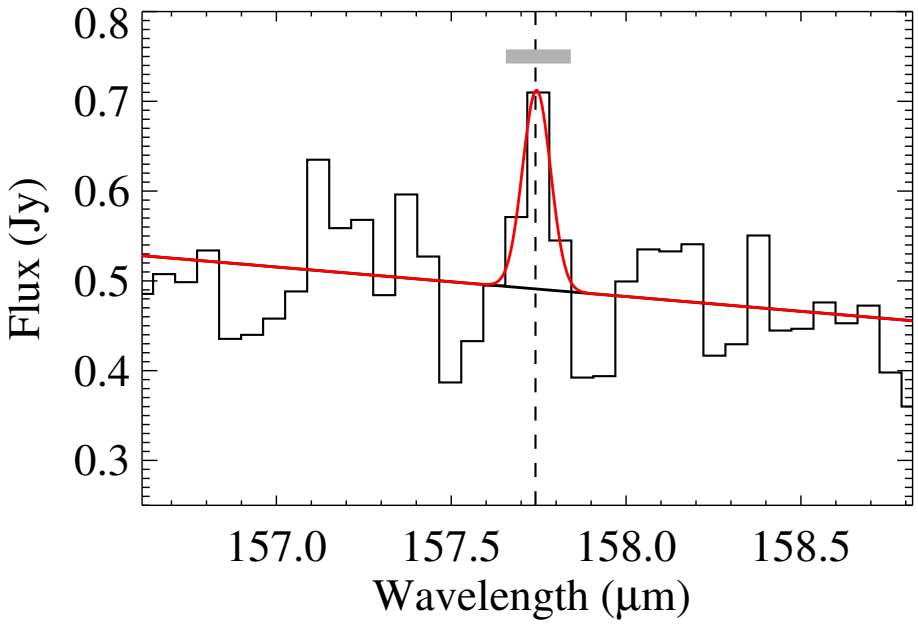

Figure 5.1: The [C II] 157.7 μm emission line from the HD32297 debris disk. The dashed line represents the expected position of the [C II] line. The continuum was fit with a straight line (black solid line), and the emission line was fit with a Gaussian (red solid line). The integrated line flux was measured from the 3 pixels surrounding the line (indicated by the gray bar). The integrated line flux is 3.7σ above the continuum.

Roberge and Kamp (2011), the column density is

$$N_{\rm CII} = \frac{4\pi\lambda}{hc}\frac{F_{10}}{A_{10}x_1\Omega}, \tag{5.1}$$

where the indices 1 and 0 indicate the upper and lower fine structure levels respectively, $\lambda = 157.7\,\mu$m, $F_{10} = 2.68 \times 10^{-18}$ W m^{-2} is the integrated line flux, $A_{10} = 2.4 \times 10^{-6}$ s^{-1} is the spontaneous transition probability, $\Omega = 0.357$ arcsec^2 is the angular source size estimated from resolved scattered light images, and x_1 is the fractional population of the upper level. Assuming local thermodynamic equilibrium (LTE), x_1 is dependent on the excitation temperature. Roberge and Kamp (2011) give this as

$$x_1 = \frac{(2J_1+1)g_1 e^{-E_1/kT_{ex}}}{Q(T_{ex})}, \tag{5.2}$$

Table 5.2: *Herschel* PACS Spectroscopy Results

Line Name	Wavelength (μm)	Continuum Flux (Jy)	Integrated Line Flux[a] $\times 10^{-18}$ (W/m^2)
O I 63	63.184	1.28 ± 0.20	< 7.29
CO 72	72.843	0.83 ± 0.23	< 7.77
H_2O 79	78.741	1.03 ± 0.23	< 9.12
CO 90	90.163	1.05 ± 0.29	< 8.13
O I 145	145.525	0.55 ± 0.09	< 3.99
C II 158 (1) [b]	157.741	0.53 ± 0.13	< 4.32
H_2O 180	179.741	0.44 ± 0.15	< 3.57
C II 158 (2) [b]	157.741	0.50 ± 0.06	2.68 ± 0.72

[a] Non-detections are reported as 3σ upper limits

[b] C II 158 line was observed twice. (1) - first rangeSpec observation (2) - second deeper rangeSpec observation

where $J_1 = 3/2$ is the angular momentum quantum number of the upper level, g_N are the nuclear statistical weights for the two levels ($g_0 = 2$ & $g_1 = 4$), $E_1/k = 91.21$ K is the energy difference between the two levels, T_{ex} is the excitation temperature, and $Q(T_{ex})$ is the partition function, which here can be approximated in a two level system by

$$Q(T_{ex}) = g_0 + g_1 e^{-E1/kT_{ex}}. \tag{5.3}$$

With only one gas line, we cannot measure the excitation temperature. However, we can derive a lower limit on the column density. Figure 5.2 shows the dependence of the column density on excitation temperature. From 1 to 300 K, we find a lower limit on the C II column density of $N_{CII} > 2.5 \times 10^{11}$ cm^{-2}. This value is similar to the column density of Na I calculated by Redfield (2007) ($N_{NaI} = 2.5 \times 10^{11}$ cm^{-2}).

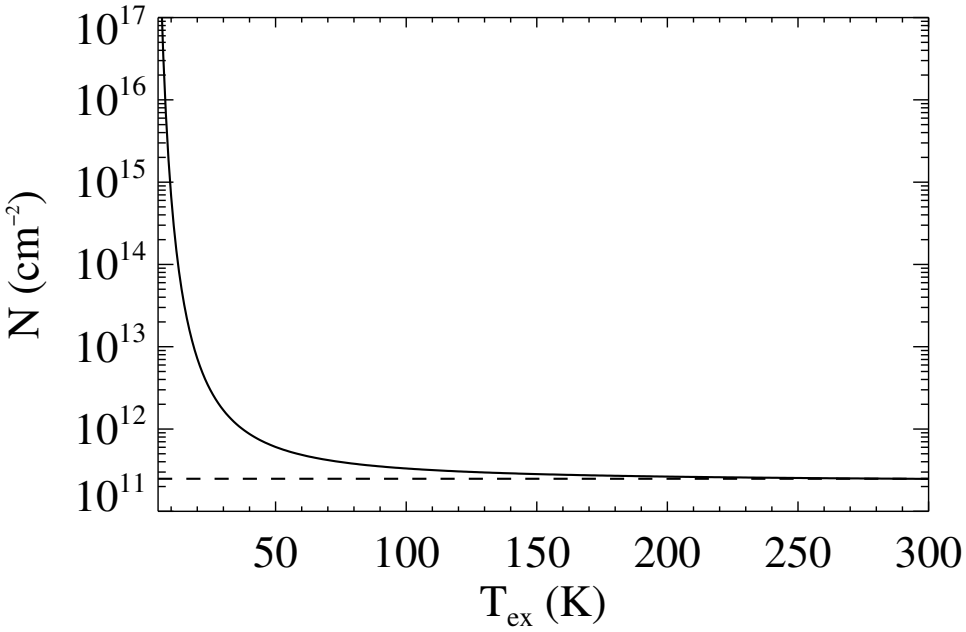

Figure 5.2: Column density of C II as a function of excitation temperature (solid line). The dashed line shows the lower limit on the column density ($N = 2.5 \times 10^{-11}$ cm^{-2}) for excitation temperatures < 300 K.

5.4 SED Modeling

5.4.1 SED data

In addition to the *Herschel* data, we collected archive data for use in our SED modeling (see Tab. 5.3). To constrain the stellar photosphere, we used *Hipparcos* B & V (Perryman and ESA 1997), *2MASS* J, H, & K_s (Cutri et al. 2003), and *WISE* bands 1 & 2 (Wright et al. 2010). For the infrared excess, we used *IRAS* 25 & 60 μm (Moór et al. 2006), *WISE* bands 3 & 4 (Wright et al. 2010), *Spitzer* MIPS 24 μm (Maness et al. 2008), and *Spitzer* IRS data taken from the enhanced data product in the *Spitzer* Heritage Archive.[3] We also included millimeter data from Meeus et al. (2012): the 1.2 mm flux from the MAMBO2 bolometer array on the

IRAM 30 m telescope and the 1.3 mm flux from the Sub-Millimeter Array (SMA). The uncertainties for these last two measurements (reported in Table 5.3) include 15% calibration uncertainties added in quadrature.

The HD32297 disk is also marginally resolved at mid-IR and millimeter wavelengths. We used the total flux from Gemini North Michelle imaging at 11.2 μm (Fitzgerald et al. 2007b), and Gemini South T-ReCS imaging at 11.7 & 18.3 μm (Moerchen et al. 2007). We used the SMA flux at 1.3 mm rather than the total flux from the CARMA 1.3 mm resolved image (Maness et al. 2008), because the unresolved data from the SMA has a smaller uncertainty. The photometric data used are listed in Table 5.3 and plotted in Figure 5.3.

We combined these data with our *Herschel* PACS and SPIRE photometry and the continuum values from the PACS spectroscopy. Our data points fill in a large gap in the SED from 60 to 500 μm (see Figure 5.3) and allow us to assess where the peak of the thermal emission is located.

Table 5.3: Additional data used in SED modeling

Wavelength (μm)	Flux & Uncertainty (Jy)	Instrument	Reference
0.438	1.952 ± 0.026	*Hipparcos* B	[1]
0.547	2.094 ± 0.023	*Hipparcos* V	[1]
1.235	1.342 ± 0.030	*2MASS* J	[2]
1.65	0.913 ± 0.044	*2MASS* H	[2]
2.16	0.611 ± 0.010	*2MASS* K_s	[2]
3.4	0.278 ± 0.010	*WISE* 1	[3]
4.6	0.150 ± 0.005	*WISE* 2	[3]
8.00	0.064 ± 0.002	*Spitzer* IRS	[4]
8.65	0.059 ± 0.003	*Spitzer* IRS	[4]
9.35	0.053 ± 0.003	*Spitzer* IRS	[4]
10.11	0.049 ± 0.002	*Spitzer* IRS	[4]

Continued on next page

[3] irsa.ipac.caltech.edu/applications/Spitzer/SHA/

Table 5.3 continued

Wavelength (μm)	Flux & Uncertainty (Jy)	Instrument	Reference
10.93	0.049 ± 0.002	*Spitzer* IRS	[4]
11.2	0.050 ± 0.002	Gemini-N/Michelle	[5]
11.56	0.053 ± 0.005	*WISE* 3	[3]
11.7	0.053 ± 0.005	Gemini-S/T-ReCS	[6]
11.81	0.050 ± 0.002	*Spitzer* IRS	[4]
12.77	0.052 ± 0.001	*Spitzer* IRS	[4]
13.80	0.054 ± 0.003	*Spitzer* IRS	[4]
14.92	0.063 ± 0.002	*Spitzer* IRS	[4]
16.13	0.072 ± 0.003	*Spitzer* IRS	[4]
17.44	0.087 ± 0.004	*Spitzer* IRS	[4]
18.3	0.090 ± 0.014	Gemini-S/T-ReCS	[6]
18.85	0.110 ± 0.004	*Spitzer* IRS	[4]
20.38	0.142 ± 0.009	*Spitzer* IRS	[4]
22	0.193 ± 0.020	*WISE* 4	[3]
22.03	0.189 ± 0.009	*Spitzer* IRS	[4]
23.68	0.210 ± 0.010	*Spitzer* MIPS	[7]
23.81	0.239 ± 0.011	*Spitzer* IRS	[4]
25	0.256 ± 0.041	*IRAS* 25	[8]
25.74	0.296 ± 0.010	*Spitzer* IRS	[4]
27.83	0.375 ± 0.011	*Spitzer* IRS	[4]
30.08	0.444 ± 0.011	*Spitzer* IRS	[4]
32.51	0.563 ± 0.014	*Spitzer* IRS	[4]
35.15	0.668 ± 0.018	*Spitzer* IRS	[4]
60	1.140 ± 0.070	*IRAS* 60	[8]
1200	0.00314 ± 0.00095	IRAM 30m/MAMBO2	[9]
1300	0.00310 ± 0.00087	SMA	[9]

Color corrected flux with 1σ error bars used in the SED modeling.

References - [1]: Høg et al. (2000), [2]: Cutri et al. (2003),
[3]: Wright et al. (2010), [4]: Spitzer Heritage Archive,
[5]: Fitzgerald et al. (2007b), [6]: Moerchen et al. (2007),
[7]: Maness et al. (2008), [8]: Moór et al. (2006), [9]: Meeus et al. (2012)

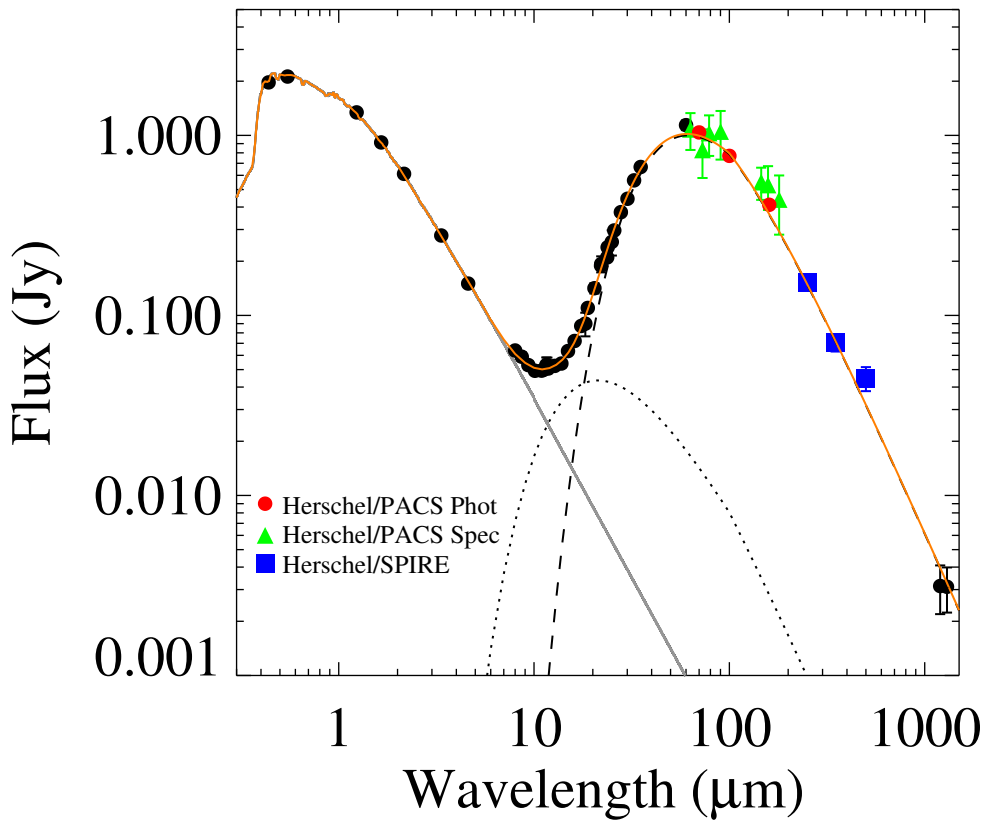

Figure 5.3: Spectral energy distribution of HD32297 with simple blackbody fits. The gray line is the best-fitting stellar photosphere model with $T = 7750$ K (see Section 5.4.2). The data points that were taken from the literature and listed in Table 5.3 are plotted here as well as the new PACS and SPIRE data given in Tables 5.1 and 5.2. A two temperature modified blackbody model is over plotted (orange solid line), with the individual components also shown - a warmer blackbody with $T = 240$ K (dotted line) and a colder blackbody with $T = 83$ K (dashed line) as described in Section 5.4.4.

5.4.2 Stellar Properties

We started our analysis by fitting for the stellar parameters of HD32297. We used the *Hipparcos* B & V, *2MASS* J, H, & K_s, and *WISE* bands 1 & 2 to constrain the stellar models. We fit the stellar data with ATLAS9 stellar photosphere models (Castelli and Kurucz 2004). The spectral type of HD32297 is usually quoted as either an A0 (Torres et al. 2006) or an A5 (Fitzgerald et al. 2007b, and references

therein). Our best fitting model with an A0V spectral type ($T = 9750$ K) is too hot and does not match the data well.

We therefore tried both adding interstellar extinction with a Fitzpatrick (1999) extinction law and varying the stellar photosphere temperature. Unfortunately, these two parameters are degenerate. Fixing the temperature to $T = 9750$ K, the best fitting model has an extinction of $A_V = 0.63 \pm 0.02$ mag, a reduced chi-squared value of $\chi^2_\nu = 0.59$, and a bolometric luminosity of $L = 11.9\,L_\odot$. The best fitting model with extinction and temperature as free parameters has $T = 8000$ K, $A_V = 0.161 \pm 0.026$ mag, and $\chi^2_\nu = 0.55$.

To break the degeneracy, we added UV continuum values at 0.26 and 0.31 μm from unpublished STIS spectra (Redfield et al. 2012, in preparation). The best model is one with no extinction, a temperature of $T = 7750$ K, and a luminosity of $L = 5.6\,L_\odot$ (Fig. 5.3). This is more consistent with an A7 spectral type than an A0. This hint in the UV spectra that the star has a cooler stellar temperature than was previously thought will be thoroughly analyzed in a future paper (Redfield et al. 2012, in preparation). We note that this lower temperature is the same used by Debes et al. (2009) and close to the temperature used by Fitzgerald et al. (2007b), both of whom note that the star appears to be under-luminous for a main sequence star of this temperature. Some reasons proposed are errors in the Hipparcos distance (Debes et al. 2009) or a sub-solar metallicity (Meeus et al. 2012).

The assumed stellar luminosity does not have a significant effect on the SED in the far-IR where the stellar contribution is negligible. However, the assumed temperature of the star is important for calculating the equilibrium temperature of the dust. An error in the stellar temperature will translate into an error in the dust temperature, which will affect the calculated grain properties, such as minimum grain size.

5.4.3 Surface Density Profile

The HD32297 disk has been well resolved in scattered light with HST NICMOS at 1.1 μm (Schneider et al. 2005), 1.6 μm, 2.05 μm (Debes et al. 2009), and K_s band ($\lambda = 2.16\,\mu$m) from the ground with Keck/NIRC2 (Currie et al. 2012), as well as H ($\lambda = 1.65\,\mu$m) and K_s bands with VLT/NACO (Boccaletti et al. 2012). These observations block out the central star with a coronagraph, and consequently obscure the inner portions of the disk as well.

The resolved images place strong geometrical constraints on the disk outside of $\sim$ 65 AU. Currie et al. (2012) and Boccaletti et al. (2012) have both recently published models of the disk based on their near-IR ground based imaging using ADI. Boccaletti et al. (2012) warn that images processed using ADI and/or the Locally Optimized Combination of Images (LOCI) are subject to self-subtraction and other artifacts (also see Milli et al. 2012). Therefore, a direct inversion of the surface brightness profile in the manner of Augereau and Beust (2006) is not practical here. For this reason, we rely on the disk modeling that takes into account the ADI and LOCI processing.

The models of Currie et al. (2012) and Boccaletti et al. (2012) agree quite well. Both see a break in the surface brightness profiles around 1″ ($\sim$ 110 AU), which was also seen by Debes et al. (2009) in the NICMOS images. Both measure an inclination of 88°, i.e. 2° from edge-on. This is notably different from the inclination measured by Schneider et al. (2005) of 79.5°.

Where the models disagree is in the anisotropic scattering factor, g. Currie et al. (2012) use a two-component Henyey-Greenstein phase function with a highly forward scattering component ($g_1 = 0.96$) and a backscattering component ($g_2 = -0.1$), while Boccaletti et al. (2012) use only a one-component phase function with a best

fit value of $g = 0.5$. They discuss how higher values of g would make the disk too bright in the inner regions. Currie et al. (2012) also note this, but they dismiss it due to the large uncertainties in surface brightness close to the star.

We chose to use the models of Boccaletti et al. (2012) because they used the GRaTer code (Augereau et al. 1999; Lebreton et al. 2012) to model the disk images, which we also used to model the SED (see Section 5.4.5). The best-fit model of Boccaletti et al. (2012) to the K_s band image has a mid-plane density of the form

$$n(r) = n_0\sqrt{2}\left(\left(\frac{r}{110\mathrm{AU}}\right)^{10} + \left(\frac{r}{110\mathrm{AU}}\right)^{-4}\right)^{-1/2}. \tag{5.4}$$

We assumed the disk is geometrically thin because the SED modeling cannot distinguish between a vertical offset from the midplane and a radial change in distance. We chose to use the Boccaletti et al. (2012) model of the K_s band image rather than the H band image because the K_s band data are of better quality.

5.4.4 Dust Disk Modeling Strategy

We started our modeling by fitting the infrared excess with a single temperature modified blackbody, i.e. a blackbody model with an opacity at longer wavelengths of the form ν^β. The exact form of the modified blackbody we used is $F_\nu \propto \tau_\nu B_\nu$ for $\lambda \geq \lambda_0$, and $F_\nu \propto B_\nu$ for $\lambda < \lambda_0$, where B_ν is a simple blackbody and τ is the optical depth, which takes the form $\tau \propto (\nu/\nu_0)^\beta \propto (\lambda/\lambda_0)^{-\beta}$. Here we have fixed $\beta = 1$ and $\lambda_0 = 100\,\mu$m, based on typical values for debris disks (Dent et al. 2000; Williams and Andrews 2006). The best fit was determined through χ^2 minimization using `MPFIT` (Markwardt 2009). The best fitting model has a temperature of $T = 80$ K. However, this model significantly underestimates the flux at mid-IR wavelengths.

To account for the missing IR flux in our model, we added a second modified blackbody. The best fitting model has two distinct components with temperatures

of $T = 83$ K and $T = 240$ K (see Fig. 5.3). The addition of the second blackbody much improves the fit over the single temperature model, suggesting there is a second inner disk. The inner component is too hot, and therefore too close to the star, to be part of the outer ring imaged in scattered light.

Spatial information is important for breaking degeneracies in SED modeling. Scattered light images of HD32297 restrict the models of the outer disk geometry. Unfortunately, no constraining images exist for the inner disk, which is too close to the star to be imaged. Therefore, we divided the dust disk modeling into two steps: first fitting the outer disk with a more complex model, then fitting the poorly constrained inner disk with a simpler one.

5.4.5 Outer disk modeling with GRaTer

For the outer disk, we limited the data to those with wavelengths larger than 25 μm. This cutoff was chosen as the point where the inner disk contributes less than 50% to the total two component blackbody model. With the *Herschel* observations, we have enough data points with wavelengths greater than 25 μm to constrain the outer disk properties.

We use the GRaTer code (Augereau et al. 1999; Lebreton et al. 2012) to fit the SED of HD32297. GRaTer is dust disk modeling code specifically designed for optically thin debris disks, which can compute large grids of models with different grain sizes and composition and use a density profile to describe the disk geometry. The code computes both the scattered light emission and the thermal emission from the grains in equilibrium with the radiation field of the central star. We constrained the spatial distribution of the dust grains by using the models of the resolved scattered light images from Boccaletti et al. (2012). We confined the grains in our SED model to be located in a ring defined by Equation 5.4. The overall

abundance was left as a free parameter that scales the radial profile to match the SED.

With the disk geometry fixed, we focused our modeling on the grain sizes and composition, which we assumed to be the same throughout the disk. GRaTer calculates Mie scattering and absorption coefficients for a large range of grain compositions. Specifically, we explored combinations of materials consisting of astrosilicate (Draine 2003), amorphous carbon (Zubko et al. 1996), amorphous water ice (Li and Greenberg 1998) and porosity. The volume ratios of the materials explored are listed in Table 5.4. If any material reaches its sublimation temperature, it is replaced by vacuum. For most of the outer disk, the temperatures are too cold for this to happen.

Table 5.4: Parameters explored in GRATER models

Parameter	range	# of values	distribution
κ	-5 to -2.5	20	linear
a_{min}	0.01 to 100 μm	77	logarithmic
Carbon Volume	0 to 100%	21	linear
Ice Volume	0 to 90%	10	linear
Porosity	0 to 95%	20	linear

For the grain sizes, we explored a range of minimum grain sizes from $a_{min} = 0.01\,\mu$m to $a_{min} = 100\,\mu$m and grain size distributions with a power-law of the form $n(a)da \propto a^{\kappa}da$, with κ ranging from -5 to -2.5. The maximum grain size is kept fixed at $a_{max} = 7.8$ mm, which is large enough compared to the longest wavelength of the data ($\lambda = 1.3\,$mm). However, we only considered grains with sizes smaller than 1 mm in calculating the dust mass (given in Table 5.5), to be consistent with other results from GASPS and other *Herschel* Key Programmes.

We modeled the disk using six different compositions with varying levels of complexity. The simplest model used only astrosilicate grains. The next three models

used silicates mixed with only one other grain type: carbonaceous material, water ice, or increased porosity. For the three and four material combinations, we kept the silicate to carbon volume ratio fixed at 1:2. This is the ratio expected from cosmic abundances and is similar to the ratio observed in comet Halley dust (Greenberg 1998).

The grains are assumed to be porous aggregates of silicate, carbon and water ice. The scattering and absorption coefficients for the aggregates are calculated using the Bruggeman mixing rule (Bohren and Huffman 1983). Silicate and carbon are mixed first, then the Si+C mixture is mixed with water ice, and finally it is all mixed with vacuum to simulate porous grains. For more details see Lebreton et al. (2012) and Augereau et al. (1999).

5.4.6 Inner disk modeling

The mid-IR flux can only be explained with a warmer component than is seen in the scattered light images. We first tried to model the disk with the geometry constrained only by the coronagraphic scattered light images of the disk. We found that the thermal emission from the grains seen in the scattered light images was not enough to reproduce the mid-IR flux in the SED. The data in this region come from several sources, and all are consistent (*Spitzer* IRS, *WISE* (Wright et al. 2010), and Gemini N (Fitzgerald et al. 2007b) and S (Moerchen et al. 2007)). Therefore, we added a warmer component to fit the mid-IR data.

We chose to model the warm component as an inner disk inside the radius masked by coronagraphs in the images. The inner disk is less constrained than the outer disk since the inner disk lacks geometrical information and the $L_{\rm IR}/L_*$ of the inner disk is an order of magnitude lower than the outer disk (6.9×10^{-4} vs. 5.6×10^{-3}; see Fig. 5.4). This leads to a degeneracy between two of the dust disk modeling

parameters: the minimum radius and the minimum grain size. The degeneracy exists because decreasing both the parameters has the same effect of increasing the grain temperature. Changing the minimum grain size also affects the amount of flux emitted from a given grain, but this can be mimicked by varying the total number of grains. With a weakly-emitting disk, the separate effects can be difficult to disentangle.

For each outer disk model with a different grain composition, we subtracted it from the SED and fit our inner disk model to the residuals. Since we lack constraining spatial information for the inner disk, we needed to use a simpler model. We used the model described in Donaldson et al. (2012), which calculates only the thermal emission from astrosilicate grains in radiative equilibrium with the central star. We fixed the outer radius to 5 AU since all values above this had no significant effect on the SED. We assumed the disk has a surface density profile of the form $\Sigma(r) \propto r^{-1.5}$, consistent with collision-dominated disks (Krivov et al. 2006; Strubbe and Chiang 2006). We also fixed the grain size distribution throughout the disk to a Dohnanyi (1969) power-law ($n(a)da \propto a^{-3.5}da$) with a maximum grain size of 1 mm. The only free parameters were the inner radius, the minimum grain size, and the dust mass.

We used the inner disk model to fit the residuals after subtraction of the outer disk model, then combined this model with those of the outer disk and the star. We calculated reduced χ^2 values (χ^2_ν) using all 43 data points listed in Tables 5.1, 5.2, and 5.3 greater than 8 μm and the number of degrees of freedom (ν) listed in Table 5.5. We calculated the errors on the parameters from the 1σ confidence intervals in the χ^2 distribution.

A similar modeling approach was recently used by Ertel et al. (2011) for HD107146. They fit the disk SED using the scattered light images to constrain the geometry,

and they also found an overabundance of *Spitzer* IRS mid-IR flux in their best fit models. They tried modeling the excess in two ways: first by adding a small grain population within the imaged disk, and second by adding an inner disk. The small grain model was unable to reproduce the mid-IR flux in HD107146; the inner disk model was needed to match the *Spitzer* IRS spectrum.

5.4.7 Results

We found the best fitting outer disk model was the 4 material composition of silicates, carbon, and water ice in a 1:2:3 ratio with a high porosity of 90% (final row of Table 5.5, Fig. 5.4). The outer disk grains have a minimum size of $a_{min} = 2.1\,\mu$m, with a grain size distribution power-law index of $\kappa = -3.3$. The best fitting total SED model also includes an inner disk from 1.1 AU with an unconstrained outer edge. The inner disk was fit with astrosilicate grains with a Dohnanyi (1969) size distribution ($\kappa = -3.5$). The minimum grain size in the inner disk for the best fitting model is $a_{min} = 2.2\,\mu$m, similar to the outer disk grains. Other grain models tested appear in Table 5.5. We determined the uncertainties given in Table 5.5 from the 1σ confidence intervals in the χ^2 distribution after fixing the other free parameters to the value that gives the smallest χ^2 value.

The 4 material composition model has the best reduced χ^2 value of the tested compositions ($\chi^2_\nu = 1.59$, $\nu = 34$). Of the 2 material composition models, astrosilicate + carbon and astrosilicate + porosity are the best fitting ($\chi^2_\nu = 4.27$ and $\chi^2_\nu = 4.42$, $\nu = 35$), but the model is much improved when all 3 materials are added together ($\chi^2_\nu = 3.60$, $\nu = 35$). The addition of ice makes a dramatic improvement in the fit from the 3 material composition to the 4 material composition. The minimum grain size in the inner disk models decreases with each improvement on the outer disk model, moving closer to the expected blowout size of $1\,\mu$m. This is likely

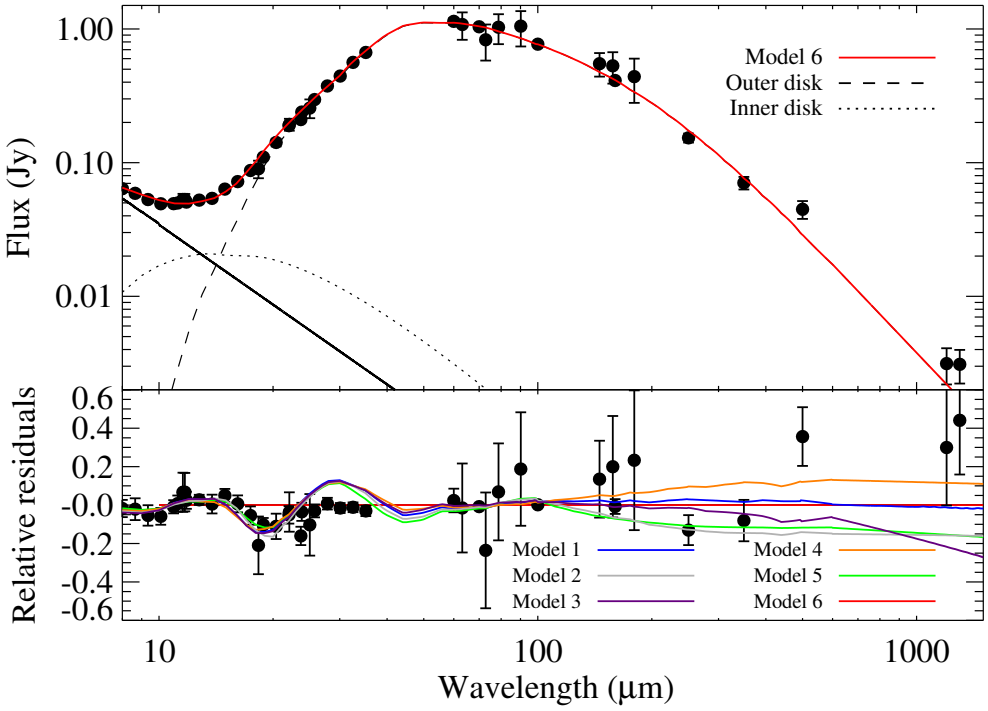

Figure 5.4: Top: Spectral energy distribution for the best-fitting total model given in Table 5.5 (Model 6). The black solid line is the fit to the stellar photosphere, the dotted and dashed lines show the inner and outer disk models respectively, and the red solid line represents the combined model of photosphere + inner disk + outer disk. The data plotted here are listed in Tables 5.1, 5.2, and 5.3. Bottom: The relative residuals of the best-fitting model shown above. The relative residuals are of the form (data - model#6)/data. Also plotted for comparison are the relative residuals of the other five models given in Table 5.5, e.g. (model#1 - model#6)/model#1. The red line marks the zero point, or the residual for model 6.

because the two material models fail to fit all the mid-IR flux coming from the outer ring, and the inner disk models have to compensate.

The blowout size given above is calculated for the inner disk only, where the assumed grain composition is astrosilicate. Given a density of $\rho = 3.5$ g cm^{-3}, the blowout size for spherical grains on circular orbits (in microns) is $a_{blow} = 1.15 L_*/(M_* \rho)$, with L_* and M_* in solar units and ρ in g cm^{-3}. For astrosilicate grains around HD32297 ($M_* = 1.84\,M_\odot$, $L_* = 5.3\,L_\odot$), the blowout size is $a_{blow} = 1\,\mu$m.

Table 5.5: Results of SED modeling

outer disk	volume	outer disk		inner disk		total disk		
model[a]	ratios	a_{min}	κ	r_{min}	a_{min}	χ^2_ν	ν	Dust Mass[b]
Model 1	–	$1.4 \pm 0.1\,\mu$m	-3.8 ± 0.2	3.3 ± 0.3 AU	$200 \pm 120\,\mu$m	4.58	36	0.32 ± 0.05 $M_\oplus$
Model 2	1:4	$2.1 \pm 0.4\,\mu$m	-4.3 ± 0.3	3.5 ± 0.5 AU	$31.6 \pm 26\,\mu$m	4.27	35	0.11 ± 0.02 $M_\oplus$
Model 3	11:9	$0.3 \pm 0.1\,\mu$m	-3.5 ± 0.2	3.6 ± 0.4 AU	$31.6 \pm 27\,\mu$m	4.42	35	0.26 ± 0.05 $M_\oplus$
Model 4	4:1	$1.0 \pm 0.1\,\mu$m	-3.7 ± 0.2	3.2 ± 0.3 AU	$39.8 \pm 22\,\mu$m	4.45	35	0.34 ± 0.12 $M_\oplus$
Model 5	1:2:12	$3.4 \pm 0.1\,\mu$m	-3.8 ± 0.2	2.8 ± 0.3 AU	$25.1 \pm 24\,\mu$m	3.60	35	0.08 ± 0.01 $M_\oplus$
Model 6	1:2:3:54	$2.1 \pm 0.3\,\mu$m	-3.3 ± 0.2	1.1 ± 0.2 AU	$2.2 \pm 0.9\,\mu$m	1.59	34	0.10 ± 0.01 $M_\oplus$

[a] Model 1: Astrosilicate (AS), Model 2: Astrosilicate + Carbon (C), Model 3: Astrosilicate + Vacuum (P), Model 4: Astrosilicate + Water Ice (I), Model 5: Astrosilicate+ Carbon + Vacuum, Model 6: Astrosilicate + Carbon + Water Ice + Vacuum

[b] The dust mass is calculated for dust grains smaller than 1 mm only. The total dust mass is dominated by the outer disk.

For the outer disk, the grains are highly porous and likely have a fractal structure. The calculation of the blowout size depends on the surface area of the grains; this is non-trivial for fractal grains. The above equation is for spherical grains only; we do not calculate the blowout size for the outer disk because it is not very realistic in this case. For more about this problem, see the discussion in Lebreton et al. (2012).

5.5 Discussion

The composition of dust grains in young debris disks is a key piece in understanding the last stages of terrestrial planet formation. A handful of debris disks, including β Pictoris and HD172555 (Lisse et al. 2009; Telesco and Knacke 1991), have solid state features in the mid-IR that indicate dust grain composition. But most debris disks, including HD32297, lack these features, and therefore, modeling of the full SED is needed to constrain the grain composition.

Unfortunately, the presence of an unresolved warm component to the HD32297 system complicates the modeling. Without resolved imaging of the inner regions, it is impossible to know the distribution of the warm component and how much mid-IR flux is coming from the outer disk versus the inner disk. The models of the inner disk depend strongly on the model chosen for the outer disk. Additionally, since there are no geometrical constraints on the inner disk, the results depend upon the distribution we assumed.

Another concern is the age of the system. Kalas (2005) states the age as 30 Myr based on an uncertain association with either the Gould belt or Taurus Aurigae. The dust mass of HD32297 (see Table 5.5) is high for a debris disk. The mass is comparable to the 8 Myr-old disk HR4796A, which suggests HD32297 may be younger than 30 Myr. HD32297 is also one of the oldest debris disks with gas

detected, another indication it may be a younger system. But the system likely not much younger than the given age of 30 Myr. There are several indicators that HD32297 is a main sequence star with an optically thin debris disk, including 1) the lack of optical extinction, 2) the low fractional dust luminosity ($L_{\rm IR}/L_* \sim 10^{-3}$) and 3) a lack of solid state features in the mid-IR indicating no small grains are present.

5.5.1 Cometary Dust?

The best fitting model to the outer disk includes grains that are highly porous and icy. High grain porosity is seen in interplanetary dust particles collected with Stardust (Brownlee et al. 2006) and in the ejecta from comet Temple 1 created by Deep Impact (A'Hearn 2008). Greenberg and Hage (1990) showed that comet Halley's spectrum could only be fit by highly porous grains with a porosity between 93 and 97.5%. Li and Greenberg (1998) modeled the β Pictoris disk with similar composition dust. They assumed the β Pic dust was cometary in origin and rejected models of compact grains with porosity lower than 90%. Polarized light observations of AU Mic also indicate that disk is dominated by highly porous grains with porosity of 91-94% (Fitzgerald et al. 2007a; Graham et al. 2007). The highly porous, icy dust around HD32297 is similar to β Pic and Solar System comets.

Dust in the outer ring of HD32297 therefore appears consistent with cometary dust particles. The ring is centered around $\sim$ 110 AU, far from the star where ices should be prevalent. If planetesimal collisions produce the dust, this indicates that comet-like bodies dominate the planetesimal population in the outer disk.

A large population of comets in the outer disk could deliver water to terrestrial planets. A significant fraction of Earth's water likely came from Kuiper Belt comets (Morbidelli et al. 2000). At an age of 30 Myr, HD32297 could still be forming terrestrial planets (Kenyon and Bromley 2006). Comets scattered into the inner

regions of the disk could deliver water to forming terrestrial planets in the habitable zone.

5.5.2 Grain Porosity and ISM interaction

The scattered light images of HD32297, as well as those of the edge-on disks HD15115 and HD61005, have asymmetric features that may be due to interaction with ISM as the systems move with respect to their surroundings. The short wavelength of images of HD32297 (Debes et al. 2009; Schneider et al. 2005) and HD61005 (Buenzli et al. 2010; Hines et al. 2007; Maness et al. 2009) show a "swept-out" feature, while HD15115 has a strong east-west asymmetry (Debes et al. 2008; Kalas et al. 2007; Rodigas et al. 2012). The ISM interaction model of Debes et al. (2009) reproduces the features of all three disks.

The ISM affects the disk grains through gas drag and/or grain-grain collision as the disk moves through a dense clump in the ISM. Unbound or weakly bound grains are swept back as they interact with the ISM. The most affected grains are typically thought to be the small grains that are nearly unbound due to the effect of radiation pressure. But larger grains with a higher porosity are also strongly affected by radiation pressure, and therefore may also be susceptible to being blown back through ISM ram pressure. The high porosity of the outer disk grains may be one factor that helps explain why this disk has such a strong ISM interaction feature. Stellar motion and environment must also play a role, since other disks modeled with a high grain porosity, such as β Pic, do not have the same feature.

5.5.3 Gas in HD32297

HD32297 is one of only a handful of debris disks that have gas detections. Redfield (2007) found Na I in absorption, aided by the disk's nearly edge-on orientation. The detection of [C II] emission from HD32297 is the fourth detection of atomic gas from a debris disk with *Herschel*, though it is weaker than the lines seen from β Pictoris, HD172555, and 49 Ceti (Brandeker et al. 2012; Riviere-Marichalar et al. 2012; Roberge et al. 2012). It is also unusual that [C II] was detected while [O I] was not. The only other debris disk with gas where this is true is 49 Ceti (Roberge et al. 2012).

Given relatively advanced age of HD32297 ($\sim$ 30 Myr; Kalas 2005) and the typical protoplanetary disk lifetime ($<$ 10 Myr; Williams and Cieza 2011), the HD32297 gas is unlikely to be primordial. The lack of sub-mm CO emission suggests a gas-to-dust ratio lower than is seen in younger protoplanetary disks (e.g. Zuckerman et al. 1995). Furthermore, the disk dust has a relatively low abundance, and shares other characteristics with debris dust (no detectable line-of-sight extinction, a lack of mid-IR solid state features from small grains). With little dust and little gas, the disk should be optically thin to stellar and interstellar dissociating UV photons and molecular gas lifetimes should be short. However, at this time, it is difficult to prove that the observed C II is not simply the tenuous end product of dissociated primordial gas, although the lack of O I emission would be puzzling in this scenario. An alternative scenario would be gas production by secondary mechanisms such as planetesimal collisions or outgassing from comet-like bodies.

To calculate the total amount of carbon gas in the disk, we assume the disk is similar to the well studied β Pictoris debris disk. Several gas species have been observed in β Pic, and their abundance ratios are summarized in Roberge et al.

(2006). The ratio of neutral and singly ionized carbon in β Pic is C I/C II $\sim$ 1. Assuming the same ionization fraction, the total column density of carbon in HD32297 is $N_C \gtrsim 5 \times 10^{11}$ cm^{-2}. The ionization fraction of sodium in β Pic is $\geq$ 0.999 (Roberge et al. 2006). This implies a total sodium column density of $N_{Na} > 2.5 \times 10^{14}$ cm^{-2}, 500 times larger than the lower limit on carbon.

By assuming solar abundances, we naively expect there to be about two orders of magnitude more carbon than sodium. This would only be the case if the excitation temperature is less than 10 K. We consider three possible explanations. The first possibility is that the excitation temperature really is less than 10 K; this would be several times lower than the excitation temperature measured in β Pic (Roberge et al. 2006). Second, the disk does not have solar abundances as assumed, but a different ratio, meaning less carbon or more sodium. Yet, we expect the opposite to be true. Carbon does not feel as strong a radiation pressure as sodium because unlike sodium, carbon does not have strong absorption lines in the optical, but in the far-UV where the star is much fainter (Roberge et al. 2006). Hence, we expect there to be more carbon than sodium relative to solar abundances, making the problem worse. The last possibility is that ISM sodium absorption lines along the line of sight contaminated the HD32297 sodium measurements, boosting the signal. We deem this to be the most likely scenario.

We can estimate a lower limit on the total gas mass in HD32297 by making a few assumptions. We start by modifying Equation 5.1 to get a C II mass lower limit of $M_{CII} > 1.7 \times 10^{-4}$ $M_\oplus$. By making the same assumptions as above (C I/C II$\sim$ 1, solar abundances), the total gas mass is $\sim$ 700 times the C II mass, giving a lower limit of $M > 0.1$ $M_\oplus$.

Gas in disks can affect the distribution of dust. Gas orbits the star at sub-keplerian speeds due to either to a gas pressure gradient or radiation pressure. The

dust grains, if large enough not to experience strong radiation pressure, orbit at keplerian speeds, and therefore feel a headwind that causes them to spiral inwards. This mechanism could be a way of transporting dust grains from the outer disk to the inner disk. Krivov et al. (2009) investigated how 0.3-30 $M_{\oplus}$ of gas would affect HD32297's radial surface brightness profiles, and found the gas has little effect on the disk outside 110 AU. The distribution of the inner disk, however, could be affected by small amounts of gas. Since we have no limiting spatial information on the gas in HD32297, we cannot determine if the gas significantly affects the distribution of the dust in the inner disk. This scenario will be further discussed in Section 5.5.4.

5.5.4 Inner Disk

Our best model for the inner disk of HD32297 starts at $\sim$ 1 AU. The outer edge of the inner disk is unconstrained, but we find a lower limit on the outer edge of $\sim$ 5 AU. We assumed the inner disk grains are astrosilicate grains, and our best fitting model has a minimum grain size of 2 μm. The fit to the inner disk depends strongly on the fit to the outer disk. Although the results of the grain size in the inner disk varied by about 2 orders of magnitude (2.2 μm - 200 μm) the inner radius only varied by a factor of a few (1.1 - 3.6 AU). This range places the inner disk near the habitable zone of the star. A simple $\sqrt{L_*}$ scaling of the Solar System's habitable zone ($\sim$ 0.7 - 1.5 AU) places the HD32297 habitable zone at $\sim 1.7 - 3.5$ AU.

The presence of dust in the habitable zone does not rule out terrestrial planets in this region. Low mass planets may not have had time to clear this region of planetesimals. In fact, some of the dust may be trapped in resonance with a planet (Stark and Kuchner 2008; Wyatt 2003).

Since the inner disk has not been resolved, we do not know how the dust is distributed. The dust distribution in the inner region depends on the location of

the parent material and dust transportation. We consider two scenarios for the origin of the inner dust disk: one where the inner dust disk is fed by dust transported from the outer disk through gas drag, and the second where there is another planetesimal belt closer to the star.

In the first scenario, the presence of gas might affect the dust distribution, such that it is no longer collision-dominated. The entire inner disk may be composed of material that has leaked inwards from the outer disk due to gas drag. If this were the case, we would expect a smooth surface density distribution from the outer disk to the inner disk. At first glance, this might seem inconsistent with an SED that is well fit by a two temperature blackbody model. This model is most easily interpreted as two rings with a gap in between. However, a gap is not needed to produce such an SED. The region closest to the star will be much warmer and thus brighter than the dust in the intermediate region. The signature of dust in the intermediate region would be hard to detect in the SED alone. Reidemeister et al. (2011) have shown that in the Eps Eri disk, even a bimodal SED curve can be reproduced with models that assume transport of dust from the outer disk (in that case, caused by stellar winds rather than gas), and thus a continuous distribution of dust from the outer to the inner region. Since the mass of the inner disk that could account for the observed warm emission is $M_{inner} \gtrsim 6 \times 10^{-9}$ $M_{\oplus}$, and assuming the radius of the inner disk of ~ 1 AU, such a continuous distribution within ~ 100 AU would imply roughly 6×10^{-5} $M_{\oplus}$ worth of dust. For gas drag to work, the gas mass should exceed the dust mass. Therefore, 0.1 $M_{\oplus}$ of gas, which is a lower limit that we placed from the [C II] observations in Sec. 5.4, would be sufficient for the transport. However, without images of the inner ~ 50 AU of the disk, we cannot confirm gas drag as the origin of the inner dust.

In our second scenario for the origin of the inner dust, there could be another

belt of planetesimals closer to the star, similar to the asteroid belt. Collisions between planetesimals, in this case, would produce the dust seen in the SED, just like in the outer belt. We made calculations with the model of Löhne et al. (2008) and a velocity-dependent critical fragmentation energy from Stewart and Leinhardt (2009). They suggest that an asteroid belt of a sub-lunar mass at 1.1 AU in a 30 Myr-old system can easily sustain $10^{-7} M_{\oplus}$ to $10^{-8} M_{\oplus}$ worth of dust through a steady-state collisional cascade. This is more than the mass of the inner disk ($M \gtrsim 6 \times 10^{-9} M_{\oplus}$). Without spatial information on the inner disk, we cannot tell if the presence of warm dust is due to an asteroid belt or from material leaked inwards from the outer disk. In any case, the mass of the inner disk is significantly less than the outer disk; only its proximity to the central star makes it outshine the outer disk in the mid-IR.

5.6 Summary

We present new *Herschel* PACS and SPIRE photometry and spectroscopy of the edge-on debris disk around HD32297. Our main conclusions are the following:

1. We detected the disk at 13 wavelengths from 63 to 500 μm, filling in a gap in the SED in this region. The new data probe the peak of the thermal emission.

2. We detected a 3.7σ [C II] line at 158 μm, making HD32297 only the fourth debris disk with atomic gas detected with *Herschel*. We estimate a lower limit on column density of $N_{CII} > 2.5 \times 10^{11}$ cm^{-2}.

3. The stellar fit to the optical, near-IR and UV data suggest the star has a later spectral type than typically quoted, likely an A7.

4. Our SED models require a warm component to fit the large mid-IR excess.

This material is too warm to be part of the ring imaged in scattered light. The geometry of the warm component is unconstrained; we were able to fit it with a low density disk at radii greater than 1 AU.

5. The best fitting model to the outer disk includes grains consisting of silicates, carbonaceous material, water ice, and a highly porous structure. These grains are similar to cometary grains found in the Solar System.

Chapter 6

Spatially Resolved Spectroscopy of the HD32297 Debris Disk

6.1 Introduction

Debris disks are the remnants of the planet formation process. The dust we observe in these systems are the result of collisions between larger bodies, the planetesimals that have been or will be incorporated into planets.

The composition of the dust grains can tell us about the properties of their progenitors, the unseen planetesimal population. However, unlike in younger protoplanetary disks, most dust grain in debris disks have grown too large ($\gtrsim 1\,\mu$m) to emit solid state features in the mid-IR (Chen et al. 2006). The optical spectrum, on the other hand, is a more useful tool for characterizing the dust composition. Large silicate grains have a neutral spectrum in the optical, water ice and small silicate grains scatter preferentially in the blue, and organic material is expected to have a red signature.

We use a technique called "coronagraphic spectroscopy" – or spectra taken with

a long slit and an occulting bar blocking the central star – to characterize a debris disk's optical spectrum as a function of radius. Spectra from 2900 Å to 10500 Å are taken of the target disk and a diskless star with a similar spectral type for PSF subtraction, resulting in a two dimensional spectrum of the disk as a function of wavelength and position. This technique has only been used once before to characterize a disk for the face-on disk TW Hydrae (Roberge et al. 2005). This is a great tool for edge-on disks specifically because the slit can be aligned along the direction of the disk and most of the disk's scattered light will fall within the area covered by the slit.

We present spatially resolved spectroscopy data from an HST program to image a few edge-on debris disks, including HR 4796A, AU Microscopii, and HD32297 (GO 12512, PI: A. Weinberger). In this chapter, we focus on the data from HD32297, a 30 Myr-old disk around an A star 112 pc away. HD32297 has been imaged before in the near-IR (Boccaletti et al. 2012; Currie et al. 2012; Esposito et al. 2014; Rodigas et al. 2014; Schneider et al. 2005), but this will be the first characterization of the optical spectrum of the disk as a function of radius.

6.2 Observations

We obtained HST STIS G430L and G750L reflectance spectra of the HD32297 debris disk as part of a coronagraphic spectroscopy survey of bright edge-on debris disks (GO 12512, PI: A. Weinberger). These spectra cover the wavelength range $\sim 2900-10200$ Å. The 52×0.2F2 aperture was used - i.e. a $0.''2$ wide slit $52''$ long with a $0.''86$ long fiducial bar placed in front of the star. The length of the slit was placed parallel to the disk (PA= 46.1°). Acquisition peak up was used to accurately align the fiducial bar in the x-direction (wavelength-direction).

Similar observations were taken of HD32297 and a reference star (HIP22984) for Point Spread Function (PSF) subtraction, chosen to have a similar color as the target star. Unocculted spectra of the two stars were also taken to correct for color brightness differences between the target and the PSF stars. These observations were taken with the same slit ($52'' \times 0.''2$) but without the fiducial bar. Contemporaneous lamp flats were taken with the G750L grating for defringing (see Section 6.3.1). The final observations have a plate scale of 50.78 milli-arcsec pixel^{-1} in the spatial direction (y-direction) and a resolving power of ~ 800 at the central wavelength of each grating. Table 6.1 lists the details of the observations, including exposure time, aperture, and grating.

Table 6.1: Datalog for STIS observations

ID	target	Exp Time (s)	Aperture	Grating	Note
OBPZ03050	HD32297	25.0	52X0.2	G750L	CCDFLAT
OBPZ03010	HD32297	1.0	52X0.2	G430L	unocculted
OBPZ03020	HD32297	1756.0	52X0.2F2	G430L	fiducial
OBPZ03030	HD32297	2763.0	52X0.2F2	G430L	fiducial
OBPZ03040	HD32297	2.0	52X0.2	G750L	unocculted
OBPZ03060	HD32297	2614.0	52X0.2F2	G750L	fiducial
OBPZ03070	HD32297	2862.0	52X0.2F2	G750L	fiducial
OBPZ04040	HIP22984	25.0	52X0.2	G750L	CCDFLAT
OBPZ04010	HIP22984	1.0	52X0.2	G430L	unocculted
OBPZ04020	HIP22984	516.0	52X0.2F2	G430L	fiducial
OBPZ04030	HIP22984	1.8	52X0.2	G750L	unocculted
OBPZ04050	HIP22984	624.0	52X0.2F2	G750L	fiducial

6.3 Data Reduction

The observations were carried out in an unsupported mode, so we reduced the data ourselves, including defringing and wavelength calibration using the STSDAS IRAF CALSTIS tasks. We started with the `_crj` files; these are the intermediate calibrated files that have had basic data reduction performed (bias and dark subtraction, simple flat fielding, and cosmic ray rejection) but still have geometric distortions. We combined the multiple observations of HD32297, and updated the exposure time in the fits header.

6.3.1 Defringing the G750L data

The G750L data suffer from a fringing pattern caused by interference from internal reflections in the CCD at wavelengths longer than ~ 7000 Å. We performed defringing IRAF tasks on all the G750L data: the combined HD32297 fiducial, the PSF fiducial, and the unocculted observations of both stars. We started by using the `normspflat` task to make a flat field with the contemporaneous lamp flat observation. We then used the `mkfringeflat` task to shift and scale the fringes to match the data, then the `defringe` task to defringe the data with the scaled fringe flat.

6.3.2 Calibration

We used the `wavecal` task to wavelength calibrate all the data. The `x1d` task was used to extract one-dimensional spectra from the unocculted observations. The `x2d` task was used to calibrate the two-dimensional fiducial spectra. This task converts the flux into cgs units of erg s^{-1} cm^{-2} $Å^{-1}$ $arcsec^{-2}$ and corrects for geometrical distortion so that wavelength is linear along the x-axis and distance is linear along the y-axis.

6.3.3 Sigma Clipping

We sigma clipped the 2D spectra to remove hot and cold pixels. This is a procedure that flags pixels that are more than 3σ away from the average flux inside a region, and removes them, thereby decreasing the overall noise. We used a 5×200 pixel box – 5 pixels in y and 200 in x. We found this shape to be optimum for our data, because the spectrum does not change as much in x as it does in y. The box is just small enough in the x-direction that the real spectral features are not removed while bad pixels are removed.

We calculated the noise inside the box from the standard deviation. We removed pixels that were more than 3 times the noise above or below the average, and replaced them with the median value inside the box. The final 2D spectrum for the G750L data appears in the top panel of Figure 6.1.

6.3.4 PSF subtraction

The raw data of the 2D fiducial spectrum are a combination of both the signal from the disk and the starlight diffracting around the fiducial bar. This includes Airy patterns from the stellar PSF that move radially outwards with wavelength (see Fig. 6.1). In order to isolate the light from the disk alone, we must remove the diffracted light through subtraction of an observation of the diskless PSF reference star.

While the PSF reference star was chosen to be a close match in spectral type, the colors of the two stars are not exactly the same. We used the 1D spectra extracted from the unocculted observations to correct for color and brightness differences between the target and the PSF reference star, by dividing one spectrum by the other, providing an array giving the relative color of the two stars.

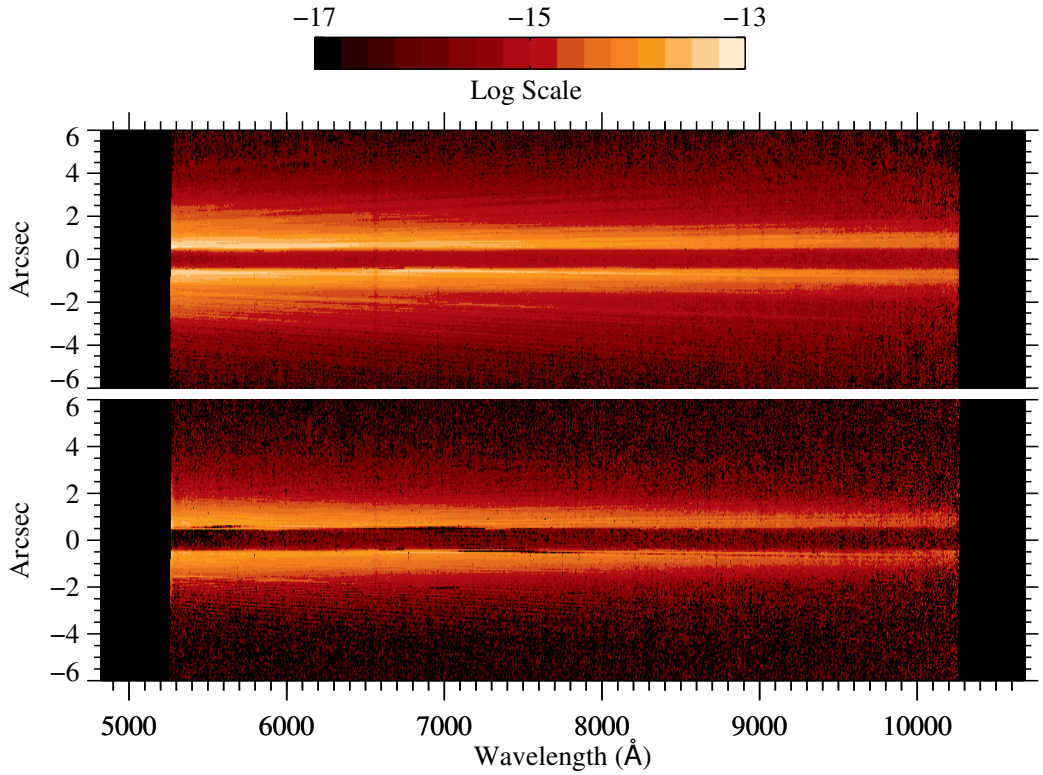

Figure 6.1: The HST STIS G750L two dimensional fiducial spectrum of HD32297 before PSF subtraction (top panel) and after PSF subtraction (bottom panel). The x-axis is the wavelength in angstroms and the y-axis the spatial direction of the slit in arcseconds, centered around the star. In the top panel, the airy rings of the PSF are visible as diagonal lines moving outwards from the center with wavelength. After the PSF subtraction, the airy rings are removed, but there are still some residual PSF subtraction artifacts visible, especially close to the fiducial bar.

We scaled the PSF reference 2D fiducial spectrum with the resulting factor, and subtracted the scaled fiducial PSF from the target fiducial spectrum. This procedure removes many PSF artifacts, such as the Airy pattern, but it is not perfect, and leaves some strong residuals close to the fiducial bar because the shape of the telescope PSF changed between the observations of the reference and target stars. The bottom panel of Figure 6.1 shows the PSF subtracted G750L fiducial data for HD32297.

6.4 Stellar Spectral Type

There has been some confusion in the literature about the spectral type of HD32297. The star is often quoted as an A0V from the Torres et al. (2006) SACY spectroscopic survey. The data for HD32297, however, comes from a smaller subset of data within that survey. The data used was only a 450 Å wide region around 6500 Å which is a much lower resolution than the rest of the survey.

Several debris disk papers noticed this spectral type does not fit the SED of HD32297 very well. Fitzgerald et al. (2007b), Debes et al. (2009), and Donaldson et al. (2013) fit the star with a cooler temperature than that of an A0 (7600 K and 7750 K). Fitzgerald et al. (2007b) could not tell with much certainty if the star an extincted A0, or a cooler star. Donaldson et al. (2013) used extra UV data points from Redfield et al. (in preparation) to help break the degeneracy between extinction and temperature to determine there was zero extinction and a temperature of 7750 K, consistent with the best fit from Fitzgerald et al. (2007b).

Our unocculted spectrum of HD32297 represents a good opportunity to finally put this debate to rest. The 1D point source spectrum is a R $\sim$ 800 spectrum from $\sim$ 3000 Å to 10000 Å. We fit the spectrum with ATLAS9 stellar photosphere models (Castelli and Kurucz 2004). We explored a grid of three parameters: temperature (7000 – 10000 K in 10 K steps), extinction (A_V from 0 to 0.5 in steps of 0.01), and log(g) (-3.0 to 5.0 in step of 0.5). We calculated the extinction using a Fitzpatrick (1999) extinction law.

The best fit model has $T = 7870 \pm 350$ K, log(g) $= 4.0 \pm 0.5$, $A_V = 0.0 \pm 0.05$, and a total luminosity of $L = 5.26\,L_\odot$. The uncertainty in the parameters were determined from the 1σ χ^2 contours from the grid. The best fit model to the stellar spectrum is show in Figure 6.2. The data are shown in black, the best fit model in

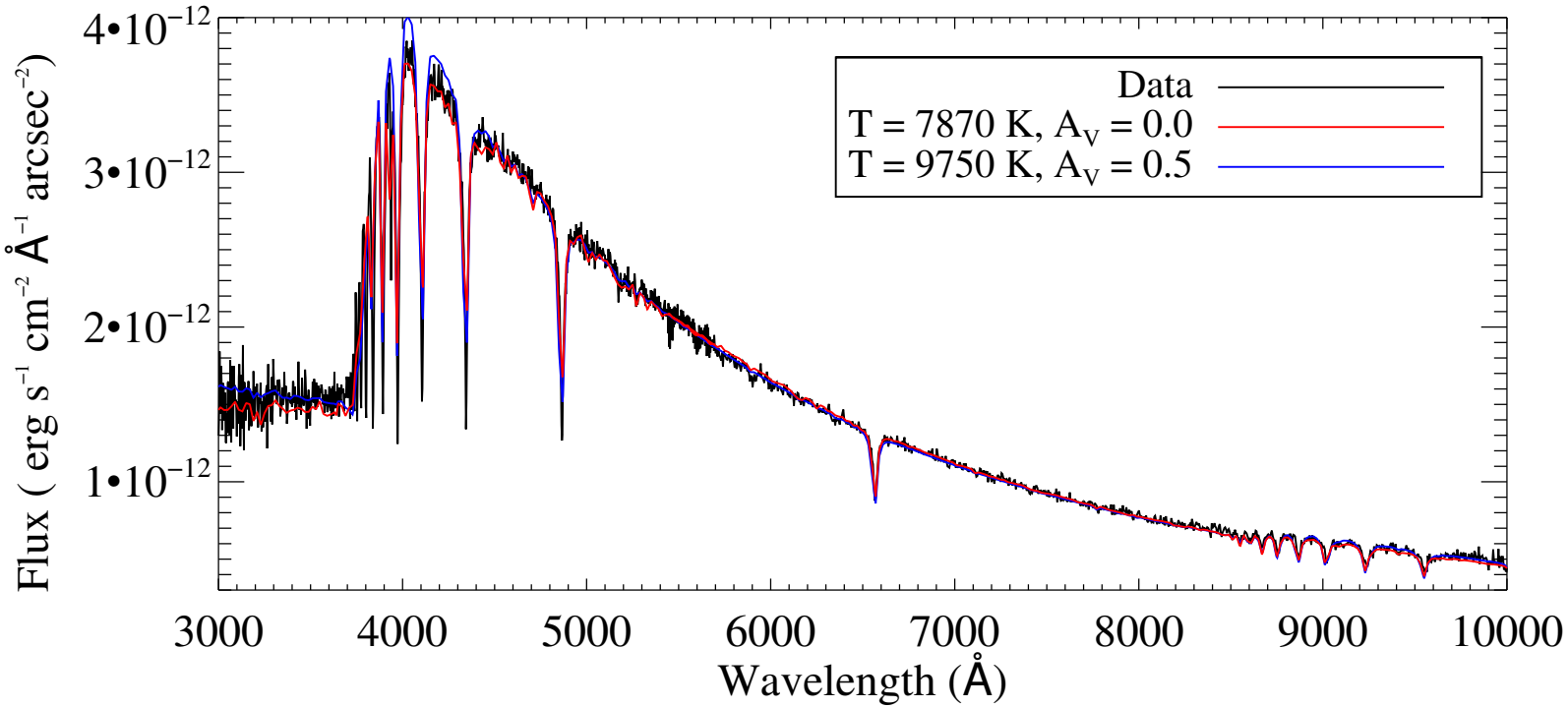

Figure 6.2: Stellar spectrum of HD32297 from the unocculted STIS data. Overplotted are two ATLAS9 stellar photosphere models. In red is our best fitting model, with $T = 7870$ K, log(g) = 4.0, and zero extinction. For comparison, in blue is the best fitting model for a fixed temperature of $T = 9750$ K. This model clearly overestimates the stellar spectrum at short wavelengths (~ 4000 Å).

red, and an A0V ($T = 9750$ K) model is shown for comparison.

6.5 Radial Profiles

Radial profiles were produced by integrating each row of the two dimensional spectra over the entire bandpass for both the G430L and the G750L data to get the disk surface brightness as a function of radius. We calculated the radial profiles separately above the fiducial bar (PA = 46.1°) and below fiducial bar (PA = 226.1°).

We define the outermost detected radius of the disk as the location where the radial profile is 1σ above the background level. The background is calculated as the standard deviation of 5 rows far from the center of the disk (10″) integrated over the wavelength range of the data. This gives us outermost detected radii of R = 179 AU for the G430L data and R = 247 AU for the G750L data.

Roberge et al. (2005) showed the largest error in this type of data is likely from systematic error of a misalignment between the PSF star and the disk due to a shift of the star position under the fiducial bar between the two observations. To account for this, we produced two more spectra where the PSF spectra was shifted up or down by 0.25 pixels before the PSF subtraction step. The radial profiles were then calculated in the same way as the unshifted spectra. The systematic error due to a possible misalignment was calculated as half of the difference between the radial profiles of the upward and downward shifted spectra. The total error is the statistical error and the systematic error added in quadrature.

Figure 6.3 shows the radial profiles for the G430L and G750L. Both figures show radial profiles from both above the fiducial bar (solid line) and below the fiducial bar (dashed line). The error bars show both the statistical error and the total error after the addition of the systematic error.

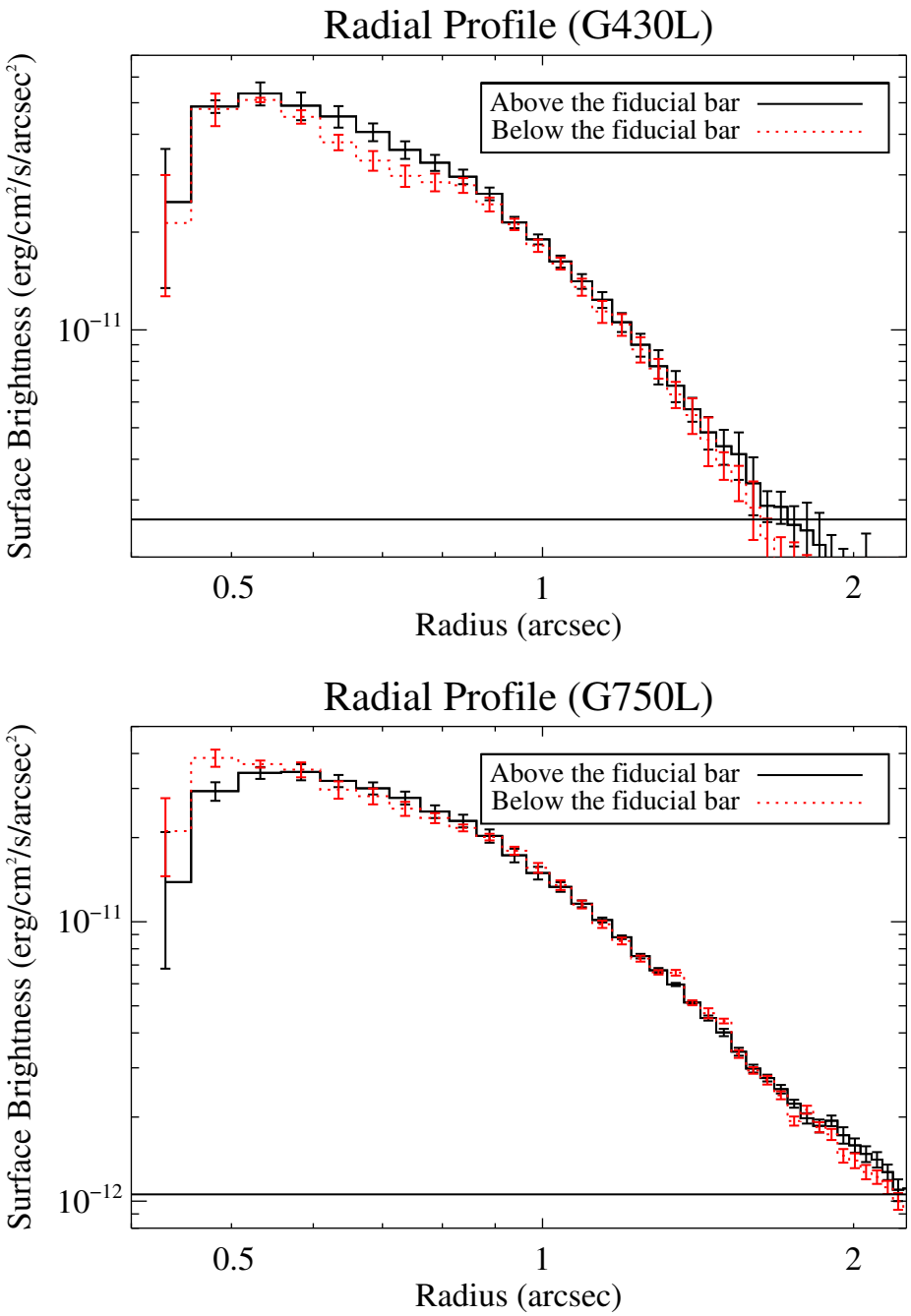

Figure 6.3: Radial profiles of the G430L (top) and G750L (bottom) data. The radial profiles were calculated by integrating each row of the 2D spectrum over wavelength. The black solid line is the radial profile above the fiducial bar (PA= 46.1°) and the red dotted line is the radial profile below the fiducial bar (PA= 226.1°). The horizontal line indicates the level of the background.

6.6 Disk Spectra

We extracted spectra of the disk as a function of disk radii, or distance from the star. The calibrated data are in units of surface brightness (erg cm^{-2} s^{-1} $Å^{-1}$ $arcsec^{-2}$), so we first needed to apply a flux conversion and a slit loss correction for point sources.

For a point source, the flux can be corrected for slit loss using the header keyword DIFF2PT, introduced during the `x2d` calibration step. The stellar spectrum was extracted by integrating over a default extraction box (7 pixels), then multiplying by the DIFF2PT value. For the disk, each pixel was converted from surface brightness to flux per angstrom by multiplying by the plate scale and the slit width (in arcsec).

This flux conversion is wavelength independent. This means that the final spectrum will be correct in the center of the bandpass, but not correct on either side. Since both the stellar and the disk flux is converted in the same wavelength independent way, this effect can be removed by dividing one by the other. Dividing the disk spectra by the stellar spectrum also removed the scattered stellar light signal, leaving us with only the intrinsic color of the grains.

The disk spectra were first binned by 10 pixels in the wavelength direction to increase signal-to-noise. Then 5 rows were averaged together in the spatial direction to reduce residual noise from the PSF subtraction. The innermost radial bin was one centered around 110.9 AU. This was the closest radius to the fiducial bar that did not show the sinusoidal residual noise variation from PSF subtraction artifacts. We then combined the spectra from radii above and below the fiducial bar. The data above and below showed no distinct differences, so they were combined to increase signal-to-noise.

Figure 6.4 shows the combined spectra of the first 4 radial bins across both the

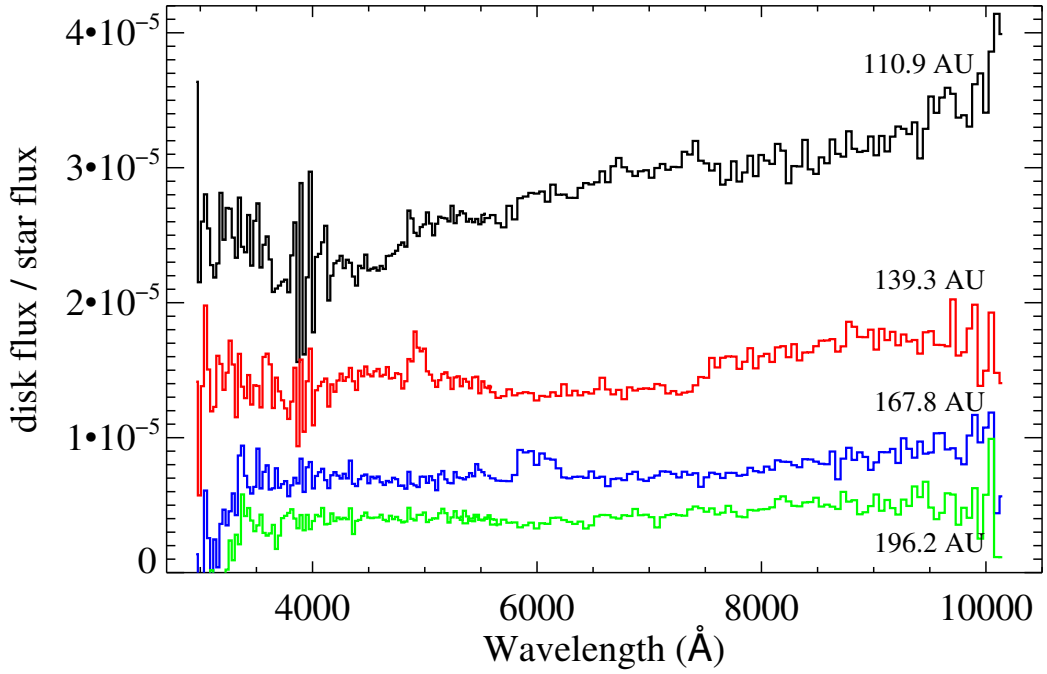

Figure 6.4: Disk spectra as a function of disk radius. Each radial bin is the average of 5 rows above the fiducial bar and 5 rows below the fiducial bar. The spectra are also binned by 10 pixels in the wavelength direction. We divided the disk spectra by the stellar spectrum extracted in the same manner. This removes any calibration errors and removes the trend of scattered starlight. The remaining disk signal represents the intrinsic scattering albedo of the dust grains. The outer radial bins all show a neutral scattering color, but the innermost radial bin, center around 110.9 AU, shows a strong red color across the wavelength range.

G430L and the G750L bandpasses. Most of the radial bins show a neutral color with no spectral features stronger than the PSF residual noise. The exception is the 110.9 AU radial bin, which shows a strong red color seen in both the G430L and G750L data. However, the long wavelength end of the data did not match up with the short wavelength end of the G750L data. We suspect this is because there is more slit loss at longer wavelengths. To connect the two spectra, we shifted the 110.9 AU G430L data down by 5×10^{-6}.

In the next few sections, we investigate the cause of the red color in the innermost radial bin. As this is the closest to the fiducial bar, we need to be more careful that

the spectrum is not still affected by improper PSF subtraction. The individual unbinned spectra outside of 100 AU show no signs of PSF subtraction residuals. However, a strong inner signal behind the fiducial bar may leak out more at longer wavelengths than at shorter wavelengths. This could affect the spectra close to the fiducial bar. We explore this possibility in Section 6.7.

If, on the other hand, the color is real, we may be seeing actual variations in grain properties as a function of disk radius. Near-IR images have shown the peak of the dust grain distribution to be near 110 AU (Boccaletti et al. 2012; Currie et al. 2012; Esposito et al. 2014; Rodigas et al. 2014). The peak of the dust distribution may indicate the location of a parent belt of planetesimals. The color difference between the inner and out spectra may be due to an actual difference in grain size of composition inside versus outside the parent belt.

6.7 Leak from behind the fiducial bar?

We investigated the question of whether the red color in the 110.9 AU spectrum is caused by a disk signal from just behind the fiducial bar. Diffraction spreads out the disk signal more at long wavelengths. Some of the light from just behind the fiducial bar might leak out more at longer wavelengths to contaminate the spectra. The leak could be due to a bright inner disk just behind the fiducial bar. Even if there is no inner disk, an edge-on system will still have a lot of light from the outer disk hidden behind the fiducial bar.

Currie et al. (2012), Donaldson et al. (2013) and Rodigas et al. (2014) have all postulated the existence of an inner disk in the HD32297 system. Currie et al. (2012) use an inner disk to explain the flattening of the radial profile inside of 50 AU. Currie et al. (2012) and Donaldson et al. (2013) also needed an inner disk to

explain the high flux of the spectral energy distribution in the mid-IR. The proposed inner disks would have been behind the coronagraph in all the near-IR images that have been taken.

To test the effect an inner disk might have on the spectra due to PSF bleeding, we simulated observations of a gray colored disk with a bright inner ring. We modeled the scattering properties of a gray disk with isotropically scattering grains. The model images were made with the same plate scale as the STIS two dimensional spectra. For the outer disk, we used the dust density distribution Boccaletti et al. (2012) used to model their near-IR data. For the inner disk, we used the same density distribution as the outer disk, but placed it near the outer edge of the fiducial bar (45 AU). This is consistent with the predictions of Currie et al. (2012) and Rodigas et al. (2014) who place the inner disk at < 50 AU.

Next, we created simulated PSFs with the Tiny Tim HST PSF modeling code (Krist et al. 2011). We made three monochromatic STIS CCD PSFs at 450, 675, and 900 nm to span the G430L and G750L wavelength coverage. The PSFs were not subsampled, but made with detector sized pixels and using the recommended PSF size of $3''$.

We convolved the three PSFs with the disk model to simulate the spreading of the inner disk with wavelength. After the convolution, the inner disk was more extended at 900 nm than at 450 nm, as predicted, but not nearly enough to affect the data at 110 AU. Figure 6.5 shows the radial profiles of the model after being convolved with the PSF at 450, 675, and 900 nm.

As a further test, we extracted spectral points of our models at 450, 675, and 900 nm in the same way as the data. At 110 AU, the color does not change more than 1%. Since the data is 12% brighter at 900 nm than 450 nm, we conclude that the red color is not caused by light leaking from behind the fiducial bar.

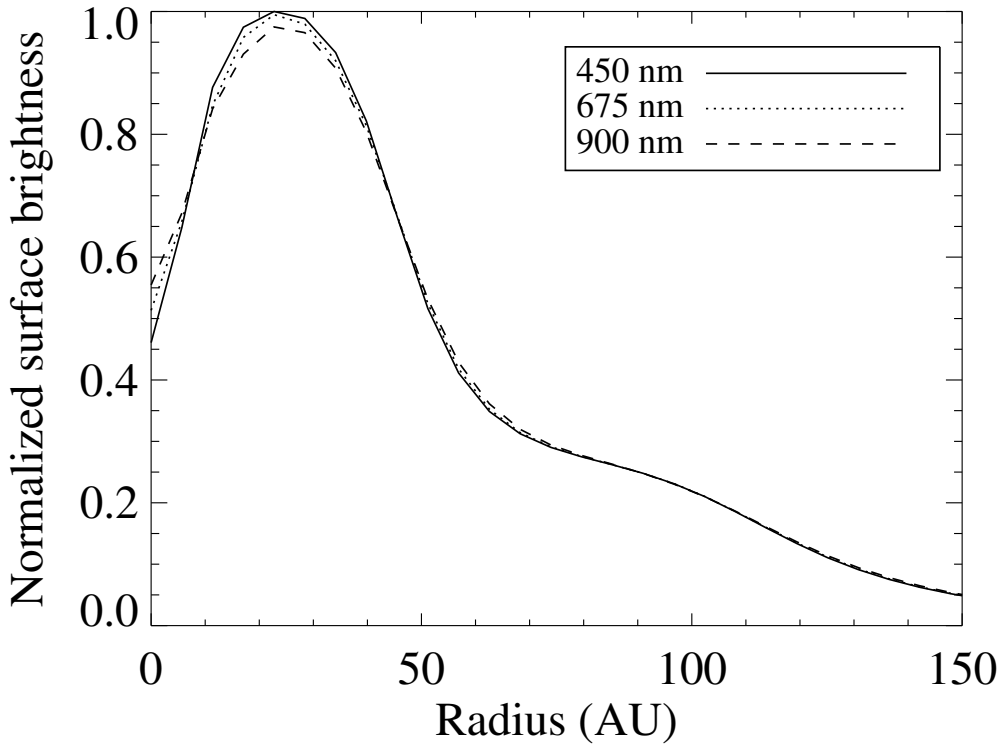

Figure 6.5: Radial profiles of gray disk models after being convolved with the PSF at 450, 675, and 900 nm. The PSF does extend the profile of the inner disk more at longer wavelengths, but this effect does not contribute to the radial profile at 110 AU.

6.8 Discussion

Now that we have shown the red color in the HD32297 spectrum is not a PSF subtraction artifact, we are left with the question of what could cause this red color to be present in the disk, and why it is visible at some radii and not others.

The first possibility is that the dust grains have an intrinsic albedo that scatters more efficiently at longer wavelengths. Debes et al. (2008) used HST spectrophotometry to determine the HR4796A debris disk also has a red color from the optical to the near-IR ($\sim 0.5-2.2\,\mu$m). Their modeling of the spectrum concluded the red color

was due to grains composed of complex organic material, called tholins. Tholins are produced from irradiation of ices containing hydrocarbons, such as methane, and have been used to explain the red color found in many outer Solar System bodies (Cruikshank et al. 2005).

While tholins may be able to reproduce the red color seen in our Solar System and in HR4796A, Köhler et al. (2008) argued they are not necessary. Simple ISM-like grains (composites of silicate, carbon, and water-ice) can also reproduce the red spectrum if the grain size and porosity are increased.

Mulders et al. (2013) also discussed the impact of grain size on the disk color, this time in relation to the protoplanetary disk, HD100546. They conclude that large grains ($\sim 2.5\,\mu$m) are much more forward scattering than smaller grains. In optical images, where the small scattering angles are blocked by the coronagraph, the effective albedo is smaller than the intrinsic albedo. At longer wavelengths, the scattering becomes more isotropic, increasing the effective albedo. This causes the disk to appear red.

Using the model of Mulders et al. (2013), the disk color can change with radius in one of two ways. First, if the forward scattering is strong enough, the disk will appear redder closer to the star. Second, the change in disk color with radius could indicate a change in grain size with radius, i.e. only large grains are present closer to the star, while small grains are present in the outer parts of the disk, making the disk appear more neutral in color.

This separation of small and large grains could be a natural consequence of radiation pressure. Small grains are constantly being produced by collisions of large planetesimals in the parent belt (thought to be located near the peak of the dust emission at $\sim$ 110 AU). These small grains feel a strong radiation pressure from the central star, and due to their large surface area to mass ratios, they are quickly

expelled from their birthplaces. Therefore, small grains are unlikely to be found inside the parent belt, but may be found outside as they make their way out of the system.

Recently, Stark et al. (2014) analyzed STIS images of the HD181327 debris disk, and found that the scattering phase function changes with semi-major axis, which seems to also indicate a spatial sorting of grain sizes in and out of the parent belt. Stark et al. (2014), however, argued that the strength of the change with radius is more consistent with the presence of a planet dynamically ejecting small grains, rather than just pure radiation pressure effects.

6.9 Future Work

The next step is to model the HD32297 disk and try to reproduce the STIS spectrum at each radius. We will start by modeling the scattering properties of an edge-on debris disk with a phase function that depends on wavelength.

The scattering of starlight off dust grains in disks is often modeled with a Henyey-Greenstein phase function of the form

$$\Phi(\theta) = \frac{1}{4\pi} \frac{1 - g^2}{(1 + g^2 - 2g\cos(\theta))^{3/2}}, \tag{6.1}$$

where g is a value between -1 and 1 that represents the anisotropy of the phase function ($g = 0$: isotropic, $g = 1$: pure forward scattering, $g = -1$: pure backscattering) (Henyey and Greenstein 1941).

This is often used to fit a disk observation at a single wavelength. In the case of HD32297, we will let g vary with wavelength to fit the observations. Since the different radial bins of the spectrum cover a different range of scattering angles, we may be able to find a $g(\lambda)$ that fits all radial bins.

Next, we will try to find a grain composition that matches the observations.

Through our collaborators, we have several tools at our disposal to help with this task. We have a library of scattering and absorption properties of several grains types, both collected from the literature (Debes et al. 2008) and calculated for aggregate compositions using Mie theory and the Bruggeman mixing rule (Lebreton et al. 2012). We also have disk scattering models from both Lebreton et al. (2012) and Stark and Kuchner (2009).

Chapter 7

Summary and Future Work

This dissertation collects four projects that aim to characterize the dust in young debris disks. Young debris disks may be the sites of ongoing terrestrial planet formation. Planetesimals in the disk are likely still being accreted onto planets, bringing with them volatile material that the planets themselves lose earlier in their formation.

By studying the dust, we are indirectly studying the planetesimals themselves. Dust grains are produced in destructive collisions between the planetesimals and have short lifetimes compared to the ages of the disk. Therefore, the dust is likely co-located with the planetesimals and composed of the same material, so the dust can tell us the location and composition of the planetesimals.

To start, we observed the dust in the far-infrared with the *Herschel Space Observatory*. We looked at mostly unresolved systems, so we characterized the dust by modeling the SED. We started with a detailed look at the 30 Myr-old disks in the Tucana-Horologium Association, then expanded our sample to include more debris disks with a wider range of ages (10-30 Myr). A few things we learned include:

- In Tucana-Horologium, the disks display a large variety in their properties,

even though they all have the same age. The processes that make disks different has probably already occurred by this age.

- Disks in our sample appear to fall into two categories, cold disks ($\lesssim$ 150 K) and warm disks ($\gtrsim$ 150 K).

- Both disk populations show a trend of increasing disk temperature vs. stellar temperature. For the cold disks, this trend could be probing the radial limit of planet formation and how it depends on stellar spectral type.

- No change as a function of age was detected in our sample. Debris disks appear to evolve slowly after the dissipation of the gas disk. Samples with larger range in ages ($\sim$ 1 Gyr) show a decline in fractional dust luminosity and temperature with age (e.g. Chen et al. 2014).

Next we focused on one disk, HD32297. This disk is relatively bright, well studied, and has been spatially resolved in the near-IR. This allows us to study the disk in more detail than we could with the fainter disks in Tuc-Hor and the other associations. We observed the disk with *Herschel* in the far-IR and sub-mm and HST in the optical/near-IR. A couple of points we noted about this disk are:

- Gas was detected in the HD32297 disk. This gas is likely secondary from collisions or outgassing of comets, not primordial. HD32297 is one of only a handful of debris disks with detectable amounts of gas.

- We modeled the disk with a two component model that included an inner disk that would have been behind the coronagraph in the scattered light images of the disk.

- The outer disk is composed of porous and icy grains similar to solar system cometary grains.

- The disk shows a red color in the optical/near-IR. This could be due to organic material, large grains, or porous grains. More modeling is needed to understand the true meaning of this color.

7.1 Future Work

The work in this dissertation can naturally be expanded into a couple of other projects, outlined below.

7.1.1 Modeling the HD32297 disk

We have collected a large amount of data on the HD32297 debris disk, and even more data is coming in from other groups. We filled in a large gap in the SED from 60 to 500 μm and detected gas emission. We also obtained optical spectra of the disk as a function of disk radius.

Several other groups are working on ground-based observations of the HD32297 disk, using Adaptive Optics and Angular Differential Imaging to resolved the disk out into the infrared. Boccaletti et al. (2012) and Currie et al. (2012) imaged the disk at 2.2 μm, and Rodigas et al. (2014) observed the disk at 3.8 μm. Additionally, Rodigas et al. (2014) have obtained data at 3.1 μm, the wavelength of an important water ice feature that could confirm or deny our model from Chapter 5. Furthermore, the disk has been imaged with high spatial resolution at several wavelengths with HST NICMOS (Debes et al. 2009; Schneider et al. 2005) and STIS (Schneider and HST/GO 12228 Team 2013).

All these data make HD32297 one of the best observed debris disks. The logical next step is to model all the data self-consistently. This would leave very little wiggle room in the model, making us more confident in the results.

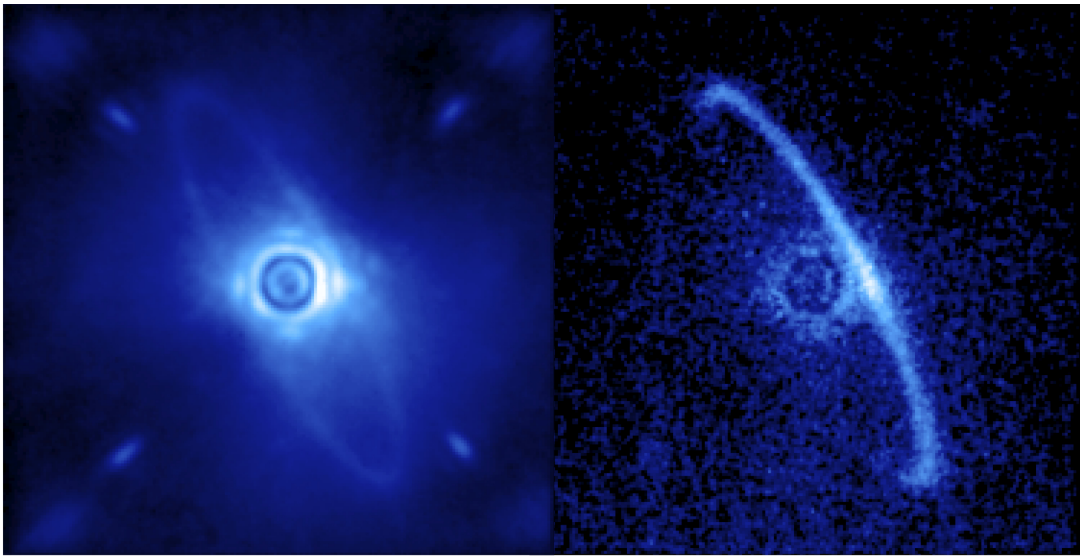

Figure 7.1: GPI's first light images of the HR4796A debris disk. **Left:** $\sim 2\,\mu$m scattered light image of the disk. **Right:** Polarized light view of the disk. The NW side of the disk, thought to be the back side, is highly polarized. Image credit: Marshall Perrin, STScI

7.1.2 HR4796A

HR4796A is another bright, young debris disk close to edge-on, similar to HD32297. This disk has been studied even more than HD32297 because it is closer and shows a narrow ring in optical/near-IR images. A recent press release image from the Gemini Planet Imager (GPI) shows a startling polarized light view of the disk (see Figure 7.1).

HR4796A is also part of the GASPS sample, so we have photometry of the disk from 60 to 500 μm. The disk is also part of our STIS program to get coronagraphic spectroscopy of edge-on debris disks. With this data, HR4796A is the perfect candidate to model the disk as we did for HD32297.

Figure 7.2: The Atacama Large Millimeter/submillimeter Array (ALMA). Eight of the full 66 antennas in the Atacama desert in Chile. Image Credit: ALMA (ESO/NAOJ/NRAO)

7.1.3 ALMA

The Atacama Large Millimeter/submillimeter Array (ALMA - see Figure 7.2) presents a new opportunity to spatially resolve debris disks. Its unmatched sensitivity and angular resolution in the millimeter/submillimeter will allow us to map the thermal emission from large grains in debris disks.

This will have a huge impact on our models. SED modeling is based on the thermal emission from a range of different size grains. The near-IR images we use to constrain the dust location, however, come from light scattering off small dust grains. These small grains are more susceptible to processes that move dust grain around in the disk, such as radiation pressure. The large grains imaged at millimeter wavelengths are more likely to be located closer to their parent bodies. It is unclear how the grain size distribution changes in the disk, and it is often assumed to be constant throughout. ALMA will allow us to measure this.

ALMA will also be more sensitive to gas in debris disks. This can help up understand the puzzling origin of debris disk gas. Dent et al. (2014) recently spatially resolved the CO gas in the 12 Myr-old debris disk, β Pic, which showed the gas is mostly confined to one or two big clumps. This suggests the gas may come from a recent collision of Mars-sized bodies.

We envision a few future projects using ALMA. They are described in more detail below.

HD32297: Imaging the mm grains – As mentioned above, resolved imaging at millimeter wavelengths will help improve out models of HD32297. HD32297 has only been marginally resolved in the sub-mm with the Sub-Millimeter Array (SMA), where it showed a somewhat asymmetrical structure. ALMA will be able to get an image of the disk with sub-arcsecond resolution and confirm whether this asymmetry is real.

In addition to aiding our modeling efforts, an ALMA image of the disk would help solve one other mystery. HD32297 is one of a handful of edge-on disks (including HD15115 and HD61005) that show strange asymmetries at short wavelengths. HD32297 has bowl-shaped wings that fan out to the NW. Debes et al. (2009) suggested the disk was interacting with a dense clump of the ISM, while Maness et al. (2008) suggested it might be due to gravitational interaction with a giant planet. A planet would affect both the small and large grains, while ISM interaction preferentially affects the small grains. Therefore, the presence or absence of the wings in the ALMA images will sort out which process is at work in the HD32297 disk.

Modeling the AU Mic disk – AU Mic is another young, edge-on debris disk, but this one surrounds an M star. The disk has already been imaged with ALMA and the disk shows a symmetrical structure in the mm (see Figure 7.3; MacGregor et al. 2013). This disk is another good candidate for further modeling. The results

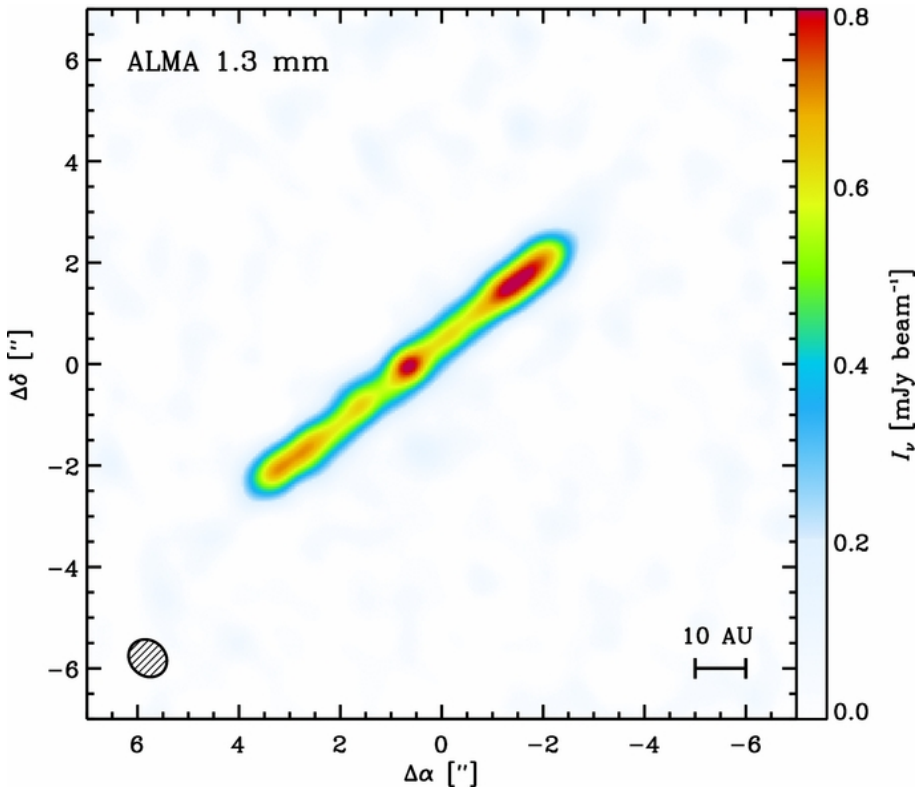

Figure 7.3: The AU Mic debris disk imaged with ALMA at 1.3 mm (MacGregor et al. 2013). At long wavelengths, ALMA images the structure of the large grain ($\sim$ 1 mm), which are more likely to be located near their parent bodies. The AU Mic disk shows a symmetrical ring structure and a mm excess near the central star.

may shed some light on the difference between debris disks around A stars vs. M stars.

Approved ALMA proposals: 49 Ceti and HD181327 – I am a co-investigator on two Cycle 2 ALMA proposals which were approved earlier this year. The first is a proposal to measure the C I gas in the young debris disk, 49 Ceti (P.I. A. Roberge). This debris disk has a relatively large amount of gas for its advanced age ($\sim$ 40 Myr). The CO gas has already been mapped with ALMA in Cycle 1. Comparing the C I and CO spatial distribution can help us understand the origin of the gas.

The other proposal is to map the dust continuum of the 12 Myr-old face-on debris disk, HD181327 (P.I. C. Stark). HD181327 is a member of BPMG and was a part

of the GASPS sample. The disk was also recently imaged with HST STIS (Stark et al. 2014), which hinted at a possible recent massive collision and spatial grain size sorting that could be due to a giant planet. Comparing the resolved images from STIS and ALMA could confirm these results.

Bibliography

Acke, B., Min, M., Dominik, C., Vandenbussche, B., Sibthorpe, B., Waelkens, C., Olofsson, G., Degroote, P., Smolders, K., Pantin, E., Barlow, M. J., Blommaert, J. A. D. L., Brandeker, A., De Meester, W., Dent, W. R. F., Exter, K., Di Francesco, J., Fridlund, M., Gear, W. K., Glauser, A. M., Greaves, J. S., Harvey, P. M., Henning, T., Hogerheijde, M. R., Holland, W. S., Huygen, R., Ivison, R. J., Jean, C., Liseau, R., Naylor, D. A., Pilbratt, G. L., Polehampton, E. T., Regibo, S., Royer, P., Sicilia-Aguilar, A., and Swinyard, B. M. (2012). Herschel images of Fomalhaut. An extrasolar Kuiper belt at the height of its dynamical activity. *A&A*, 540:A125.

Agnor, C. and Asphaug, E. (2004). Accretion Efficiency during Planetary Collisions. *ApJ*, 613:L157–L160.

A'Hearn, M. F. (2008). Deep Impact and the Origin and Evolution of Cometary Nuclei. *Space Sci. Rev.*, 138:237–246.

Alexander, R. D. and Armitage, P. J. (2007). Dust dynamics during protoplanetary disc clearing. *MNRAS*, 375:500–512.

Alibert, Y., Mordasini, C., Benz, W., and Winisdoerffer, C. (2005). Models of giant planet formation with migration and disc evolution. *A&A*, 434:343–353.

Andre, P. and Montmerle, T. (1994). From T Tauri stars to protostars: Circumstellar material and young stellar objects in the rho Ophiuchi cloud. *ApJ*, 420:837–

862.

Andre, P., Ward-Thompson, D., and Barsony, M. (1993). Submillimeter continuum observations of Rho Ophiuchi A - The candidate protostar VLA 1623 and prestellar clumps. *ApJ*, 406:122–141.

Andrews, S. M., Rosenfeld, K. A., Kraus, A. L., and Wilner, D. J. (2013). The Mass Dependence between Protoplanetary Disks and their Stellar Hosts. *ApJ*, 771:129.

Andrews, S. M. and Williams, J. P. (2007). High-Resolution Submillimeter Constraints on Circumstellar Disk Structure. *ApJ*, 659:705–728.

Andrews, S. M., Wilner, D. J., Espaillat, C., Hughes, A. M., Dullemond, C. P., McClure, M. K., Qi, C., and Brown, J. M. (2011). Resolved Images of Large Cavities in Protoplanetary Transition Disks. *ApJ*, 732:42.

Apai, D., Janson, M., Moro-Martín, A., Meyer, M. R., Mamajek, E. E., Masciadri, E., Henning, T., Pascucci, I., Kim, J. S., Hillenbrand, L. A., Kasper, M., and Biller, B. (2008). A Survey for Massive Giant Planets in Debris Disks with Evacuated Inner Cavities. *ApJ*, 672:1196–1201.

Arzoumanian, D., André, P., Didelon, P., Könyves, V., Schneider, N., Men'shchikov, A., Sousbie, T., Zavagno, A., Bontemps, S., di Francesco, J., Griffin, M., Hennemann, M., Hill, T., Kirk, J., Martin, P., Minier, V., Molinari, S., Motte, F., Peretto, N., Pezzuto, S., Spinoglio, L., Ward-Thompson, D., White, G., and Wilson, C. D. (2011). Characterizing interstellar filaments with Herschel in IC 5146. *A&A*, 529:L6.

Augereau, J.-C. and Beust, H. (2006). On the AU Microscopii debris disk. Density profiles, grain properties, and dust dynamics. *A&A*, 455:987–999.

Augereau, J. C., Lagrange, A. M., Mouillet, D., Papaloizou, J. C. B., and Grorod, P. A. (1999). On the HR 4796 A circumstellar disk. *A&A*, 348:557–569.

Augereau, J. C., Nelson, R. P., Lagrange, A. M., Papaloizou, J. C. B., and Mouillet,

D. (2001). Dynamical modeling of large scale asymmetries in the beta Pictoris dust disk. *A&A*, 370:447–455.

Aumann, H. H., Beichman, C. A., Gillett, F. C., de Jong, T., Houck, J. R., Low, F. J., Neugebauer, G., Walker, R. G., and Wesselius, P. R. (1984). Discovery of a shell around Alpha Lyrae. *ApJ*, 278:L23–L27.

Backman, D. E. and Paresce, F. (1993). Main-sequence stars with circumstellar solid material - The VEGA phenomenon. In E. H. Levy & J. I. Lunine, editor, *Protostars and Planets III*, pages 1253–1304.

Ballering, N. P., Rieke, G. H., Su, K. Y. L., and Montiel, E. (2013). A Trend between Cold Debris Disk Temperature and Stellar Type: Implications for the Formation and Evolution of Wide-orbit Planets. *ApJ*, 775:55.

Barrado Y Navascués, D. (2006). On the age of the TW Hydrae association and 2M1207334-393254. *A&A*, 459:511–518.

Barrado y Navascués, D., Stauffer, J. R., Song, I., and Caillault, J.-P. (1999). The Age of beta Pictoris. *ApJ*, 520:L123–L126.

Beichman, C. A., Bryden, G., Stapelfeldt, K. R., Gautier, T. N., Grogan, K., Shao, M., Velusamy, T., Lawler, S. M., Blaylock, M., Rieke, G. H., Lunine, J. I., Fischer, D. A., Marcy, G. W., Greaves, J. S., Wyatt, M. C., Holland, W. S., and Dent, W. R. F. (2006). New Debris Disks around Nearby Main-Sequence Stars: Impact on the Direct Detection of Planets. *ApJ*, 652:1674–1693.

Bergfors, C., Brandner, W., Janson, M., Daemgen, S., Geissler, K., Henning, T., Hippler, S., Hormuth, F., Joergens, V., and Köhler, R. (2010). Lucky Imaging survey for southern M dwarf binaries. *A&A*, 520:A54.

Biller, B. A., Close, L. M., Masciadri, E., Nielsen, E., Lenzen, R., Brandner, W., McCarthy, D., Hartung, M., Kellner, S., Mamajek, E., Henning, T., Miller, D., Kenworthy, M., and Kulesa, C. (2007). An Imaging Survey for Extrasolar Planets

around 45 Close, Young Stars with the Simultaneous Differential Imager at the Very Large Telescope and MMT. *ApJS*, 173:143–165.

Boccaletti, A., Augereau, J.-C., Lagrange, A.-M., Milli, J., Baudoz, P., Mawet, D., Mouillet, D., Lebreton, J., and Maire, A.-L. (2012). Morphology of the very inclined debris disk around HD 32297. *A&A*, 544:A85.

Bodenheimer, P. and Pollack, J. B. (1986). Calculations of the accretion and evolution of giant planets The effects of solid cores. *Icarus*, 67:391–408.

Bohren, C. F. and Huffman, D. R. (1983). *Absorption and scattering of light by small particles*.

Booth, M., Kennedy, G., Sibthorpe, B., Matthews, B. C., Wyatt, M. C., Duchêne, G., Kavelaars, J. J., Rodriguez, D., Greaves, J. S., Koning, A., Vican, L., Rieke, G. H., Su, K. Y. L., Moro-Martín, A., and Kalas, P. (2013). Resolved debris discs around A stars in the Herschel DEBRIS survey. *MNRAS*, 428:1263–1280.

Boss, A. P. (1997). Giant planet formation by gravitational instability. *Science*, 276:1836–1839.

Boulanger, F., Abergel, A., Bernard, J.-P., Burton, W. B., Desert, F.-X., Hartmann, D., Lagache, G., and Puget, J.-L. (1996). The dust/gas correlation at high Galactic latitude. *A&A*, 312:256–262.

Brandeker, A., Jayawardhana, R., and Najita, J. (2003). Keck Adaptive Optics Imaging of Nearby Young Stars: Detection of Close Multiple Systems. *AJ*, 126:2009–2014.

Brandeker, A., Olofsson, and SDE - GTKP (2012). Herschel Reveals A Low C / O Ratio In The Disk Around Beta Pictoris. submitted.

Brown, J. M., Blake, G. A., Qi, C., Dullemond, C. P., Wilner, D. J., and Williams, J. P. (2009). Evidence for Dust Clearing Through Resolved Submillimeter Imaging. *ApJ*, 704:496–502.

Brownlee, D., Tsou, P., Aléon, J., Alexander, C. M. O. ., Araki, T., Bajt, S., Baratta, G. A., Bastien, R., Bland, P., Bleuet, P., Borg, J., Bradley, J. P., Brearley, A., Brenker, F., Brennan, S., Bridges, J. C., Browning, N. D., Brucato, J. R., Bullock, E., Burchell, M. J., Busemann, H., Butterworth, A., Chaussidon, M., Cheuvront, A., Chi, M., Cintala, M. J., Clark, B. C., Clemett, S. J., Cody, G., Colangeli, L., Cooper, G., Cordier, P., Daghlian, C., Dai, Z., D'Hendecourt, L., Djouadi, Z., Dominguez, G., Duxbury, T., Dworkin, J. P., Ebel, D. S., Economou, T. E., Fakra, S., Fairey, S. A. J., Fallon, S., Ferrini, G., Ferroir, T., Fleckenstein, H., Floss, C., Flynn, G., Franchi, I. A., Fries, M., Gainsforth, Z., Gallien, J.-P., Genge, M., Gilles, M. K., Gillet, P., Gilmour, J., Glavin, D. P., Gounelle, M., Grady, M. M., Graham, G. A., Grant, P. G., Green, S. F., Grossemy, F., Grossman, L., Grossman, J. N., Guan, Y., Hagiya, K., Harvey, R., Heck, P., Herzog, G. F., Hoppe, P., Hörz, F., Huth, J., Hutcheon, I. D., Ignatyev, K., Ishii, H., Ito, M., Jacob, D., Jacobsen, C., Jacobsen, S., Jones, S., Joswiak, D., Jurewicz, A., Kearsley, A. T., Keller, L. P., Khodja, H., Kilcoyne, A. L. D., Kissel, J., Krot, A., Langenhorst, F., Lanzirotti, A., Le, L., Leshin, L. A., Leitner, J., Lemelle, L., Leroux, H., Liu, M.-C., Luening, K., Lyon, I., MacPherson, G., Marcus, M. A., Marhas, K., Marty, B., Matrajt, G., McKeegan, K., Meibom, A., Mennella, V., Messenger, K., Messenger, S., Mikouchi, T., Mostefaoui, S., Nakamura, T., Nakano, T., Newville, M., Nittler, L. R., Ohnishi, I., Ohsumi, K., Okudaira, K., Papanastassiou, D. A., Palma, R., Palumbo, M. E., Pepin, R. O., Perkins, D., Perronnet, M., Pianetta, P., Rao, W., Rietmeijer, F. J. M., Robert, F., Rost, D., Rotundi, A., Ryan, R., Sandford, S. A., Schwandt, C. S., See, T. H., Schlutter, D., Sheffield-Parker, J., Simionovici, A., Simon, S., Sitnitsky, I., Snead, C. J., Spencer, M. K., Stadermann, F. J., Steele, A., Stephan, T., Stroud, R., Susini, J., Sutton, S. R., Suzuki, Y., Taheri, M., Taylor, S., Teslich, N., Tomeoka,

K., Tomioka, N., Toppani, A., Trigo-Rodríguez, J. M., Troadec, D., Tsuchiyama, A., Tuzzolino, A. J., Tyliszczak, T., Uesugi, K., Velbel, M., Vellenga, J., Vicenzi, E., Vincze, L., Warren, J., Weber, I., Weisberg, M., Westphal, A. J., Wirick, S., Wooden, D., Wopenka, B., Wozniakiewicz, P., Wright, I., Yabuta, H., Yano, H., Young, E. D., Zare, R. N., Zega, T., Ziegler, K., Zimmerman, L., Zinner, E., and Zolensky, M. (2006). Comet 81P/Wild 2 Under a Microscope. *Science*, 314:1711–.

Bryden, G., Beichman, C. A., Trilling, D. E., Rieke, G. H., Holmes, E. K., Lawler, S. M., Stapelfeldt, K. R., Werner, M. W., Gautier, T. N., Blaylock, M., Gordon, K. D., Stansberry, J. A., and Su, K. Y. L. (2006). Frequency of Debris Disks around Solar-Type Stars: First Results from a Spitzer MIPS Survey. *ApJ*, 636:1098–1113.

Buenzli, E., Thalmann, C., Vigan, A., Boccaletti, A., Chauvin, G., Augereau, J. C., Meyer, M. R., Ménard, F., Desidera, S., Messina, S., Henning, T., Carson, J., Montagnier, G., Beuzit, J. L., Bonavita, M., Eggenberger, A., Lagrange, A. M., Mesa, D., Mouillet, D., and Quanz, S. P. (2010). Dissecting the Moth: discovery of an off-centered ring in the HD 61005 debris disk with high-resolution imaging. *A&A*, 524:L1.

Burns, J. A., Lamy, P. L., and Soter, S. (1979). Radiation forces on small particles in the solar system. *Icarus*, 40:1–48.

Burrows, C. J., Stapelfeldt, K. R., Watson, A. M., Krist, J. E., Ballester, G. E., Clarke, J. T., Crisp, D., Gallagher, III, J. S., Griffiths, R. E., Hester, J. J., Hoessel, J. G., Holtzman, J. A., Mould, J. R., Scowen, P. A., Trauger, J. T., and Westphal, J. A. (1996). Hubble Space Telescope Observations of the Disk and Jet of HH 30. *ApJ*, 473:437.

Butler, R. P., Wright, J. T., Marcy, G. W., Fischer, D. A., Vogt, S. S., Tinney, C. G., Jones, H. R. A., Carter, B. D., Johnson, J. A., McCarthy, C., and Penny,

A. J. (2006). Catalog of Nearby Exoplanets. *ApJ*, 646:505–522.

Campo Bagatin, A., Cellino, A., Davis, D. R., Farinella, P., and Paolicchi, P. (1994). Wavy size distributions for collisional systems with a small-size cutoff. *Planet. Space Sci.*, 42:1079–1092.

Canup, R. M. (2004). Simulations of a late lunar-forming impact. *Icarus*, 168:433–456.

Carpenter, J. M., Bouwman, J., Mamajek, E. E., Meyer, M. R., Hillenbrand, L. A., Backman, D. E., Henning, T., Hines, D. C., Hollenbach, D., Kim, J. S., Moro-Martin, A., Pascucci, I., Silverstone, M. D., Stauffer, J. R., and Wolf, S. (2009). Formation and Evolution of Planetary Systems: Properties of Debris Dust Around Solar-Type Stars. *ApJS*, 181:197–226.

Carpenter, J. M., Bouwman, J., Silverstone, M. D., Kim, J. S., Stauffer, J., Cohen, M., Hines, D. C., Meyer, M. R., and Crockett, N. (2008). The Formation and Evolution of Planetary Systems: Description of the Spitzer Legacy Science Database. *ApJS*, 179:423–450.

Carpenter, J. M., Mamajek, E. E., Hillenbrand, L. A., and Meyer, M. R. (2006). Evidence for Mass-dependent Circumstellar Disk Evolution in the 5 Myr Old Upper Scorpius OB Association. *ApJ*, 651:L49–L52.

Castelli, F. and Kurucz, R. L. (2004). New Grids of ATLAS9 Model Atmospheres. *ArXiv Astrophysics e-prints*.

Chambers, J. (2011). *Terrestrial Planet Formation*, pages 297–317.

Chauvin, G., Lagrange, A.-M., Bonavita, M., Zuckerman, B., Dumas, C., Bessell, M. S., Beuzit, J.-L., Bonnefoy, M., Desidera, S., Farihi, J., Lowrance, P., Mouillet, D., and Song, I. (2010). Deep imaging survey of young, nearby austral stars . VLT/NACO near-infrared Lyot-coronographic observations. *A&A*, 509:A52.

Chauvin, G., Lagrange, A.-M., Zuckerman, B., Dumas, C., Mouillet, D., Song, I.,

Beuzit, J.-L., Lowrance, P., and Bessell, M. S. (2005). A companion to AB Pic at the planet/brown dwarf boundary. *A&A*, 438:L29–L32.

Chen, C. H., Mittal, T., Kuchner, M., Forrest, W. J., Lisse, C. M., Manoj, P., Sargent, B. A., and Watson, D. M. (2014). The Spitzer Infrared Spectrograph Debris Disk Catalog. I. Continuum Analysis of Unresolved Targets. *ApJS*, 211:25.

Chen, C. H., Sargent, B. A., Bohac, C., Kim, K. H., Leibensperger, E., Jura, M., Najita, J., Forrest, W. J., Watson, D. M., Sloan, G. C., and Keller, L. D. (2006). Spitzer IRS Spectroscopy of IRAS-discovered Debris Disks. *ApJS*, 166:351–377.

Chiang, E., Kite, E., Kalas, P., Graham, J. R., and Clampin, M. (2009). Fomalhaut's Debris Disk and Planet: Constraining the Mass of Fomalhaut b from disk Morphology. *ApJ*, 693:734–749.

Cieza, L. A., Padgett, D. L., Allen, L. E., McCabe, C. E., Brooke, T. Y., Carey, S. J., Chapman, N. L., Fukagawa, M., Huard, T. L., Noriga-Crespo, A., Peterson, D. E., and Rebull, L. M. (2009). Primordial Circumstellar Disks in Binary Systems: Evidence for Reduced Lifetimes. *ApJ*, 696:L84–L88.

Cieza, L. A., Schreiber, M. R., Romero, G. A., Williams, J. P., Rebassa-Mansergas, A., and Merin, B. (2012). The Nature of Transition Circumstellar Disks III. Perseus, Taurus, and Auriga. *ArXiv e-prints*.

Clarke, C. J., Gendrin, A., and Sotomayor, M. (2001). The dispersal of circumstellar discs: the role of the ultraviolet switch. *MNRAS*, 328:485–491.

Cruikshank, D. P., Imanaka, H., and Dalle Ore, C. M. (2005). Tholins as coloring agents on outer Solar System bodies. *Advances in Space Research*, 36:178–183.

Currie, T., Rodigas, T. J., Debes, J., Plavchan, P., Kuchner, M., Jang-Condell, H., Wilner, D., Andrews, S., Kraus, A., Dahm, S., and Robitaille, T. (2012). Keck/NIRC2 Imaging of the Warped, Asymmetric Debris Disk around HD 32297. *ApJ*, 757:28.

Cutri, R. M., Skrutskie, M. F., van Dyk, S., Beichman, C. A., Carpenter, J. M., Chester, T., Cambresy, L., Evans, T., Fowler, J., Gizis, J., Howard, E., Huchra, J., Jarrett, T., Kopan, E. L., Kirkpatrick, J. D., Light, R. M., Marsh, K. A., McCallon, H., Schneider, S., Stiening, R., Sykes, M., Weinberg, M., Wheaton, W. A., Wheelock, S., and Zacarias, N. (2003). 2MASS All-Sky Catalog of Point Sources (Cutri+ 2003). *VizieR Online Data Catalog*, 2246:0.

Cuzzi, J. N., Hogan, R. C., and Shariff, K. (2008). Toward Planetesimals: Dense Chondrule Clumps in the Protoplanetary Nebula. *ApJ*, 687:1432–1447.

Cuzzi, J. N. and Weidenschilling, S. J. (2006). *Particle-Gas Dynamics and Primary Accretion*, pages 353–381.

D'Angelo, G., Durisen, R. H., and Lissauer, J. J. (2010). *Giant Planet Formation*, pages 319–346.

Debes, J. H., Weinberger, A. J., and Kuchner, M. J. (2009). Interstellar Medium Sculpting of the HD 32297 Debris Disk. *ApJ*, 702:318–326.

Debes, J. H., Weinberger, A. J., and Schneider, G. (2008). Complex Organic Materials in the Circumstellar Disk of HR 4796A. *ApJ*, 673:L191–L194.

Decin, G., Dominik, C., Waters, L. B. F. M., and Waelkens, C. (2003). Age Dependence of the Vega Phenomenon: Observations. *ApJ*, 598:636–644.

Dent, W. R. F., Thi, W. F., Kamp, I., and Williams, J. (2012). GASPS - a Herschel survey of gas and dust in Protoplanetary Disks: Survey Description and Early Results. submitted.

Dent, W. R. F., Thi, W. F., Kamp, I., Williams, J. P., Menard, F., Andrews, S., Ardila, D., Aresu, G., Augereau, J.-C., Barrado y Navascues, D., Brittain, S., Carmona, A., Ciardi, D., Danchi, W., Donaldson, J., Duchene, G., Eiroa, C., Fedele, D., Grady, C., de Gregorio-Molsalvo, I., Howard, C., Huélamo, N., Krivov, A., Lebreton, J., Liseau, R., Martin-Zaidi, C., Mathews, G., Meeus, G.,

Mendigutía, I., Montesinos, B., Morales-Calderon, M., Mora, A., Nomura, H., Pantin, E., Pascucci, I., Phillips, N., Pinte, C., Podio, L., Ramsay, S. K., Riaz, B., Riviere-Marichalar, P., Roberge, A., Sandell, G., Solano, E., Tilling, I., Torrelles, J. M., Vandenbusche, B., Vicente, S., White, G. J., and Woitke, P. (2013). GASPS - A Herschel Survey of Gas and Dust in Protoplanetary Disks: Summary and Initial Statistics. *PASP*, 125:477–505.

Dent, W. R. F., Walker, H. J., Holland, W. S., and Greaves, J. S. (2000). Models of the dust structures around Vega-excess stars. *MNRAS*, 314:702–712.

Dent, W. R. F., Wyatt, M. C., Roberge, A., Augereau, J.-C., Casassus, S., Corder, S., Greaves, J. S., de Gregorio-Monsalvo, I., Hales, A., Jackson, A. P., Hughes, A. M., Lagrange, A.-M., Matthews, B., and Wilner, D. (2014). Molecular Gas Clumps from the Destruction of Icy Bodies in the β Pictoris Debris Disk. *Science*, 343:1490–1492.

Desch, S. J. (2007). Mass Distribution and Planet Formation in the Solar Nebula. *ApJ*, 671:878–893.

Dodson-Robinson, S. E. and Salyk, C. (2011). Transitional Disks as Signposts of Young, Multiplanet Systems. *ApJ*, 738:131.

Dodson-Robinson, S. E., Veras, D., Ford, E. B., and Beichman, C. A. (2009). The Formation Mechanism of Gas Giants on Wide Orbits. *ApJ*, 707:79–88.

Dohnanyi, J. S. (1969). Collisional Model of Asteroids and Their Debris. *J. Geophys. Res.*, 74:2531–+.

Dominik, C., Blum, J., Cuzzi, J. N., and Wurm, G. (2007). Growth of Dust as the Initial Step Toward Planet Formation. *Protostars and Planets V*, pages 783–800.

Dominik, C. and Decin, G. (2003). Age Dependence of the Vega Phenomenon: Theory. *ApJ*, 598:626–635.

Donaldson, J. K., Lebreton, J., Roberge, A., Augereau, J.-C., and Krivov, A. V.

(2013). Modeling the HD32297 Debris Disk with Far-IR Herschel Data. *ArXiv e-prints*.

Donaldson, J. K., Roberge, A., Chen, C. H., Augereau, J.-C., Dent, W. R. F., Eiroa, C., Krivov, A. V., Mathews, G. S., Meeus, G., Ménard, F., Riviere-Marichalar, P., and Sandell, G. (2012). Herschel PACS Observations and Modeling of Debris Disks in the Tucana-Horologium Association. *ApJ*, 753:147.

Draine, B. T. (2003). Interstellar Dust Grains. *ARA&A*, 41:241–289.

Draine, B. T. (2006). On the Submillimeter Opacity of Protoplanetary Disks. *ApJ*, 636:1114–1120.

Draine, B. T. (2011). *Physics of the Interstellar and Intergalactic Medium*.

Draine, B. T. and Lee, H. M. (1984). Optical properties of interstellar graphite and silicate grains. *ApJ*, 285:89–108.

Drake, M. J. and Righter, K. (2002). Determining the composition of the Earth. *Nature*, 416:39–44.

Duchêne, G. (2010). Planet Formation in Binary Systems: A Separation-Dependent Mechanism? *ApJ*, 709:L114–L118.

Dullemond, C. P. and Dominik, C. (2005). Dust coagulation in protoplanetary disks: A rapid depletion of small grains. *A&A*, 434:971–986.

Duquennoy, A. and Mayor, M. (1991). Multiplicity among solar-type stars in the solar neighbourhood. II - Distribution of the orbital elements in an unbiased sample. *A&A*, 248:485–524.

Ehrenreich, D., Lagrange, A.-M., Montagnier, G., Chauvin, G., Galland, F., Beuzit, J.-L., and Rameau, J. (2010). Deep infrared imaging of close companions to austral A- and F-type stars. *A&A*, 523:A73.

Eiroa, C., Fedele, D., Maldonado, J., González-García, B. M., Rodmann, J., Heras, A. M., Pilbratt, G. L., Augereau, J., Mora, A., Montesinos, B., Ardila, D., Bry-

den, G., Liseau, R., Stapelfeldt, K., Launhardt, R., Solano, E., Bayo, A., Absil, O., Arévalo, M., Barrado, D., Beichmann, C., Danchi, W., Del Burgo, C., Ertel, S., Fridlund, M., Fukagawa, M., Gutiérrez, R., Grün, E., Kamp, I., Krivov, A., Lebreton, J., Löhne, T., Lorente, R., Marshall, J., Martínez-Arnáiz, R., Meeus, G., Montes, D., Morbidelli, A., Müller, S., Mutschke, H., Nakagawa, T., Olofsson, G., Ribas, I., Roberge, A., Sanz-Forcada, J., Thébault, P., Walker, H., White, G. J., and Wolf, S. (2010). Cold DUst around NEarby Stars (DUNES). First results. A resolved exo-Kuiper belt around the solar-like star ζ^2 Ret. *A&A*, 518:L131+.

Eiroa, C., Marshall, J. P., Mora, A., Montesinos, B., Absil, O., Augereau, J. C., Bayo, A., Bryden, G., Danchi, W., del Burgo, C., Ertel, S., Fridlund, M., Heras, A. M., Krivov, A. V., Launhardt, R., Liseau, R., Löhne, T., Maldonado, J., Pilbratt, G. L., Roberge, A., Rodmann, J., Sanz-Forcada, J., Solano, E., Stapelfeldt, K., Thébault, P., Wolf, S., Ardila, D., Arévalo, M., Beichmann, C., Faramaz, V., González-García, B. M., Gutiérrez, R., Lebreton, J., Martínez-Arnáiz, R., Meeus, G., Montes, D., Olofsson, G., Su, K. Y. L., White, G. J., Barrado, D., Fukagawa, M., Grün, E., Kamp, I., Lorente, R., Morbidelli, A., Müller, S., Mutschke, H., Nakagawa, T., Ribas, I., and Walker, H. (2013). DUst around NEarby Stars. The survey observational results. *A&A*, 555:A11.

Eisner, J. A., Hillenbrand, L. A., Carpenter, J. M., and Wolf, S. (2005). Constraining the Evolutionary Stage of Class I Protostars: Multiwavelength Observations and Modeling. *ApJ*, 635:396–421.

Ertel, S., Wolf, S., Marshall, J. P., Eiroa, C., Augereau, J.-C., Krivov, A. V., Loehne, T., Absil, O., Ardila, D., Arevalo, M., Bayo, A., Bryden, G., del Burgo, C., Greaves, J., Kennedy, G., Lebreton, J., Liseau, R., Maldonado, J., Montesinos, B., Mora, A., Pilbratt, G. L., Sanz-Forcada, J., Stapelfeldt, K., and White, G. J. (2012). A peculiar class of debris disks from Herschel/DUNES - A steep fall off

in the far infrared. *ArXiv e-prints*.

Ertel, S., Wolf, S., Metchev, S., Schneider, G., Carpenter, J. M., Meyer, M. R., Hillenbrand, L. A., and Silverstone, M. D. (2011). Multi-wavelength modeling of the spatially resolved debris disk of HD 107146. *A&A*, 533:A132.

Espaillat, C., Muzerolle, J., Najita, J., Andrews, S., Zhu, Z., Calvet, N., Kraus, S., Hashimoto, J., Kraus, A., and D'Alessio, P. (2014). An Observational Perspective of Transitional Disks. *ArXiv e-prints*.

Esposito, T. M., Fitzgerald, M. P., Graham, J. R., and Kalas, P. (2014). Modeling Self-subtraction in Angular Differential Imaging: Application to the HD 32297 Debris Disk. *ApJ*, 780:25.

Evans, T. M., Ireland, M. J., Kraus, A. L., Martinache, F., Stewart, P., Tuthill, P. G., Lacour, S., Carpenter, J. M., and Hillenbrand, L. A. (2012). Mapping the Shores of the Brown Dwarf Desert. III. Young Moving Groups. *ApJ*, 744:120.

Fitzgerald, M. P., Kalas, P. G., Duchêne, G., Pinte, C., and Graham, J. R. (2007a). The AU Microscopii Debris Disk: Multiwavelength Imaging and Modeling. *ApJ*, 670:536–556.

Fitzgerald, M. P., Kalas, P. G., and Graham, J. R. (2007b). A Ring of Warm Dust in the HD 32297 Debris Disk. *ApJ*, 670:557–564.

Fitzpatrick, E. L. (1999). Correcting for the Effects of Interstellar Extinction. *PASP*, 111:63–75.

Gammie, C. F. (2001). Nonlinear Outcome of Gravitational Instability in Cooling, Gaseous Disks. *ApJ*, 553:174–183.

Goldreich, P., Lithwick, Y., and Sari, R. (2004). Final Stages of Planet Formation. *ApJ*, 614:497–507.

Goldreich, P. and Ward, W. R. (1973). The Formation of Planetesimals. *ApJ*, 183:1051–1062.

Graham, J. R., Kalas, P. G., and Matthews, B. C. (2007). The Signature of Primordial Grain Growth in the Polarized Light of the AU Microscopii Debris Disk. *ApJ*, 654:595–605.

Greenberg, J. M. (1998). Making a comet nucleus. *A&A*, 330:375–380.

Greenberg, J. M. and Hage, J. I. (1990). From interstellar dust to comets - A unification of observational constraints. *ApJ*, 361:260–274.

Griffin, M. J., Abergel, A., Abreu, A., Ade, P. A. R., André, P., Augueres, J., Babbedge, T., Bae, Y., Baillie, T., Baluteau, J., Barlow, M. J., Bendo, G., Benielli, D., Bock, J. J., Bonhomme, P., Brisbin, D., Brockley-Blatt, C., Caldwell, M., Cara, C., Castro-Rodriguez, N., Cerulli, R., Chanial, P., Chen, S., Clark, E., Clements, D. L., Clerc, L., Coker, J., Communal, D., Conversi, L., Cox, P., Crumb, D., Cunningham, C., Daly, F., Davis, G. R., de Antoni, P., Delderfield, J., Devin, N., di Giorgio, A., Didschuns, I., Dohlen, K., Donati, M., Dowell, A., Dowell, C. D., Duband, L., Dumaye, L., Emery, R. J., Ferlet, M., Ferrand, D., Fontignie, J., Fox, M., Franceschini, A., Frerking, M., Fulton, T., Garcia, J., Gastaud, R., Gear, W. K., Glenn, J., Goizel, A., Griffin, D. K., Grundy, T., Guest, S., Guillemet, L., Hargrave, P. C., Harwit, M., Hastings, P., Hatziminaoglou, E., Herman, M., Hinde, B., Hristov, V., Huang, M., Imhof, P., Isaak, K. J., Israelsson, U., Ivison, R. J., Jennings, D., Kiernan, B., King, K. J., Lange, A. E., Latter, W., Laurent, G., Laurent, P., Leeks, S. J., Lellouch, E., Levenson, L., Li, B., Li, J., Lilienthal, J., Lim, T., Liu, S. J., Lu, N., Madden, S., Mainetti, G., Marliani, P., McKay, D., Mercier, K., Molinari, S., Morris, H., Moseley, H., Mulder, J., Mur, M., Naylor, D. A., Nguyen, H., O'Halloran, B., Oliver, S., Olofsson, G., Olofsson, H., Orfei, R., Page, M. J., Pain, I., Panuzzo, P., Papageorgiou, A., Parks, G., Parr-Burman, P., Pearce, A., Pearson, C., Pérez-Fournon, I., Pinsard, F., Pisano, G., Podosek, J., Pohlen, M., Polehampton, E. T., Pouliquen, D., Rigopoulou,

D., Rizzo, D., Roseboom, I. G., Roussel, H., Rowan-Robinson, M., Rownd, B., Saraceno, P., Sauvage, M., Savage, R., Savini, G., Sawyer, E., Scharmberg, C., Schmitt, D., Schneider, N., Schulz, B., Schwartz, A., Shafer, R., Shupe, D. L., Sibthorpe, B., Sidher, S., Smith, A., Smith, A. J., Smith, D., Spencer, L., Stobie, B., Sudiwala, R., Sukhatme, K., Surace, C., Stevens, J. A., Swinyard, B. M., Trichas, M., Tourette, T., Triou, H., Tseng, S., Tucker, C., Turner, A., Vaccari, M., Valtchanov, I., Vigroux, L., Virique, E., Voellmer, G., Walker, H., Ward, R., Waskett, T., Weilert, M., Wesson, R., White, G. J., Whitehouse, N., Wilson, C. D., Winter, B., Woodcraft, A. L., Wright, G. S., Xu, C. K., Zavagno, A., Zemcov, M., Zhang, L., and Zonca, E. (2010). The Herschel-SPIRE instrument and its in-flight performance. *A&A*, 518:L3+.

Güttler, C., Blum, J., Zsom, A., Ormel, C. W., and Dullemond, C. P. (2010). The outcome of protoplanetary dust growth: pebbles, boulders, or planetesimals?. I. Mapping the zoo of laboratory collision experiments. *A&A*, 513:A56.

Hauschildt, P. H., Allard, F., and Baron, E. (1999). The NextGen Model Atmosphere Grid for 3000=T_eff=10,000 K. *ApJ*, 512:377–385.

Hayashi, C. (1981). Structure of the Solar Nebula, Growth and Decay of Magnetic Fields and Effects of Magnetic and Turbulent Viscosities on the Nebula. *Progress of Theoretical Physics Supplement*, 70:35–53.

Heap, S. R., Lindler, D. J., Lanz, T. M., Cornett, R. H., Hubeny, I., Maran, S. P., and Woodgate, B. (2000). Space Telescope Imaging Spectrograph Coronagraphic Observations of β Pictoris. *ApJ*, 539:435–444.

Henyey, L. G. and Greenstein, J. L. (1941). Diffuse radiation in the Galaxy. *ApJ*, 93:70–83.

Hernández, J., Calvet, N., Hartmann, L., Briceño, C., Sicilia-Aguilar, A., and Berlind, P. (2005). Herbig Ae/Be Stars in nearby OB Associations. *AJ*, 129:856–

871.

Higdon, S. J. U., Devost, D., Higdon, J. L., Brandl, B. R., Houck, J. R., Hall, P., Barry, D., Charmandaris, V., Smith, J. D. T., Sloan, G. C., and Green, J. (2004). The SMART Data Analysis Package for the Infrared Spectrograph on the Spitzer Space Telescope. *PASP*, 116:975–984.

Hillenbrand, L. A., Carpenter, J. M., Kim, J. S., Meyer, M. R., Backman, D. E., Moro-Martín, A., Hollenbach, D. J., Hines, D. C., Pascucci, I., and Bouwman, J. (2008). The Complete Census of 70 μm-bright Debris Disks within "the Formation and Evolution of Planetary Systems" Spitzer Legacy Survey of Sun-like Stars. *ApJ*, 677:630–656.

Hines, D. C., Backman, D. E., Bouwman, J., Hillenbrand, L. A., Carpenter, J. M., Meyer, M. R., Kim, J. S., Silverstone, M. D., Rodmann, J., Wolf, S., Mamajek, E. E., Brooke, T. Y., Padgett, D. L., Henning, T., Moro-Martín, A., Stobie, E., Gordon, K. D., Morrison, J. E., Muzerolle, J., and Su, K. Y. L. (2006). The Formation and Evolution of Planetary Systems (FEPS): Discovery of an Unusual Debris System Associated with HD 12039. *ApJ*, 638:1070–1079.

Hines, D. C., Schneider, G., Hollenbach, D., Mamajek, E. E., Hillenbrand, L. A., Metchev, S. A., Meyer, M. R., Carpenter, J. M., Moro-Martín, A., Silverstone, M. D., Kim, J. S., Henning, T., Bouwman, J., and Wolf, S. (2007). The Moth: An Unusual Circumstellar Structure Associated with HD 61005. *ApJ*, 671:L165–L168.

Høg, E., Fabricius, C., Makarov, V. V., Urban, S., Corbin, T., Wycoff, G., Bastian, U., Schwekendiek, P., and Wicenec, A. (2000). The Tycho-2 catalogue of the 2.5 million brightest stars. *A&A*, 355:L27–L30.

Hollenbach, D., Gorti, U., Meyer, M., Kim, J. S., Morris, P., Najita, J., Pascucci, I., Carpenter, J., Rodmann, J., Brooke, T., Hillenbrand, L., Mamajek, E., Padgett, D., Soderblom, D., Wolf, S., and Lunine, J. (2005). Formation and Evolution of

Planetary Systems: Upper Limits to the Gas Mass in HD 105. *ApJ*, 631:1180–1190.

Hollenbach, D., Johnstone, D., Lizano, S., and Shu, F. (1994). Photoevaporation of disks around massive stars and application to ultracompact H II regions. *ApJ*, 428:654–669.

Houck, J. R., Roellig, T. L., van Cleve, J., Forrest, W. J., Herter, T., Lawrence, C. R., Matthews, K., Reitsema, H. J., Soifer, B. T., Watson, D. M., Weedman, D., Huisjen, M., Troeltzsch, J., Barry, D. J., Bernard-Salas, J., Blacken, C. E., Brandl, B. R., Charmandaris, V., Devost, D., Gull, G. E., Hall, P., Henderson, C. P., Higdon, S. J. U., Pirger, B. E., Schoenwald, J., Sloan, G. C., Uchida, K. I., Appleton, P. N., Armus, L., Burgdorf, M. J., Fajardo-Acosta, S. B., Grillmair, C. J., Ingalls, J. G., Morris, P. W., and Teplitz, H. I. (2004). The Infrared Spectrograph (IRS) on the Spitzer Space Telescope. *ApJS*, 154:18–24.

Hubickyj, O., Bodenheimer, P., and Lissauer, J. J. (2005). Accretion of the gaseous envelope of Jupiter around a 5 10 Earth-mass core. *Icarus*, 179:415–431.

Ida, S. and Makino, J. (1993). Scattering of planetesimals by a protoplanet - Slowing down of runaway growth. *Icarus*, 106:210.

Janson, M., Carson, J. C., Lafrenière, D., Spiegel, D. S., Bent, J. R., and Wong, P. (2012). Infrared Non-detection of Fomalhaut b: Implications for the Planet Interpretation. *ApJ*, 747:116.

Johansen, A., Klahr, H., and Henning, T. (2006). Gravoturbulent Formation of Planetesimals. *ApJ*, 636:1121–1134.

Johansen, A., Oishi, J. S., Mac Low, M.-M., Klahr, H., Henning, T., and Youdin, A. (2007). Rapid planetesimal formation in turbulent circumstellar disks. *Nature*, 448:1022–1025.

Jura, M., Chen, C. H., Furlan, E., Green, J., Sargent, B., Forrest, W. J., Watson,

D. M., Barry, D. J., Hall, P., Herter, T. L., Houck, J. R., Sloan, G. C., Uchida, K., D'Alessio, P., Brandl, B. R., Keller, L. D., Kemper, F., Morris, P., Najita, J., Calvet, N., Hartmann, L., and Myers, P. C. (2004). Mid-Infrared Spectra of Dust Debris around Main-Sequence Stars. *ApJS*, 154:453–457.

Kalas, P. (2005). First Optical Images of Circumstellar Dust Surrounding the Debris Disk Candidate HD 32297. *ApJ*, 635:L169–L172.

Kalas, P., Fitzgerald, M. P., and Graham, J. R. (2007). Discovery of Extreme Asymmetry in the Debris Disk Surrounding HD 15115. *ApJ*, 661:L85–L88.

Kalas, P., Graham, J. R., Chiang, E., Fitzgerald, M. P., Clampin, M., Kite, E. S., Stapelfeldt, K., Marois, C., and Krist, J. (2008). Optical Images of an Exosolar Planet 25 Light-Years from Earth. *Science*, 322:1345–.

Kalas, P., Graham, J. R., and Clampin, M. (2005). A planetary system as the origin of structure in Fomalhaut's dust belt. *Nature*, 435:1067–1070.

Kalas, P., Graham, J. R., Fitzgerald, M. P., and Clampin, M. (2013). STIS Coronagraphic Imaging of Fomalhaut: Main Belt Structure and the Orbit of Fomalhaut b. *ApJ*, 775:56.

Kant, I. (1755). *Allgemeine Naturgeschichte und Theorie des Himmels*.

Kasper, M., Apai, D., Janson, M., and Brandner, W. (2007). A novel L-band imaging search for giant planets in the Tucana and β Pictoris moving groups. *A&A*, 472:321–327.

Kennedy, G. M. and Wyatt, M. C. (2010). Are debris discs self-stirred? *MNRAS*, 405:1253–1270.

Kenyon, S. J. and Bromley, B. C. (2006). Terrestrial Planet Formation. I. The Transition from Oligarchic Growth to Chaotic Growth. *AJ*, 131:1837–1850.

Kenyon, S. J. and Bromley, B. C. (2008). Variations on Debris Disks: Icy Planet Formation at 30-150 AU for 1-3 $M_{\odot}$ Main-Sequence Stars. *ApJS*, 179:451–483.

Kessler-Silacci, J., Augereau, J.-C., Dullemond, C. P., Geers, V., Lahuis, F., Evans, II, N. J., van Dishoeck, E. F., Blake, G. A., Boogert, A. C. A., Brown, J., Jørgensen, J. K., Knez, C., and Pontoppidan, K. M. (2006). c2d Spitzer IRS Spectra of Disks around T Tauri Stars. I. Silicate Emission and Grain Growth. *ApJ*, 639:275–291.

Köhler, M., Mann, I., and Li, A. (2008). Complex Organic Materials in the HR 4796A Disk? *ApJ*, 686:L95–L98.

Kokubo, E. and Ida, S. (1998). Oligarchic Growth of Protoplanets. *Icarus*, 131:171–178.

Kraus, A. L., Ireland, M. J., Hillenbrand, L. A., and Martinache, F. (2012). The Role of Multiplicity in Disk Evolution and Planet Formation. *ApJ*, 745:19.

Krist, J. (2007). Coronagraphic Imaging of Debris Disks with HST. In *In the Spirit of Bernard Lyot: The Direct Detection of Planets and Circumstellar Disks in the 21st Century*.

Krist, J. E., Ardila, D. R., Golimowski, D. A., Clampin, M., Ford, H. C., Illingworth, G. D., Hartig, G. F., Bartko, F., Benítez, N., Blakeslee, J. P., Bouwens, R. J., Bradley, L. D., Broadhurst, T. J., Brown, R. A., Burrows, C. J., Cheng, E. S., Cross, N. J. G., Demarco, R., Feldman, P. D., Franx, M., Goto, T., Gronwall, C., Holden, B., Homeier, N., Infante, L., Kimble, R. A., Lesser, M. P., Martel, A. R., Mei, S., Menanteau, F., Meurer, G. R., Miley, G. K., Motta, V., Postman, M., Rosati, P., Sirianni, M., Sparks, W. B., Tran, H. D., Tsvetanov, Z. I., White, R. L., and Zheng, W. (2005). Hubble Space Telescope Advanced Camera for Surveys Coronagraphic Imaging of the AU Microscopii Debris Disk. *AJ*, 129:1008–1017.

Krist, J. E., Hook, R. N., and Stoehr, F. (2011). 20 years of Hubble Space Telescope optical modeling using Tiny Tim. In *Society of Photo-Optical Instrumentation Engineers (SPIE) Conference Series*, volume 8127 of *Society of Photo-Optical*

Instrumentation Engineers (SPIE) Conference Series.

Krivov, A. V. (2010). Debris disks: seeing dust, thinking of planetesimals and planets. *Research in Astronomy and Astrophysics*, 10:383–414.

Krivov, A. V., Herrmann, F., Brandeker, A., and Thébault, P. (2009). Can gas in young debris disks be constrained by their radial brightness profiles? *A&A*, 507:1503–1516.

Krivov, A. V., Löhne, T., and Sremčević, M. (2006). Dust distributions in debris disks: effects of gravity, radiation pressure and collisions. *A&A*, 455:509–519.

Lada, C. J. and Wilking, B. A. (1984). The nature of the embedded population in the Rho Ophiuchi dark cloud - Mid-infrared observations. *ApJ*, 287:610–621.

Lagrange, A., Bonnefoy, M., Chauvin, G., Apai, D., Ehrenreich, D., Boccaletti, A., Gratadour, D., Rouan, D., Mouillet, D., Lacour, S., and Kasper, M. (2010). A Giant Planet Imaged in the Disk of the Young Star β Pictoris. *Science*, 329:57–.

Laor, A. and Draine, B. T. (1993). Spectroscopic constraints on the properties of dust in active galactic nuclei. *ApJ*, 402:441–468.

Laplace, P. S. (1796). Exposition du systeme du monde.

Larson, R. B. (1981). Turbulence and star formation in molecular clouds. *MNRAS*, 194:809–826.

Lebreton, J., Augereau, J.-C., Thi, W.-F., Roberge, A., Donaldson, J., Schneider, G., Maddison, S. T., Ménard, F., Riviere-Marichalar, P., Mathews, G. S., Kamp, I., Pinte, C., Dent, W. R. F., Barrado, D., Duchêne, G., Gonzalez, J.-F., Grady, C. A., Meeus, G., Pantin, E., Williams, J. P., and Woitke, P. (2012). An icy Kuiper belt around the young solar-type star HD 181327. *A&A*, 539:A17.

Lestrade, J.-F., Matthews, B. C., Sibthorpe, B., Kennedy, G. M., Wyatt, M. C., Bryden, G., Greaves, J. S., Thilliez, E., Moro-Martín, A., Booth, M., Dent, W. R. F., Duchêne, G., Harvey, P. M., Horner, J., Kalas, P., Kavelaars, J. J.,

Phillips, N. M., Rodriguez, D. R., Su, K. Y. L., and Wilner, D. J. (2012). A DEBRIS disk around the planet hosting M-star GJ 581 spatially resolved with Herschel. *A&A*, 548:A86.

Li, A. and Greenberg, J. M. (1998). A comet dust model for the beta Pictoris disk. *A&A*, 331:291–313.

Lisse, C. M., Chen, C. H., Wyatt, M. C., Morlok, A., Song, I., Bryden, G., and Sheehan, P. (2009). Abundant Circumstellar Silica Dust and SiO Gas Created by a Giant Hypervelocity Collision in the ˜12 Myr HD172555 System. *ApJ*, 701:2019–2032.

Löhne, T., Augereau, J.-C., Ertel, S., Marshall, J. P., Eiroa, C., Mora, A., Absil, O., Stapelfeldt, K., Thébault, P., Bayo, A., Del Burgo, C., Danchi, W., Krivov, A. V., Lebreton, J., Letawe, G., Magain, P., Maldonado, J., Montesinos, B., Pilbratt, G. L., White, G. J., and Wolf, S. (2012). Modelling the huge, Herschel-resolved debris ring around HD 207129. *A&A*, 537:A110.

Löhne, T., Krivov, A. V., and Rodmann, J. (2008). Long-Term Collisional Evolution of Debris Disks. *ApJ*, 673:1123–1137.

Lovis, C., Ségransan, D., Mayor, M., Udry, S., Benz, W., Bertaux, J.-L., Bouchy, F., Correia, A. C. M., Laskar, J., Lo Curto, G., Mordasini, C., Pepe, F., Queloz, D., and Santos, N. C. (2011). The HARPS search for southern extra-solar planets. XXVIII. Up to seven planets orbiting HD 10180: probing the architecture of low-mass planetary systems. *A&A*, 528:A112.

Low, F. J., Smith, P. S., Werner, M., Chen, C., Krause, V., Jura, M., and Hines, D. C. (2005). Exploring Terrestrial Planet Formation in the TW Hydrae Association. *ApJ*, 631:1170–1179.

Lowrance, P. J., Becklin, E. E., Schneider, G., Kirkpatrick, J. D., Weinberger, A. J., Zuckerman, B., Dumas, C., Beuzit, J.-L., Plait, P., Malumuth, E., Heap,

S., Terrile, R. J., and Hines, D. C. (2005). An Infrared Coronagraphic Survey for Substellar Companions. *AJ*, 130:1845–1861.

MacGregor, M. A., Wilner, D. J., Rosenfeld, K. A., Andrews, S. M., Matthews, B., Hughes, A. M., Booth, M., Chiang, E., Graham, J. R., Kalas, P., Kennedy, G., and Sibthorpe, B. (2013). Millimeter Emission Structure in the First ALMA Image of the AU Mic Debris Disk. *ApJ*, 762:L21.

Malo, L., Doyon, R., Lafrenière, D., Artigau, É., Gagné, J., Baron, F., and Riedel, A. (2013). Bayesian Analysis to Identify New Star Candidates in Nearby Young Stellar Kinematic Groups. *ApJ*, 762:88.

Mamajek, E. E. (2009). Initial Conditions of Planet Formation: Lifetimes of Primordial Disks. In Usuda, T., Tamura, M., and Ishii, M., editors, *American Institute of Physics Conference Series*, volume 1158 of *American Institute of Physics Conference Series*, pages 3–10.

Maness, H. L., Fitzgerald, M. P., Paladini, R., Kalas, P., Duchene, G., and Graham, J. R. (2008). CARMA Millimeter-Wave Aperture Synthesis Imaging of the HD 32297 Debris Disk. *ApJ*, 686:L25–L28.

Maness, H. L., Kalas, P., Peek, K. M. G., Chiang, E. I., Scherer, K., Fitzgerald, M. P., Graham, J. R., Hines, D. C., Schneider, G., and Metchev, S. A. (2009). Hubble Space Telescope Optical Imaging of the Eroding Debris Disk HD 61005. *ApJ*, 707:1098–1114.

Markwardt, C. B. (2009). Non-linear Least-squares Fitting in IDL with MPFIT. In D. A. Bohlender, D. Durand, & P. Dowler, editor, *Astronomical Society of the Pacific Conference Series*, volume 411 of *Astronomical Society of the Pacific Conference Series*, pages 251–+.

Marois, C., Macintosh, B., Barman, T., Zuckerman, B., Song, I., Patience, J., Lafrenière, D., and Doyon, R. (2008). Direct Imaging of Multiple Planets Orbiting

the Star HR 8799. *Science*, 322:1348–.

Marshall, J. P., Löhne, T., Montesinos, B., Krivov, A. V., Eiroa, C., Absil, O., Bryden, G., Maldonado, J., Mora, A., Sanz-Forcada, J., Ardila, D., Augereau, J.-C., Bayo, A., Del Burgo, C., Danchi, W., Ertel, S., Fedele, D., Fridlund, M., Lebreton, J., González-García, B. M., Liseau, R., Meeus, G., Müller, S., Pilbratt, G. L., Roberge, A., Stapelfeldt, K., Thébault, P., White, G. J., and Wolf, S. (2011). A Herschel resolved far-infrared dust ring around HD 207129. *A&A*, 529:A117.

Masciadri, E., Mundt, R., Henning, T., Alvarez, C., and Barrado y Navascués, D. (2005). A Search for Hot Massive Extrasolar Planets around Nearby Young Stars with the Adaptive Optics System NACO. *ApJ*, 625:1004–1018.

Mason, B. D., Wycoff, G. L., Hartkopf, W. I., Douglass, G. G., and Worley, C. E. (2001). The 2001 US Naval Observatory Double Star CD-ROM. I. The Washington Double Star Catalog. *AJ*, 122:3466–3471.

Mathews, G. S., Dent, W. R. F., Williams, J. P., Howard, C. D., Meeus, G., Riaz, B., Roberge, A., Sandell, G., Vandenbussche, B., Duchêne, G., Kamp, I., Ménard, F., Montesinos, B., Pinte, C., Thi, W. F., Woitke, P., Alacid, J. M., Andrews, S. M., Ardila, D. R., Aresu, G., Augereau, J. C., Barrado, D., Brittain, S., Ciardi, D. R., Danchi, W., Eiroa, C., Fedele, D., Grady, C. A., de Gregorio-Monsalvo, I., Heras, A., Huelamo, N., Krivov, A., Lebreton, J., Liseau, R., Martin-Zaidi, C., Mendigutía, I., Mora, A., Morales-Calderon, M., Nomura, H., Pantin, E., Pascucci, I., Phillips, N., Podio, L., Poelman, D. R., Ramsay, S., Rice, K., Riviere-Marichalar, P., Solano, E., Tilling, I., Walker, H., White, G. J., and Wright, G. (2010). GAS in Protoplanetary Systems (GASPS). I. First results. *A&A*, 518:L127+.

Mathews, G. S., Pinte, C., Duchêne, G., Williams, J. P., and Ménard, F. (2013).

A Herschel PACS survey of the dust and gas in Upper Scorpius disks. *A&A*, 558:A66.

Mathews, G. S., Williams, J. P., and Ménard, F. (2012). 880 μm Imaging of a Transitional Disk in Upper Scorpius: Holdover from the Era of Giant Planet Formation? *ApJ*, 753:59.

Matthews, B. C., Sibthorpe, B., Kennedy, G., Phillips, N., Churcher, L., Duchêne, G., Greaves, J. S., Lestrade, J., Moro-Martin, A., Wyatt, M. C., Bastien, P., Biggs, A., Bouvier, J., Butner, H. M., Dent, W. R. F., di Francesco, J., Eislöffel, J., Graham, J., Harvey, P., Hauschildt, P., Holland, W. S., Horner, J., Ibar, E., Ivison, R. J., Johnstone, D., Kalas, P., Kavelaars, J., Rodriguez, D., Udry, S., van der Werf, P., Wilner, D., and Zuckerman, B. (2010). Resolving debris discs in the far-infrared: Early highlights from the DEBRIS survey. *A&A*, 518:L135+.

Mawet, D., Serabyn, E., Stapelfeldt, K., and Crepp, J. (2009). Imaging the Debris Disk of HD 32297 with a Phase-Mask Coronagraph at High Strehl Ratio. *ApJ*, 702:L47–L50.

Mayor, M. and Queloz, D. (1995). A Jupiter-mass companion to a solar-type star. *Nature*, 378:355–359.

McCarthy, C., Butler, R. P., Tinney, C. G., Jones, H. R. A., Marcy, G. W., Carter, B., Penny, A. J., and Fischer, D. A. (2004). Multiple Companions to HD 154857 and HD 160691. *ApJ*, 617:575–579.

McKee, C. F. and Ostriker, E. C. (2007). Theory of Star Formation. *ARA&A*, 45:565–687.

Meeus, G., Montesinos, B., Mendigutía, I., Kamp, I., Thi, W. F., Eiroa, C., Grady, C. A., Mathews, G., Sandell, G., Martin-Zaïdi, C., Brittain, S., Dent, W. R. F., Howard, C., Ménard, F., Pinte, C., Roberge, A., Vandenbussche, B., and Williams, J. P. (2012). Observations of Herbig Ae/Be stars with Herschel/PACS.

The atomic and molecular contents of their protoplanetary discs. *A&A*, 544:A78.

Metchev, S. A. and Hillenbrand, L. A. (2009). The Palomar/Keck Adaptive Optics Survey of Young Solar Analogs: Evidence for a Universal Companion Mass Function. *ApJS*, 181:62–109.

Meyer, M. R., Hillenbrand, L. A., Backman, D., Beckwith, S., Bouwman, J., Brooke, T., Carpenter, J., Cohen, M., Cortes, S., Crockett, N., Gorti, U., Henning, T., Hines, D., Hollenbach, D., Kim, J. S., Lunine, J., Malhotra, R., Mamajek, E., Metchev, S., Moro-Martin, A., Morris, P., Najita, J., Padgett, D., Pascucci, I., Rodmann, J., Schlingman, W., Silverstone, M., Soderblom, D., Stauffer, J., Stobie, E., Strom, S., Watson, D., Weidenschilling, S., Wolf, S., and Young, E. (2006). The Formation and Evolution of Planetary Systems: Placing Our Solar System in Context with Spitzer. *PASP*, 118:1690–1710.

Meyer, M. R., Hillenbrand, L. A., Backman, D. E., Beckwith, S. V. W., Bouwman, J., Brooke, T. Y., Carpenter, J. M., Cohen, M., Gorti, U., Henning, T., Hines, D. C., Hollenbach, D., Kim, J. S., Lunine, J., Malhotra, R., Mamajek, E. E., Metchev, S., Moro-Martin, A., Morris, P., Najita, J., Padgett, D. L., Rodmann, J., Silverstone, M. D., Soderblom, D. R., Stauffer, J. R., Stobie, E. B., Strom, S. E., Watson, D. M., Weidenschilling, S. J., Wolf, S., Young, E., Engelbracht, C. W., Gordon, K. D., Misselt, K., Morrison, J., Muzerolle, J., and Su, K. (2004). The Formation and Evolution of Planetary Systems: First Results from a Spitzer Legacy Science Program. *ApJS*, 154:422–427.

Mie, G. (1908). Beiträge zur Optik trüber Medien, speziell kolloidaler Metallösungen. *Annalen der Physik*, 330:377–445.

Milli, J., Mouillet, D., Lagrange, A.-M., Boccaletti, A., Mawet, D., Chauvin, G., and Bonnefoy, M. (2012). Impact of angular differential imaging on circumstellar disk images. *A&A*, 545:A111.

Mizuno, H. (1980). Formation of the Giant Planets. *Progress of Theoretical Physics*, 64:544–557.

Moerchen, M. M., Telesco, C. M., De Buizer, J. M., Packham, C., and Radomski, J. T. (2007). 12 and 18 μm Images of Dust Surrounding HD 32297. *ApJ*, 666:L109–L112.

Moór, A., Ábrahám, P., Derekas, A., Kiss, C., Kiss, L. L., Apai, D., Grady, C., and Henning, T. (2006). Nearby Debris Disk Systems with High Fractional Luminosity Reconsidered. *ApJ*, 644:525–542.

Moór, A., Apai, D., Pascucci, I., Ábrahám, P., Grady, C., Henning, T., Juhász, A., Kiss, C., and Kóspál, Á. (2009). The Discovery of New Warm Debris Disks Around F-type Stars. *ApJ*, 700:L25–L29.

Morales, F. Y., Rieke, G. H., Werner, M. W., Bryden, G., Stapelfeldt, K. R., and Su, K. Y. L. (2011). Common Warm Dust Temperatures Around Main-sequence Stars. *ApJ*, 730:L29.

Morales, F. Y., Werner, M. W., Bryden, G., Plavchan, P., Stapelfeldt, K. R., Rieke, G. H., Su, K. Y. L., Beichman, C. A., Chen, C. H., Grogan, K., Kenyon, S. J., Moro-Martin, A., and Wolf, S. (2009). Spitzer Mid-IR Spectra of Dust Debris Around A and Late B Type Stars: Asteroid Belt Analogs and Power-Law Dust Distributions. *ApJ*, 699:1067–1086.

Morbidelli, A., Chambers, J., Lunine, J. I., Petit, J. M., Robert, F., Valsecchi, G. B., and Cyr, K. E. (2000). Source regions and time scales for the delivery of water to Earth. *Meteoritics and Planetary Science*, 35:1309–1320.

Moro-Martín, A. and Malhotra, R. (2005). Dust Outflows and Inner Gaps Generated by Massive Planets in Debris Disks. *ApJ*, 633:1150–1167.

Moshir, M., Kopman, G., and Conrow, T. A. O. (1992). *IRAS Faint Source Survey, Explanatory supplement version 2*.

Mouillet, D., Larwood, J. D., Papaloizou, J. C. B., and Lagrange, A. M. (1997). A planet on an inclined orbit as an explanation of the warp in the Beta Pictoris disc. *MNRAS*, 292:896–+.

Mulders, G. D., Min, M., Dominik, C., Debes, J. H., and Schneider, G. (2013). Why circumstellar disks are so faint in scattered light: the case of HD 100546. *A&A*, 549:A112.

Mustill, A. J. and Wyatt, M. C. (2009). Debris disc stirring by secular perturbations from giant planets. *MNRAS*, 399:1403–1414.

Najita, J. and Williams, J. P. (2005). An 850 μm Survey for Dust around Solar-Mass Stars. *ApJ*, 635:625–635.

Najita, J. R., Strom, S. E., and Muzerolle, J. (2007). Demographics of transition objects. *MNRAS*, 378:369–378.

Nilsson, R., Liseau, R., Brandeker, A., Olofsson, G., Pilbratt, G. L., Risacher, C., Rodmann, J., Augereau, J.-C., Bergman, P., Eiroa, C., Fridlund, M., Thébault, P., and White, G. J. (2010). Kuiper belts around nearby stars. *A&A*, 518:A40.

Nilsson, R., Liseau, R., Brandeker, A., Olofsson, G., Risacher, C., Fridlund, M., and Pilbratt, G. (2009). A submillimetre search for cold extended debris disks in the β Pictoris moving group. *A&A*, 508:1057–1065.

Ott, S. (2010). The Herschel Data Processing System – HIPE and Pipelines – Up and Running Since the Start of the Mission. In Y. Mizumoto, K.-I. Morita, & M. Ohishi, editor, *Astronomical Data Analysis Software and Systems XIX*, volume 434 of *Astronomical Society of the Pacific Conference Series*, page 139.

Oudmaijer, R. D., van der Veen, W. E. C. J., Waters, L. B. F. M., Trams, N. R., Waelkens, C., and Engelsman, E. (1992). SAO stars with infrared excess in the IRAS Point Source Catalog. *A&AS*, 96:625–643.

Paardekooper, S.-J. and Mellema, G. (2004). Planets opening dust gaps in gas disks.

A&A, 425:L9–L12.

Pawellek, N., Krivov, A. V., Marshall, J. P., Montensinos, B., Ábrahám, P., Bryden, G., Moór, A., and Eiroa, C. (2014). Dust grain sizes in Herschel-resolved debris disks. submitted.

Pecaut, M. J., Mamajek, E. E., and Bubar, E. J. (2012). A Revised Age for Upper Scorpius and the Star Formation History among the F-type Members of the Scorpius-Centaurus OB Association. *ApJ*, 746:154.

Pepin, R. O. (2006). Atmospheres on the terrestrial planets: Clues to origin and evolution. *Earth and Planetary Science Letters*, 252:1–14.

Perri, F. and Cameron, A. G. W. (1974). Hydrodynamic instability of the solar nebula in the presence of a planetary core. *Icarus*, 22:416–425.

Perryman, M. A. C. and ESA, editors (1997). *The HIPPARCOS and TYCHO catalogues. Astrometric and photometric star catalogues derived from the ESA HIPPARCOS Space Astrometry Mission*, volume 1200 of *ESA Special Publication*.

Petigura, E. A., Howard, A. W., and Marcy, G. W. (2013). Prevalence of Earth-size planets orbiting Sun-like stars. *Proceedings of the National Academy of Science*, 110:19273–19278.

Pilbratt, G. L., Riedinger, J. R., Passvogel, T., Crone, G., Doyle, D., Gageur, U., Heras, A. M., Jewell, C., Metcalfe, L., Ott, S., and Schmidt, M. (2010). Herschel Space Observatory. An ESA facility for far-infrared and submillimetre astronomy. *A&A*, 518:L1+.

Poglitsch, A., Waelkens, C., Geis, N., Feuchtgruber, H., Vandenbussche, B., Rodriguez, L., Krause, O., Renotte, E., van Hoof, C., Saraceno, P., Cepa, J., Kerschbaum, F., Agnèse, P., Ali, B., Altieri, B., Andreani, P., Augueres, J., Balog, Z., Barl, L., Bauer, O. H., Belbachir, N., Benedettini, M., Billot, N., Boulade, O., Bischof, H., Blommaert, J., Callut, E., Cara, C., Cerulli, R., Cesarsky, D., Con-

tursi, A., Creten, Y., De Meester, W., Doublier, V., Doumayrou, E., Duband, L., Exter, K., Genzel, R., Gillis, J., Grözinger, U., Henning, T., Herreros, J., Huygen, R., Inguscio, M., Jakob, G., Jamar, C., Jean, C., de Jong, J., Katterloher, R., Kiss, C., Klaas, U., Lemke, D., Lutz, D., Madden, S., Marquet, B., Martignac, J., Mazy, A., Merken, P., Montfort, F., Morbidelli, L., Müller, T., Nielbock, M., Okumura, K., Orfei, R., Ottensamer, R., Pezzuto, S., Popesso, P., Putzeys, J., Regibo, S., Reveret, V., Royer, P., Sauvage, M., Schreiber, J., Stegmaier, J., Schmitt, D., Schubert, J., Sturm, E., Thiel, M., Tofani, G., Vavrek, R., Wetzstein, M., Wieprecht, E., and Wiezorrek, E. (2010). The Photodetector Array Camera and Spectrometer (PACS) on the Herschel Space Observatory. *A&A*, 518:L2+.

Pollack, J. B., Hubickyj, O., Bodenheimer, P., Lissauer, J. J., Podolak, M., and Greenzweig, Y. (1996). Formation of the Giant Planets by Concurrent Accretion of Solids and Gas. *Icarus*, 124:62–85.

Preibisch, T., Brown, A. G. A., Bridges, T., Guenther, E., and Zinnecker, H. (2002). Exploring the Full Stellar Population of the Upper Scorpius OB Association. *AJ*, 124:404–416.

Preibisch, T. and Zinnecker, H. (1999). The History of Low-Mass Star Formation in the Upper Scorpius OB Association. *AJ*, 117:2381–2397.

Press, W. H., Teukolsky, S. A., Vetterling, W. T., and Flannery, B. P. (1992). *Numerical recipes in C (2nd ed.): the art of scientific computing*. Cambridge University Press, New York, NY, USA.

Press, W. H., Teukolsky, S. A., Vetterling, W. T., and Flannery, B. P. (1992). *Numerical recipes in C. The art of scientific computing*.

Qi, C., Ho, P. T. P., Wilner, D. J., Takakuwa, S., Hirano, N., Ohashi, N., Bourke, T. L., Zhang, Q., Blake, G. A., Hogerheijde, M., Saito, M., Choi, M., and Yang, J. (2004). Imaging the Disk around TW Hydrae with the Submillimeter Array.

ApJ, 616:L11–L14.

Quillen, A. C. (2006). Predictions for a planet just inside Fomalhaut's eccentric ring. *MNRAS*, 372:L14–L18.

Rafikov, R. R. (2005). Can Giant Planets Form by Direct Gravitational Instability? *ApJ*, 621:L69–L72.

Rebull, L. M., Stapelfeldt, K. R., Werner, M. W., Mannings, V. G., Chen, C., Stauffer, J. R., Smith, P. S., Song, I., Hines, D., and Low, F. J. (2008). Spitzer MIPS Observations of Stars in the β Pictoris Moving Group. *ApJ*, 681:1484–1504.

Redfield, S. (2007). Gas Absorption Detected from the Edge-on Debris Disk Surrounding HD 32297. *ApJ*, 656:L97–L100.

Reidemeister, M., Krivov, A. V., Stark, C. C., Augereau, J.-C., Löhne, T., and Müller, S. (2011). The cold origin of the warm dust around ϵ Eridani. *A&A*, 527:A57.

Rice, W. K. M., Lodato, G., Pringle, J. E., Armitage, P. J., and Bonnell, I. A. (2006). Planetesimal formation via fragmentation in self-gravitating protoplanetary discs. *MNRAS*, 372:L9–L13.

Rieke, G. H., Su, K. Y. L., Stansberry, J. A., Trilling, D., Bryden, G., Muzerolle, J., White, B., Gorlova, N., Young, E. T., Beichman, C. A., Stapelfeldt, K. R., and Hines, D. C. (2005). Decay of Planetary Debris Disks. *ApJ*, 620:1010–1026.

Rieke, G. H., Young, E. T., Engelbracht, C. W., Kelly, D. M., Low, F. J., Haller, E. E., Beeman, J. W., Gordon, K. D., Stansberry, J. A., Misselt, K. A., Cadien, J., Morrison, J. E., Rivlis, G., Latter, W. B., Noriega-Crespo, A., Padgett, D. L., Stapelfeldt, K. R., Hines, D. C., Egami, E., Muzerolle, J., Alonso-Herrero, A., Blaylock, M., Dole, H., Hinz, J. L., Le Floc'h, E., Papovich, C., Pérez-González, P. G., Smith, P. S., Su, K. Y. L., Bennett, L., Frayer, D. T., Henderson, D., Lu, N., Masci, F., Pesenson, M., Rebull, L., Rho, J., Keene, J., Stolovy, S., Wachter,

S., Wheaton, W., Werner, M. W., and Richards, P. L. (2004). The Multiband Imaging Photometer for Spitzer (MIPS). *ApJS*, 154:25–29.

Riviere-Marichalar, P., Barrado, D., Augereau, J.-C., Thi, W. F., Roberge, A., Eiroa, C., Montesinos, B., Meeus, G., Howard, C., Sandell, G., Duchêne, G., Dent, W. R. F., Lebreton, J., Mendigutía, I., Huélamo, N., Ménard, F., and Pinte, C. (2012). HD 172555: detection of 63 μm [OI] emission in a debris disc. *A&A*, 546:L8.

Riviere-Marichalar, P., Barrado, D., Montesinos, B., Duchêne, G., Bouy, H., Pinte, C., Menard, F., Donaldson, J., Eiroa, C., Krivov, A. V., Kamp, I., Mendigutía, I., Dent, W. R. F., and Lillo-Box, J. (2014). Gas and dust in the Beta Pictoris Moving Group as seen by the Herschel Space Observatory. *ArXiv e-prints*.

Riviere-Marichalar, P., Pinte, C., Barrado, D., Thi, W. F., Eiroa, C., Kamp, I., Montesinos, B., Donaldson, J., Augereau, J. C., Huélamo, N., Roberge, A., Ardila, D., Sandell, G., Williams, J. P., Dent, W. R. F., Menard, F., Lillo-Box, J., and Duchêne, G. (2013). Gas and dust in the TW Hydrae association as seen by the Herschel Space Observatory. *A&A*, 555:A67.

Roberge, A., Feldman, P. D., Weinberger, A. J., Deleuil, M., and Bouret, J.-C. (2006). Stabilization of the disk around βPictoris by extremely carbon-rich gas. *Nature*, 441:724–726.

Roberge, A. and Kamp, I. (2010). Protoplanetary & Debris Disks. In S. Seager, editor, *Exoplanets*, pages 269–295.

Roberge, A. and Kamp, I. (2011). *Protoplanetary and Debris Disks*, pages 269–295.

Roberge, A., Kamp, I., Montesinos, B., Dent, W. R. F., Meeus, G., Donaldson, J. K., Olofsson, J., Moór, A., Augereau, J.-C., Howard, C., Eiroa, C., Thi, W.-F., Ardila, D. R., Sandell, G., and Woitke, P. (2013). Herschel Observations of Gas and Dust in the Unusual 49 Ceti Debris Disk. *ApJ*, 771:69.

Roberge, A., Montesinos, B., and Kamp, I. (2012). Herschel observations of gas and dust in the unusual 49 Ceti circumstellar disk. *ApJ.* submitted.

Roberge, A., Weinberger, A. J., and Malumuth, E. M. (2005). Spatially Resolved Spectroscopy and Coronagraphic Imaging of the TW Hydrae Circumstellar Disk. *ApJ*, 622:1171–1181.

Rodigas, T. J., Debes, J. H., Hinz, P. M., Mamajek, E. E., Pecaut, M. J., Currie, T., Bailey, V., Defrere, D., De Rosa, R. J., Hill, J. M., Leisenring, J., Schneider, G., Skemer, A. J., Skrutskie, M., Vaitheeswaran, V., and Ward-Duong, K. (2014). Does the Debris Disk around HD 32297 Contain Cometary Grains? *ApJ*, 783:21.

Rodigas, T. J., Hinz, P. M., Leisenring, J., Vaitheeswaran, V., Skemer, A. J., Skrutskie, M., Su, K. Y. L., Bailey, V., Schneider, G., Close, L., Mannucci, F., Esposito, S., Arcidiacono, C., Pinna, E., Argomedo, J., Agapito, G., Apai, D., Bono, G., Boutsia, K., Briguglio, R., Brusa, G., Busoni, L., Cresci, G., Currie, T., Desidera, S., Eisner, J., Falomo, R., Fini, L., Follette, K., Fontana, A., Garnavich, P., Gratton, R., Green, R., Guerra, J. C., Hill, J. M., Hoffmann, W. F., Jones, T. J., Krejny, M., Kulesa, C., Males, J., Masciadri, E., Mesa, D., McCarthy, D., Meyer, M., Miller, D., Nelson, M. J., Puglisi, A., Quiros-Pacheco, F., Riccardi, A., Sani, E., Stefanini, P., Testa, V., Wilson, J., Woodward, C. E., and Xompero, M. (2012). The Gray Needle: Large Grains in the HD 15115 Debris Disk from LBT/PISCES/Ks and LBTI/LMIRcam/L' Adaptive Optics Imaging. *ApJ*, 752:57.

Rodriguez, D. R. and Zuckerman, B. (2012). Binaries among Debris Disk Stars. *ApJ*, 745:147.

Schneider, G. and HST/GO 12228 Team (2013). Probing for Exoplanets Hiding in Dusty Debris Disks III: Disk Imaging, Characterization, and Exploration with HST/STIS Multi-Roll Coronagraphy - Completing the Survey. In *American Astro-*

nomical Society Meeting Abstracts, volume 221 of *American Astronomical Society Meeting Abstracts*, page 104.05.

Schneider, G., Silverstone, M. D., and Hines, D. C. (2005). Discovery of a Nearly Edge-on Disk around HD 32297. *ApJ*, 629:L117–L120.

Schneider, G., Silverstone, M. D., Hines, D. C., Augereau, J., Pinte, C., Ménard, F., Krist, J., Clampin, M., Grady, C., Golimowski, D., Ardila, D., Henning, T., Wolf, S., and Rodmann, J. (2006). Discovery of an 86 AU Radius Debris Ring around HD 181327. *ApJ*, 650:414–431.

Shu, F. H., Adams, F. C., and Lizano, S. (1987). Star formation in molecular clouds - Observation and theory. *ARA&A*, 25:23–81.

Smith, B. A. and Terrile, R. J. (1984). A circumstellar disk around Beta Pictoris. *Science*, 226:1421–1424.

Smith, P. S., Hines, D. C., Low, F. J., Gehrz, R. D., Polomski, E. F., and Woodward, C. E. (2006). Spitzer Far-Infrared Detections of Cold Circumstellar Disks. *ApJ*, 644:L125–L128.

Smith, R. and Wyatt, M. C. (2010). Warm dusty discs: exploring the A star 24 μm debris population. *A&A*, 515:A95+.

Spangler, C., Sargent, A. I., Silverstone, M. D., Becklin, E. E., and Zuckerman, B. (2001). Dusty Debris around Solar-Type Stars: Temporal Disk Evolution. *ApJ*, 555:932–944.

Stark, C. C. and Kuchner, M. J. (2008). The Detectability of Exo-Earths and Super-Earths Via Resonant Signatures in Exozodiacal Clouds. *ApJ*, 686:637–648.

Stark, C. C. and Kuchner, M. J. (2009). A New Algorithm for Self-consistent Three-dimensional Modeling of Collisions in Dusty Debris Disks. *ApJ*, 707:543–553.

Stark, C. C., Schneider, G., Weinberger, A. J., Debes, J. H., Grady, C. A., Jang-Condell, H., and Kuchner, M. J. (2014). Revealing Asymmetries in the HD 181327

Debris Disk: A Recent Massive Collision or ISM Warping. *ArXiv e-prints*.

Stewart, S. T. and Leinhardt, Z. M. (2009). Velocity-Dependent Catastrophic Disruption Criteria for Planetesimals. *ApJ*, 691:L133–L137.

Strubbe, L. E. and Chiang, E. I. (2006). Dust Dynamics, Surface Brightness Profiles, and Thermal Spectra of Debris Disks: The Case of AU Microscopii. *ApJ*, 648:652–665.

Su, K. Y. L., Rieke, G. H., Malhotra, R., Stapelfeldt, K. R., Hughes, A. M., Bonsor, A., Wilner, D. J., Balog, Z., Watson, D. M., Werner, M. W., and Misselt, K. A. (2013). Asteroid Belts in Debris Disk Twins: Vega and Fomalhaut. *ApJ*, 763:118.

Su, K. Y. L., Rieke, G. H., Stansberry, J. A., Bryden, G., Stapelfeldt, K. R., Trilling, D. E., Muzerolle, J., Beichman, C. A., Moro-Martin, A., Hines, D. C., and Werner, M. W. (2006). Debris Disk Evolution around A Stars. *ApJ*, 653:675–689.

Swift, J. J., Johnson, J. A., Morton, T. D., Crepp, J. R., Montet, B. T., Fabrycky, D. C., and Muirhead, P. S. (2013). Characterizing the Cool KOIs. IV. Kepler-32 as a Prototype for the Formation of Compact Planetary Systems throughout the Galaxy. *ApJ*, 764:105.

Telesco, C. M. and Knacke, R. F. (1991). Detection of silicates in the Beta Pictoris disk. *ApJ*, 372:L29–L31.

Thébault, P., Augereau, J. C., and Beust, H. (2003). Dust production from collisions in extrasolar planetary systems. The inner beta Pictoris disc. *A&A*, 408:775–788.

Thébault, P. and Wu, Y. (2008). Outer edges of debris discs. How sharp is sharp? *A&A*, 481:713–724.

Thi, W. F., Blake, G. A., van Dishoeck, E. F., van Zadelhoff, G. J., Horn, J. M. M., Becklin, E. E., Mannings, V., Sargent, A. I., van den Ancker, M. E., and Natta, A. (2001). Substantial reservoirs of molecular hydrogen in the debris disks around young stars. *Nature*, 409:60–63.

Toomre, A. (1981). What amplifies the spirals. In Fall, S. M. and Lynden-Bell, D., editors, *Structure and Evolution of Normal Galaxies*, pages 111–136.

Torres, C. A. O., da Silva, L., Quast, G. R., de la Reza, R., and Jilinski, E. (2000). A New Association of Post-T Tauri Stars near the Sun. *AJ*, 120:1410–1425.

Torres, C. A. O., Quast, G. R., da Silva, L., de La Reza, R., Melo, C. H. F., and Sterzik, M. (2006). Search for associations containing young stars (SACY). I. Sample and searching method. *A&A*, 460:695–708.

van Leeuwen, F. (2007). Validation of the new Hipparcos reduction. *A&A*, 474:653–664.

Wahhaj, Z., Liu, M. C., Biller, B. A., Nielsen, E. L., Hayward, T. L., Kuchner, M., Close, L. M., Chun, M., Ftaclas, C., and Toomey, D. W. (2014). The Gemini NICI Planet-Finding Campaign: The Offset Ring of HR 4796 A. *ArXiv e-prints*.

Weidenschilling, S. J. (1977). The distribution of mass in the planetary system and solar nebula. *Ap&SS*, 51:153–158.

Weidenschilling, S. J., Spaute, D., Davis, D. R., Marzari, F., and Ohtsuki, K. (1997). Accretional Evolution of a Planetesimal Swarm. *Icarus*, 128:429–455.

Weingartner, J. C. and Draine, B. T. (2001). Dust Grain-Size Distributions and Extinction in the Milky Way, Large Magellanic Cloud, and Small Magellanic Cloud. *ApJ*, 548:296–309.

Wetherill, G. W. and Stewart, G. R. (1989). Accumulation of a swarm of small planetesimals. *Icarus*, 77:330–357.

Wetherill, G. W. and Stewart, G. R. (1993). Formation of planetary embryos - Effects of fragmentation, low relative velocity, and independent variation of eccentricity and inclination. *Icarus*, 106:190.

Wiechert, U., Halliday, A. N., Lee, D.-C., Snyder, G. A., Taylor, L. A., and Rumble, D. (2001). Oxygen Isotopes and the Moon-Forming Giant Impact. *Science*,

294:345–348.

Williams, J. P. and Andrews, S. M. (2006). The Dust Properties of Eight Debris Disk Candidates as Determined by Submillimeter Photometry. *ApJ*, 653:1480–1485.

Williams, J. P. and Cieza, L. A. (2011). Protoplanetary Disks and Their Evolution. *ARA&A*, 49:67–117.

Wolf, S. and Hillenbrand, L. A. (2003). Model Spectral Energy Distributions of Circumstellar Debris Disks. I. Analytic Disk Density Distributions. *ApJ*, 596:603–620.

Wright, E. L., Eisenhardt, P. R. M., Mainzer, A. K., Ressler, M. E., Cutri, R. M., Jarrett, T., Kirkpatrick, J. D., Padgett, D., McMillan, R. S., Skrutskie, M., Stanford, S. A., Cohen, M., Walker, R. G., Mather, J. C., Leisawitz, D., Gautier, III, T. N., McLean, I., Benford, D., Lonsdale, C. J., Blain, A., Mendez, B., Irace, W. R., Duval, V., Liu, F., Royer, D., Heinrichsen, I., Howard, J., Shannon, M., Kendall, M., Walsh, A. L., Larsen, M., Cardon, J. G., Schick, S., Schwalm, M., Abid, M., Fabinsky, B., Naes, L., and Tsai, C.-W. (2010). The Wide-field Infrared Survey Explorer (WISE): Mission Description and Initial On-orbit Performance. *AJ*, 140:1868–1881.

Wyatt, M. C. (2003). Resonant Trapping of Planetesimals by Planet Migration: Debris Disk Clumps and Vega's Similarity to the Solar System. *ApJ*, 598:1321–1340.

Wyatt, M. C. (2005). The insignificance of P-R drag in detectable extrasolar planetesimal belts. *A&A*, 433:1007–1012.

Wyatt, M. C., Clarke, C. J., and Booth, M. (2011). Debris disk size distributions: steady state collisional evolution with Poynting-Robertson drag and other loss processes. *Celestial Mechanics and Dynamical Astronomy*, 111:1–28.

Wyatt, M. C., Kennedy, G., Sibthorpe, B., Moro-Martín, A., Lestrade, J.-F., Ivison,

R. J., Matthews, B., Udry, S., Greaves, J. S., Kalas, P., Lawler, S., Su, K. Y. L., Rieke, G. H., Booth, M., Bryden, G., Horner, J., Kavelaars, J. J., and Wilner, D. (2012). Herschel imaging of 61 Vir: implications for the prevalence of debris in low-mass planetary systems. *MNRAS*, 424:1206–1223.

Yamamura, I., Makiuti, S., Ikeda, N., Fukuda, Y., Oyabu, S., Koga, T., and White, G. J. (2010). AKARI/FIS All-Sky Survey Point Source Catalogues (ISAS/JAXA, 2010). *VizieR Online Data Catalog*, 2298:0.

Zubko, V. G., Mennella, V., Colangeli, L., and Bussoletti, E. (1996). Optical constants of cosmic carbon analogue grains - I. Simulation of clustering by a modified continuous distribution of ellipsoids. *MNRAS*, 282:1321–1329.

Zuckerman, B., Forveille, T., and Kastner, J. H. (1995). Inhibition of giant-planet formation by rapid gas depletion around young stars. *Nature*, 373:494–496.

Zuckerman, B., Rhee, J. H., Song, I., and Bessell, M. S. (2011). The Tucana/Horologium, Columba, AB Doradus, and Argus Associations: New Members and Dusty Debris Disks. *ApJ*, 732:61.

Zuckerman, B. and Song, I. (2004). Young Stars Near the Sun. *ARA&A*, 42:685–721.

Zuckerman, B. and Webb, R. A. (2000). Identification of a Nearby Stellar Association in theHipparcos Catalog: Implications for Recent, Local Star Formation. *ApJ*, 535:959–964.